Characterization of scattering mechanisms in soil and vegetation for roughness and moisture estimation using active and passive microwave observations

Cumulative Dissertation

for the attainment of the degree of

Doctor of Natural Sciences (Dr. rer. nat.)

at the

Faculty of Applied Computer Science

of the

University of Augsburg

by

M.Sc. Anke Fluhrer

May 2024

First Examiner:	Prof. Dr. Harald Kunstmann
Second Examiner:	Prof. Dr. Wolfgang Buermann
Third Examiner:	Prof. Dr. Jian Peng
Date of oral exam:	06/06/2025

TABLE OF CONTENTS

TABLE OF FIGURES

Acknowledgments

I would like to take this opportunity and express my sincere thanks to the following people, without whose help the preparation of this PhD thesis would never have been possible:

My most sincere gratitude has to go to one of the best supervisors I ever had in my entire academic career: Dr. Thomas Jagdhuber. Without his unconditional support, admirable dedication to science, and introduction to the research community, I would not be at this point today. Thank you for always encouraging and supporting me. I really appreciate working with you and hope that we will continue researching together for a long time to come.

Not less do I thank my supervisor Prof. Dr. Harald Kunstmann, who has always supported me and introduced me to research at high level. His ability for quick comprehension and apparently endless expertise are admirable and desirable.

I would like to thank Prof. Dr. Wolfgang Buermann and Prof. Dr. Jian Peng for their helpful and scientific support as my examiners. I greatly appreciate your efforts.

I would also like to thank the entire team at the HR institute of the DLR for constantly broadening my knowledge of microwave frequency technology, for simply allowing me to do what I enjoy so much, and for their uncompromising support.

Without my family, this work would not have been possible in the first place and I would not be the person I am today. Therefore, my infinite thanks and gratitude go to my mother Iris, and my sisters Pia & Tamara. Thank you very much for always supporting and motivating me to try my very best.

Abstract

The complexity of our Earth system makes the investigation of its critical variables indispensable in order to understand the interrelationships and interactions of different sub-systems and processes in detail. Various parameters play a key role in the global weather and climate system of our Earth, as they control interactions and exchange processes as well as link the water, carbon, and energy cycles worldwide. Accordingly, the global determination and long-term monitoring of important geophysical parameters, such as soil moisture and soil surface roughness, is of significant relevance, especially in terms of, for instance, improving weather and climate forecasts, quantifying net carbon fluxes, and monitoring the condition assessment of existing infrastructures (e.g., roads).

In this PhD thesis, active and passive microwave remote sensing is exploited to estimate soil moisture and soil surface roughness. The associated methods developed herein and conducted analyses are of high importance, since the recording of geophysical parameters makes an essential contribution to climate and ecosystem research. This study is divided into three sub-studies. It addresses the possibility to close a research and knowledge gap in remote sensing and proposes new approaches in the field of microwave remote sensing for soil- and vegetation-related parameter estimation. The innovation of this study lies specifically in the detailed analysis of longwave microwaves of low frequencies (L- to P-band).

The first sub-study focused on a combined method of L-band radar and radiometer satellite observations for the simultaneous determination of soil surface roughness parameters on global and temporal continuous scales. It was found that the proposed covariation-based active-passive microwave retrieval algorithm for soil surface roughness estimation is independent of soil permittivity (soil moisture) inputs in non-arid areas (permittivity > 10 [-]). The determined surface roughness parameters correspond to local land surface conditions, e.g., rather smooth surfaces over non-vegetated, sandy and dry deserts, and rather rough surfaces at the edge of deserts, where smaller vegetation appears. Further, no correlations between roughness patterns and precipitation or soil texture could be found at the investigated scale.

In the second sub-study, low frequency (P-band) synthetic aperture radar (SAR) data are employed to investigate the penetration and scattering behavior of active microwaves interacting with different vegetation covers and soil types. The investigation relies on a proposed hybrid decomposition technique for separating the total SAR signal into individual scattering mechanisms (soil, dihedral, and volume), and is subsequently used for lateral soil moisture estimation in the upper root zone

(~20-30 cm) as well as P-band penetration depth calculations. The proposed moisture estimation approach is the first method (to the best of my knowledge) for estimating complex permittivity from microwave remote sensing. The method was validated at different monitoring sites across the United States and it was shown that P-band microwaves can penetrate up to 35 cm into the soil, depending on the local landcover and moisture conditions.

In the third sub-study, a combined approach of active microwave remote sensing and soil hydrological modeling is proposed for the determination of vertically continuous soil moisture profiles. For that, airborne P-band SAR data are compared to soil hydrological model simulations based on the HYDRUS-1D for estimating the vertical discontinuity and variability of soil moisture with depth. With this combined approach, vertically continuous soil moisture profiles can be estimated with medium to high Pearson's coefficients of determination (R^2 of 0.48 to 0.92).

In summary, innovative retrieval approaches are proposed for soil moisture and surface roughness estimation from microwave remote sensing. High consistencies between retrieval results and auxiliary data (*in situ*, model and reanalysis) confirm the feasibility of the proposed approaches. These approaches can be extended for future research, for example, in the prospect of upcoming P-band satellite missions – the BIOMASS mission of the European Space Agency (ESA) or the SigNals Of Opportunity P-band Investigation (SNOOPI) mission of the National Aeronautics and Space Administration (NASA).

Zusammenfassung

Die Komplexität unseres Erdsystems macht die Untersuchung wichtiger Variablen unverzichtbar, um Wechselbeziehungen und Interaktionen von Subsystemen und Prozessen im Detail zu verstehen. Verschiedene Parameter nehmen dabei eine Schlüsselrolle im globalen Wetter- und Klimasystem unserer Erde ein, da sie Wechselwirkungen und Austauschprozesse kontrollieren sowie die weltweiten Wasser-, Kohlenstoff- und Energiekreisläufe miteinander verbinden. Dementsprechend ist die globale Bestimmung und langfristige Überwachung wichtiger geophysikalischer Parameter, wie der Bodenfeuchte oder der Bodenoberflächenrauheit, von erheblicher Relevanz, insbesondere in Hinblick auf die Verbesserung von Wetter- und Klimavorhersagen, die Quantifizierung von Nettokohlenstoffflüssen oder die Überwachung der Beschaffenheit bestehender Infrastrukturen (z. B. Straßen).

In dieser Doktorarbeit werden Daten aus der aktiven und passiven Mikrowellen-Fernerkundung genutzt, um die Parameter Bodenfeuchte und Bodenoberflächenrauheit zu bestimmen. Die hierbei entwickelten Methoden und durchgeführten Analysen sind von hoher Bedeutung, da die Bestimmung geophysikalischer Parameter einen wesentlichen Beitrag zur Klima- und Ökosystemforschung leistet. Die vorgestellte Forschung ist unterteilt in drei Teilstudien. Sie adressiert die Möglichkeit, eine Forschungs- und Wissenslücke in der Fernerkundung zu schließen und schlägt neue Ansätze im Bereich der Mikrowellen-Fernerkundung für die Boden- und Vegetations-Parameterschätzung vor. Die Innovation dieser Forschungsarbeit liegt speziell in der detaillierten Analyse von langwelligen Mikrowellen bei niedrigen Frequenzen (L- bis P-Band).

Die erste Teilstudie konzentrierte sich auf die Entwicklung und Validierung einer kombinierten Methode von L-Band Radar- und Radiometer- Satellitendaten für die simultane Bestimmung der Bodenrauheit auf globaler und zeitlich kontinuierlicher Skala. Es wurde festgestellt, dass der vorgeschlagene Aktiv-Passiv-Mikrowellen-Ansatz zur Bestimmung von Bodenrauheitsparametern unabhängig von der Permittivität (Bodenfeuchte) in nicht ariden Regionen (Permittivität > 10 [-]) ist. Die resultierenden Rauhigkeitsparameter stimmen mit den lokalen Landoberflächenbedingungen überein, was bedeutet, dass eher geringe Oberflächenrauhigkeit über unbewachsenen, sandigen und trockenen Wüstenregionen und eher raue Oberflächen am Rande von Wüsten mit niedrige Vegetationsbeständen vorkommen. Darüber hinaus konnten keine Korrelationen zwischen Rauheitsmustern und Niederschlägen oder Bodentexturen gefunden werden.

In der zweiten Teilstudie werden Radardaten mit synthetischer Apertur (SAR) bei niedriger Frequenz (P-Band) verwendet, um das Eindringungs- und Streuverhalten von aktiven Mikrowellen zu untersuchen, und wie diese mit unterschiedlichen Vegetationsdeckungen und Bodentypen interagieren. Die Untersuchungen beruhen hierbei auf einer hybriden Zerlegungstechnik zur Separierung des gesamten SAR Signales in einzelne Streumechanismen (Boden, Dihedral und Volumen) und wird anschließend zur Abschätzung der lateralen Bodenfeuchte in der oberen Wurzelzone (~ 20-30 cm) sowie für die Bestimmung der möglichen Eindringtiefen von P-band Mikrowellen verwendet. Die vorgeschlagene Methode ist die erste (nach bestem Wissen) zur Bestimmung der komplexen Permittivität aus fernerkundlich bestimmten Mikrowellendaten. Die Methode wurde über verschiedenen Regionen der USA validiert und es konnte gezeigt werden, dass P-Band Mikrowellen, je nach lokaler Landbedeckung und Feuchtebedingung, bis zu 35 cm in den Boden eindringen können.

In der dritten Teilstudie wurde ein kombinierter Ansatz von aktiver Mikrowellenfernerkundung und hydrologischer Bodenmodellierung vorgeschlagen, um vertikal kontinuierliche Bodenfeuchteprofile zu bestimmen. Zu diesem Zweck wurden flugzeuggetragene SAR Daten mit hydrologischen Modellierungen (basierend auf HYDRUS-1D) verglichen, um die vertikale Diskontinuität und Variabilität der Bodenfeuchte mit der Tiefe zu bestimmen. Die Ergebnisse zeigen, dass mit dem kombinierten Ansatz vertikal kontinuierliche Bodenfeuchteprofile mit mittleren bis hohen Übereinstimmungen geschätzt werden können (R^2 von 0.48 bis 0.92).

Zusammenfassend werden in dieser Arbeit innovative Methoden für die Abschätzung von Bodenfeuchte und Oberflächenrauhigkeit aus der Mikrowellen-Fernerkundung vorgeschlagen. Dabei bestätigen hohe Übereinstimmungen zwischen den bestimmten Ergebnissen und Validierungs- oder Vergleichsdaten (*in situ*, Modell und Reanalyse) die Performance der vorgeschlagenen Methoden bestätigen. Die Methoden können für zukünftige Forschungen erweitert werden, beispielsweise in Hinblick auf bevorstehende P-Band-Satellitenmissionen - die Mission BIOMASS der Europäischen Weltraumagentur (ESA) oder Mission SigNals Of Opportunity P-band Investigation (SNOOPI) der National Aeronautics and Space Administration (NASA).

1 Background and Motivation

We still do not know one thousandth of one percent of what nature has revealed to us.

Albert Einstein

1.1 The role of the land surface in the climate system

The impact of the human-induced climate change is globally observable (Lansbury Hall and Crosby, 2022; Njagi et al., 2022; Reed et al., 2022). Global warming due to too high amounts of greenhouse gases in the atmosphere, such as carbon dioxide and methane, is slowly changing the climate and increasing weather extremes such as storms, floods, heat waves, droughts, and forest fires (Vereecken et al., 2022), with enormous consequences not only for millions of people but also flora and fauna. In earth science, based on the principles of mathematics, biology, chemistry, and physics, various disciplines, such as geology, meteorology, mineralogy, hydrology, and soil science (Dingman, 2015; Engelhardt and Zimmermann, 1988), are dedicated to the exploration of the earth system. The understanding of our Earth, its structure, constitution, processes, and how they are linked, is crucial when investigating and predicting the consequences of global climate change. The Intergovernmental Panel on Climate Change (IPCC) is using the expression 'climate change' to refer to all changes in the climate system over time due to an overall global warming, and confirms "with high confidence that human-induced climate change is the main driver" (IPCC, 2021). Climate change can already be witnessed by everyone, as weather extremes are becoming more frequent with impacts on our local and global climate. Hydrology is the earth science of water, studying the occurrence, distribution, and circulation of (fresh) water on Earth (Dingman, 2015; Ward and Robinson, 1990). The interdependent movement of fresh water on land is described by the concept of the hydrological cycle, including the spatial and temporal variations of water in the oceans and the atmosphere, "as well as the terrestrial compartments of the global water system" (Dingman, 2015). As the central component within the Earth's climate system at all spatial and temporal scales, the hydrological cycle helps to understand the relationship between various hydrological processes, such as precipitation, evaporation, runoff, and soil moisture (Dingman, 2015; Vereecken et al., 2022; Ward and Robinson, 1990).

In times of climate change and thus, the increasing vulnerability of the global ecosystem, the (long-term) monitoring and improved understanding of essential hydrological and environmental processes is crucial. In these processes, which are

related to water, energy, carbon, nutrient flux and exchange, land surface parameters, like soil moisture and soil surface roughness, play an important role, e.g., (Bojinski et al., 2014; Marzahn and Ludwig, 2009).

Soil moisture, as one of the essential climate variables (GCOS, 2015), has direct impact on the hydrological and biogeochemical cycles (Bojinski et al., 2014), although it represents less than 0.001 % of all available water on Earth (Dingman, 2015; McColl et al., 2017). This means, soil moisture has a direct impact on exchange processes of water and energy occurring at the boundary between the land surface and the atmosphere, such as infiltration, evaporation, and runoff (Srivastava et al., 2015). Further, the soil moisture state has influence on the ecosystem and its water supply and hence, the health of vegetation or agricultural plants, with direct impact on transpiration, local weather, microclimate, agricultural production, and lastly food security (Almendra-Martín et al., 2021; Vereecken et al., 2022). Additionally, soil moisture in the root zone (up to one meter) "is an important regulator of both the hydrological and energy cycle" (Peterson et al., 2016), influencing evapotranspiration and the water availability for the vegetation (Pablos et al., 2018; Peterson et al., 2016). As is evident, soil moisture significantly contributes to the characterization and modification of the Earth's climate (Bojinski et al., 2014) and, therefore, is of great importance in earth science, including hydrological, meteorological, ecological and agricultural applications (Alemohammad et al., 2018; Babaeian et al., 2019; Etminan et al., 2020; GCOS, 2015; Hoeben and Troch, 2000; Truong-Loi et al., 2015; Ward and Robinson, 1990). Similar to soil moisture, soil surface roughness, as the boundary condition between the pedosphere and the atmosphere defining the three-dimensional land surface geometry, plays an important role within environmental and hydrological exchange processes. It strongly influences water related processes like infiltration, evaporation, soil erosion, surface run off, and growth of plants (crops and vegetation) (Marzahn and Ludwig, 2009; Pan et al., 2018). In addition, soil roughness is, among others, an indispensable influencing factor in surface soil moisture research.

In summary, the global determination and long-term monitoring of geophysical variables relevant to the Earth system and its processes, such as soil moisture and soil surface roughness, is of significant importance, especially in terms of improving weather and climate forecasts, developing improved flood forecasting and drought monitoring capabilities, and quantifying net carbon fluxes. In addition to the climatological importance of such measurement data, knowledge on soil properties is also of paramount relevance for safety-related tasks. Examples of applications are the analysis of trafficability and condition of terrain in case of catastrophes, the temporal and spatial behavior of certain areas for ground exploration and terrain assessment in

case of large construction projects (e.g., highways, power lines, large industrial plants), as well as the condition assessment of existing infrastructures (e.g., roads).

The estimation and monitoring of these variables can be done with various tools and instruments at field scale (conventional), from remote, or by (hydrological) modeling. *In situ* field measurements of soil moisture can be conducted in units of volume, the volumetric moisture, or in units of mass, the gravimetric moisture. The latter is the default technique for estimating soil moisture at field scale (Wagner et al., 1999). Soil surface roughness can be measured with needle and laser profilers, mesh boards, as well as photogrammetry, e.g., (Álvarez-Mozos et al., 2009; Marzahn et al., 2012; Marzahn and Ludwig, 2009), which are invasive and often destroy the soil surface, leading to altered surface roughness. These direct methods of estimating moisture and roughness in the field are very time consuming, locally constrained, and cost intensive. Further, many regions on Earth are inaccessible for humans or of dangerous nature and cannot be entered easily. Lastly, *in situ* field measurements can only achieve data collections at point scale and are not available or representative over larger regions. Hence, there is a lack of spatial coverage and sometimes temporal continuity with field scale measured soil parameters.

Modeling of important soil parameters, like moisture, can be done with several hydrological and land surface models. These models simulate feedback processes between the land and the atmosphere as well as water, energy or nutrient transports and flows in a simplified way (in comparison to the complexity of nature). For one, models are always strongly dependent on the configured initialization as well as the quality and availability of the required input parameters that drive the model. Second, they need to provide transferability for the simulations to be generalizable and comparable when applying them to climate change research (Thirel et al., 2015). The latter is mostly the reason why model simulations are of coarse spatial resolution (Dirmeyer et al., 2016). Lastly, the in this study employed HYDRUS-1D (Šimůnek et al., 2013), as many hydrological models, numerically solves the Richards equation for describing water flow in variable saturated soils. The Richards equation is based on the mass conservation law, or continuity principle (Sadeghi et al., 2016), and the Darcy-Buckingham equation (Dingman, 2015) for describing unsaturated flow depending upon the saturated hydraulic conductivity, an additional proportionality factor, as well as the gradient of total hydraulic head (Bakker and Nieber, 2004; Dingman, 2015; Reichardt and Timm, 2020; Shukla, 2014). Due to the dependence of the hydraulic conductivity and the soil water content on the soil water pressure head, the equation is highly nonlinear. Hence, depending on the complexity, models are computationally expensive and require a considerable amount of processing time.

Remote sensing fills the gap between *in situ* field measurements and hydrological modeling since it is a powerful application for large-scale, temporal continuous soil parameter estimation and monitoring based on observations. It provides the opportunity to advance research on the impacts and consequences of human-induced climate change on regional and global scales, and can be used to enhance weather and climate forecast models (Dirmeyer et al., 2018; Koster et al., 2011). The exploration of the Earth's surface by means of remotely sensed information from unmanned aerial vehicles (UAV), airborne or spaceborne systems, e.g., (Alemohammad et al., 2018; Luo et al., 2019; McColl et al., 2017) has constantly evolved over the last decades and gained significant relevance.

In addition, it is to be noted that the three techniques (*in situ* field measurements, hydrological modeling, and remote sensing observations) can also be combined for various environmental and hydrological research objectives, such as assimilation of *in situ* or remote sensing data in models, e.g., (Montzka et al., 2013; Wagner et al., 2022).

1.2 Fundamentals of Active and Passive Microwave Remote Sensing

In order to detect and measure various objects of interest from remote, some kind of propagated signal, such as an optical or a radio wave is needed. The fields of optical and hyperspectral remote sensing have become powerful tools and are highly researched disciplines for classifying the Earth's landscape or analyzing the changes within ecosystems over time, e.g., (Gómez et al., 2016; Upadhyay and Kumar, 2018). A separate technique, besides optical and hyperspectral remote sensing, is microwave remote sensing, which is the technique employed in this study.

Microwaves are defined as electromagnetic waves in the frequency range from 300 MHz to 300 GHz of the electromagnetic spectrum (Lillesand et al., 2013). Microwave radiation is classified in different, historically conditioned frequency bands (Fig. 1). It is known that microwaves of different frequencies (wavelengths) have different penetration capabilities and scattering behavior on irradiated objects (Ulaby and Long, 2014). Depending on the wavelength (among others, such as sensor and land surface characteristics), microwaves can penetrate in or through vegetation, ice, and the land surface. Therefore, depending on the nature of the research objective, different frequency ranges are used. Environmental studies, military surveillance and reconnaissance, mapping of human activities as well as global change detection are only a few of the potential applications of microwave remote sensing (Schowengerdt, 2007). Currently, microwave sensors operate mainly in the frequency domains of the X- (8.2-12.4 GHz), C- (3.95-5.8 GHz), S- (2.6-3.95 GHz), L- (1-2.6 GHz), and P-band (0.23- 1 GHz) (Fig. 1). However, in recent decades, microwave remote sensing has been limited to narrow frequency bands (mainly C- to X-band) due to official restrictions on

available operating frequencies (Federal Communications Commission, 2022). Hence, the current microwave research satellites in space mostly operate in the C-, X-, and L-band, such as the Sentinel-1 mission from the European Space Agency (ESA) (Sentinel-1 Team (ESA), 2013), the German TerraSAR-X and TanDEM-X missions (Klenk et al., 2022), the Soil moisture Active Passive (SMAP) mission from the National Aeronautics and Space Administration (NASA) (Entekhabi et al., 2014), and the Soil Moisture Ocean Salinity (SMOS) mission from ESA (Kerr et al., 2016).

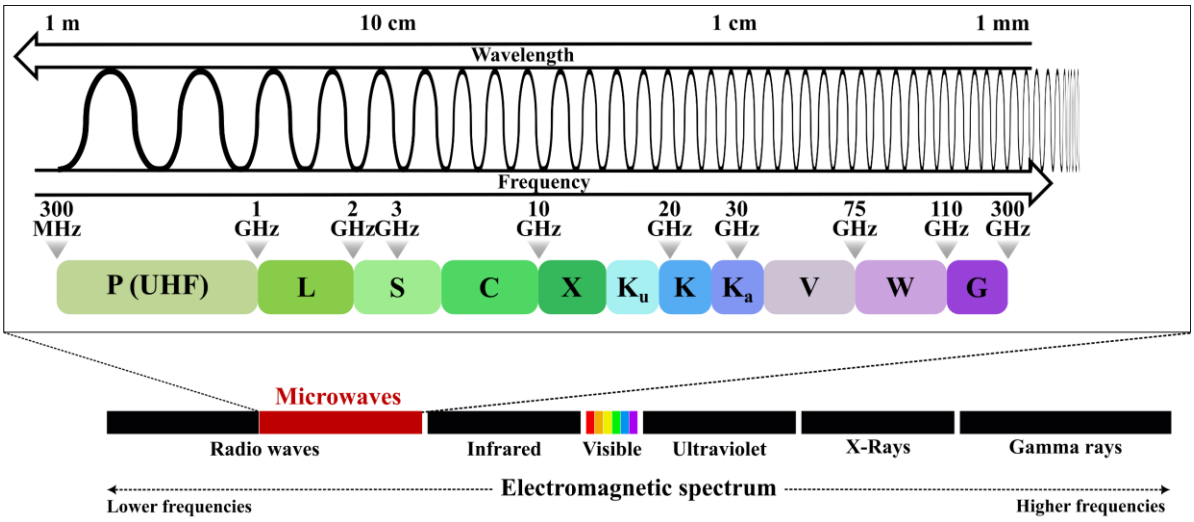

Figure 1. Electromagnetic spectrum with indication of the respective wavelengths and frequencies of the microwave portion as well as common IEEE band names. Source: Own illustration adapted after (Kamutzki et al., 2021).

In contrast, low frequency microwave ranges, like at P-band, have been much less studied, since these systems are limited to ground-based observations and have not been operated from satellites at the time of this writing. The first P-band satellite missions in space will be the BIOMASS of ESA in 2025 (Gelas et al., 2021), and the SigNals Of Opportunity P-band Investigation (SNOOPI) from NASA in 2024 (Garrison et al., 2024; Kim et al., 2023).

In order to be able to evaluate collected information and data in an unbiased and correct manner, knowledge on the employed techniques and methods is of significant importance. At microwave frequencies, it is essential to understand the behavior and interaction of the electromagnetic waves with the environment in terms of scattering mechanisms as well as penetration capabilities in vegetation and soil.

Microwave instruments can be divided into two groups – actively sending radars and passively recording radiometers. Both groups include antennas and receivers (Ulaby and Long, 2014). Active radars emit microwaves with an additional transmitter towards the Earth's surface and measure the amount of backscatter. In contrast, passive radiometers simply measure the amount of thermal emission without actively

emitting microwave radiation. While passive radiometers are one type of passive sensors mostly operating with real-aperture antennas, active radars comprise several types of sensor systems. Besides non-imaging radar systems, like altimeters operating with real-aperture antennas, the most important imaging radar system is the synthetic aperture radar (SAR) (Ulaby and Long, 2014). The main drawback of real-aperture systems is the coarse spatial resolution since, for radars, the resolution along the flight line of a satellite (azimuth resolution) depends on the physical size of the antenna. SAR systems synthesize the real antenna along the flight line to one longer effective antenna and hence, are able to achieve a comparable higher spatial resolution (Lee and Pottier, 2009). SAR was invented in 1951, and since then, microwave remote sensing has become one of the most useful techniques for recording and analyzing the Earth's surface.

In order to estimate geophysical parameters, e.g. from soil, based on active and/or passive microwave sensor systems, some kind of electromagnetic wave-medium interaction models are necessary. One focus of this research study is on optimization procedures between remote sensing observations and model simulations in order to estimate relevant soil parameters. The following paragraphs will elaborate on the background knowledge required to estimate soil moisture as well as soil surface roughness from microwave remote sensing.

Soil Moisture estimation from microwave remote sensing

Soil moisture can be indirectly estimated from microwave remote sensing based on the correlation of wave propagation and the characteristics of the subjected medium. The change in propagation direction of an electromagnetic wave, when it enters a certain dielectric medium, is connected to the medium's relative electric permittivity ε_r [-] and magnetic permeability μ_r [-] ($\mu_r = 1$, except for ferromagnetics) (Kraus and Carver, 1973; Ulaby and Long, 2014). This means, the higher the medium's permittivity, the slower the wave propagation. It is convenient to use the relative permittivity ε_r as the ratio of the actual dielectric's permittivity ε $[F/m]$ to that of the permittivity of vacuum ε_0 $[F/m]$, "[s]ince the permittivity of a dielectric is always greater than the permittivity of vacuum" (Kraus and Carver, 1973), with $\varepsilon_0 = 8.85 * 10^{-12}\ F/m$ (Kraus and Carver, 1973; Ulaby and Long, 2014). The permittivity of a soil, denoted by ε_s [-], is a complex number with a real (ε_s') and an imaginary (ε_s'') part:

$$\varepsilon_s = \varepsilon_s' - j\varepsilon_s'', \tag{1}$$

with

$$\varepsilon_s'' = \sigma/(\omega_f \varepsilon_0), \tag{2}$$

where σ is the soil conductivity [S/m], and ω_f is the angular frequency [rad/s]. The real part is associated with energy or heat storage, whereas the imaginary part is associated with energy or heat loss, often called dielectric loss factor (Kelleners et al., 2005; Ulaby and Long, 2014). Since ε_s'' is dependent on the conductivity of the soil (Eq. (2)), it follows that for a lossless medium, where $\sigma = 0$ and $\varepsilon_s'' = 0$, (1) reduces to $\varepsilon_s = \varepsilon_s'$ (Ulaby and Long, 2014). However, in general, soils are lossy media with specific σ and $\varepsilon_s'' \neq 0$, and thus ε_s'' is of significant importance when describing the actual permittivity of a soil. In many studies, mainly the real part ε_s' is investigated, e.g. (Bannawat et al., 2020; Gururaj et al., 2021; Jagdhuber, 2012; Jagdhuber et al., 2015; Shi et al., 2021). Finally, permittivity can be converted to soil moisture, denoted by θ_s [-], and vice versa, by employing dielectric mixing models, such as the one from Topp et al., (Topp et al., 1980), Dobson et al., (Dobson et al., 1985), and Mironov et al., (Mironov et al., 2009). The most employed dielectric mixing model for soil moisture conversion is given by the polynomial equation from (Topp et al., 1980), due to its simplicity. Only the real part of the permittivity (ε_s') is associated to θ_s, and no additional information are needed:

$$\theta_s = -0.053 + 0.0292 * \varepsilon_s' - 5.5e^{-4} * \varepsilon_s'^2 + 4.3e - 6 * \varepsilon_s'^3. \quad (3)$$

Other models, such as the one from (Mironov et al., 2009), need, e.g., soil texture (clay fraction), soil temperature, and frequency information next to permittivity and are hence, more complex. An extended review of dielectric mixing models for soils can be found in (Park et al., 2017).

One of the potential applications, for which complex permittivity is needed, is the estimation of penetration depths of microwave signals into soil and vegetation. The penetration depth δ_P [cm] is defined as the depth after which the power density of the propagating electromagnetic radiation is reduced by a factor of $1/e$ (~ 0.37 %) and confined to the region in the observed medium that is important for soil and volume scattering (Ulaby et al., 1982; Ulaby and Long, 2014). In general, δ_p is dependent on the attenuation factor α [-] (Eq. (4)), which is the basis for all available formulations to calculate δ_p, i.e., (Klausing and Holpp, 2000; Mironov et al., 2002; Schaber et al., 1986; Ulaby et al., 1982; von Hippel, 1954; Wilheit, 1978; Zhang et al., 2019):

$$\delta_P = \frac{1}{2}\alpha. \quad (4)$$

Although, δ_P is influenced by many factors, such as sensor characteristics (e.g., incidence angle, transmitted energy, band width) and soil characteristics (e.g., roughness, texture, bulk density, microstructure), most formulations are only dependent on the microwave frequency (represented by the wavelength λ [cm]) of the employed sensor and the complex soil permittivity, like one of the earliest and most-

known formula for penetration depth estimation from (von Hippel, 1954), adapted after (Schaber et al., 1986):

$$\delta_p = \frac{1}{2} * \left(\frac{\lambda}{2\pi} * \left[\frac{2}{\varepsilon'_s * \left(\sqrt{1 + tan^2(\varepsilon''_s / \varepsilon'_s)} - 1 \right)} \right]^{\frac{1}{2}} \right). \quad (5)$$

Soil Surface Roughness estimation from microwave remote sensing

Soil surface roughness represents the three-dimensional topography of the soil surface. The micro structure of soil roughness cannot be described deterministically due to its small, but countless features along space and time. Therefore, a statistical description needs to be adopted. The vertical (relief) component is described by the standard deviation of the surface height variation, called vertical root mean square (RMS) height s [cm]. The horizontal (landscape) component is expressed by the horizontal correlation length l [cm]. The parameter l is defined as the displacement at which the autocorrelation equals $1/e$ and hence, as the reference length up to which the vertical RMS heights at two locations of one soil surface can be regarded as statistically independent from each other. This means, for a perfectly smooth soil surface, l is infinite, since every point on this surface correlates with all other points.

In the past, soil roughness has mainly been estimated on global scale from passive remote sensing due to the fact that radiometers are more sensitive to surface roughness, and because vegetation has stronger impacts on the radar backscatter than on the passive emissivity. In passive microwave remote sensing, the roughness parameter H_R [-] is established that can be related to the vertical RMS height s by (6):

$$H_R = (2 \cdot s \cdot k)^2, \quad (6)$$

with the wave number k [cm^{-1}] given by

$$k = 2\pi/\lambda. \quad (7)$$

The parameter H_R is relevant in emission models which are based on the radiative transfer equation for describing the radiation passively emitted from the Earth's surface. The most employed models are the τ-ω model (Mo et al., 1982), the Kirchhoff scattering model (Ulaby and Long, 2014), and the QHN model (Wigneron et al., 2017). In these models, roughness strongly affects the magnitude of thermal emission because of its direct influence on the reflectivity components linked to the soil emissivity (Ulaby and Long, 2014).

In this study, a combined approach of active and passive microwave remote sensing is employed for soil surface roughness parameter estimation in order to

improve surface roughness estimation. For that, a quasi-linear relationship between active backscatter ($|S_{PP}|^2$ [dB]) and passive emissivity (E_P [-]) is assumed:

$$E_P = \alpha_{P-PP} + \beta_{P-PP} * |S_{PP}|^2, \quad (8)$$

with P representing the respective polarization. In the absence of vegetation, the intercept α [-] of the linear regression becomes one, and the slope β [-] of the linear regression can be used to describe the covariation between backscatter and emissivity:

$$\beta_{P-PP} = \frac{E_P - 1}{|S_{PP}|^2}. \quad (9)$$

This covariation parameter β_{P-PP} [-], for varying polarization P, is calculated, on the one hand, based on radar and radiometer measurements of NASA's SMAP mission (β_{P-PP}^{Data}). On the other hand, β_{P-PP} can also be modeled based on simulations of backscatter and emissivity from electromagnetic soil scattering models (β_{P-PP}^{Model}), such as the small perturbation method (SPM), the improved integral equation model (I²EM), and the numerical Maxwell model in 3D (NMM3D) (Fung et al., 2002; Tsang et al., 2013; Ulaby and Long, 2014). Finally, by determining the best fit between β_{P-PP}^{Data}, based on SMAP observations, and the ensemble of simulated β_{P-PP}^{Model}, soil surface roughness parameters s and l can be estimated:

$$s, l = min(\beta_{P-PP}^{Model} - \beta_{P-PP}^{Data}). \quad (10)$$

In the field of microwave remote sensing, soil surface roughness can only be estimated at the scale of the wavelength of the employed microwave sensor. Therefore the electromagnetic roughness parameters ks [-] and kl [-] are often used, where s and l are scaled according to the wave number, which is based on the wavelength and hence, the frequency (Eq. (7)) of the employed sensor (Ulaby and Long, 2014).

In general, surface roughness strongly influences the wave interaction with the soil surface and its penetration capabilities, e.g., (Choudhury et al., 1979). However, at the time of this writing, surface roughness is mostly fixed to static values and assumed to be constant over time (Marzahn et al., 2012; Srivastava et al., 2015). This assumption on static values is considerably more difficult to apply when analyzing soil moisture with remote sensing techniques.

1.3 Research Questions

In this study, the focus is on the retrieval of the previously described geophysical soil parameters - the soil moisture and the soil surface roughness - based on remotely sensed microwave observations. The following overarching research questions guided the accomplishment of the soil parameter retrieval:

1. How can the combination of active and passive microwave remote sensing data be used to determine soil roughness parameters, and what are the advantages and disadvantages?

Many studies and methods exist for the retrieval of soil parameters from either active or passive microwave remote sensing, e.g., (Mengen et al., 2023; Narvekar et al., 2015; Njoku et al., 2002). However, very few of them focus on the combination of both types of sensing systems, in particular, the potential advantages and drawbacks of such a methodology. Hence, research question one examines the potentials of a combined active-passive microwave retrieval method with focus on estimating soil surface roughness (see chapter 1.2).

2. How do longwave (P-band) microwaves behave in interactions with different soil types and vegetation covers in terms of scattering mechanisms, soil moisture, and penetration depth?

In recent decades, remote sensing studies focused on the analysis of narrow frequency bands, like C- and L-band, that are available for satellite-based microwave remote sensing (see chapter 1.2). This means, the understanding of the behavior of microwaves in the C- and L-bands with interaction of the land surface has been extensively studied and is well researched. However, due to the lack of available satellite remote sensing systems operating at lower frequencies, basic research studies analyzing the behavior of P-band microwaves in interaction with soils and vegetation are missing. Hence, research question two is intended to provide in-depth knowledge on longwave microwave behaviors in interaction with natural media in terms of scattering mechanisms, soil moisture assessment, and realistic penetration capabilities.

3. How can polarimetric active microwave remote sensing and soil hydrological modeling be combined for the estimation of vertically continuous soil moisture profiles?

One of the limitations in microwave remote sensing is that soil parameter retrievals are only possible at single soil layers, providing spatial (two-dimensional) maps of soil characteristics. However, backscatter signals in particular, contain information about soil moisture dynamics from the soil surface until the average penetration depth of the microwave in the soil. Hence, research for answering question three combines two of the previously described assessment approaches (remote sensing, soil hydrological modeling, see chapter 1.1), and explores their advantages and limitations in order to extend knowledge from remote sensing to the three-dimensional space (lateral and vertical). To that end, research regarding the

combination of microwave remote sensing and soil hydrological modeling for estimating the vertical distribution and variability of soil moisture with depth is conducted and analyzed.

1.4 Framework of the Thesis

To answer the previously defined overarching research questions (see chapter 1.3), this research study includes three peer-reviewed articles, which are presented in chapters 2 to 4.

In figure 2, the connection between the three research articles, their overall commonalities and differences regarding datasets, study regions, methods, and performance metrics, are visualized. It can be seen that for all articles remotely sensed microwave observations at L-band (article I) and P-band (article II & III) are employed together with auxiliary information from digital elevation models (DEMs) and *in situ* measuring networks. The focus of the study regions varies from the subregion Africa-Asia-Australia (article I) to different parts of the continental U.S (CONUS). (article II & III). All articles deal with the retrieval of important soil parameters, the soil surface roughness (article I) or the lateral (article I) and vertical (article III) soil moisture by using various types of retrieval algorithms and models. In order to evaluate the proposed approaches, different performing metrices are used, such as sensitivity studies (article I & II), correlation and error measures (all articles), as well as shape measures (article III). Lastly, the key achievements of all three articles are described in detail in chapter 1.5.

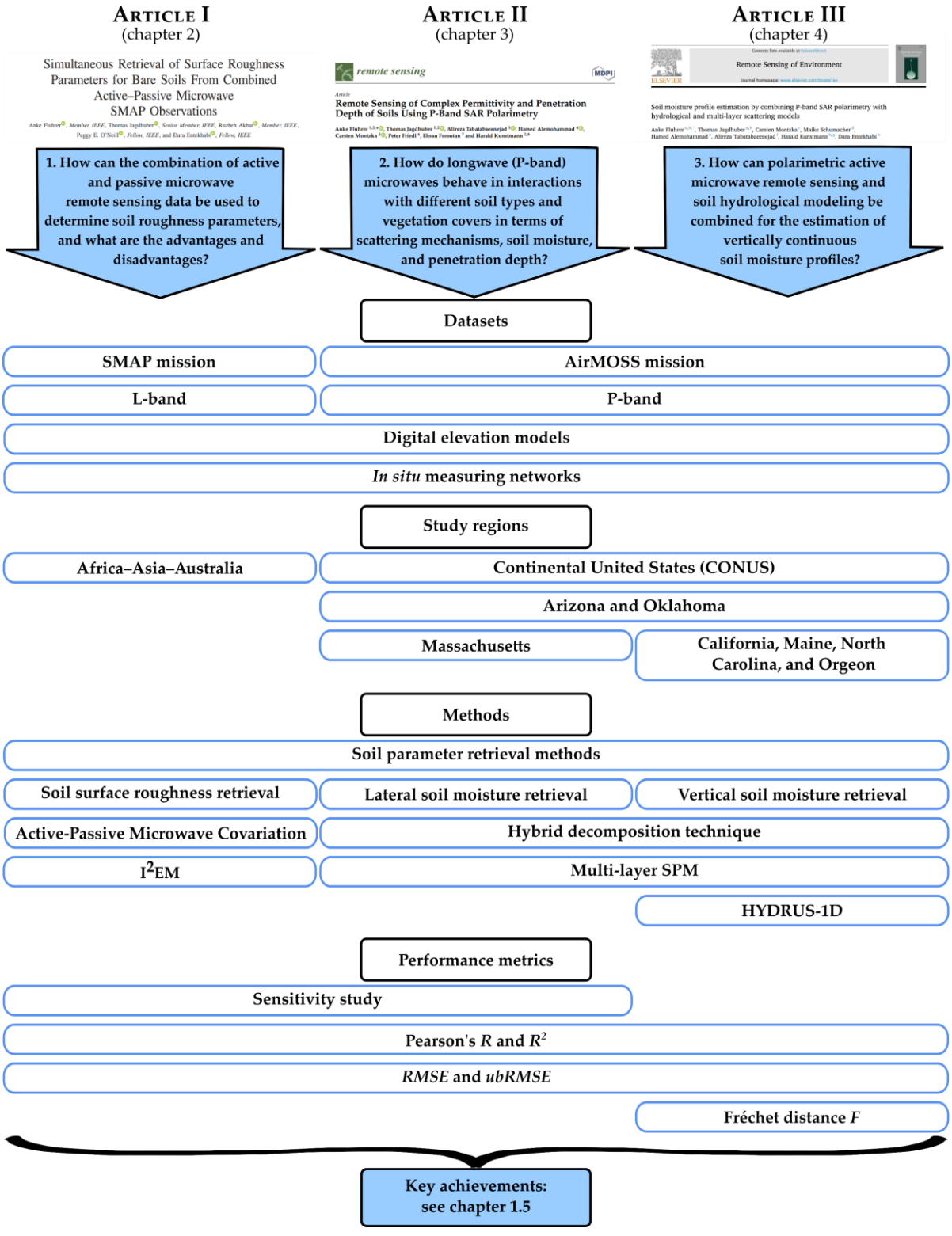

Figure 2. Overview of the study framework with connections between the three research articles regarding datasets, study regions, methods, and performance metrics represented by boxes spanning the columns of every article.

In the following, a short summary is given for each article:

Article I: Simultaneous Retrieval of Surface Roughness Parameters for Bare Soils From Combined Active–Passive Microwave SMAP Observations

A. Fluhrer, T. Jagdhuber, R. Akbar, P. E. O'Neill, and D. Entekhabi, 'Simultaneous Retrieval of Surface Roughness Parameters for Bare Soils From Combined Active–Passive Microwave SMAP Observations,' in *IEEE Transactions on Geoscience and Remote Sensing*, vol. 59, no. 10, pp. 8182-8194, Oct. 2021, doi: 10.1109/TGRS.2020.3035204.

In this publication, an active-passive microwave combined retrieval algorithm for the simultaneous estimation of surface roughness parameters is proposed and analyzed. The newly developed approach combines active radar and passive radiometer observations at L-band frequencies by assuming a quasi-linear relationship between the radar backscatter and the radiometer emissivity, for respective horizontal and vertical polarization (Eq. (8), chapter 1.2). The advantage of a combined retrieval approach (compared to radar- and radiometer-only approaches) is the reduction of the parameter space for possible solutions as well as the beneficial amplification of individual strengths while mitigating certain limitations. Active radar observations are particularly sensitive to soil moisture and achieve a good spatial resolution, while passive radiometer measurements are more sensitive to surface roughness but yield rather coarse spatial resolution. Hence, by combining the complementary physics of both domains, the parameter search space is reduced, narrowing down the space for potential retrieval errors. Consequently, the susceptibility of radar sensors to soil moisture and the susceptibility of radiometer sensors to soil surface roughness is reduced as shown by a conducted sensitivity study (Fig. 1 in (Fluhrer et al., 2020)). Additionally, the beneficial spatial resolution of active radars enhances the resolution of the resulting roughness parameters in comparison to, for instance, radiometer-only approaches.

The focus in the presented study was on bare and low vegetated areas due to the increasing algorithm complexity when assuming additional vegetation scattering. Results are presented for the subregion North Africa-Asia-Australia in the period from 14th of April to 7th of July 2015 and showed that wavelength-dependent surface roughness parameters can be retrieved for every resolution cell and time step by minimizing the influence of the soil permittivity/moisture. The estimated surface roughness parameters, with s varying between 0.35 cm to 7 cm and l between 1.75 cm and 20.5 cm, are consistent with local conditions (i.e., topography, landcover, soil conditions) as well as reported roughness values in previously published studies.

Article II: Remote Sensing of Complex Permittivity and Penetration Depth of Soils Using P-Band SAR Polarimetry

A. Fluhrer, T. Jagdhuber, A. Tabatabaeenejad, H. Alemohammad, C. Montzka, P. Friedl, E. Forootan, and H. Kunstmann, 'Remote Sensing of Complex Permittivity and Penetration Depth of Soils Using P-Band SAR Polarimetry,' in *MDPI Remote Sensing*, 2022, 14(12), 2755, doi: 10.3390/rs14122755.

In this publication, a complex soil permittivity estimation method based on fully polarimetric P-band SAR observations of NASA's Airborne Microwave Observatory of Subcanopy and Subsurface (AirMOSS) mission is proposed. By improving and adapting already existing hybrid (combined eigen- and model-based) decomposition techniques, complex permittivity and subsequently P-band penetration depths are estimated without prior knowledge on land surface characteristics. Further, because of the incorporation of a complex soil scattering model, complex permittivity can be estimated for the first time (to the best of my knowledge) from SAR observations directly. This advantage allows the estimation of P-band microwave penetration capabilities (from the real and imaginary part of the complex permittivity) to help to understand the soil depth to which microwaves of low frequencies are in fact sensitive to.

Results showed that at P-band frequency (430 MHz) the dihedral scattering mechanism is the dominant one over forests. Here, the strong vertical structures of tree trunks comprise the highest contribution to the SAR signal, aligning with reports in previous studies. In addition, comparisons of estimated soil permittivity, or converted soil moisture according to the dielectric mixing model from (Topp et al., 1980), with *in situ* measurements at selected stations are rather unsatisfying due to the discrepancy in measuring depths. This strengthens the need for soil moisture information at several soil depths, not only near the soil surface (~5 cm). Nevertheless, estimated moisture patterns across the investigated regions in the U.S. agree well with local conditions (i.e. soil characteristics, land cover, and climate). Subsequently, calculated permittivity-based penetration depths revealed that P-band microwaves penetrate, on average, between 5 cm and 35 cm, depending on the type of vegetation cover and moisture state of the soil.

Article III: Soil Moisture Profile Estimation by Combining P-band SAR Polarimetry with Hydrological and Multi-Layer Scattering Models

A. Fluhrer, T. Jagdhuber, C. Montzka, M. Schumacher, H. Alemohammad, A. Tabatabaeenejad, H. Kunstmann, and D. Entekhabi, 'Soil Moisture Profile Estimation by Combining P-band SAR Polarimetry with Hydrological and Multi-Layer Scattering Models', in *Elsevier's Remote Sensing of Environment*, Volume 305, 2024, 114067, doi: 10.1016/j.rse.2024.114067.

In this publication, the combination of remote sensing with soil (hydrological) modeling is investigated in order to enhance soil parameter retrieval approaches. From remote sensing alone, soil moisture can only be retrieved at one soil depth, although the received intensity is proportional to the integral over the vertical soil column, from the soil surface until the penetration depth of the microwave, and contains information on vertical soil moisture variability. Hence, by combining high resolution P-band remote sensing observations with soil hydrological modeling the vertical variability and discontinuity of soil moisture, called soil moisture profile, can be estimated.

In this study, on the one hand, airborne P-band SAR observations from NASA's AirMOSS mission are decomposed into the individual scattering mechanisms (soil, dihedral, and volume) to get the soil surface scattering component only. On the other hand, the HYDRUS-1D model is used to simulate soil moisture profiles based on meteorological observations (e.g., precipitation, temperature, solar radiation, etc.), atmospheric boundary conditions for water flow and heat transport, as well as soil information (e.g., hydraulic properties, amount of gridding points (nodes), etc.). During simulations with HYDRUS-1D some of the assumptions on certain initial input parameters, such as the initial pressure head and the soil depth, when no prior knowledge was available, are kept variable. Hence, an ensemble of simulated soil moisture profiles is created. Every simulated soil moisture profile is then compared to the soil scattering component from the SAR observations to get the most suitable soil moisture profile from their best fit.

The proposed retrieval method for soil moisture profile estimation was analyzed at eight monitoring stations within six different AirMOSS sites across the continental U.S. between 2013 to 2015. Results proved the overall feasibility of the approach and validation with *in situ* measured soil moisture values showed medium to high correlations from 0.48 to 0.92.

1.5 Innovations and Key Achievements

In this thesis, innovations center around developing retrieval algorithms and their application to active and passive microwave signals for the estimation of essential soil parameters. The essence of the presented research is:

- First time application of newly developed innovative and non-iterative physics-based retrieval algorithms for soil moisture and soil surface roughness estimation that can be applied globally on any spatial and temporal scales.
- Provision of an improved understanding regarding low-frequency microwave scattering behavior in interaction with different soil types and vegetation covers.
- First time combination of airborne P-band SAR remote sensing and soil hydrological modeling for vertically continuous soil moisture profile estimation from the soil surface until the upper root zone.
- Detailed analyses on how remote sensing methods can be improved and support climate research as well as how the joint use of remote sensing and hydrological modeling can broaden scientific applications.

These innovations lead to the key achievements of the conducted research:

- The combination of active and passive microwave data reduces the susceptibility of radars to soil permittivity and radiometers to soil roughness and hence, improves soil roughness estimations, and in the end soil moisture retrievals.
- The enhanced determination of vertical and horizontal surface roughness parameters can be done simultaneously over time and variable in space.
- Radar microwave signals of low frequencies are suitable for soil moisture estimation in the upper root zone based on an improved polarimetric decomposition method adapted to P-band frequency. The proposed method enables, for the first time in remote sensing, the estimation of complex soil permittivity (Eq. (1), chapter 1.2).
- The combination of remote sensing and soil hydrological modeling significantly enhances the estimation of physically meaningful and vertically continuous soil moisture profiles until the upper root zone. From remote sensing alone, the vertical variability and discontinuity of soil moisture cannot be estimated. However, by combining remote sensing with soil hydrological modeling, both assessment approaches benefit from each other and provide new possibilities for soil parameter retrievals.

- The combined P-band microwave remote sensing and soil hydrological modeling approach provides the ability of estimating continuous near-surface soil moisture dynamics (between 0 cm to 5 cm soil depth), where *in situ* field measurements are not feasible due to the fact that field sensors require a certain volume of soil material for realistic soil moisture measurements.

1.6 Contributions of the Author to the Presented Research Articles

Article I: Simultaneous Retrieval of Surface Roughness Parameters for Bare Soils From Combined Active–Passive Microwave SMAP Observations (doi: 10.1109/TGRS.2020.3035204).

The research concept and method development were conducted by Anke Fluhrer and Thomas Jagdhuber. The data (active radar and passive radiometer observations from the SMAP mission) were provided by Dara Entekhabi & his team, and extended for auxiliary information by Anke Fluhrer. The data curation and method implementation in MATLAB© was performed by Anke Fluhrer. The analysis, validation, and visualization of all results was done by Anke Fluhrer, supervised by Thomas Jagdhuber. The article design was developed by Anke Fluhrer, Thomas Jagdhuber, and Dara Entekhabi. The article was written by Anke Fluhrer with contributions and comments from all co-authors.

Article II: Remote Sensing of Complex Permittivity and Penetration Depth of Soils Using P-Band SAR Polarimetry (doi: 10.3390/rs14122755).

The research concept and model development were elaborated by Anke Fluhrer and Thomas Jagdhuber. The data (P-band SAR observations) were provided by Hamed Alemohammad, and extended for auxiliary information by Anke Fluhrer. The data curation was performed by Anke Fluhrer, Hamed Alemohammad, and Peter Friedl. The method implementation in MATLAB© was done by Anke Fluhrer. The implementation of the soil scattering model (multi-layer SPM) was done by Alireza Tabatabaeenejad. The analysis, validation, and visualization of all results in Python© was done by Anke Fluhrer, supervised by Thomas Jagdhuber and Harald Kunstmann. The article design was developed by Anke Fluhrer and Thomas Jagdhuber. The article was written by Anke Fluhrer with contributions and comments from all co-authors. The acquisition of the funding for the AssimEO project (50EE1914A), within which this research study was conducted, and the project administration was done by Thomas Jagdhuber and Carsten Montzka.

Article III: Soil Moisture Profile Estimation by Combining P-band SAR Polarimetry with Hydrological and Multi-Layer Scattering Models (doi: 10.1016/j.rse.2024.114067).

The research concept and model development were done by Anke Fluhrer and Thomas Jagdhuber, with input from Dara Entekhabi. The data (P-band SAR observations) were provided by Hamed Alemohammad, and extended for auxiliary information by Anke Fluhrer. The data curation was performed by Anke Fluhrer and Hamed Alemohammad. The method implementation in Python© was done by Anke Fluhrer. The implementation of the soil scattering model (multi-layer SPM) was done by Alireza Tabatabaeenejad. The implementation of the hydrological model (HYDRUS-1D) in Python© was done by Anke Fluhrer with input from Carsten Montzka and Harald Kunstmann. The analysis, validation, and visualization of all results was done by Anke Fluhrer, supervised by Thomas Jagdhuber and Harald Kunstmann. The article design was developed by Anke Fluhrer. The article was written by Anke Fluhrer with contributions and comments from all co-authors. The acquisition of the funding for the AssimEO project (50EE1914A), within which this research study was partly conducted, and the project administration was done by Thomas Jagdhuber and Carsten Montzka.

2 Article I

A. Fluhrer, T. Jagdhuber, R. Akbar, P. E. O'Neill, and D. Entekhabi, 'Simultaneous Retrieval of Surface Roughness Parameters for Bare Soils From Combined Active–Passive Microwave SMAP Observations,' in *IEEE Transactions on Geoscience and Remote Sensing*, vol. 59, no. 10, pp. 8182-8194, Oct. 2021, doi: 10.1109/TGRS.2020.3035204.

Simultaneous Retrieval of Surface Roughness Parameters for Bare Soils From Combined Active–Passive Microwave SMAP Observations

Anke Fluhrer, *Member, IEEE*, Thomas Jagdhuber, *Senior Member, IEEE*, Ruzbeh Akbar, *Member, IEEE*, Peggy E. O'Neill, *Fellow, IEEE*, and Dara Entekhabi, *Fellow, IEEE*

***Abstract*— An active–passive microwave retrieval algorithm for simultaneous determination of soil surface roughness parameters [vertical root-mean-square (RMS) height (s) and horizontal correlation length (l)] is presented for bare soils. The algorithm is based on active–passive microwave covariation, including the improved Integral Equation Method (I^2EM), and is tested with global soil moisture active passive (SMAP) observations. The estimated retrieval results for s and l are overall consistent with values in the literature, indicating the validity of the proposed algorithm. Sensitivity analyses showed that the developed roughness retrieval algorithm is independent of permittivity for $\varepsilon_s > 10$ [-]. Furthermore, the physical model basis of this approach (I^2EM) allows the application of different autocorrelation functions (ACF), such as Gaussian and exponential ACFs. Global roughness retrieval results confirm bare areas in deserts such as Sahara or Gobi. However, the type of ACF used within roughness parameter estimation is important. Retrieval results for the Gaussian ACF describe a rougher surface than retrieval results for the exponential ACF. No correlations were found between roughness results and the amount of precipitation or the soil texture, which could be due to the coarse spatial resolution of the SMAP data. The extension of this approach to vegetated soils is planned as an add-on study.**

***Index Terms*— Correlation length, I^2EM, radar, radiometer, root-mean-square (RMS) height, soil moisture active passive (SMAP).**

Manuscript received May 4, 2020; revised July 9, 2020 and October 7, 2020; accepted October 27, 2020. Date of publication November 24, 2020; date of current version September 27, 2021. This work was supported in part by the Massachusetts Institute of Technology (MIT)-Germany Seed Fund "Global Water Cycle and Environmental Monitoring using Active and Passive Satellite-based Microwave Instruments." *(Corresponding author: Anke Fluhrer.)*

Anke Fluhrer is with the German Aerospace Center, Microwaves and Radar Institute, Muenchener Strasse 20, 82234 Weßling, Germany, and also with the Institute of Geography, University of Augsburg, Alter Postweg 118, 86159 Augsburg, Germany (e-mail: anke.fluhrer@dlr.de).

Thomas Jagdhuber is with the German Aerospace Center, Microwaves and Radar Institute, Muenchener Strasse 20, 82234 Weßling, Germany.

Ruzbeh Akbar and Dara Entekhabi are with the Department of Civil and Environmental Engineering, Massachusetts Institute of Technology, Cambridge, MA 02139 USA.

Peggy E. O'Neill is with the NASA Goddard Space Flight Center, Greenbelt, MD 20771 USA.

Digital Object Identifier 10.1109/TGRS.2020.3035204

I. Introduction

A. Motivation for Surface Roughness Estimation

THE estimation and monitoring of geophysical parameters via Earth-observation satellites are crucial for improving our understanding of global environmental and hydrological processes. Soil roughness is an essential parameter in physical processes related to water, energy, and nutrient flow and exchange since it characterizes the boundary between the pedosphere and atmosphere [1]. Soil roughness influences microwave signals from soil surfaces and contributes to measurements from active and passive sensors. Both radar backscatter $|S_{PP}|^2$ [dB] and microwave emissivity E_P [-], based on brightness temperature TB_P [K], are sensitive to surface roughness [2], [3].

Despite its importance for environmental applications, soil roughness has played a minor role in land parameter retrieval with microwave remote sensing in recent decades [4], [5]. For instance, soil roughness is an important parameter in land surface modeling of soil erosion applications because it defines the soil surfaces that represent "the interface between the eroding soil body and the erosive agent" [6], [1], [3], [5].

Retrieval of geophysical parameters, such as soil roughness or soil moisture, is mainly performed at lower frequencies, such as at L-band (1.4 GHz), due to the higher sensitivity of active and passive microwave signatures to soil moisture (under vegetation) compared with the C-band (~6 GHz) and higher frequency bands [3], [7], [8]. Furthermore, the operational monitoring of soil moisture content on global scales has been mainly performed continuously with passive microwave sensors up until now. Passive microwave sensors are used predominantly since soil roughness and vegetation hold a stronger influence on backscatter than on soil-emitted brightness temperature [9].

The primary disadvantage of passive-only retrievals is the coarse spatial resolution of microwave radiometers (>40 km), which is sufficient for large-scale applications, such as global climate modeling. Yet, for weather forecasting and agricultural yield management, soil moisture information of at least 10 km spatial resolution is desired [10]. Active microwave sensors

provide a higher spatial resolution than passive microwave sensors. Unfortunately, studies in recent years have shown that estimations of geophysical parameters, more precisely soil moisture, on the basis of radar-only retrievals are more prone to errors than radiometer-only or combined methods [9]. This might be due to two reasons: first, there are difficulties in quantifying all occurring scattering effects [9], [11]–[13]; second, the impact of terrain and vegetation morphology is often not considered adequately in radar retrievals due to complex plant structures [9]. Thus, the combination of both active and passive sensor systems can improve the monitoring of geophysical parameters, such as soil surface roughness, by leveraging the advantages of both sensors while overcoming their individual limitations.

Currently, the existing soil moisture retrieval algorithms for joint processing of radar and radiometer microwave satellite data are neural network-based approaches (e.g., [14], [15]), the change detection method [7], [16]–[18], and the soil moisture active passive (SMAP) optional [10] and the SMAP baseline [10], [19] downscaling algorithms. In all of these algorithms, soil roughness is considered only as a secondary effect. For one, soil roughness is corrected either by collecting multiconfiguration data (variety of frequency and/or polarization) or by optimizing it within the parameter retrieval algorithm until the model predictions coincided with the actual measured data. Second, roughness is considered as static and fixed to a constant value for single land cover classes according to the classification of the International Geosphere-Biosphere Program (IGBP), as done within the SMAP L2 and L3 soil moisture algorithms [20]. However, Saatchi *et al.* [21] noted that, for precise monitoring of soil moisture, accurate determination of surface roughness is key for correctly deriving soil moisture information from radar data.

B. Parameterization of Surface Roughness in Remote Sensing

The two fundamental parameters describing soil surface roughness are the standard deviation of the surface height variation [or vertical root-mean-square (RMS) height], with its related autocorrelation function (ACF), and the horizontal correlation length [8]. The degree of correlation between two laterally separated locations of one surface can be estimated through the surface correlation function $p(\xi)$, with ξ as displacement between those two locations. With the increasing separation between two locations on the surface, $p(\xi)$ decreases, and at a certain distance, the so-called horizontal correlation length and the vertical RMS heights at the two locations are considered statistically uncorrelated [8].

Due to the nonstandardized naming convention, the terminology for both parameters is ambiguous. Common parameterizations for the vertical RMS height are S_D, σ, or s [4], [8], [22], [23] and for the horizontal correlation length L_C or l [2], [24]. In this study, the standard deviation of the surface height variation is denoted by s [cm], with its related ACF [-], and the horizontal correlation length by l [cm], which is the naming convention already used, e.g., in [1], [8], [25], and [26].

For the sake of completeness, it should be mentioned that passive microwave retrievals often refer to a different roughness parameter. They are using a radiative transfer model to simulate the effects of surface roughness on measured brightness temperature TB_P [4]. This model is the analytical zero-order solution to the radiative transfer equation, commonly referred to as the tau–omega ($\tau-\omega$) model [27], which is the basis for numerous microwave emission models, such as the L-band Microwave Emission of the Biosphere (L-MEB) model, employed in the current Soil Moisture and Ocean Salinity (SMOS) L2 algorithm [23]. Within these models, soil emission is calculated based on a semiempirical approach first proposed by Wang and Choudhury [28], known as HQN [24] or $H-Q$ model [29]. Wang and Choudhury [28] pointed out that the Fresnel equations can be used to describe the reflectivity of a smooth but not a rough soil surface. In the latter case, scattering of the incident wave occurs in many directions, and the reflected parts "in the specular direction would be lower than the Fresnel reflectivity" [28]. To consider reflectivity losses caused by increasing surface roughness, the soil roughness loss factor, $h = H_R \cdot \cos^N\theta$, was introduced [4]. Here, another roughness parameter, called H_R [23], is used to characterize roughness effects on passive microwave signatures.

In this study, we determine the vertical RMS height and the horizontal correlation length of a surface and can link h with s by $H_R = (2\cdot s\cdot k)^2$, where k [cm^{-1}] is the wavenumber ($k = 2\pi/\lambda$) [4], [22], [23], [30]. In the HQN model, the parameter Q is called the polarization mixing factor that accounts for differences in values between the horizontal polarization and the vertical polarization. Finally, within the HQN model to describe the reflectivity of a rough surface, the parameter N accounts for multiangular and dual-polarization measurements, which is set equal to two in most studies [24], [28].

In addition to s and l, a third roughness parameter is defined as the RMS slope m, "a quantity proportional to the ratio of [s to l]" [8], indicating the degree of roughness of one surface. For a 1-D height profile for one random surface, m is defined as $m = [-s^2 p''(0)]^{1/2}$, with $p''(0)$ being the second derivative of the surface correlation function $p(\xi)$, evaluated at the origin ($\xi = 0$). Since $p(\xi)$ is an even function, $p''(0)$ is a negative quantity [8]. For modeling of electromagnetic scattering at soil surfaces, assumptions of the functional forms of $p(\xi)$ have to be made. The most common forms are the exponential and Gaussian correlation functions. In the case of a Gaussian ACF, m can be calculated by $m = \sqrt{2}\, s/l$ [8], [31]. In theory, in the case of an exponential ACF, a surface does not have an RMS slope. This is due to the fact that this correlation function is not differentiable at the origin since, in order to describe a correlation, it has to be an even function [32]. Hence, Dierking [31] presented the derivation of an "effective" RMS slope for exponentially correlated surfaces, which always has to be considered in relation to the frequency of the acquisition system. Therefore, the exponential RMS slope can be calculated by $m = (2/\pi)^{1/2} * s/l * (5kl - \arctan(5kl))^{1/2}$ [31]. The RMS slope m is one of the validation criteria for the small perturbation model (SPM) [8]. In general, for L-band, m should be lower than 0.3 [8] or 0.4 [31], [32] in the case of bare soil surfaces with moderate RMS heights [32].

Overall, the type of employed wave scattering model is essential for modeling of electromagnetic wave interaction

with vegetation or soil and should be considered carefully depending on its advantages and disadvantages.

When observing soil surfaces with remote sensing techniques, the observed roughness scales are mainly a function of the wavelength of the sensing system. In detail, the observable roughness scales can either be equivalent or larger (but limited by resolution cell extent) than the wavelength of the sensing system, whereas smaller scales would not contribute significantly to the signal [8]. In the field of microwave remote sensing, surface roughness is mainly observed at centimeter scale since, "[a]t microwave frequencies, the wavelength is on the order of centimeters to a few tens of centimeters" [8]. Exceptions are found for surfaces that include the effects of large-scale topography when resolution cell sizes are in the order of the topographic variations.

The objective of this study is to simultaneously determine the vertical (s) and horizontal (l) components of bare soil surface roughness through the combination of active and passive microwave data on a global scale.

II. Data

Data for this study come from the NASA SMAP mission [3]. This mission was launched in 2015 with the aim to exploit synergies between active and passive instruments at L-band frequency. It is the first soil moisture dedicated spaceborne mission developed to provide moisture products from active and passive microwave satellite data [3], [33]. Unfortunately, the SMAP radar went out of service in July 2015 after only three months of operations, but the SMAP radiometer continues to deliver high-quality data [34]. Due to the radar failure, the investigation period with SMAP data in this study is limited to the period from April 14 to July 7, 2015.

The data used in this study are the SMAP L1B Radar Half-Orbit Time-Ordered low-resolution backscatter $|S_{\mathrm{PP}}|^2$ [35], the SMAP L1C Radiometer Half-Orbit Time-Ordered Brightness Temperatures TB_P [36], the physical soil temperature T_S, and the soil moisture obtained from the SMAP L3SM_P products [37], all posted on a 36-km Equal-Area Scalable Earth-2 (EASE-2) grid [20], [38].

In order to guarantee analyses exclusively over bare soils, we filter the global surface roughness results for vegetation, water, or snow. We used the vegetation optical depth (VOD) posted on a 36-km EASE-2 grid from the SMAP data set processed with the multitemporal dual-channel retrieval algorithm (MT-DCA) [38] and the surface condition quality flags for snow and frozen ground from the SMAP L3 Radiometer Global and Northern Hemisphere Daily 36 km EASE-Grid Freeze/Thaw State [39] for filtering. Pixels with VOD greater than 0.06, with more than one day covered by snow or frozen ground during the investigation period, or with more than 5% water fraction are masked out.

Previous studies emphasized the impact of large-scale roughness effects due to topography on satellite microwave observations (e.g., [40], [41]). Therefore, significant topography is normally excluded or treated with special care in satellite data products of various missions, such as SMOS [42] or SMAP [33]. In this study, the effects of topography on 36 km-scale SMAP observation-based soil roughness estimates are assumed to be nonsignificant mainly due to two reasons. First, after filtering of SMAP retrieval input parameters (backscatter and emissivity), only regions with digital elevation model (DEM) slope angles, extracted from the Shuttle Radar Topography Mission (SRTM) V4 [43], smaller than 25° are analyzed. Hence, only bare soils with flat to moderate terrain are considered. Second, at the resolution cell size of 36 km intra-cell variations in DEM slope angles are assumed to compensate themselves (cooccurrence of up and down slopes) up to a certain degree. This might be reflected in nonsignificant correlations ($R = 0.42$ for s and $R = -0.32$ for l) between SMAP retrieval results and the standard deviation of DEM slopes within the 36 km resolution cells.

III. Methods

In the course of developing combined active–passive microwave retrieval algorithms for geophysical parameters (e.g., soil moisture), the relationship between the radar backscatter ($|S_{\mathrm{PP}}|^2$) and the emissivity ($E_P = T_{b_P}/T$) of a radiometer was found to be quasi-linear [20]. For the SMAP algorithms, it is expressed by the two regression parameters α and β, with $\alpha_{P-\mathrm{PP}}$ [-] being the P-polarized intercept and $\beta_{P-\mathrm{PP}}$ [-] being the P-polarized slope of the linear regression (1) [20], [44]:

$$E_P = \alpha_{P-\mathrm{PP}} + \beta_{P-\mathrm{PP}} * |S_{\mathrm{PP}}|^2 \tag{1}$$

For bare soils, the intercept $\alpha_{P-\mathrm{PP}}$ is 1 due to the fact that vegetation cover is absent [45]. Therefore, the slope $\beta_{P-\mathrm{PP}}$ describes the covariation between emissivity and backscatter for bare soils and is defined as follows [44]:

$$\beta_{P-\mathrm{PP}} = \frac{E_P - 1}{|S_{\mathrm{PP}}|^2} = \frac{\frac{T_{\mathrm{bP}}}{T_S} - 1}{|S_{\mathrm{PP}}|^2} \tag{2}$$

where T_S is the surface physical temperature within the top 5 cm of the soil [2].

In (2), $\beta_{P-\mathrm{PP}}$ is referred to as the covariation parameter for respective polarization P. The specific form of (2) allows us to calculate $\beta_{P-\mathrm{PP}}$ based on electromagnetic interaction models of bare surface backscatter and emissivity, $\beta^{\mathrm{Model}}_{P-\mathrm{PP}}$ [-], such as the SPM, $\mathrm{I}^2\mathrm{EM}$, or the numerical Maxwell model in 3-D (NMM3-D), ordered with increasing model complexity.

$\beta_{P-\mathrm{PP}}$ can also be calculated from quasi-simultaneously acquired active and passive microwave measurements, henceforth $\beta^{\mathrm{Data}}_{P-\mathrm{PP}}$. The only limiting factor is that both sensors (radar and radiometer) must have the same spatial resolution in order to observe roughness at the same scales.

For surface roughness estimation, we calculate $\beta^{\mathrm{Model}}_{P-\mathrm{PP}}$ and $\beta^{\mathrm{Data}}_{P-\mathrm{PP}}$ based on the simulated and data-based backscatter and emissivity, respectively. Then, we minimize the absolute difference between model prediction $\beta^{\mathrm{Model}}_{P-\mathrm{PP}}$ and the calculated observations-driven $\beta^{\mathrm{Data}}_{P-\mathrm{PP}}$ for s and l estimations by selecting the $\beta^{\mathrm{Model}}_{P-\mathrm{PP}}$ based on the permittivity closest to the actual permittivity of the SMAP L3SM_P product (see Section II) (converted according to the dielectric mixing model of Topp *et al.* [46]).

In order to avoid invalid combinations of surface roughness parameters, we use the RMS slope m with $m < 0.4$ to filter the retrieval results (see Section I-B). As mentioned earlier, this condition is also used as a validity criterion for the SPM [8], which is equivalently valid for I^{2}EM when the L-band frequency is applied [47]. The details for modeled and data-based covariation parameters are as follows.

A. Model-Based Retrieval of Active–Passive Microwave Covariation

$\beta_{P-\mathrm{PP}}^{\mathrm{Model}}$ is calculated by forward simulations of surface emissivity (E_P) and backscatter ($|S_{\mathrm{PP}}|^2$) using (2). We first defined a physically meaningful and sufficiently large range of values for $s \in [0, 10]$ cm in 0.1 cm steps and $l \in [1, 40]$ cm in 0.5 cm steps. The third input parameter is soil permittivity and ranges from $\varepsilon_s \in [2.6, 78]$ in 0.1 steps. Within forward wave scattering models, several types of ACFs for simulations can be assumed. It is a requirement for simulating the surface backscatter and emissivity and is detached from *in situ* or remote sensing data. In this study, results for s and l are calculated using either Gaussian or Exponential ACF.

In this study, we simulate backscatter and emissivity values with the I^{2}EM to calculate $\beta_{P-\mathrm{PP}}^{\mathrm{Model}}$ [8]. The reason for employing the I^{2}EM is its common physical basis for backscatter and emissivity based on s and l, frequency f, type of ACF, incident angle θ, and soil permittivity ε_s [8], [47], [48]. Details on model formulations (computer codes) can be found in the supplement of [8]. Because of its analytical formulation, I^{2}EM is preferred over computationally more expensive numerical methods, such as the NMM3-D [49].

B. Data-Based Retrieval of Active–Passive Microwave Covariation

The covariation parameter calculated with (2) based on microwave observations is called the data-based covariation parameter $\beta_{P-\mathrm{PP}}^{\mathrm{Data}}$ [-]. This parameter is dependent on the observation conditions and the sensitivity of the recording system to the natural phenomenon.

In this study, $\beta_{P-\mathrm{PP}}^{\mathrm{Data}}$ is calculated based on SMAP observations specified in Section II.

C. Advantage of Active and Passive Microwave Signature Combination

As an example of how the joint use of radar and radiometer can improve soil moisture estimations, Fig. 1 shows overlays of radar-only and radiometer-only cost functions along with permittivity ε_s and the roughness parameter s simulated with the I^{2}EM.

Similar to Akbar *et al.* [34], the computed backscatter $\Delta|S_{\mathrm{PP}}|^2$ (radar-only) and emissivity ΔE_P (radiometer-only) spaces are displayed for a vector of unknowns ($\bar{x} = [\varepsilon_s, s, l]$). ε_s ranges from 2.6 to 50 in 0.1 steps, s values from 0.05 to 10 cm, and l values from 1 to 21 cm, each in 0.1 cm steps. In Fig. 1, we assume $l = 14$ cm and plot $\Delta|S_{\mathrm{PP}}|^2 < -30$ dB and $\Delta E_P < 0.01[-]$ to emphasize model predictions in the vicinity of the true test point (black cross), which is

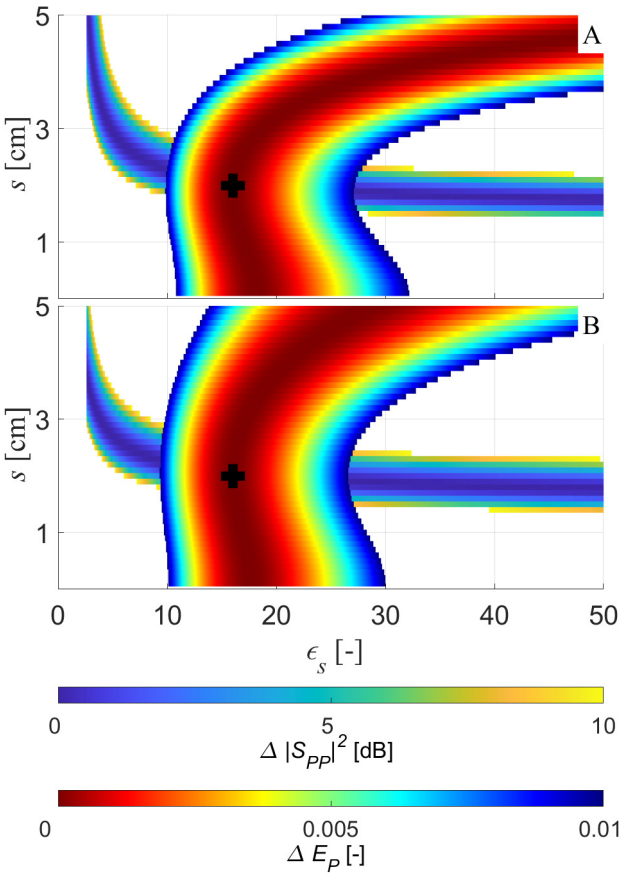

Fig. 1. Overlay of radar-only ($\Delta|S_{\mathrm{PP}}|^2 = ||S_{\mathrm{PP}}|^2(\bar{x}) - |S_{\mathrm{PP}}|^2_{\mathrm{True}}|^2$ [dB]) and radiometer-only ($\Delta E_P = |E_P(\bar{x}) - E_{P\mathrm{True}}|^2$ [-]) cost functions modeled with I^{2}EM assuming a Gaussian ACF. (a) Overlay for horizontal polarization. (b) Overlay for vertical polarization. The black cross is the true test point (global minimum) at input parameters $\varepsilon_s = 15[-]$, $s = 2$ cm, and $l = 14$ cm. Study similar to Akbar *et al.* [34].

the global minimum of the cost function. The results for the horizontal polarization [see Fig. 1(a)] and the vertical polarization [see Fig. 1(b)] are shown individually since "scattering polarization behaviors are different" [34].

It can be understood from Fig. 1 that the possible range of valid permittivity values that yield $\Delta|S_{\mathrm{PP}}|^2 \cong 0$ extend over the entire range of initial ε_s values. This holds true for both polarizations. The possible range of values for s spans from 1.2 to 5 cm. In the case of the radiometer, the possible range of permittivity values is slightly reduced and extends from 14 to 50 for the horizontal polarization [see Fig. 1(a)] and from 14 to 30 for the vertical polarization [see Fig. 1(b)]. However, the range of possible values for s now covers the entire range of initial s values (from 0.05 to 5 cm). Therefore, if only radars or radiometers are used, it is not clear which pairs (ε_s, s) lead to the most accurate estimates. This disadvantage is further amplified by the presence of measurement noise.

By combining radar- and radiometer-only cost functions, the search space for optimum parameter values is significantly reduced since the complementary physics of backscatter and emissivity limits the possible parameter search space. Consequently, lower retrieval errors can be achieved compared with retrievals only based on one sensor. The combined approach

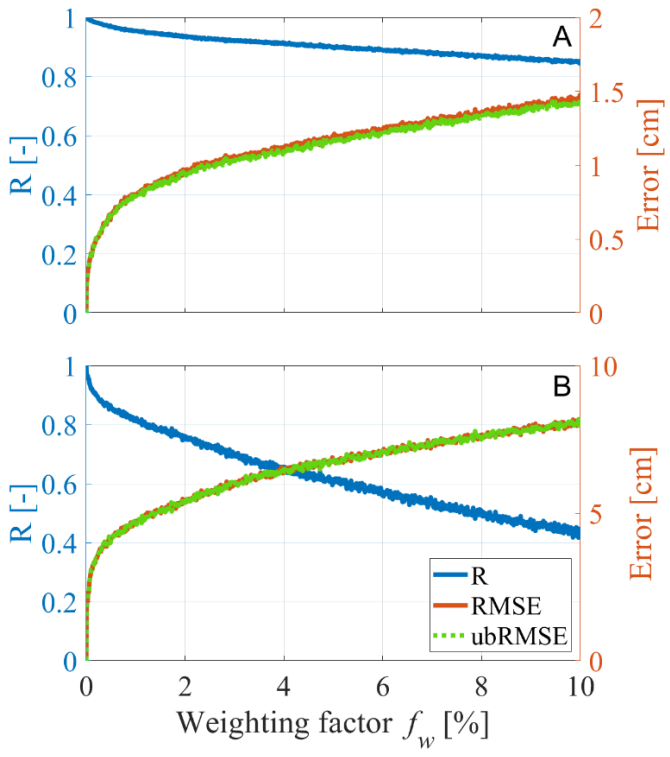

Fig. 2. Comparison of correlation coefficient (R), RMSE, and ubRMSE between the original roughness parameters s and l and perturbated roughness parameters $\hat{s}$ and $\hat{l}$ from retrieval input parameters with added random noise, along with the weighting factor f_w controlling the strength of added random noise ranging from 0% to 10%. (a) Vertical RMS-height (s, $\hat{s}$). (b) Horizontal correlation length (l, $\hat{l}$).

effectively reduces the susceptibility of radars to permittivity and the susceptibility of radiometers to roughness.

IV. Sensitivity Analyzes

A. Simulation-Based Performance Assessment of the Retrieval Algorithm

In order to assess the performance of the proposed active–passive covariation-based retrieval algorithm for surface roughness parameter estimation, simulations with noise-added retrieval input parameters have been performed. We simulated backscatter coefficients and emissivity values with the I^{2}EM for a wide range of roughness and permittivity values, based on which we estimated the surface roughness parameters s and l with the proposed approach. Afterward, we added random noise to the I^{2}EM simulated backscatter and emissivity. The subsequently estimated surface roughness parameters based on the noise-added simulations are denoted by $\hat{s}$ and $\hat{l}$. The random noise is generated based on the variance of the respective simulated parameter (backscatter and emissivity), randomly generated values uniformly distributed in the interval [0, 1], and a weighting factor f_w for each realization between 0% and 10%. In total, 1001 realizations are incorporated. The results for $\hat{s}$ and $\hat{l}$ are then compared with the originally estimated roughness parameters s and l. Fig. 2 displays the correlation coefficient (R), root-mean-square error (RMSE), and unbiased root-mean-square error (ubRMSE) between the original and perturbated surface roughness estimates as a function of the weighting factor f_w (strength of added noise).

It can be seen that correlation coefficients decrease to 0.85 between s and $\hat{s}$ and 0.43 between l and $\hat{l}$ for the maximum f_w of 10%. Here, the decrease in the surface parameter l is more rapid and larger in magnitude than for surface parameter s, showing that l is more sensitive to added noise on input parameters (backscatter and emissivity). The RMSE and ubRMSE increase concurrently with increasing f_w from 0 to 1.42 cm for s and from 0 to 7.98 cm for l. In summary, this simulation study serves as a first-order performance assessment of the proposed retrieval approach. However, the validation of the approach with real-world observations is paramount in a follow-on study.

B. Analysis of Sensitivity on Soil Permittivity

As shown in Fig. 1 in an overlay study, the influence on backscatter and emissivity is twofold with roughness and permittivity of the soil. In order to minimize the influence of permittivity, the covariation formulation in (2) was developed in this study. As (2) represents a ratio, it is anticipated that the permittivity-dependent reflectivity term in the emissivity and backscatter formulation (see [44] for modeling details) is comparable and minimizes its influence.

In order to evaluate this permittivity influence on our proposed covariation-based retrieval algorithm, we compared the full range of physically reasonable ε_s-values with the estimated model-based covariation parameter $\beta_{P-\mathrm{PP}}^{\mathrm{Model}}$, computed with NMM3-D and I^{2}EM (see Section III-A). As shown in Fig. 3, $\beta_{P-\mathrm{PP}}^{\mathrm{Model}}$ remains nearly constant over the entire range of permittivity values for both employed models except for small permittivity values. $\beta_{P-\mathrm{PP}}^{\mathrm{Model}}$ changes only for ε_s lower than approximately ten, representing arid and hyperarid soils. The reason for this is found in the formulation of covariation with emission over backscatter [see (2)]. The backscatter falls exponentially to very low values for these small permittivity values, which, in turn, causes larger dynamics in covariation. However, for $\varepsilon_s > 10$, $\beta_{P-\mathrm{PP}}^{\mathrm{Model}}$ calculated based on backscatter and emissivity from I^{2}EM is insensitive to permittivity dynamics. Consequently, both model simulations (NMM3-D and I^{2}EM) predict that the retrieval algorithm is independent of permittivity variations in the case of nonarid soils.

As the independence of our approach for $\varepsilon_s > 10$ is only based on NMM3-D and I^{2}EM simulations, the exact permittivity value from which our approach is insensitive may vary with other models, depending on the respective model design.

V. Results

This section presents the roughness results obtained from SMAP observations using the proposed covariation-based active–passive algorithm [see (2)]. In addition, the results for varying ACFs are compared and analyzed in the context of changing weather and soil conditions.

A. Results of Surface Roughness Parameter Estimation

In the following, the retrieval results for the roughness parameters s and l are presented. Note that the proposed

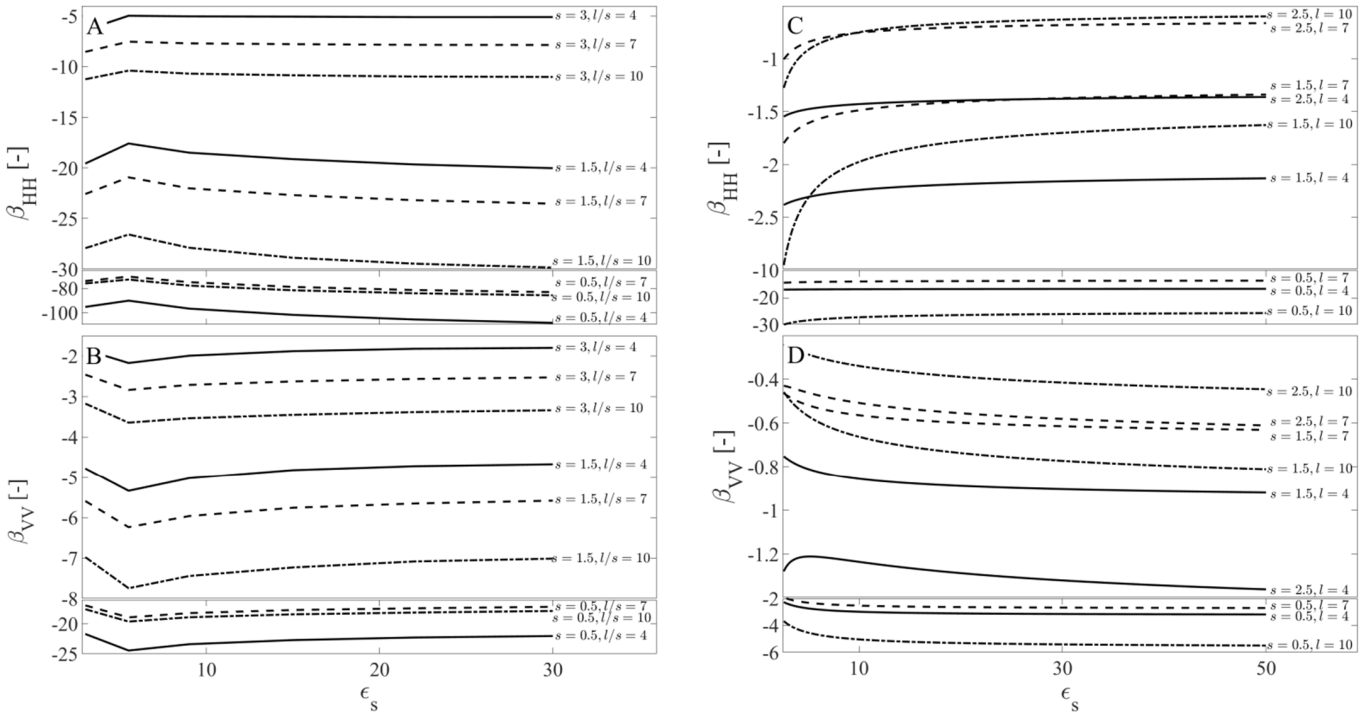

Fig. 3. Influence of soil permittivity ε_s on covariation parameter $\beta_{P-\mathrm{PP}}^{\mathrm{Model}}$ modeled with NMM3-D or I^{2}EM assuming a Gaussian ACF, s of 0.5, 1.5 and 3 cm and the ratio l/s of 4, 7, and 10 cm. (a) NMM3-D results for $\beta_{H-\mathrm{HH}}^{\mathrm{Model}}$. (b) NMM3-D results for $\beta_{V-\mathrm{VV}}^{\mathrm{Model}}$. (c) I^{2}EM results for $\beta_{H-\mathrm{HH}}^{\mathrm{Model}}$. (d) I^{2}EM results for $\beta_{V-\mathrm{VV}}^{\mathrm{Model}}$. The y-axes are interrupted since $\beta_{P-\mathrm{PP}}^{\mathrm{Model}}$ increases to large negative values for very smooth surfaces.

approach only applies to bare surfaces. These regions are located almost exclusively in North Africa, Asia, or Australia. For reasons of better readability, we will, therefore, only display results for this subregion.

Fig. 4 illustrates the median of estimated s and l for the subregion Africa–Asia–Australia, which was calculated assuming a Gaussian ACF. The results for s are between 0.35 and 7 cm, with a majority of the values (∼72.3%) between 0.35 and 2.5 cm. The lowest values for s are found within the Sahara and the highest values at the edges of deserts (e.g., Sahara and Gobi) or in the Arabian Peninsula due to increasing vegetation cover (e.g., shrublands) or rocks [see Fig. 4(a)]. The results for l range between 1.75 and 20.5 cm, with correlation lengths mostly (∼86.4%) of 6–16 cm. The lowest values for l are estimated, for example, in the Sahara or in the southern part of Australia. The highest values for l are found in the northwestern part of Australia as well as in Kazakhstan and Mongolia [see Fig. 4(b)].

Comparing the roughness estimates calculated assuming either a Gaussian (see Fig. 4) or an exponential ACF (see Fig. 5), the roughness patterns for the two ACFs generally appear similar. However, results for the Gaussian ACF are higher for s and lower for l compared with the results for the exponential ACF. About 72.3% of all s values assuming a Gaussian ACF are between 0.35 and 2.5 cm, whereas over 82.2% of all s values are located in the same range when assuming an exponential ACF. In addition, over 86.4% of values for l are located between 6 and 16 cm for the Gaussian ACF, but only 60.2% are located in that same range for the exponential ACF since overall larger l values are retrieved (see Fig. 5).

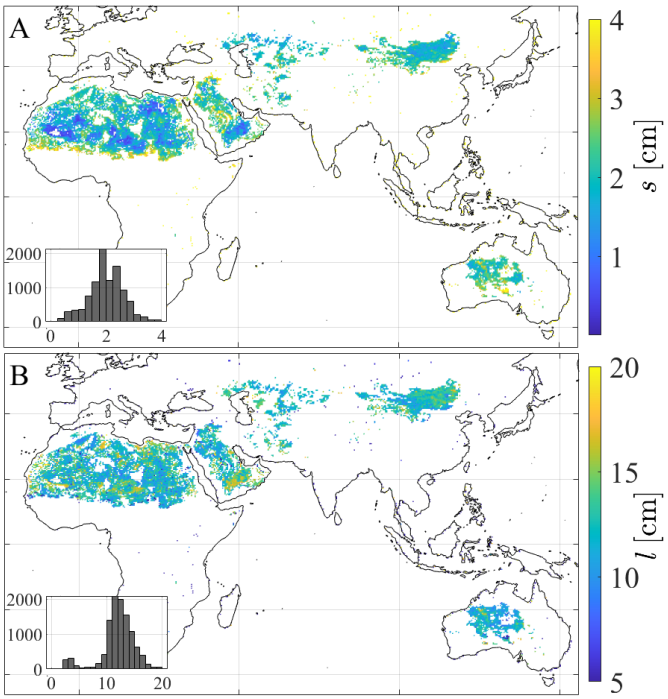

Fig. 4. Temporal median (April–July 2015) of the estimated surface roughness parameters s and l from SMAP observations for the subregion Africa–Asia–Australia assuming a Gaussian ACF. (a) Vertical RMS height s. (b) Horizontal correlation length l.

Based on the estimated roughness results for s and with $N = 2$ (see Section I-B), the roughness loss factor h is calculated assuming a Gaussian ACF [see Fig. 6(a)] or an exponential ACF [see Fig. 6(b)]. The values for h are in the

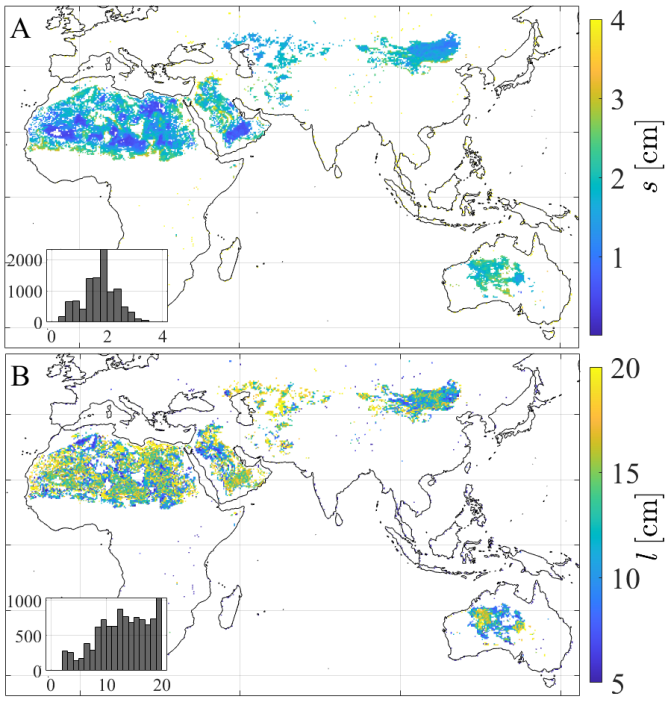

Fig. 5. Temporal median (April–July 2015) of the estimated surface roughness parameters s and l from SMAP observations for the subregion Africa–Asia–Australia assuming an exponential ACF. (a) Vertical RMS height s. (b) Horizontal correlation length l.

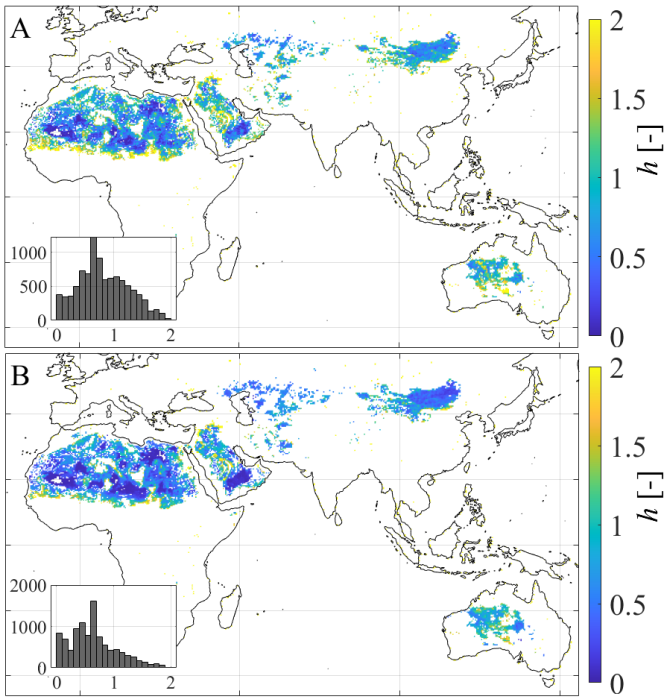

Fig. 6. Temporal median (April–July 2015) of the estimated roughness loss factor h for the subregion Africa–Asia–Australia based on surface roughness parameters s from SMAP observations. (a) Gaussian ACF. (b) Exponential ACF.

range between 0 and 2. As can be seen in Fig. 6, assuming a Gaussian ACF, the majority of values (∼79.7%) are located between 0 and 1.5 with a peak between 0.6 and 0.7 [see inset of Fig. 6(a)]. In the case of an exponential ACF, approximately

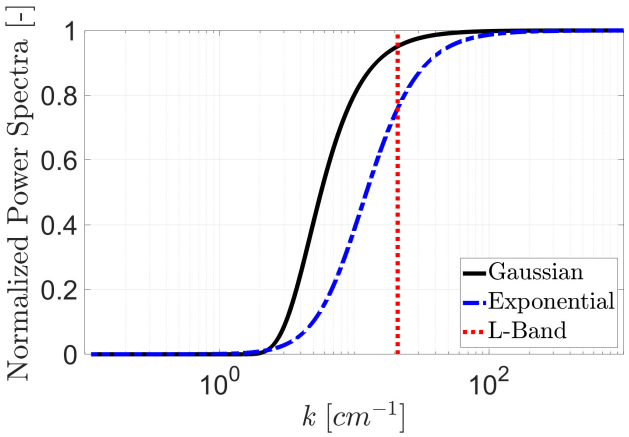

Fig. 7. Comparison of the normalized power spectra [-] for the Gaussian (black line) and exponential (blue dashes–dotted line) ACF at the L-band (red dashed line) along with the wavenumber k [cm^{-1}], calculated based on (9) and (10) of [50].

86.1% of all values for h are located in the range between 0 and 1.5. However, its peak is also between 0.6 and 0.7, whereas the magnitude is dropping significantly toward higher values. Hence, overall lower values for h are obtained assuming an exponential instead of a Gaussian ACF. By definition, the spatial patterns of h are equivalent to the ones of s (see Figs. 4–6).

For a more detailed investigation of the differences between the results of both ACFs, we analyzed their power spectra, as described in [50]. Defined as "a measure of the amplitude of each Fourier component scattered by a rough surface" [51], the power spectrum explains the surface type assumed for the ACF. We calculated the respective power spectrum for both ACFs along with different wave numbers according to [50] and normalized them by their respective amplitude to allow direct comparisons.

Fig. 7 shows the normalized power spectra of both ACFs and the case for L-band ($\lambda = 21$ cm) as a red dashed line. The roughness values calculated with an exponential ACF stay below the level of the values calculated with the Gaussian ACF. Hence, the Gaussian ACF describes a rougher soil surface, whereas the exponential ACF describes a smoother soil surface at the L-band, according to the presented retrieval results displayed in Figs. 4 and 5.

B. Comparison of Surface Roughness Estimates With Precipitation and Soil Conditions

Analyses are performed to investigate possible correlations between the estimated roughness parameters and external factors, such as weather or soil conditions, since precipitation or wind, as well as specific soil textures, potentially influence soil surface roughness.

For temporal analyzes, we used data from the Yanco Agricultural Institute, Bureau of Meteorology, Australia [52], to investigate the influence of precipitation on soil surface roughness with time.

In Fig. 8, we compare the daily *in situ* precipitation measurements and the corresponding SMAP soil moisture [37]

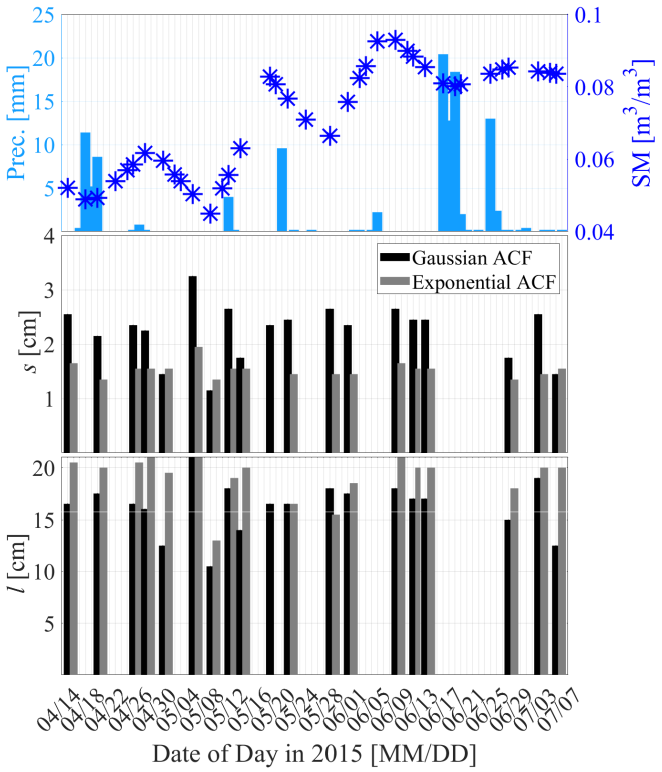

Fig. 8. Daily precipitation measurements from the Yanco agricultural institute, Bureau of Meteorology, Australia [52], (bright blue bars) and soil moisture from SMAP [37] (dark blue stars) in comparison with retrieval results for surface roughness parameters s and l, based on SMAP observations, assuming a Gaussian ACF (black bars) or exponential ACF (gray bars), at the Yanco weather station (NSW, 34.60°S, 146.42°E).

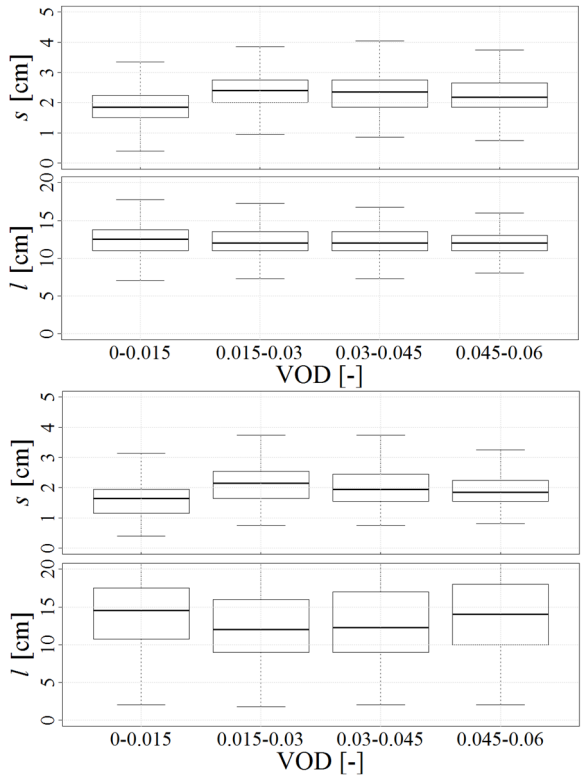

Fig. 9. Comparison of estimated surface roughness parameters s and l with VOD [-] [38], both from SMAP observations for the subregion Africa–Asia–Australia. (a) Gaussian ACF. (b) Exponential ACF.

values with roughness retrieval results at the Yanco test site, Australia.

For one, the variations in surface roughness parameters across the entire period from April 14 to July 7, 2015, show differences between the lowest and highest estimates of 2 cm for s and 10 cm for l, assuming a Gaussian ACF, as well as differences of 0.75 cm for s and 8 cm for l, assuming an exponential ACF. Hence, the estimated roughness parameters s and l vary less during the investigated period if an exponential ACF is assumed.

Second, it can be seen that the soil moisture and precipitation follow each other and correlate, as expected. However, both show no correlation with the SMAP-based results for s and l, regardless of the type of ACF (see Fig. 8). This lack of correlation between roughness results and precipitation was also tested between the roughness and soil moisture for the entire subregion Africa–Asia–Australia (not shown here). The analysis of the temporal correlation between the change of estimated roughness parameters s and l and the SMAP soil moisture dynamics shows no significant correlation, whereby the most frequent value in the analyzed histograms is zero with a standard deviation of 0.14.

In addition, the estimated roughness patterns were compared with VOD from SMAP MT-DCA retrievals [38] and sand or clay fractions of soils from [53], both posted on the 36-km EASE-2 grid.

Fig. 9 shows that retrieval results for s are slightly increasing until VOD class 0.015–0.03 and then slightly decrease. In contrast, the results for l are slightly decreasing until VOD class 0.015–0.03 and then slightly increase. Despite the overall similar distribution patterns, the value ranges for both ACFs are significantly different for roughness parameter l with much larger ranges for the exponential ACF. However, no influence of vegetation could be observed at higher VOD values. In extended analyses up to VOD of 1.12 (not shown here), we get higher values for s and lower values for l. The reason for this is that, with increasing vegetation canopy, we rather get a mix of signal effects from the ground (roughness) and vegetation. The value ranges of estimated s and l for all VOD classes from 0 to 0.06, thus, confirm the effective filtering before estimating the surface roughness parameters (see Section II).

Finally, we compared surface roughness results with the sand and clay fractions used as ancillary data within the SMAP parameter retrievals [53] in order to analyze if soil texture might influence the roughness retrieval of a soil surface. Fig. 10 shows that the overall distribution patterns are quite similar for both employed ACFs. Similar to the results displayed in Fig. 9, the value ranges are larger for the exponential ACF than for the Gaussian ACF. It can be seen that the estimated s peaks for the smallest sand fraction (0%–10%). On the contrary, the results for estimated l are lowest for the smallest sand fraction. In addition, the overall dynamic of l along increasing sand fractions (from 20% to 90%) is very low with absolute differences in median values of only 0.75 cm (Gaussian ACF) and 2.5 cm (exponential ACF) (see Fig. 10). In summary, the value ranges for s are similar for both ACFs, whereas the ranges for l assuming an exponential

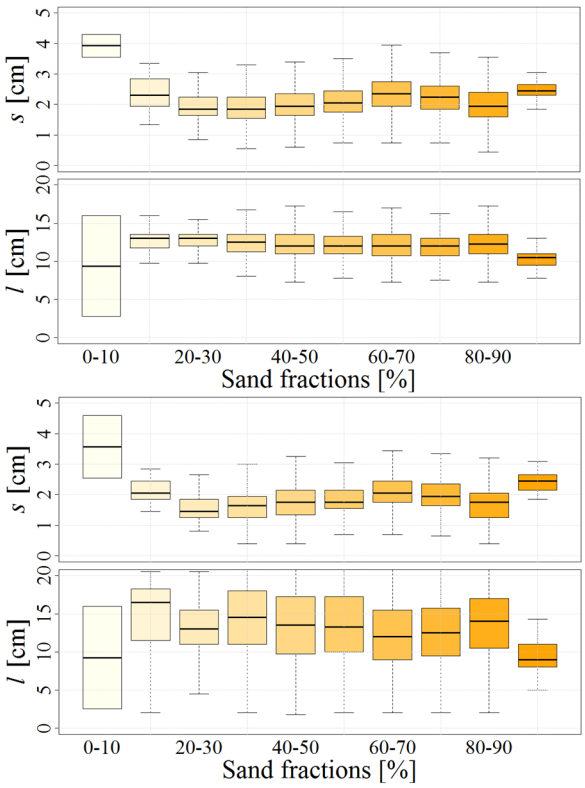

Fig. 10. Comparison of estimated surface roughness parameters s and l retrieved from SMAP observations with sand fractions from [53] for the subregion Africa–Asia–Australia. (a) Gaussian ACF. (b) Exponential ACF.

ACF are approximately two to three times larger than for the Gaussian ACF. However, the variation between sand fractions is reasonable and does not show a distinct correlation between roughness parameters and sand fractions.

When comparing the roughness results with clay fractions (not shown here), the most significant finding is that there is no correlation between clay fractions and the soil surface roughness parameters, similar to the case for sand fractions. Another finding is that there are no estimates of s and l for clay fractions greater than 70%. The fact that no roughness results overlap with clay fractions greater than 70% is consistent with the global distribution of clay fractions from the Harmonized World Soil Database (HWSD) [54].

VI. Discussion

Our covariation-based approach requires equivalent spatial resolution for radar and radiometer acquisitions in order to observe roughness at the same scales. Most space-borne radar sensors provide a much higher resolution than radiometer sensors. In the case of the SMAP mission, the radar had a spatial resolution of ∼3 km until its failure, whereas the radiometer has a resolution of ∼40 km [3]. In this study, we used the SMAP low-resolution radar and radiometer data with the same spatial resolution of 36 km. Since our approach is limited to simultaneously acquired polarimetric active/passive microwave data sets with comparable spatial resolutions, the data suitable beyond this study include the airborne passive and active L and S band sensor (PALS) data sets [16], [55] or the space-borne AQUARIUS data [56]. Despite these limitations in acquisition and resolution, our roughness retrieval technique outperforms ground-based sensing methods in terms of acquisition time and spatial coverage.

For evaluation of the proposed approach, we conducted several model-based sensitivity studies, compared retrieval results with literature values, and investigated possible correlations of roughness parameters with precipitation or soil texture. These analyzes will be discussed in the following. A direct validation based on experimental surface roughness data is not feasible due to the lack of available (*in situ*) data sets at the satellite footprint scale (36 km).

The covariation-based approach, including the forward model I^2EM for the retrieval of s and l, provides the possibility of employing varying ACFs and the simultaneous estimation of both roughness components with centimeter precision. Although we are only able to retrieve a wavelength-dependent roughness scales (here L-band), this approach enables the simultaneous estimation of both surface roughness parameters s and l by minimizing the influence of soil moisture (see Section IV). The study from [47] showed that the I^2EM is in good agreement with the SPM at low frequencies and the standard Kirchhoff model (KM) at high-frequency regions.

For SPM, the roughness influence on backscatter and emissivity is a multiplicative factor to the reflection coefficient, detailed in [44]. Hence, forming the ratio in (2) should cancel the permittivity influence if the reflection coefficients in backscatter (Bragg scattering) and emission (Fresnel scattering) are identical. This is the case for horizontal polarization but not for vertical polarization [44]. Thus, a residual dependence on soil moisture remains, which we have analyzed in Section IV-B. These analyzes showed that this dependence is the strongest for low permittivity and approaches toward a constant value for higher permittivity. In detail, for permittivity values of ten and higher, the value of the SPM-based ratio of Bragg to Fresnel scattering coefficients is approaching a constant value of six. Therefore, a quasi-independence from soil permittivity for values of ten and higher is found when estimating roughness parameters, which motivates the combined active–passive microwave approach. Similar to SPM, analyses presented in this study based on I^2EM delineated that our covariation-based approach is independent of permittivity for values $\varepsilon_s > 10$ (see Section IV-B).

However, in this study, we are only presenting results for subregion Africa–Asia–Australia since our approach is limited to bare soils. These regions are mostly arid to hyperarid with very low permittivity, which hardly changes in space and time due to the lack of precipitation. Hence, the approach presented in this study minimizes the permittivity dependence in two ways. On the one hand, our covariation-based approach is independent of permittivity for nonarid soils ($\varepsilon_s > 10$) by utilizing the covariation formulation [see (2)]. On the other hand, our presented roughness retrievals (see Section V) are quasi-independent of permittivity since we are only analyzing bare soils of dry regions with almost static soil moisture content. We tested this in a small add-on study where we fixed the input permittivity for all bare soil areas to a constant value of three and retrieved s and l. Analyses showed that we achieved very similar results as with inserting SMAP-based

permittivity, with average RMSE for the entire subregion Africa–Asia–Australia of 0.33 cm (s) or 0.87 cm (l) assuming a Gaussian ACF.

Within the proposed approach, we consider the two commonly applied ACFs of Gaussian and exponential type for characterization of the soil surface. Previous studies by [25] and [45] showed that, for rather smooth bare surfaces, the correlation function is close to the exponential ACF, whereas, for very rough surfaces, it is close to the Gaussian ACF. Especially for surface roughness of agriculturally managed soils, parameterization is more complex and variable since the ACF is affected by the characteristics of tillage, spanning several roughness scales. Nonetheless, also for agriculturally managed soils, most studies confirm an exponential ACF for smooth and Gaussian ACF for very rough surfaces (e.g., after plowing) [25], [57], [58]. Moreover, previous studies pointed out that surface roughness parameters are close to an exponential ACF when sensing over bare soils at L-Band [11], [29], [59]. A comparison of roughness results outlined the differences between both ACFs. We estimated values for s mainly in the range between 0.35 and 2.5 cm and for l between 6 and 16 cm, assuming a Gaussian ACF. For the assumption of an exponential ACF, we estimated overall lower s and higher l values. Thus, the exponential ACF describes a smoother roughness pattern, whereas the Gaussian ACF describes a rather rough surface roughness pattern, equivalent to the literature [25], [57], [58]. Ogilvy and Foster [51] investigated, in a numerical study, Gaussian and exponential correlation functions of theoretically generated random rough surfaces. They found that the exponential ACF tends to correlate roughness on a fine-scale due to a rapid loss of correlation. By contrast, the Gaussian ACF decreases more slowly over distance and, hence, tends to correlate roughness, not on a very fine scale [51]. Their explanation for varying roughness correlations was found to be the shape of the respective power spectra. In the case of the exponential ACF, it is a Lorentzian transform of the correlation function, whereas, in the case of the Gaussian ACF, it is given by the Fourier transform of the correlation function [51]. Hence, the influence of the employed ACF type is distinct and the assumption of Zhixiong *et al.* [60] that, for homogeneous agricultural fields, the ACF is unrelated to surface roughness conditions cannot be confirmed here.

In this study, we also presented the results for the roughness loss factor h, which is the prominent parameter used in passive microwave retrievals based on the HQN-model [24], [28] (see Section I-B). The results for h are located mainly between 0 and 1.5 with most values between 0.6 and 0.7, independent of the employed type of ACF. In the literature, typical values for H_R are located between 0 and 1.7, depending on the type and amount of vegetation canopy [24]. These correspond to h values between 0 and 1 (see Section I-B). The values for H_R greater than 1 are only estimated for forests, with typical values for the grass or open shrublands mostly around 0.4 [24], which is equal to an h value of 0.23.

With our covariation-based approach, where h peaks between 0.6 and 0.7, we are apparently overestimating h since our study areas are limited to bare soils only. Nonetheless, similar studies that are estimating the single scattering albedo ω directly instead within the $\tau - \omega$ model are also retrieving higher values compared with theoretical definitions [61]. Hence, we directly retrieve s and subsequently h, with estimated roughness values for h fitting to the expected smooth to moderately rough bare surfaces.

For detailed analyses of temporal changes within estimated surface roughness parameters and possible correlations with precipitation, we investigated results at the Yanko station, Australia. Surface roughness changes with weather (e.g., precipitation and wind) and agricultural managing techniques (e.g., plowing) [1]. Hence, we correlated retrieved s and l parameters with respective precipitation measurements over the entire investigation period (April to July 2015) but could not find significant correlations. Although, consequential "meteorological impacts cause a smoothing of the soil surface" [1], no such influence of rain events on estimated roughness parameters could be detected in this study. The reason for this is most likely related to the coarse spatial resolution of the SMAP data since the impacts of rainfall events are limited to the respective affected surface. Also, the study in [62] showed that precipitation can lead to changes in surface roughness, but these changes strongly dependent on the initial condition of the soil surface. Furthermore, the assumption may be only applies to agricultural managed soils right after tilling when the soil surface is disturbed. Zhao *et al.* [62] point to various studies regarding soil surface roughness variation due to different tillage practices and water erosion processes.

Surface roughness results and analyzes based on small-scale experimental microwave data from NASA's APEX12 campaign can be found in [63].

For detailed analyses of globally retrieved roughness patterns from SMAP observations, we compared the results for s and l with sand or clay fractions. From those analyses, it can be understood that, for our study setup, the respective sand or clay fraction of soil shows no distinct influence on s and l. However, we compared all roughness results retrieved from SMAP observations at once. This means that we do not consider different types of soils. Thus, comparisons of roughness results with individual major soil types to account for sand or clay dominated soils are needed to investigate the relationship between surface roughness and specific soil types in more detail [64].

VII. Conclusion and Summary

This study presents a covariation-based active–passive microwave retrieval algorithm for simultaneous estimation of vertical and horizontal soil surface roughness components (s, l) from bare soils. Within this approach, we use radar and radiometer data from both horizontal and vertical polarizations with an equivalent spatial resolution to calculate the active–passive microwave covariation for each individual radar-radiometer acquisition pair (no time series needed). This way, the approach enables a simultaneous retrieval of both roughness parameters (s, l) over a larger area (compared with *in situ* measurements).

Results show that the proposed approach leads to valid retrievals of s and l, with consistencies of more than 90% between model simulations and roughness results.

By conducting a series of model-based (NMM3-D and I^{2}EM) sensitivity tests, it was found that the influence of permittivity (soil moisture) on our covariation-based approach is only significant for (hyper) arid soils with $\varepsilon_s < 10$ (see Section IV). However, for these soils, the permittivity is small and static along space and time, which enables fixing its value to a constant. First tests (not shown) for the subregion Africa–Asia–Australia affirm this option.

We also tested the effectiveness of our filtering of data, in order to ensure analyses exclusively over bare soils, based on VOD values. Since no influence of vegetation could be observed at higher VOD values, we concluded that the filtering prior to the estimation of roughness results for vegetation was successful.

Moreover, no significant correlation between precipitation and surface roughness parameters could be found despite the often applied assumption that soil surface roughness smoothens with precipitation. One reason could be that this assumption only applies to agricultural managed soils after tilling. Furthermore, results outline that the changes in surface roughness are not correlated with changes in soil moisture.

Similar to correlations between the estimated roughness patterns and precipitation or soil moisture, no correlation could be found between roughness parameters and sand or clay fractions. The reason for the lack of correlations in all correlation analyses might be that we investigate global roughness patterns from SMAP observations with ∼36 km spatial resolution where precipitation effects might be nondominant in the recorded signal.

Detailed investigations regarding the influence of the assumed type of ACF revealed that both Gaussian and exponential ACF describe different types of roughness patterns, and our conclusions are consistent with previous studies. Hence, the employed type of ACF for surface roughness estimation is crucial and must be considered carefully.

In summary, the retrieved roughness parameters have the potential to improve soil moisture estimates, even from satellite data and for global scales. This supports soil moisture estimation for hydrometeorology or climate research.

The proposed technique for surface roughness retrieval from the combined active and passive microwave signatures is currently limited to bare soils. In order to enable the estimation under vegetated soils, our covariation-based algorithm needs to be updated for vegetation-based scattering and emission [44].

ACKNOWLEDGMENT

The authors would like to thank Mark Luetzner from DLR for English proofreading. The authors are grateful to MIT for supporting this research with the MIT-Germany Seed Fund "Global Water Cycle and Environmental Monitoring using Active and Passive Satellite-based Microwave Instruments."

REFERENCES

[1] P. Marzahn and R. Ludwig, "On the derivation of soil surface roughness from multi parametric PolSAR data and its potential for hydrological modeling," *Hydrol. Earth Syst. Sci.*, vol. 13, no. 3, pp. 381–394, Mar. 2009, doi: 10.5194/hess-13-381-2009.

[2] P. K. Srivastava, P. O'Neill, M. Cosh, M. Kurum, R. Lang, and A. Joseph, "Evaluation of dielectric mixing models for passive microwave soil moisture retrieval using data from ComRAD ground-based SMAP simulator," *IEEE J. Sel. Topics Appl. Earth Observ. Remote Sens.*, vol. 8, no. 9, pp. 4345–4354, Sep. 2015, doi: 10.1109/JSTARS.2014.2372031.

[3] D. Entekhabi *et al.*, "The soil moisture active passive (SMAP) mission," *Proc. IEEE*, vol. 98, no. 5, pp. 704–716, May 2010, doi: 10.1109/JPROC.2010.2043918.

[4] B. J. Choudhury, T. J. Schmugge, A. Chang, and R. W. Newton, "Effect of surface roughness on the microwave emission from soils," *J. Geophys. Res., Oceans*, vol. 84, no. C9, pp. 5699–5706, 1979, doi: 10.1029/JC084iC09p05699.

[5] P. Marzahn, D. Rieke-Zapp, and R. Ludwig, "Assessment of soil surface roughness statistics for microwave remote sensing applications using a simple photogrammetric acquisition system," *ISPRS J. Photogramm. Remote Sens.*, vol. 72, pp. 80–89, Aug. 2012, doi: 10.1016/j.isprsjprs.2012.06.005.

[6] D. Rieke-Zapp, H. Wegmann, F. Santel, and M. A. Nearing, "Digital photogrammetry for measuring soil surface roughness," in *Proc. Amer. Soc. Photogramm. Remote Sens.*, St. Louis, MI, USA, Apr. 2001, pp. 23–27.

[7] E. G. Njoku *et al.*, "Observations of soil moisture using a passive and active low-frequency microwave airborne sensor during SGP99," *IEEE Trans. Geosci. Remote Sens.*, vol. 40, no. 12, pp. 2659–2673, Dec. 2002, doi: 10.1109/TGRS.2002.807008.

[8] F.T. Ulaby *et al.*, *Microwave Radar and Radiometric Remote Sensing*. Ann Arbor, MI, USA: Univ. Michigan Press, 2014.

[9] P. S. Narvekar, D. Entekhabi, S.-B. Kim, and E. G. Njoku, "Soil moisture retrieval using L-band radar observations," *IEEE Trans. Geosci. Remote Sens.*, vol. 53, no. 6, pp. 3492–3506, Jun. 2015, doi: 10.1109/TGRS.2014.2377714.

[10] N. N. Das, D. Entekhabi, and E. G. Njoku, "An algorithm for merging SMAP radiometer and radar data for high-resolution soil-moisture retrieval," *IEEE Trans. Geosci. Remote Sens.*, vol. 49, no. 5, pp. 1504–1512, May 2011, doi: 10.1109/TGRS.2010.2089526.

[11] J. Shi, J. Wang, A. Y. Hsu, P. E. O'Neill, and E. T. Engman, "Estimation of bare surface soil moisture and surface roughness parameter using L-band SAR image data," *IEEE Trans. Geosci. Remote Sens.*, vol. 35, no. 5, pp. 1254–1266, Sep. 1997, doi: 10.1109/36.628792.

[12] Y. Oh, K. Sarabandi, and F. T. Ulaby, "An empirical model and an inversion technique for radar scattering from bare soil surfaces," *IEEE Trans. Geosci. Remote Sens.*, vol. 30, no. 2, pp. 370–381, Mar. 1992, doi: 10.1109/36.134086.

[13] M. C. Dobson and F. T. Ulaby, "Preliminaly evaluation of the SIR-B response to soil moisture, surface roughness, and crop canopy cover," *IEEE Trans. Geosci. Remote Sens.*, vol. GE-24, no. 4, pp. 517–526, Jul. 1986, doi: 10.1109/TGRS.1986.289666.

[14] J. Kolassa, R. H. Reichle, and C. S. Draper, "Merging active and passive microwave observations in soil moisture data assimilation," *Remote Sens. Environ.*, vol. 191, pp. 117–130, Mar. 2017, doi: 10.1016/j.rse.2017.01.015.

[15] E. Santi, S. Paloscia, S. Pettinato, and G. Fontanelli, "Application of artificial neural networks for the soil moisture retrieval from active and passive microwave spaceborne sensors," *Int. J. Appl. Earth Observ. Geoinf.*, vol. 48, pp. 61–73, Jun. 2016, doi: 10.1016/j.jag.2015.08.002.

[16] U. Narayan, "Retrieval of soil moisture from passive and active L/S band sensor (PALS) observations during the soil moisture experiment in 2002 (SMEX02)," *Remote Sens. Environ.*, vol. 92, no. 4, pp. 483–496, Sep. 2004, doi: 10.1016/j.rse.2004.05.018.

[17] M. Piles, D. Entekhabi, and A. Camps, "A change detection algorithm for retrieving high-resolution soil moisture from SMAP radar and radiometer observations," *IEEE Trans. Geosci. Remote Sens.*, vol. 47, no. 12, pp. 4125–4131, Dec. 2009, doi: 10.1109/TGRS.2009.2022088.

[18] J. D. Ouellette *et al.*, "A time-series approach to estimating soil moisture from vegetated surfaces using L-band radar backscatter," *IEEE Trans. Geosci. Remote Sens.*, vol. 55, no. 6, pp. 3186–3193, Jun. 2017.

[19] N. N. Das, D. Entekhabi, E. G. Njoku, J. J. C. Shi, J. T. Johnson, and A. Colliander, "Tests of the SMAP combined radar and radiometer algorithm using airborne field campaign observations and simulated data," *IEEE Trans. Geosci. Remote Sens.*, vol. 52, no. 4, pp. 2018–2028, Apr. 2014, doi: 10.1109/TGRS.2013.2257605.

[20] D. Entekhabi, N. N. Das, E. G. Njoku, S. Yueh, J. T. Johnson, and J. Shi, "Soil moisture active passive (SMAP). Algorithm theoretical basis document L2 & L3 radar/radiometer soil moisture (active/passive) data products," Revision A. Jet Propulsion Lab., California Inst. Technol., Pasadena, CA, USA, Tech. Rep., 2014. [Online]. Available: https://smap.jpl.nasa.gov/system/internal_resources/details/original/277_L2_3_SM_AP_RevA_web.pdf

[21] S. Saatchi, E. Njoku, and U. Wegmuller, "Synergism of active and passive microwave data for estimating bare soil surface moisture," in *Proc. ESA/NASA Int. Workshop Passive Microw. Remote Sens. Res. Related Land-Atmos. Interact.*, Saint-Lary, France, Jan. 1993, pp. 205–224.

[22] F. T. Ulaby, R. K. Moore, and A. K. Fung, *Microwave Remote Sensing: Active and Passive: Radar, Remote Sensing and Surface Scattering and Emission Theory*. Boston, MA, USA: Artech House, 1982.

[23] J.-P. Wigneron *et al.*, "L-band microwave emission of the biosphere (L-MEB) model: Description and calibration against experimental data sets over crop fields," *Remote Sens. Environ.*, vol. 107, no. 4, pp. 639–655, Apr. 2007, doi: 10.1016/j.rse.2006.10.014.

[24] J.-P. Wigneron *et al.*, "Modelling the passive microwave signature from land surfaces: A review of recent results and application to the L-band SMOS & SMAP soil moisture retrieval algorithms," *Remote Sens. Environ.*, vol. 192, pp. 238–262, Apr. 2017, doi: 10.1016/j.rse.2017.01.024.

[25] N. Verhoest, H. Lievens, W. Wagner, J. Álvarez-Mozos, M. Moran, and F. Mattia, "On the soil roughness parameterization problem in soil moisture retrieval of bare surfaces from synthetic aperture radar," *Sensors*, vol. 8, no. 7, pp. 4213–4248, Jul. 2008, doi: 10.3390/s8074213.

[26] U. Wegmuller and C. Matzler, "Rough bare soil reflectivity model," *IEEE Trans. Geosci. Remote Sens.*, vol. 37, no. 3, pp. 1391–1395, May 1999, doi: 10.1109/36.763303.

[27] T. Mo, B. J. Choudhury, T. J. Schmugge, J. R. Wang, and T. J. Jackson, "A model for microwave emission from vegetation-covered fields," *J. Geophys. Res.*, vol. 87, no. C13, pp. 229–237, 1982, doi: 10.1029/JC087iC13p11229.

[28] J. R. Wang and B. J. Choudhury, "Remote sensing of soil moisture content over bare field at 1.4 GHz frequency," *J. Geophys. Res.*, vol. 86, no. C6, pp. 5277–5282, 1981, doi: 10.1029/JC086iC06p05277.

[29] H. Lawrence, J.-P. Wigneron, F. Demontoux, A. Mialon, and Y. H. Kerr, "Evaluating the semiempirical H–Q model used to calculate the L-band emissivity of a rough bare soil," *IEEE Trans. Geosci. Remote Sens.*, vol. 51, no. 7, pp. 4075–4084, Jul. 2013, doi: 10.1109/TGRS.2012.2226995.

[30] T. Mo and T. J. Schmugge, "A parameterization of the effect of surface roughness on microwave emission," *IEEE Trans. Geosci. Remote Sens.*, vol. GE-25, no. 4, pp. 481–486, Jul. 1987, doi: 10.1109/TGRS.1987.289860.

[31] W. Dierking, "RMS slope of exponentially correlated surface roughness for radar applications," *IEEE Trans. Geosci. Remote Sens.*, vol. 38, no. 3, pp. 1451–1454, May 2000, doi: 10.1109/36.843040.

[32] A. K. Fung, *Microwave Scattering and Emission Models and Their Applications*. Boston, MA, USA: Artech House, 1994.

[33] D. Entekhabi, S. Yueh, P. E. O'Neill, and K. Kellogg, "SMAP handbook," Pasadena, CA, USA, Tech. Rep. JPL 400-1567, 2014.

[34] R. Akbar, M. H. Cosh, P. E. O'Neill, D. Entekhabi, and M. Moghaddam, "Combined radar–radiometer surface soil moisture and roughness estimation," *IEEE Trans. Geosci. Remote Sens.*, vol. 55, no. 7, pp. 4098–4110, Jul. 2017, doi: 10.1109/TGRS.2017.2688403.

[35] *Dataset: SMAP_L1B_S0_LoRes_V2. Retrieved from ASF DAAC 7*, SMAP Data 2015 (NASA), Washington, DC, USA, Dec. 2015, doi: 10.5067/J4SZZV52B88J.

[36] S. Chan, E. G. Njoku, and A. Colliander, *SMAP L1C Radiometer Half-Orbit 36 km EASE-Grid Brightness Temperatures, Version 3. Global Projection*, NASA Nat. Snow Ice Data Center Distrib. Active Arch. Center, Boulder, CO, USA, 2016, doi: 10.5067/E51BSP6V3KP7.

[37] P. E. O'Neill, "SMAP L3 radiometer global daily 36 km EASE-grid soil moisture, version 4. Global projection," NASA Nat. Snow Ice Data Center Distrib. Active Arch. Center, Boulder, CO, USA, Tech. Rep., 2016, doi: 10.5067/OBBHQ5W22HME.

[38] A. G. Konings, M. Piles, N. Das, and D. Entekhabi, "L-band vegetation optical depth and effective scattering albedo estimation from SMAP," *Remote Sens. Environ.*, vol. 198, pp. 460–470, Sep. 2017, doi: 10.1016/j.rse.2017.06.037.

[39] X. Xu, "SMAP L3 radiometer northern hemisphere daily 36 km EASE-grid freeze/thaw state, version 1. Global projection," NASA Nat. Snow Ice Data Center Distrib. Active Arch. Center, Boulder, CO, USA, Tech. Rep., 2016, doi: 10.5067/RDEJQEETCNWV.

[40] C. Utku and D. M. Le Vine, "Topographic signatures in aquarius radiometer and scatterometer response," *IEEE Trans. Geosci. Remote Sens.*, vol. 52, no. 7, pp. 4141–4154, Jul. 2014, doi: 10.1109/TGRS.2013.2280015.

[41] A. Monerris *et al.*, "Assessment of the topography impact on microwave radiometry at L-band," *J. Geophys. Res.*, vol. 113, no. B12, 2008, Art. no. B12202, doi: 10.1029/2008JB005602.

[42] A. Mialon, L. Coret, Y. H. Kerr, F. Secherre, and J.-P. Wigneron, "Flagging the topographic impact on the SMOS signal," *IEEE Geosci. Remote Sens. Lett.*, vol. 46, no. 3, pp. 689–694, Mar. 2008, doi: 10.1109/TGRS.2007.914788.

[43] Jarvis A., H.I. Reuter, A. Nelson, E. Guevara. (2008). *Hole-Filled Seamless SRTM Data V4*, International Centre for Tropical Agriculture (CIAT). [Online]. Available: http://srtm.csi.cgiar.org

[44] T. Jagdhuber *et al.*, "Physics-based modeling of active and passive microwave covariations over vegetated surfaces," *IEEE Trans. Geosci. Remote Sens.*, vol. 57, no. 2, pp. 788–802, Feb. 2019, doi: 10.1109/TGRS.2018.2860630.

[45] T. Jagdhuber *et al.*, "Physically-based retrieval of SMAP active-passive measurements covariation and vegetation structure parameters," in *Proc. IEEE Int. Geosci. Remote Sens. Symp. (IGARSS)*, Beijing, China, Jul. 2016, pp. 3078–3081, doi: 10.1109/IGARSS.2016.7729796.

[46] G. C. Topp, J. L. Davis, and A. P. Annan, "Electromagnetic determination of soil water content: Measurements in coaxial transmission lines," *Water Resour. Res.*, vol. 16, no. 3, pp. 574–582, Jun. 1980, doi: 10.1029/WR016i003p00574.

[47] K. S. Chen, T.-D. Wu, L. Tsang, Q. Li, J. Shi, and A. K. Fung, "Emission of rough surfaces calculated by the integral equation method with comparison to three-dimensional moment method simulations," *IEEE Trans. Geosci. Remote Sens.*, vol. 41, no. 1, pp. 90–101, Jan. 2003, doi: 10.1109/TGRS.2002.807587.

[48] A. K. Fung, W. Y. Liu, K. S. Chen, and M. K. Tsay, "An improved iem model for bistatic scattering from rough surfaces," *J. Electromagn. Waves Appl.*, vol. 16, no. 5, pp. 689–702, Jan. 2002, doi: 10.1163/156939302X01119.

[49] L. Tsang *et al.*, "Active and passive vegetated surface models with rough surface boundary conditions from NMM3D," *IEEE J. Sel. Topics Appl. Earth Observ. Remote Sens.*, vol. 6, no. 3, pp. 1698–1709, Jun. 2013, doi: 10.1109/JSTARS.2013.2257694.

[50] C. A. Mack, "Analytic form for the power spectral density in one, two, and three dimensions," *J. Micro/Nanolithography, MEMS, MOEMS*, vol. 10, no. 4, Oct. 2011, Art. no. 040501, doi: 10.1117/1.3663567.

[51] J. A. Ogilvy and J. R. Foster, "Rough surfaces: Gaussian or exponential statistics?" *J. Phys. D: Appl. Phys.*, vol. 22, no. 9, pp. 1243–1251, Sep. 1989, doi: 10.1088/0022-3727/22/9/001.

[52] Australian Government. Agricultural Institute. *Bureau of Meteorology*. Accessed: Jul. 27, 2018. [Online]. Available: http://www.bom.gov.au/climate/data/index.shtml?bookmark=136

[53] N. N. Das, "Ancillary data report: Soil attributes," Jet Propuls. Lab., Calif. Inst. Technol., Pasadena, CA, USA, Tech. Rep. JPL D-53058, 2013.

[54] W. R. Wieder, J. Boehnert, G. B. Bonan, and M. Langseth, "Regridded harmonized world soil database v1.2. Data set," Oak Ridge Nat. Lab. Distrib. Active Arch. Center, Oak Ridge, TN, USA, Tech. Rep., 2014. [Online]. Available: http://daac.ornl.gov and http://daac.ornl.gov, doi: 10.3334/ORNLDAAC/1247.

[55] R. Bindlish, T. Jackson, R. Sun, M. Cosh, S. Yueh, and S. Dinardo, "Combined passive and active microwave observations of soil moisture during CLASIC," *IEEE Geosci. Remote Sens. Lett.*, vol. 6, no. 4, pp. 644–648, Oct. 2009, doi: 10.1109/LGRS.2009.2028441.

[56] D. M. Le Vine, G. S. E. Lagerloef, F. R. Colomb, S. H. Yueh, and F. A. Pellerano, "Aquarius: An instrument to monitor sea surface salinity from space," *IEEE Trans. Geosci. Remote Sens.*, vol. 45, no. 7, pp. 2040–2050, Jul. 2007, doi: 10.1109/TGRS.2007.898092.

[57] V. Gupta and R. Jangid, "Microwave response of rough surfaces with autocorrelation functions, RMS heights and correlation lengths using active remote sensing," *Indian J. Radio Space Phys.*, vol. 40, pp. 137–146, Jun. 2011.

[58] N. Baghdadi *et al.*, "Semi-empirical calibration of the integral equation model for co-polarized L-band backscattering," *Remote Sens.*, vol. 7, no. 10, pp. 13626–13640, Oct. 2015, doi: 10.3390/rs71013626.

[59] J. Peng, A. Loew, O. Merlin, and N. E. C. Verhoest, "A review of spatial downscaling of satellite remotely sensed soil moisture," *Rev. Geophys.*, vol. 55, pp. 1–26, Jun. 2017, doi: 10.1002/2016RG000543.

[60] L. Zhixiong, C. Nan, U. D. Perdok, and W. B. Hoogmoed, "Characterisation of soil profile roughness," *Biosystems Eng.*, vol. 91, no. 3, pp. 369–377, Jul. 2005, doi: 10.1016/j.biosystemseng.2005.04.004.

[61] M. Kurum, P. E. O'Neill, R. H. Lang, A. T. Joseph, M. H. Cosh, and T. J. Jackson, "Effective tree scattering and opacity at L-band," *Remote Sens. Environ.*, vol. 118, pp. 1–9, Mar. 2012, doi: 10.1016/j.rse.2011.10.024.

[62] L. Zhao, X. Liang, and F. Wu, "Soil surface roughness change and its effect on runoff and erosion on the Loess Plateau of China," *J. Arid Land*, vol. 6, no. 4, pp. 400–409, Aug. 2014, doi: 10.1007/s40333-013-0246-z.

[63] A. Fluhrer *et al.*, "Physics-based retrieval of surface roughness parameters for bare soils from combined active-passive microwave signatures," in *Proc. IEEE Int. Geosci. Remote Sens. Symp. (IGARSS)*, Valencia, Spain, Jul. 2018, pp. 337–340, doi: 10.1109/IGARSS.2018.8519563.

[64] D. van der Wal, P. M. J. Herman, and A. Wielemaker-van den Dool, "Characterisation of surface roughness and sediment texture of intertidal flats using ERS SAR imagery," *Remote Sens. Environ.*, vol. 98, no. 1, pp. 96–109, Sep. 2005, doi: 10.1016/j.rse.2005.06.004.

Anke Fluhrer (Member, IEEE) received the B.S. degree in geography from the Julius-Maximilians-University Würzburg, Würzburg, Germany, in 2014, and the M.S. degree in physical geography from the Friedrich-Alexander University Erlangen-Nuremberg, Erlangen, Germany, in 2018.

She is a Research Associate with the prospect of a Ph.D. with the Microwaves and Radar Institute (HR), German Aerospace Center (DLR), Weßling, Germany. Her research interests include terrestrial remote sensing, satellite image processing, and data assimilation.

Thomas Jagdhuber (Senior Member, IEEE) received the Diploma degree (Hons.) in physical geography, physics, remote sensing, and geoinformatics from the Ludwig Maximilian University of Munich, Munich, Germany, in 2006, and the Ph.D. degree (Hons.) in hydrology from the Faculty of Science, University of Potsdam, Potsdam, Germany, in 2012.

His main research interests include physics-based multisensor data integration with a focus on active and passive microwave interaction theory and on polarimetric techniques for hydrological, cryosphere, and agricultural parameter modeling and estimation. Since 2007, he has been affiliated with the Microwaves and Radar Institute (HR), German Aerospace Center (DLR), Weßling, Germany. From 2014 to 2019, he was a Yearly Visiting Scientist with the Massachusetts Institute of Technology (MIT), Cambridge, MA, USA, contributing to the preparation and continuation of the SMAP and SMAP/Sentinel-1 missions. In addition, he serves as a Lecturer for the University of Jena, Jena, Germany, and the University of Augsburg, Augsburg, Germany, as well as a Reviewer for several international journals and conference boards.

Dr. Jagdhuber was honored with the DLR Science Award for his research on polarimetric synthetic aperture radar (SAR) decomposition techniques in 2014. Together with Dr. Entekhabi (MIT), he was awarded the MIT International Science and Technology Initiatives (MISTI) Grant for global water cycle and environmental monitoring using active and passive satellite-based microwave instruments.

Ruzbeh Akbar (Member, IEEE) received the B.S. (*summa cum laude*) degree from The George Washington University, Washington, DC, USA, in 2009, the M.S. degree from the University of Michigan, Ann Arbor, MI, USA, in 2011, and the Ph.D. degree from the University of Southern California, Los Angeles, CA, USA, in 2016, all in electrical engineering.

He is a Postdoctoral Research Associate with the Massachusetts Institute of Technology, Cambridge, MA, USA. His research interests include terrestrial remote sensing, electromagnetic theory, and hydrology.

Dr. Akbar was a recipient of the NASA Earth and Space Science Fellowship from 2010 to 2014.

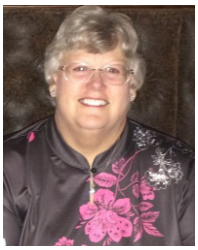

Peggy E. O'Neill (Fellow, IEEE) received the B.S. (*summa cum laude*) degree (Hons.) in geography from Northern Illinois University, DeKalb, IL, USA, in 1976, and the M.A. degree in geography from the University of California at Santa Barbara, Santa Barbara, CA, USA, in 1979. She has done postgraduate research in civil and environmental engineering with Cornell University, Ithaca, NY, USA.

Since 1980, she has been a Physical Scientist with the Hydrological Sciences Laboratory, NASA/Goddard Space Flight Center, Greenbelt, MD, USA, where she conducts research in soil moisture retrieval and land surface hydrology, primarily through microwave remote sensing techniques. She is the SMAP Deputy Project Scientist.

Dara Entekhabi (Fellow, IEEE) received the B.S. and two M.S. degrees in geography from Clark University, Worcester, MA, USA, in 1983, 1985, and 1988, respectively, and the Ph.D. degree in civil and environmental engineering from the Massachusetts Institute of Technology (MIT), Cambridge, MA, USA, in 1990.

He is a Professor with the Department of Civil and Environmental Engineering and the Department of Earth, Atmospheric and Planetary Sciences, MIT. He is also the Science Team Lead for the National Aeronautics and Space Administration's Soil Moisture Active and Passive (SMAP) Mission that was launched January 31, 2015. His research includes terrestrial remote sensing, data assimilation, and coupled land–atmosphere systems modeling.

Dr. Entekhabi is a member of the National Academy of Engineering. He is also a Fellow of the American Meteorological Society and the American Geophysical Union.

3 Article II

A. Fluhrer, T. Jagdhuber, A. Tabatabaeenejad, H. Alemohammad, C. Montzka, P. Friedl, E. Forootan, and H. Kunstmann, 'Remote Sensing of Complex Permittivity and Penetration Depth of Soils Using P-Band SAR Polarimetry,' in *MDPI Remote Sensing*, 2022, 14(12), 2755, doi: 10.3390/rs14122755.

remote sensing

MDPI

Article

Remote Sensing of Complex Permittivity and Penetration Depth of Soils Using P-Band SAR Polarimetry

Anke Fluhrer [1,2,*], Thomas Jagdhuber [1,2], Alireza Tabatabaeenejad [3], Hamed Alemohammad [4], Carsten Montzka [5], Peter Friedl [6], Ehsan Forootan [7] and Harald Kunstmann [2,8]

1 Microwaves and Radar Institute, German Aerospace Center (DLR), Muenchenerstraße 20, 82234 Weßling, Germany; thomas.jagdhuber@dlr.de
2 Institute of Geography, Augsburg University, Alter Postweg 118, 86159 Augsburg, Germany; harald.kunstmann@kit.edu
3 The Aerospace Corporation, El Segundo, CA 90245, USA; alirezat@aero.org
4 Radiant Earth Foundation, Washington, DC 20005, USA; h.alemohammad@gmail.com
5 Institute of Bio- and Geosciences: Agrosphere (IBG-3), Forschungszentrum Jülich, Wilhelm-Johnen-Straße, 52428 Jülich, Germany; c.montzka@fz-juelich.de
6 Earth Observation Center, German Aerospace Center (DLR), Muenchenerstraße 20, 82234 Weßling, Germany; peter.friedl@dlr.de
7 Geodesy Group, Department of Planning, Aalborg University, Rendsburggade 14, 9000 Aalborg, Denmark; efo@plan.aau.dk
8 Institute of Meteorology and Climate Research, Karlsruhe Institute of Technology, Kreuzeckbahnstraße 19, 82467 Garmisch-Partenkirchen, Germany
* Correspondence: anke.fluhrer@dlr.de; Tel.: +49-8153-28-3908

Abstract: A P-band SAR moisture estimation method is introduced for complex soil permittivity and penetration depth estimation using fully polarimetric P-band SAR signals. This method combines eigen- and model-based decomposition techniques for separation of the total backscattering signal into three scattering components (soil, dihedral, and volume). The incorporation of a soil scattering model allows for the first time the estimation of complex soil permittivity and permittivity-based penetration depth. The proposed method needs no prior assumptions on land cover characteristics and is applicable to a variety of vegetation types. The technique is demonstrated for airborne P-band SAR measurements acquired during the AirMOSS campaign (2012–2015). The estimated complex permittivity agrees well with climate and soil conditions at different monitoring sites. Based on frequency and permittivity, P-band penetration depths vary from 5 cm to 35 cm. This value range is in accordance with previous studies in the literature. Comparison of the results is challenging due to the sparsity of vertical soil in situ sampling. It was found that the disagreement between in situ measurements and SAR-based estimates originates from the discrepancy between the in situ measuring depth of the top-soil layer (0–5 cm) and the median penetration depth of the P-band waves (24.5–27 cm).

Keywords: AirMOSS; polarimetric decomposition; soil moisture; multi-layer SPM

Citation: Fluhrer, A.; Jagdhuber, T.; Tabatabaeenejad, A.; Alemohammad, H.; Montzka, C.; Friedl, P.; Forootan, E.; Kunstmann, H. Remote Sensing of Complex Permittivity and Penetration Depth of Soils Using P-Band SAR Polarimetry. *Remote Sens.* **2022**, *14*, 2755. https://doi.org/10.3390/rs14122755

Academic Editor: Frédérique Seyler

Received: 4 May 2022
Accepted: 6 June 2022
Published: 8 June 2022

1. Introduction

Soil moisture is one of the essential climate variables (ECVs) [1] "that critically contribute [. . .] to the characterization of [the] Earth's climate" [2] and its changes. Hence, it plays a crucial role within the hydrological and biogeochemical cycles [1,3–7]. Many approaches exist to retrieve soil moisture from air- or space-borne remote sensing observations, taking advantage of the sensitivity of active (radar) and/or passive (radiometer) microwave signals to soil moisture [8–12]. These studies allow an estimation of soil moisture predominantly from L-band measurements: on the one hand, because of the larger penetration capabilities compared to higher frequency bands, such as C- or X-band, and on the other hand, due to the availability of global L-band satellite data, e.g., from Soil

Moisture and Ocean Salinity (SMOS) (since 2009) [10] or Soil Moisture Active Passive (SMAP) (since 2015) [8] missions. Lower frequency bands such as P-band have only rarely been used to estimate soil moisture from space, mainly due to the lack of sensors operating at P-band frequencies. Nevertheless, with the European Space Agency (ESA) BIOMASS mission in 2023, the first P-band sensor in space will be launched [13]. In addition, the first on-orbit demonstration of the remote sensing technique will be started by the National Aeronautics and Space Administration (NASA) SigNals of Opportunity: P-band Investigation (SNoOPI) mission in 2022 [14,15]. Moreover, P-band airborne datasets, e.g., from the Airborne Microwave Observatory of Subcanopy and Subsurface (AirMOSS) campaign, are already available [16]. Hence, P-band data can also be employed for estimating soil moisture, e.g., by decomposing fully polarimetric radar signals into individual scattering mechanisms.

Incoherent decomposition theorems have been developed to decompose scattering from natural media and disentangle the different scattering contributions of the signal. Fully polarimetric synthetic aperture radar (PolSAR) provides measurements of the Earth's surface represented by a complex scattering matrix [S], based on which the 3×3 covariance [C] or coherence [T] matrices can be calculated [9,17–19]. Among many decomposition methods, two basic categories can be distinguished: eigen-based, introduced by [20], or model-based, established by [21]. The first is based on the eigenvalue decomposition of the [C] or [T] matrix, leading to three parameters: the polarimetric entropy H, expressing the randomness of the polarimetric scattering process, the polarimetric anisotropy A, characterizing the secondary scattering processes, and the polarimetric scattering angle α, representing an intrinsic scattering mechanism [17,22,23].

The model-based decomposition simulates backscattering as the linear sum of multiple, mostly simple physical scattering mechanisms of canonical objects (e.g., spheres, dipoles) [18,22,24]. Here, [C] or [T] are decomposed into three components: surface, dihedral (double-bounce), and volume scattering. More detailed reviews of the decomposition theorems can be found in [25–30].

In order to take advantage of both, a combination of eigen- and model-based incoherent decomposition techniques was suggested by [24,31]. By including a generalized volume scattering model and under the assumption of scattering reflection symmetry ($\langle S_{HH} S_{HV}^* \rangle = 0$ & $\langle S_{VV} S_{HV}^* \rangle = 0$), an iterative hybrid decomposition method was proposed, combining eigen- and model-based techniques to decompose [T] into the three canonical scattering components: surface [T_s], dihedral [T_d], and volume [T_v] [24]. Assumed scattering reflection symmetry may only be violated significantly in urban or high mountain regions [27]. The authors of [24] demonstrated the feasibility of the proposed iterative hybrid decomposition method and the inversion algorithm for soil moisture estimation across various agricultural vegetation covers, based on L-band airborne SAR data of the operational discharge and flooding predictions in head catchments (OPAQUE), Synthetic Aperture Radar within TERENO framework (SARTEO), and AgriSAR campaigns from 2006 to 2008. Within this decomposition, two iterations to determine the appropriate initial permittivity and the best physically "constrained volume intensity component f_V" [24] are necessary. Although the results showed that the separation of volume scattering from ground scattering components is physically meaningful compared to in situ measurements, this iterative approach is complex in algorithmics, computationally expensive, and requires certain assumptions on initial conditions. Hence, [3] presented an adapted hybrid decomposition technique by combining the model-based decomposition technique of [18,21] with the eigen-based decomposition technique, as proposed in [24,27]. By employing observations of the AirMOSS campaign, [3] were the first to apply the hybrid decomposition method on P-band SAR data across a wide range of vegetation covers (from grasslands to dense forests). Further, no assumptions on initial vegetation conditions are made in that study, since "[volume] scattering is modeled using a cloud of randomly-oriented dipoles" [3]. For the decomposition of the total backscattering signal into the three scattering components [T_s], [T_d], and [T_v], the volume scattering intensity f_V is estimated from the cross-polarized signal directly [31] by fixing the vegetation representations to

dipoles that are randomly distributed [3] (cf. Section 3.2). The authors of [19] further explored the proposed hybrid decomposition approach by comparing results based on L- and P-band SAR observations from the AirMOSS campaign. Both studies demonstrated the applicability of the hybrid decomposition technique to P-band data of various biomes. Thus, results for soil and dihedral scattering contributions proved the usability of such hybrid techniques for designing soil moisture retrieval algorithms using polarimetric low frequency observations [3,19]. However, the authors concluded that the approach can be further improved by considering more than just one vegetation representation [3]. In the end, one main disadvantage of decomposition approaches is the well-known problem of overestimating the volume scattering component due to "discrimination [problems] between vegetation and oriented buildings" [32], leading to negative powers (physically impossible) [9,22,27,33].

The change in direction of the electromagnetic wave when it enters a dielectric medium can be related to its relative electric permittivity ε_r [–], formerly also called the dielectric constant [34,35]. In this study, the relative permittivity of soil is denoted by ε_s, which is a complex number with a real $\varepsilon_s{}'$ and an imaginary part $\varepsilon_s{}''$. In most studies, only the real part of ε_s is considered and investigated, e.g., [24,31,36–38]. However, in general, soils are lossy media, where $\varepsilon_s{}''$ is of significant importance when describing the soil permittivity and, hence, is investigated in this study.

The advantage of microwave remote sensing is the ability of electromagnetic waves to penetrate through vegetation or into the soil. In general, the lower the frequency, the larger the penetration into the soil, e.g., [5,35,39,40]. However, the penetration ability of microwaves is more complex and depends on varying factors besides frequency, such as the sensor itself, as well as soil or vegetation cover characteristics (e.g., incidence angle, polarization, soil texture, density, moisture, and surface roughness). Since the penetration depth is defined as depth after which the power density of the propagating electromagnetic radiation is reduced by a factor of $1/e$ ($\approx$0.37), e.g., [35,39,41], it is an important measure and indication in microwave remote sensing. For example, if the penetration depth is low, the contribution of the underlying soil to the backscattered waves is questionable and, hence, the signal may be insensitive to estimated soil moistures [42].

Dependent on ε_s, several more or less complex formulations to calculate the microwave penetration depth δ_p have been published, e.g., in [35,41,43–45]. Many of them depend mainly on the permittivity of the medium, the wavelength (frequency), and incidence angle of the incoming wave and, hence, do not account for scattering effects, system (e.g., sensitivity, calibration uncertainty), or medium (e.g., dielectric discontinuity) characteristics, but only attenuation effects of the medium [39]. Ref. [39] compared penetration depths at L-band (1.26 GHz) and P-band (430 MHz) frequencies across varying top-layer permittivities and concluded that δ_p "significantly underestimates the depths that radar backscatter can actually detect" [39]. One reason is that δ_p does not account for discrepancies between decreasing wave intensity with depth and the depth contribution to the total radar signal. However, in the case the radar signal-to-noise ratio is sufficiently high, variations beyond δ_p will be detected [46]. Furthermore, results showed smaller penetration capabilities of L-band frequencies compared to P-band [39]. Similarly, [40] determined the moisture retrieval depth from polarimetric L-band (1.400–1.426 GHz) and P-band (0.742–0.752 GHz) radiometer data, measured during the P-band Radiometer Inferred Soil Moisture (PRISM) project in 2019 at Core Lynn, Australia. The study was conducted to investigate the assumption of increasing moisture retrieval depths for longer wavelengths, and thus to show the potential of P-band wavelengths to retrieve soil moisture at larger depths than L-band. Their results overall confirmed that this assumption proves the potential of P-band measurements for subsurface soil moisture retrievals. However, the results also indicated that the moisture retrieval depth is not only dependent on frequency but also on the soil moisture gradient with depth, which diminishes the differences in retrieval depths of P- and L-band for higher moistures in the top soil layer [40]. Smaller penetration capabilities of L-band frequencies compared to P-band are also confirmed by the studies

of [40,41,47], concluding that at P-band, influences of soil surface roughness and vegetation canopy are diminished. Nevertheless, numerical results from [48] revealed limited influence of small scale roughness on P-band backscatter simulations, but an increasing complexity between P-band signals and soil roughness at spatially larger scales.

In the literature, P-band is assumed to be able to estimate soil moisture across the root-zone of the soil (up to approx. 2 m depth) [5,49,50]. Consequently, a wide range of P-band penetration and sensing depths can be found in the literature, from some centimeters up to one meter or more [5,39,46,51]. Following the assumption that soil depths are accessible "in the order of one half to one tenth of the [employed] wavelength [52]" [45,47,53], P-band penetration depths of 6.97 to 34.86 cm at 430 MHz ($\lambda = 69.72$ cm) are potentially realistic. This value range was estimated, e.g., by [46] in a ten-year study based on P-band data near the Ameriflux site at Vaira Ranch, CA, USA. Additionally, within the AirMOSS P-band root-zone, soil moisture (RZSM) product sensing depths of typically 45 cm are considered [51]. Here, RZSM is estimated based on AirMOSS measurements together with simulations from a vegetation, surface, and subsurface scattering model by assuming a second-order polynomial function of the profile [54].

In this study, an adapted non-iterative hybrid P-band SAR decomposition method for moisture estimation is proposed to separate scattering mechanisms in fully polarimetric SAR data (Section 3.2). The proposed method utilizes a soil scattering model, which is suitable for P-band wavelengths (Section 3.1). The decomposition results are used in a consecutive step for the estimation of the complex permittivity, which in turn is applied for penetration depth calculations (Section 3.3). Thus, this study seeks to estimate complex permittivity from decomposed SAR signals and to determine permittivity-based P-band penetration capabilities to better understand P-band microwave behavior in soil along depth. For that, the proposed P-band SAR moisture estimation method continues the efforts of [3,24], and is the first of its kind, to the best of our knowledge, for complex soil permittivity estimation from (P-band) SAR data.

2. Materials

The polarimetric P-band SAR observations employed in this study were acquired during the AirMOSS campaign (a NASA Earth Venture-1 project) from 2012 to 2015 over nine different biomes across ten sites in Northern and Central America. This campaign was the first P-band airborne mission designed to estimate RZSM. The monitoring sites comprise varying land cover classes from bare soils to tropical rain forests. Each site covers an area of approximately 25 $\times$ 100 km at ~100 m spatial resolution and was revisited at least two to four times every year during the campaign. The P-band instrument operated at a center frequency of 430 MHz ($\lambda \approx 69.72$ cm). With a high radiometric calibration accuracy (0.5 dB) and a noise equivalent σ^0 of -40 dB, the AirMOSS dataset provides P-band SAR measurements, which are very well suited for estimating soil and vegetation parameters [3]. Detailed information on the campaign can be found in, e.g., [3,16].

The AirMOSS dataset provides measurements for a total of 168 dates at ten sites, each of them covering an area of 25 $\times$ 100 km. Hence, in this study, only a subset of the dataset was processed and analyzed, with focus on the three AirMOSS monitoring sites "MOISST" in Oklahoma, "Walnut Gulch" in Arizona, and "Harvard Forest" in Massachusetts, USA. By choosing these three monitoring sites, varying vegetation types and climatic conditions are analyzed. Furthermore, every study area is filtered for pixels classified as water, snow, wetlands, developed ground, bare soil, and pasture/hay, as well as for incidence angles smaller than 30° and greater than 50°, to narrow down the amount of data to be processed and to focus on vegetated soils.

Lastly, only four dates per year and monitoring site are evaluated, in the case data for more than four dates are available (Figure 1). Walnut Gulch in Arizona is characterized by an arid to semi-arid climate of a hot desert (BWh), MOISST in Oklahoma by a temperate climate with hot summers (Cfa), and Harvard Forest in Massachusetts by a cold humid continental climate with warm summers (Dfb) [55].

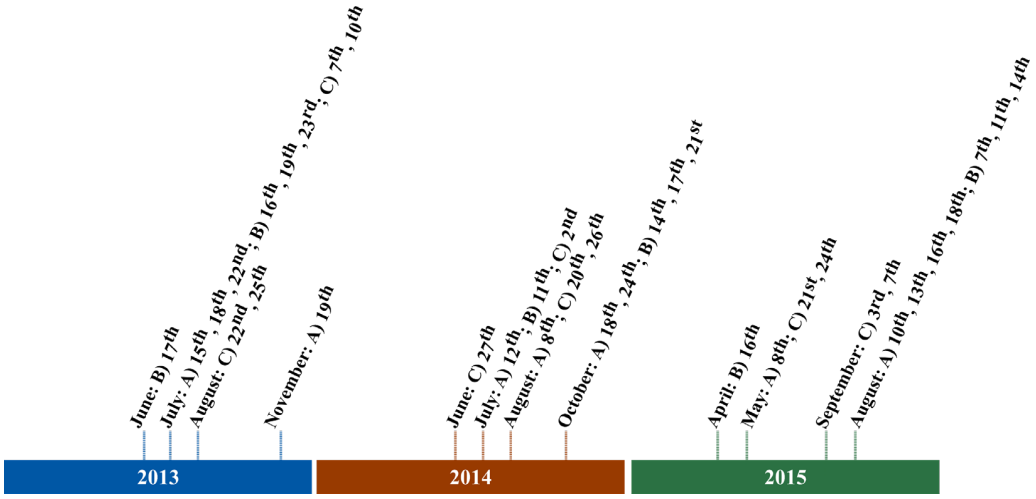

Figure 1. Timeline of processed AirMOSS dates per year and for every monitoring site. (A) Walnut Gulch, AZ, USA. (B) MOISST, OK, USA. (C) Harvard Forest, MA, USA.

In Figure 2, the land cover types according to the National Land Cover Database (NLCD) [56], as provided within the AirMOSS datasets, are shown for every monitoring site. The percentages in Table 1 represent the respective number of pixels per land cover class in comparison to all processed pixels (after filtering). Walnut Gulch (Figure 2A) is mostly covered by shrub/scrub (92.5%) while other classes represent less than 5% of all pixels (Table 1). The monitoring site MOISST (Figure 2B) is mainly covered by grassland/herbaceous (51.5%) and cultivated crops (38.3%), while Harvard Forest (Figure 2C) is covered by deciduous (49%), mixed (30.4%), and evergreen (25.1%) forests (Table 1).

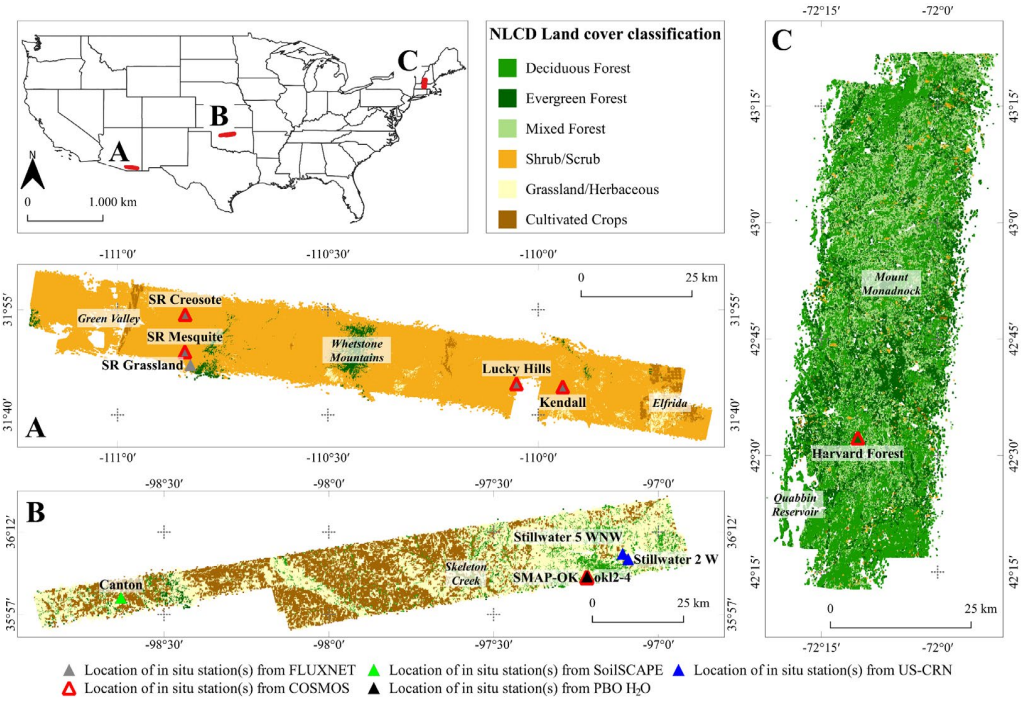

Figure 2. Overview of NLCD land cover classifications at the study areas of individual AirMOSS monitoring sites in the US with locations (triangles) of in situ measurement stations from various networks. (**A**) Walnut Gulch, AZ, USA. (**B**) MOISST, OK, USA. (**C**) Harvard Forest, MA, USA. Political state boundaries of the U.S. are from https://hifld-geoplatform.opendata.arcgis.com/.

Table 1. Distribution of NLCD land cover classes at every AirMOSS monitoring site (%) (in relation to the total of all processed pixels after filtering).

NLCD Land Cover Class	AirMOSS Monitoring Site		
	Walnut Gulch	MOISST	Harvard Forest
Grassland/herbaceous	2.2	51.5	0.3
Shrub/scrub	92.5	0	1.8
Cultivated crops	2.2	38.3	0.3
Deciduous forest	<0.1	8.3	49
Evergreen forest	3	1.7	25.1
Mixed forest	<0.1	0.3	30.4

For a later comparison of SAR-based estimates, the daily averages of in situ soil moisture measurements from five different networks at 17 stations are used as shown in Figure 2. At Walnut Gulch, five stations from the FLUXNET2015 dataset [57] and four stations from the Cosmic-ray Soil Moisture Observing System (COSMOS) [58,59] are employed. At MOISST, one station from the Soil moisture Sensing Controller And oPtimal Estimator (SoilSCAPE) project [60], and COSMOS, two stations from the US Climate Reference Network (US-CRN) [61], and three stations from the Plate Boundary Observatory to study the water cycle (PBO H_2O) project [62] are used. Lastly, at Harvard Forest, one station from COSMOS is employed (Figure 2).

3. Methods

In this study, the proposed P-band SAR moisture estimation method consists of a hybrid decomposition method and a subsequent moisture estimation procedure. The hybrid decomposition method combines eigen- and model-based decomposition techniques to separate P-band SAR signals into individual scattering mechanisms. For the determination of the scattering components, the method is supported by a soil scattering model, the first-order multi-layer small perturbation method (SPM) [63]. Subsequently, based on the decomposed scattering components, the complex soil permittivity is estimated. The individual processing steps of the method are shown in Figure 3 and explained in detail in the following.

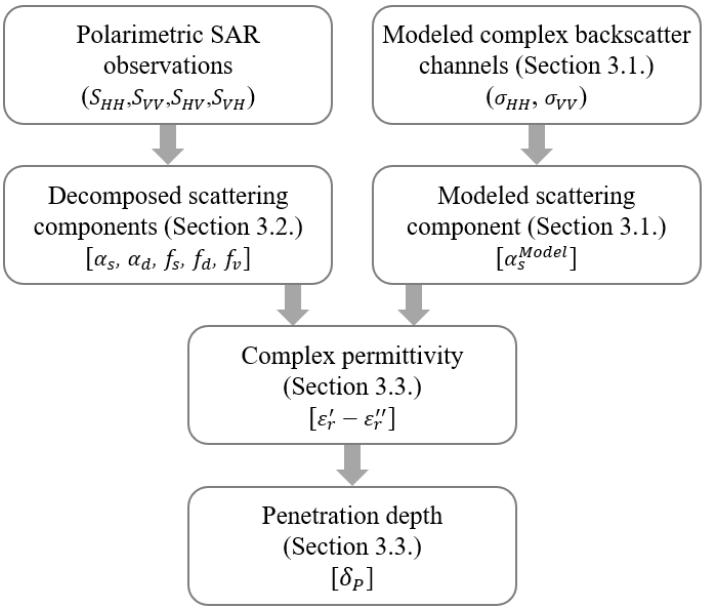

Figure 3. Flow chart of the proposed P-band SAR moisture estimation method for complex soil permittivity and penetration depth estimation based on decomposed scattering components.

3.1. Soil Scattering Based on Multi-Layer SPM

The first-order multi-layer SPM [63] is employed to model the scattering angle α_s^{Model}, needed within the proposed hybrid decomposition method (cf. Section 3.2).

As shown on the right side of Figure 3, modeled complex backscatter channels, denoted by σ_{pp} [–] for horizontal or vertical polarization, are required to estimate the model-based α_s^{Model}. In this study, σ_{pp} are modeled with the first-order solution of the multi-layer SPM [63], which computes backscatter coefficients based on soil characteristics for multiple soil layers with depth. The ability of this model to consider backscattering from multiple subsurface layers qualifies it to be more suitable for analyzing P-band soil interactions than a soil surface-only scattering model such as the SPM, also called Bragg model [27,64], as shown in [63]. The multi-layer SPM computes first-order scattering from layered surfaces by considering "multiple scattering processes between the boundaries" [63]. Since the model was originally designed to compute backscattering coefficients σ_{pp}^o, it was adapted in order to simulate complex backscatter channels σ_{pp}, where $\sigma_{pp}^o = |\sigma_{pp}|^2$ holds. The complex backscatter channels σ_{pp} are estimated by:

$$\sigma_{pp} = \sqrt{4\pi k_0^2 cos^2\theta_s \xi^2 * \begin{pmatrix} \left(\alpha_{pp}^{f_1}(k_\perp^s) * \alpha_{pp}^{f_1^*}(k_\perp^s)\right) W_{f_1}(k_\perp^s - k_\perp^i) + 2\Re\left\{\alpha_{pp}^{f_1}(k_\perp^s)\alpha_{pp}^{f_2^*}(k_\perp^s)\right\} * \\ W_{f_1 f_2}(k_\perp^s - k_\perp^i) + \left(\alpha_{pp}^{f_2}(k_\perp^s) * \alpha_{pp}^{f_2^*}(k_\perp^s)\right) * W_{f_2}(k_\perp^s - k_\perp^i) \end{pmatrix}} \quad (1)$$

with $\alpha_{pp}^{f_1}(k_\perp^s)$ and $\alpha_{pp}^{f_2}(k_\perp^s)$ as coefficients related to the incident field, $W_{f_1}(k_\perp)$ and $W_{f_2}(k_\perp)$ as the power spectral densities of the rough boundaries, and with $W_{f_1 f_2}(k_\perp)$ as their joint spectral density [63]. In detail, if the incident electric field is p-polarized, the first-order p-polarized scattered electric field in the direction k^s is a linear function of the Fourier transforms of the rough boundary functions f_1 and f_2, with the corresponding coefficients denoted by $\alpha_{pp}^{f_1}(k_\perp^s)$ and $\alpha_{pp}^{f_2}(k_\perp^s)$. Lastly, the square root of a complex number is calculated according to Moivre's theorem [65]. The reader is referred to [63] for detailed information on backscatter coefficient calculations.

In Table 2, the required input parameters of the multi-layer SPM for simulating σ_{pp} are listed together with their respective values used in this study. Please note that the chosen values are one possible approximation for the acquisition scenario in this study and may need to be adapted for different scenarios and other studies.

Table 2. Required input parameters of the multi-layer SPM for σ_{pp} simulations with the applied values in this study.

Parameter	Value
Frequency, f [MHz]	430
Number of layers, N [–]	2
Incidence angle in range, θ_i, and azimuth, φ_i [°]	θ_i from AirMOSS; $\varphi_i = 0$
Scattering angle in range θ_s, and azimuth, φ_s [°]	$\theta_s = \theta_i$; $\varphi_s = 180$
z-coordinates of the respective boundary layer, d_1 [cm]	$d_1 = \lambda/2 = 34.86$
Surface roughness parameters of each layer [cm] (vertical RMS height s, horizontal correlation length l)	s_1, l_1, s_2, and l_2 are dependent on roughness indicator derived from TanDEM-X (Table 3, right column)
Autocorrelation function, ACF [–]	Exponential
Complex permittivity $\varepsilon_s = \varepsilon_s' - j\varepsilon_s''$ of each layer [–]	ε_{s_1} : $\varepsilon_s' \in [6, 40]$, $\varepsilon_s'' \in [0, 10]$ $\varepsilon_{s_2} = \varepsilon_{s_1} + (10 + j0.5)$

Table 3. Surface roughness parameter sets of each layer (vertical RMS height s, horizontal correlation length l) as input for the multi-layer SPM based on TanDEM-X derived roughness indicator R_{TDX}.

Roughness Indicator from TanDEM-X [m]	Input Roughness Parameters [cm]
$R_{TDX} < 5$	$s_1 = 0.5; l_1 = 30; s_2 = 0.25; l_2 = 60$
$5 \leq R_{TDX} < 10$	$s_1 = 1.5; l_1 = 25; s_2 = 0.75; l_2 = 50$
$10 \leq R_{TDX} < 15$	$s_1 = 2; l_1 = 20; s_2 = 1; l_2 = 40$
$R_{TDX} \geq 15$	$s_1 = 3; l_1 = 15; s_2 = 1.5; l_2 = 30$

Following findings by [48] (cf. Section 1), the surface roughness parameters, required for modeling P-band backscatter channels, are not fixed to static values in this study. However, since no information on surface roughness is available for AirMOSS monitoring sites with comparable spatial resolution, the DLR TanDEM-X DEM at 90 m resolution [66], downloadable at https://download.geoservice.dlr.de/TDM90/ (accessed on 5 March 2021), is used to derive a first-order roughness indicator for each site. For this, TanDEM-X elevations were resampled to the AirMOSS resolution, converted to roughness values with the GDAL DEM utility algorithm [67] in QGIS© [68], and scaled according to the employed wavelength ($\lambda = 69.72$ cm). The resulting roughness values, giving the degree of irregularity of the surface, serve as roughness indicators in this study. Hence, depending on this roughness indicator R_{TDX} (Table 3, left column), typical surface roughness parameter sets for each layer (Table 3, right column) were fixed as model input to account for varying roughness during simulations (from smooth to rather rough). It can be seen that the chosen values for vertical RMS height s vary from 0.25 to 3 cm, and for horizontal correlation length l from 15 to 60 cm. These values were fixed based on several sensitivity analyses and after reviewing the literature.

Lastly, complex backscatter channels σ_{pp}, for respective horizontal and vertical polarization, are used to calculate α_s^{Model}. In this study, the formulation by [27] is used, valid for $0 \leq \alpha_s \leq \frac{\pi}{2}$:

$$\alpha_s^{Model} = tan^{-1}\left(\frac{\sigma_{HH} - \sigma_{VV}}{\sigma_{HH} + \sigma_{VV}}\right). \quad (2)$$

In this study, α_s^{Model} is calculated for realistic ranges of complex soil permittivity ε_s [–] (real part: $\varepsilon_s' \in [6, 40]$, imaginary part: $\varepsilon_s'' \in [0, 10]$, with $0.1 < \varepsilon_s''/\varepsilon_s' < 0.5$).

3.2. Polarimetric Hybrid Decomposition Method

The hybrid decomposition method was originally introduced by [24] as an iterative approach (cf. Section 1) specifically designed for L-band data. However, it is adapted here to be applied in a non-iterative way to P-band observations, and for estimating complex permittivity. As illustrated in Figure 3, the hybrid decomposition method separates polarimetric SAR observations into individual scattering components (surface, dihedral, and volume).

First, the polarimetric coherency $[T]$ matrix is defined as:

$$[T] = \begin{bmatrix} T_{11} & T_{12} & 0 \\ T_{12}^* & T_{22} & 0 \\ 0 & 0 & T_{33} \end{bmatrix} \quad (3)$$

with T_{12}^* as complex conjugate. By assuming reflection symmetry of the observed media, the correlation terms between co- and cross-polarized signals are zero (T_{13}, T_{23}, T_{31}, and T_{32}). Reflection symmetry can be assumed for one, because the correlation terms that are set to zero (due to reflection symmetry) are neither important for the decomposition, nor for the soil permittivity estimation. Second, areas where this symmetry may be violated, such as urban or high mountain regions, are not considered during the analyses (cf. Section 2) [27].

$[T]$ can be decomposed into the three canonical scattering components of surface $[T_s]$, dihedral $[T_d]$, and volume $[T_v]$:

$$\begin{bmatrix} T_{11} & T_{12} & 0 \\ T_{12}^* & T_{22} & 0 \\ 0 & 0 & T_{33} \end{bmatrix} = [T_s] + [T_d] + [T_v]. \tag{4}$$

The rank-3, model-based vegetation volume component $[T_v]$ is described by:

$$[T_v] = \frac{f_v}{2 + 2A_p^2} \begin{bmatrix} V_{11} & V_{12} & 0 \\ V_{12}^* & V_{22} & 0 \\ 0 & 0 & V_{33} \end{bmatrix} \tag{5}$$

with f_v as volume scattering intensity, and A_p [–] as particle anisotropy, which describes the shape of vegetation volume scatterers from vertical dipoles ($A_p = 0$) and spheres ($A_p = 1$) to horizontal dipoles ($A_p = \infty$). f_v is given by:

$$f_v = \frac{4V_{12}cos(2\alpha_s)\left(T_{12}^* - T_{12} + \left(T_{12} + T_{12}^*\right)cos(2\alpha_s)\right) + (T_{11} - T_{22})(V_{11} - V_{22})(cos(4\alpha_s) - 1) - \sqrt{RT}}{4V_{12}^2 - V_{11}^2 + 2V_{11}V_{12} - V_{22}^2 + \left(4V_{12}^2 + (V_{11} - V_{22})^2\right)cos(4\alpha_s)} \tag{6}$$

with $RT = \left|\left(2\left(T_{12} - T_{12}^*\right)(V_{11} - V_{22})sin(2\alpha_s) + \left(2(T_{11} - T_{22})V_{12} - \left(T_{12} + T_{12}^*\right)(V_{11} - V_{22})\right)sin(4\alpha_s)\right)^2\right|$, and the polarimetric scattering angle α_s as model-based α_s^{Model} [24,31] (cf. Section 3.1). Further, the parameters for estimating the vegetation volume component are given by:

$$V_{11} = \left(A_p + 1\right)^2, \tag{7}$$

$$V_{12} = \left(A_p^2 - 1\right)sinc(2\Delta\psi), \tag{8}$$

$$V_{22} = \frac{1}{2}\left(A_p - 1\right)^2(1 + sinc(4\Delta\psi)), \tag{9}$$

$$V_{33} = \frac{1}{2}\left(A_p - 1\right)^2(1 - sinc(4\Delta\psi)), \tag{10}$$

with $\Delta\psi$ [°] as width of the orientation angle distribution, which describes the degree of orientation of the vegetation volume from oriented ($\Delta\psi = 0°$) to random ($\Delta\psi = 90°$).

Hence, (4) can be rearranged together with (5) in order to determine the soil parameters from the individual soil scattering components ($[T_s]$, $[T_d]$), by subtracting the volume component:

$$[T_s] + [T_d] = \begin{bmatrix} T_{11} & T_{12} & 0 \\ T_{12}^* & T_{22} & 0 \\ 0 & 0 & T_{33} \end{bmatrix} - \frac{f_v}{2 + 2A_p^2} \begin{bmatrix} V_{11} & V_{12} & 0 \\ V_{12}^* & V_{22} & 0 \\ 0 & 0 & V_{33} \end{bmatrix}. \tag{11}$$

As already mentioned, [24] originally proposed an iterative estimation procedure to find the most suited volume descriptions, namely f_v, A_p, and $\Delta\psi$. However, since this approach is computationally expensive and needs certain assumptions (bare soil regions in the observation area) to be initialized, a non-iterative way for estimating f_v is proposed here, independent of bare areas, by employing the model-based α_s^{Model} and a realistic parameter space for vegetation volume parameters, with $Ap \in [0, 1]$ and $\Delta\psi \in [0°, 90°]$.

Thus, together with α_s^{Model}, the SAR measurements are decomposed into the two eigen-based scattering angles α_s and α_d [°], as well as the scattering intensities of surface f_s, dihedral f_d, and volume f_v [–] for multiple $Ap - \Delta\psi$ combinations. The ability of the method to estimate five variables (α_s, α_d, f_s, f_d, and f_v) out of four SAR observations ($|S_{HH}|^2$, $|S_{VV}|^2$, $|S_{HV}|^2$, $|S_{VH}|^2$) is possible, since the ambiguity for α_s and α_d is solved by assuming an orthogonality condition with $\alpha_s = \pi/2 - \alpha_d$ [27], meaning, if the decomposed polarimetric scattering angle α is smaller than or equal to 45°, surface scattering is

assumed, denoted by α_s, whereas in the case α is greater than 45°, dihedral scattering is assumed, denoted by α_d [24]. This way, in contrast to model-based-only approaches, the proposed method needs no prior assumptions on vegetation characteristics, and provides the advantage of incorporating actual SAR measurements.

The surface $[T_s]$ and dihedral $[T_d]$ scattering components are defined in (12) and (13), respectively, assuming that both are orthogonal rank-1 components [3,24]:

$$[T_s] = f_s \begin{bmatrix} cos^2\alpha_s & -sin\alpha_s & 0 \\ -cos\alpha_s & sin^2\alpha_s & 0 \\ 0 & 0 & 0 \end{bmatrix}, \tag{12}$$

$$[T_d] = f_d \begin{bmatrix} sin^2\alpha_d & cos\alpha_d & 0 \\ sin\alpha_d & cos^2\alpha_d & 0 \\ 0 & 0 & 0 \end{bmatrix}. \tag{13}$$

Finally, (11) can be reformulated to:

$$\begin{bmatrix} T_{11} & T_{12} & 0 \\ T_{12}^* & T_{22} & 0 \\ 0 & 0 & T_{33} \end{bmatrix} - f_v \begin{bmatrix} V_{11} & V_{12} & 0 \\ V_{12}^* & V_{22} & 0 \\ 0 & 0 & V_{33} \end{bmatrix} = \begin{bmatrix} f_s cos^2\alpha_s + f_d sin^2\alpha_d & (f_d - f_s) cos\alpha_{d,s} sin\alpha_{d,s} & 0 \\ (f_d - f_s) cos\alpha_{d,s} sin\alpha_{d,s} & f_d cos^2\alpha_d + f_s sin^2\alpha_s & 0 \\ 0 & 0 & 0 \end{bmatrix} \tag{14}$$

with the surface scattering intensities given by [24]:

$$\begin{aligned} f_{s,d} &= \tfrac{1}{2}\left(T_{11} + T_{22} - f_v * (V_{11} + V_{22})\right) \\ &\pm \sqrt{\left|-4\left(T_{22}(T_{11} - f_v T_{11}) + (T_{12} - f_v T_{12})(f_v V_{12} - T_{12}^*) + f_v(f_v V_{11} - T_{11})V_{22}\right) + \left(T_{11} + T_{22} - f_v * (V_{11} + V_{22})\right)^2\right|} \end{aligned} \tag{15}$$

and the eigen-based scattering angle α to separate contributions from surface and dihedral scattering, given by [24]:

$$\alpha_{s,d} = acos\left(\left(1 + 4 * \left(\frac{T_{12}^* - f_v V_{12}}{T_{11} - T_{22} - f_v V_{11} + f_v V_{22} \pm \sqrt{RT}}\right)^2\right)^{-\frac{1}{2}}\right) \tag{16}$$

with $RT = \left|T_{11}^2 + (T_{22} + f_v V_{11})^2 + 4(T_{12} - f_v V_{12})(T_{12}^* - f_v V_{12}) - 2T_{11}(T_{22} + f_v(V_{11} - V_{22})) - 2f_v(T_{22} + f_v V_{11})V_{22} + f_v^2 V_{22}^2\right|$.

In summary, from polarimetric SAR observations and simulated α_s^{Model}, the decomposition results for α_s, α_d, f_s, f_d, and f_v can be estimated for varying ε_s and individual $Ap - \Delta\psi$ combinations. Hence, the proposed method overcomes the computationally expensive iterative procedure as proposed in [24], and provides the possibility of including multiple vegetation characteristics (Ap, $\Delta\psi$) as suggested by [3] (cf. Section 1). In this study, not all $Ap - \Delta\psi$ combinations are applied. Firstly, to ensure non-negative decomposed powers, scattering intensities for any $Ap - \Delta\psi$ combination that are smaller than zero are eliminated for subsequent analyses in order to avoid possible overestimation of the volume scattering component (cf. Section 1.). Secondly, the radar vegetation index (RVI) is used to exclude unrealistic $Ap - \Delta\psi$ combinations. Here, the RVI_{model} is modeled according to [31,69] for all $Ap - \Delta\psi$ combinations used within the approach. Afterwards, the data-based RVI_{data} is calculated for every pixel based on the respective SAR backscatter observations. Finally, all $Ap - \Delta\psi$ combinations, where the RVI_{model} deviates from RVI_{data} around the average value ($\overline{RVI_{model}}$) of all RVI_{model} ($RVI_{model} \notin RVI_{data} \pm \overline{RVI_{model}}$), are excluded from further analyses.

3.3. Complex Permittivity Estimation

The P-band SAR moisture estimation method proposed in this study provides the advantage of complex permittivity estimation. The real part of the permittivity ε_s' is associated with energy or heat storage, and the imaginary part of the permittivity ε_s''

is associated with energy or heat loss, often called dielectric loss factor [35,70]. Since model-based α_s^{Model} is used to estimate f_v during the decomposition of polarimetric SAR observations, decomposition results can be calculated for a realistic range of soil permittivity values. Subsequently, by determining the closest fit between decomposed data-based α_s^{Data} and model-based α_s^{Model} for individual $Ap - \Delta\psi$ combinations (cf. Section 3.2.), the corresponding ε_s value can be estimated.

For that, the absolute value of the modulus r [–] and phase angle ϕ [–] of the real (α_s') and imaginary (α_s'') parts of α_s^{Data} and α_s^{Model}, respectively, are calculated:

$$r_{\alpha_s}(\varepsilon_s,\ Ap, \Delta\psi) = \left|\sqrt{\alpha_s'^2 + \alpha_s''^2}\right|, \tag{17}$$

$$\phi_{\alpha_s}(\varepsilon_s,\ Ap, \Delta\psi) = \left|tan^{-1}\left(\frac{\alpha_s''}{\alpha_s'}\right)\right|. \tag{18}$$

Afterwards, the smallest sum of the absolute differences between data- and model-based r_{α_s} and ϕ_{α_s} is used to determine ε_s:

$$\varepsilon_s(Ap, \Delta\psi) = argmin\left(\left|r_{\alpha_s^{Data}} - r_{\alpha_s^{Model}}\right| + \left|\phi_{\alpha_s^{Data}} - \phi_{\alpha_s^{Model}}\right|\right). \tag{19}$$

Since complex ε_s are estimated for multiple $Ap - \Delta\psi$ combinations to cover realistic vegetation volume characteristics (cf. Section 3.2), the final complex ε_s is the average value of $\varepsilon_s(Ap, \Delta\psi)$ for all remaining realistic $Ap - \Delta\psi$ combinations (non-negative surface scattering powers, modeled RVI_{model} around data-based RVI_{data}) (cf. Section 3.2).

For comparison, permittivity can be converted to soil moisture and vice versa, by employing dielectric mixing models, such as the one by Topp et al., [71], Dobson et al., [72], or Mironov et al., [73]. An extended review of dielectric mixing models for soils can be found in [74]. In this study, ε_s' results are converted to soil moisture θ [vol.%] according to the dielectric mixing model of [71].

Based on estimated complex ε_s from decomposed polarimetric SAR observations, one possible application is the estimation of the penetration depth δ_p [cm]. In this study, the well-known formulation of [75] is adapted to calculate δ_p [44]:

$$\delta_p = \frac{1}{2} * \left(\frac{\lambda}{2\pi} * \left[\frac{2}{\varepsilon_s' * \left(\sqrt{1 + tan^2(\varepsilon_s''/\varepsilon_s')} - 1\right)}\right]^{\frac{1}{2}}\right). \tag{20}$$

This formulation was chosen because almost all available equations to estimate δ_p are comparable and mainly dependent on the attenuation factor α, a measure for the penetration depth of an electromagnetic wave in a medium. However, this is one of the first to be published and well known.

Sensitivity studies and analyses with other published formulations for δ_p, e.g., [41,43,45,76], showed overall similar results ($R^2 > 0.99$) with small deviations ($\sigma < 5$ cm). In fact, deviations were only noticeable at very low permittivity.

Since δ_p is only dependent on complex permittivity and wavelength (frequency) (cf. Equation (20)), it is considered in this study as permittivity-based penetration depth to analyze potential depths for P-band signals. For a better understanding of how δ_p behaves across varying permittivity levels at P-band (430 MHz), modeling results are displayed in Figure 4. It can be seen that δ_p decreases with increasing permittivity, as expected. Further, δ_p estimates significantly decrease with increasing ε_s'', proving the importance of ε_s'' for δ_p calculations.

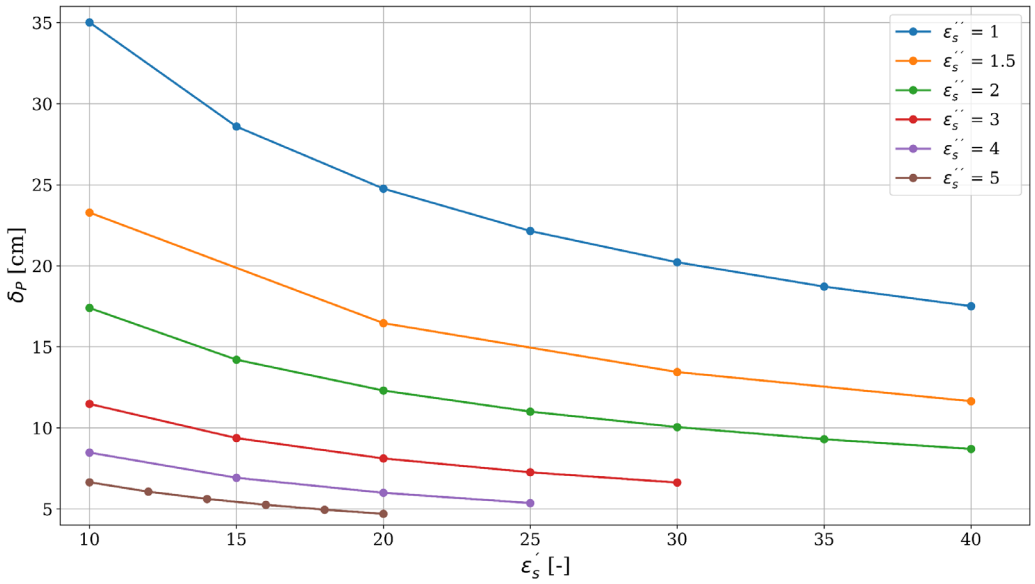

Figure 4. Variations in penetration depth estimates for P-band frequency (430 MHz) along varying real ε_s' and imaginary ε_s'' parts of complex permittivity based on the formulation from [44,75] (cf. Equation (20)).

4. Results

In this section, the results of the P-band SAR moisture estimation method are presented, comprising filtered and decomposed SAR signals, estimated complex permittivity, and soil moisture, as well as permittivity-based penetration depths. Furthermore, the results are related to in situ measurements from various networks (cf. Section 2) to compare the complex permittivity estimates.

4.1. Decomposition Results

Based on the proposed hybrid decomposition method, the relative indices P_s / P_t, P_d / P_t, and P_v / P_t for soil, dihedral, and volume are estimated to analyze the normalized contribution of each scattering mechanism. The indices are calculated based on the decomposition results for scattering angles and intensities according to [3].

In Figure 5, only the dominant scattering mechanisms, characterized by their relative indices, are shown for each AirMOSS monitoring site. Apparent data gaps (white areas in Figure 5) in the results originate from filtering for specific land cover classes and incidence angles prior to the processing (cf. Section 2). Here, brown regions represent dominant soil scattering, meaning the normalized contribution of soil scattering is the highest of all three contributions. Accordingly, beige regions represent dominant dihedral scattering, while dark green regions represent dominant volume scattering.

It can be seen that Walnut Gulch is mainly characterized by volume scattering, with dihedral scattering in the eastern part of the site, where cultivated crops are the main land cover class, as well as soil and dihedral scattering in the western part of the site near the *Green Valley* south of *Tucson* (Figure 2, Section 2). In this particular region, the influence of the incidence angle is evident since dominant volume scattering is mixed with dominant soil scattering, despite the same land cover class (shrublands). Here, the incidence angles vary across the entire possible range, from 30° to 50°, and the terrain heights are lowest, which leads to dominant soil scattering components instead of dominant volume scattering contributions (Figure 5A). At the monitoring site MOISST, dihedral scattering is dominant in the eastern part around the city *Stillwater* (Figure 5B), where the land is predominantly covered by grassland/herbaceous and smaller evergreen forests (Figure 2, Section 2). In contrast, regions mainly characterized by cultivated crops show dominant volume scattering, e.g., in the center of the site. Again, the results are influenced by the varying incidence angles, for instance, in the center of the site, where higher incidence angles lead to rather dominant soil scattering (Figure 5B). Lastly, Harvard Forest shows

primarily dihedral scattering with only some regions in the northern part of the monitoring site, where soil or volume scattering are dominant (Figure 5C).

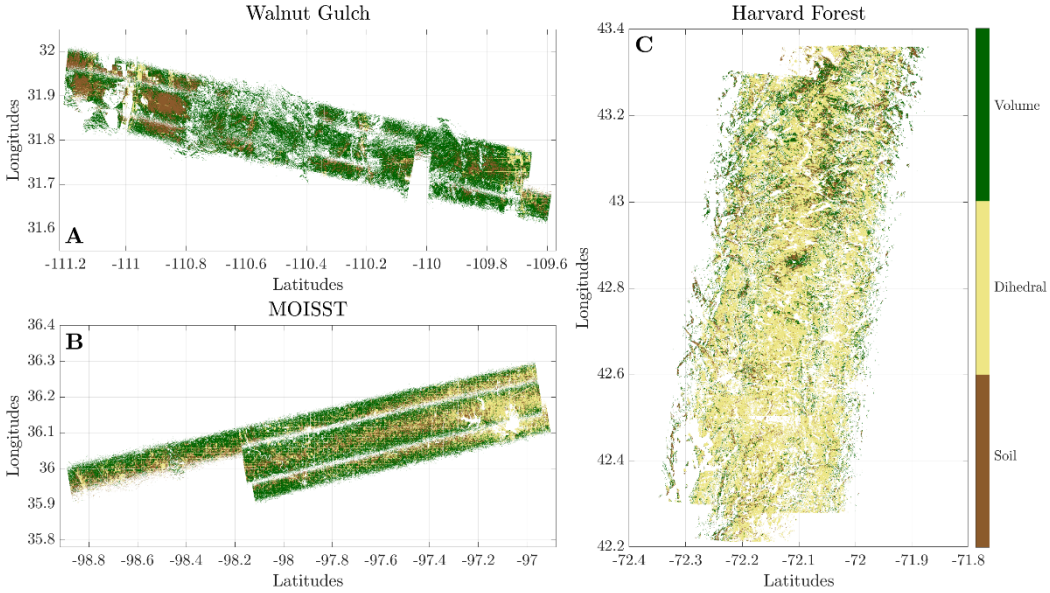

Figure 5. Estimated normalized, relative power indices representing dominant soil (P_s/P_t), dihedral (P_d/P_t), or volume (P_v/P_t) scattering at the AirMOSS monitoring sites. The average values of the most dominant scattering mechanism of all dates are displayed (Figure 1, Section 2). White data gaps originate from initial filtering of the input parameters. (**A**) Walnut Gulch, AZ, USA. (**B**) MOISST, OK, USA. (**C**) Harvard Forest, MA, USA.

For a comparison of all decomposition results for varying years, Figure 6 displays the average probability distribution function (PDF) of the normalized scattering contributions at each monitoring site. It can be seen that the PDF for soil scattering peaks at the lowest value but with the highest probability at Harvard Forest, while at Walnut Gulch and MOISST the normalized soil scattering is located between dihedral and volume scattering as second dominant scattering contribution, respectively (Figure 6, first row).

The dihedral scattering contribution is lowest at Walnut Gulch and MOISST but highest at Harvard Forest (Figure 6, second row), while the volume scattering contribution is highest at Walnut Gulch but lowest at Harvard Forest, with MOISST in between (Figure 6, third row). Moreover, there are hardly any differences in the estimated PDFs of all three relative indices between the years 2013 and 2015. Only the PDF for soil scattering contribution at Harvard Forest slightly decreases from 2013 to 2015, whereas the PDF for dihedral and volume scattering slightly increases (Figure 6, right column).

In summary, the monitoring site mainly covered by shrub/scrub (Walnut Gulch) displays the lowest dihedral and the highest volume scattering, while the monitoring site covered by forests (Harvard Forest) displays almost exclusively dihedral and the lowest vegetation scattering. The mixed monitoring site covered by grassland/herbaceous or cultivated crops (MOISST) shows almost balanced contributions of soil or volume scattering with dihedral scattering being predominant in regions of grassland/herbaceous and volume scattering in regions with extensive agriculture.

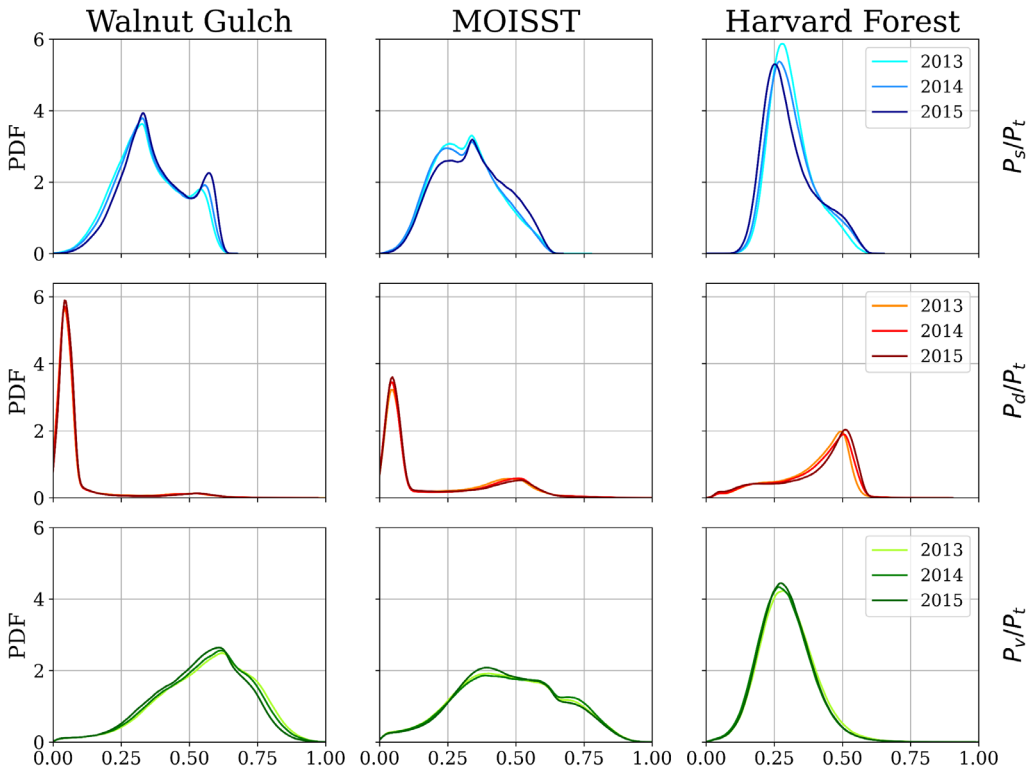

Figure 6. Probability density functions (PDFs) of estimated normalized, relative power indices representing soil (P_s/P_t; first row), dihedral (P_d/P_t; second row), or volume (P_v/P_t, third row) scattering at the AirMOSS monitoring sites. The average values of all four dates per year are shown (Figure 1, Section 2). Left column: Walnut Gulch, AZ, USA. Middle column: MOISST, OK, USA. Right column: Harvard Forest, MA, USA.

4.2. Results for Complex Soil Permittivity and P-Band Penetration Depth

In Figure 7, the real ε_s' and imaginary ε_s'' part of the estimated complex soil permittivity ε_s, determined with the proposed P-band SAR moisture estimation method (cf. Section 3.3), are displayed for the main land cover classes for each monitoring site and date (Table 1).

Walnut Gulch, covered by shrub/scrub (cf. Section 2), shows the overall lowest permittivity results with a median value of $\varepsilon_S = 11.2 - j1.5$. At the monitoring site MOISST, the main land cover class grassland/herbaceous shows slightly higher permittivity results with a median value of $\varepsilon_S = 14.9 - j1.7$. The latter is in contrast to the second dominant land cover class cultivated crops (cf. Section 2) with a median value of $\varepsilon_S = 13.8 - j1.5$. However, the results for cultivated crops span the largest value ranges of all classes and monitoring sites with the real part of permittivity varying from 6 to 31 and the imaginary part of permittivity varying from 1 to 3.2. The three main land cover classes, deciduous, mixed, and evergreen forest (cf. Section 2), at Harvard Forest display the overall smallest value ranges and the highest permittivity results with comparable median values of $\sim\varepsilon_S = 16 - j1.8$. Hence, the forest site Harvard Forest, characterized by a cold humid continental climate (cf. Section 2), shows the highest permittivity with the smallest deviations, while the driest monitoring site, mainly covered by shrub/scrub due to the arid climate (Walnut Gulch), shows the lowest permittivity results. The monitoring site characterized by a temperate climate and grassland/herbaceous or cultivated crops (MOISST) displays permittivity results in between.

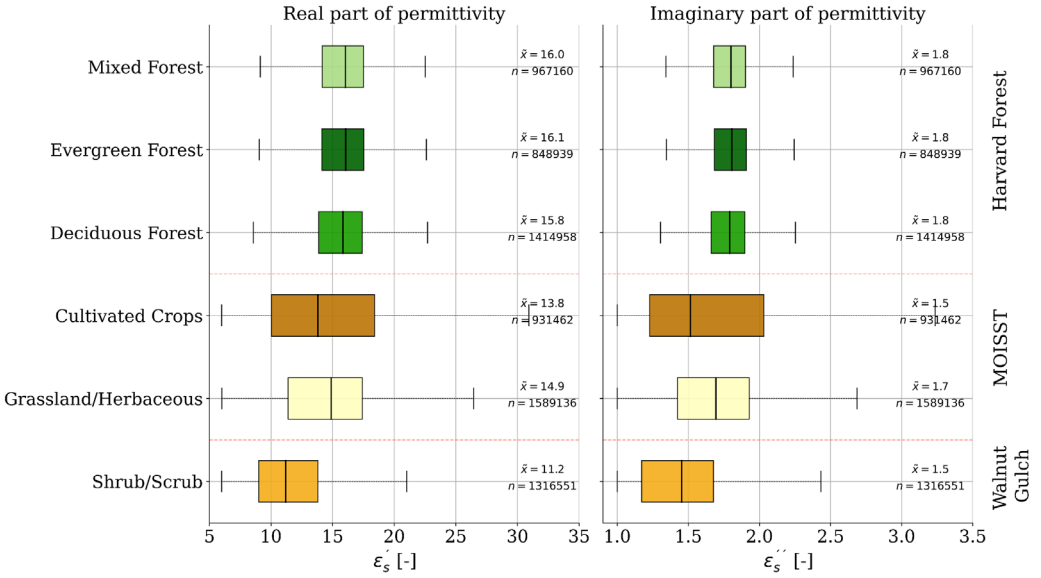

Figure 7. Estimated real ε_s' (**left**) and imaginary ε_s'' (**right**) part of complex soil permittivity for main land cover classes of the AirMOSS monitoring sites Walnut Gulch, MOISST, and Harvard Forest. The results are displayed for all acquisition dates (Figure 1, Section 2). $\tilde{x}$ represents the respective median value, n is the total amount of values per boxplot.

Converted to soil moisture, Walnut Gulch revealed values in a range from 12.6 vol.% to 34 vol.% with a median value of 18.8 vol.%. At MOISST, values ranged from 12.6 vol.% to 47.5 vol.% with a median value of 27.5 vol.%, and at Harvard Forest from 25.6 vol.% to 32.6 vol.% with a median value of 29.3 vol.%.

Based on the complex permittivity results, the penetration depth δ_P for each monitoring site is estimated according to Equation (20) (cf. Section 3.3). In Figure 8, areal results for δ_P are displayed for every AirMOSS monitoring site. At all sites, δ_P varies in comparable ranges from 5.7 cm, 5.4 cm, or 7.7 cm to 35 cm, with the majority of values from 20 cm to 35 cm. Walnut Gulch and MOISST show higher variations in results according to varying land cover classes, for instance, lower depths in regions where grassland/herbaceous or forests are dominant, and greater depths where shrublands or cultivated crops are dominant (Figure 2, Section 2). In contrast, at Harvard Forest only small deviations in results are observed with the majority of δ_P values being at around 25 cm. The two slightly apparent vertical stripes in the results with overall higher δ_P values originate from varying incidence angles of the sensing system across the monitoring site (Figure 8C).

In detail, variations in δ_P are largest, where land cover is rather heterogeneous. For instance, the monitoring site Harvard Forest, which is almost fully covered by forests (Figure 2, Section 2), displays the smallest deviations in results and a homogeneous map of δ_P across the entire site (Figure 8C). In contrast, in the eastern part of the monitoring site Walnut Gulch around the city *Elfrida*, highest variations in δ_P are estimated because in that region the land cover is a rather heterogeneous mixture of cultivated crops, grassland/herbaceous, and shrub/scrub. Further, in the center of the site Walnut Gulch at the *Whetstone Mountains*, which are covered by forests, the estimated δ_P are lower than in the surrounding areas, where shrub/scrub is dominant (Figure 2, Section 2). In the western part of Walnut Gulch, at the dip east of the *Green Valley* (Figure 2, Section 2), δ_P are lowest (Figure 8A).

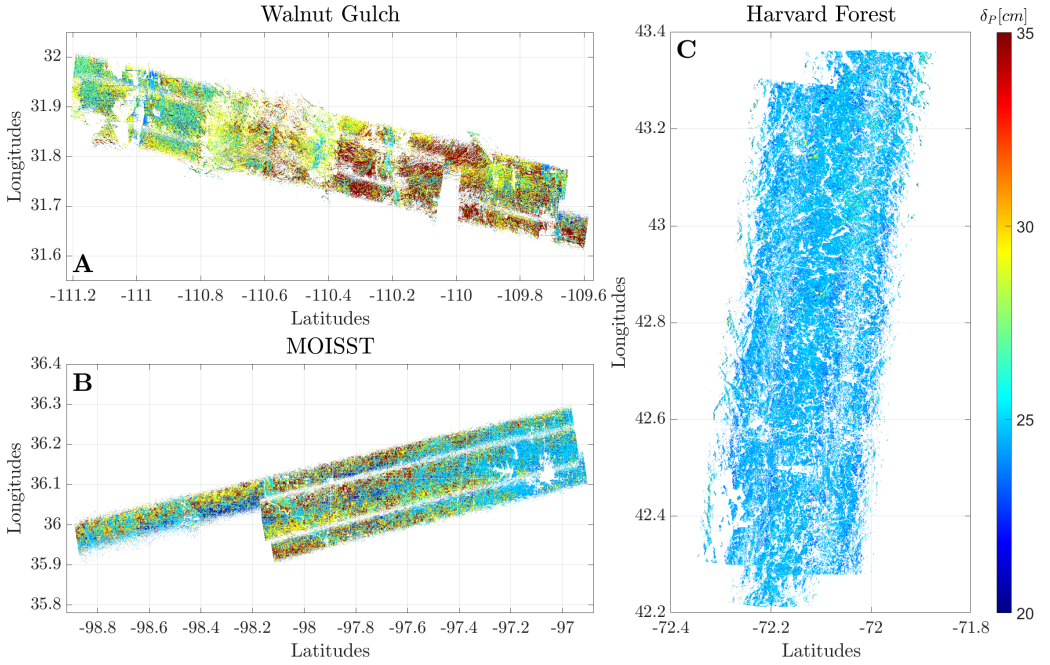

Figure 8. Estimated permittivity-based penetration depth δ_P at the AirMOSS monitoring sites. The average values of penetration depths of all dates are displayed (Figure 1, Section 2). White data gaps originate from initial filtering of the input parameters. (**A**) Walnut Gulch, AZ, USA. (**B**) MOISST, OK, USA. (**C**) Harvard Forest, MA, USA.

For detailed analyses, δ_P results are displayed in Figure 9 for the main land cover classes of the three monitoring sites. As can be seen in the upper plot of Figure 9, the land cover classes for forests (deciduous, evergreen, and mixed) at Harvard Forest have the lowest δ_P values of all landcover classes at ~24.6 cm, with the smallest variations in results, varying from ~22.8 cm to ~26.4 cm only. In contrast, at Walnut Gulch the highest median δ_P value is estimated at 27 cm, varying in the range from 16.8 to 35 cm. The results at the monitoring site MOISST display a median δ_P of 25.1 cm for grasslands/herbaceous and 25.7 cm for cultivated crops with the largest deviations in the latter land cover class (varying from 13.6 to 35 cm). Accordingly, PDFs in the lower plot of Figure 9 display the highest densities with the narrowest distributions for forest land cover classes, peaking from 24 to 25 cm, while other land cover classes reveal more distributed results, covering a broader range of δ_P estimates at lower densities (Figure 9).

4.3. Comparison of Permittivity Estimates with In Situ Measurements

For a comparison of the estimated soil permittivity with in situ soil moisture measurements at single locations (cf. Section 2), the results for ε_s' are converted to soil moisture θ [vol.%] according to the dielectric mixing model of [71].

In Figure 10, retrieved θ, based on the proposed P-band SAR moisture estimation method and P-band SAR measurements, are compared with in situ measured θ at the driest AirMOSS site, Walnut Gulch in Arizona. While retrieved values are in the range from 12.6 vol.% to 34 vol.% with a highest PDF from 12.5 vol.% to 19 vol.%, in situ measurements vary from 2.6 vol.% to 15.4 vol.% with the PDF peaking at 6.7 vol.%. Conducted statistical tests between retrieved and in situ measured θ values with a correlation coefficient (R^2) [–] and medium root-mean square error (RMSE) [vol.%] of $R^2 = 0.2$ and $RMSE = 14.1$ vol.% confirm a clear overestimation of retrieved θ compared to in situ measurements. The main reason for the low correlation could be the discrepancy between measuring depths since available in situ values are measured near the soil surface at ~0–5 cm, while for retrieved θ, based on decomposed P-band SAR observations, penetration depths proved to vary from 16.8 cm to 35 cm with median δ_P at 27 cm (Figure 9).

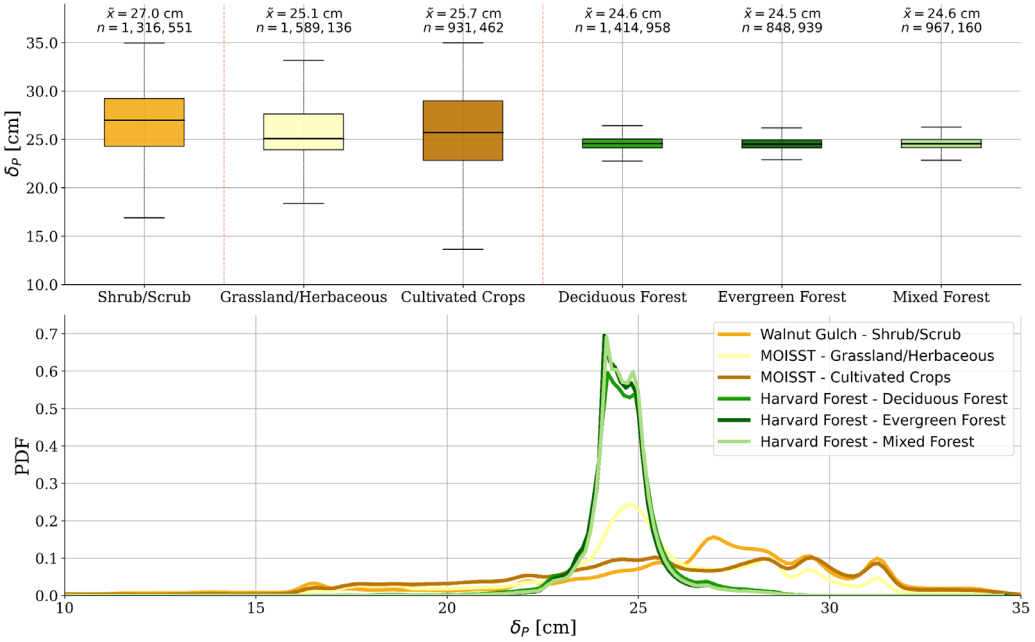

Figure 9. Boxplots and probability density functions (PDFs) of estimated permittivity-based penetration depths δ_P for main land cover classes at the AirMOSS monitoring sites Walnut Gulch, MOISST, and Harvard Forest. The results are displayed for all acquisition dates (Figure 1, Section 2). $\tilde{x}$ represents the respective median value, n is the total amount of values per boxplot.

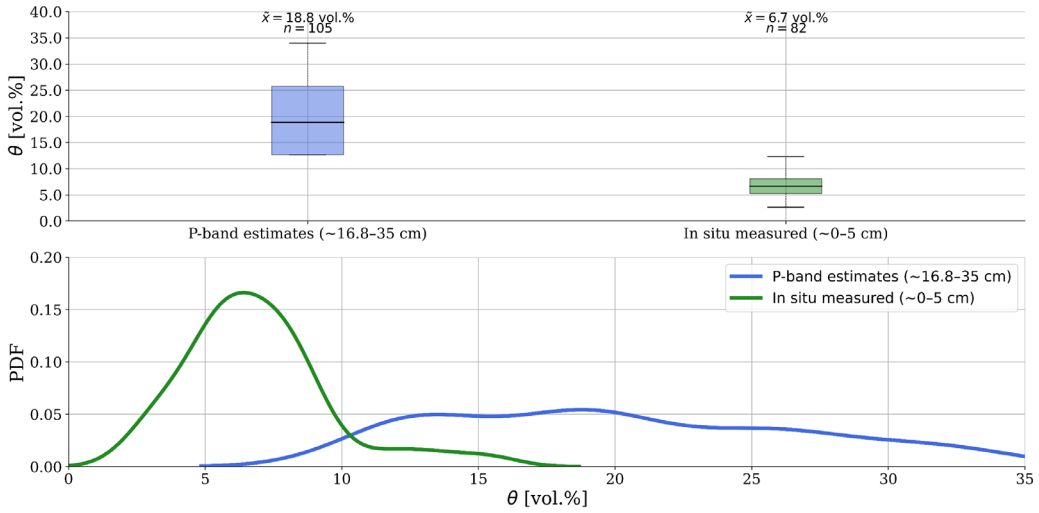

Figure 10. Comparison of retrieved soil moisture values, estimated with the proposed P-band SAR method and converted from permittivity according to the dielectric mixing model from [71], with in situ measured soil moisture values from various networks (cf. Section 2) at the AirMOSS monitoring site Walnut Gulch, AZ. $\tilde{x}$ represents the respective median value, n is the total amount of values per boxplot.

In Figure 11, the comparison is shown for the AirMOSS test site Harvard Forest. While retrieved θ vary in the range from 25.6 vol.% to 32.6 vol.%, with the PDF peaking at 29.3 vol.%, in situ measurements vary from 25.6 vol.% and 38.8 vol.%, with a median value of 32.4 vol.%.

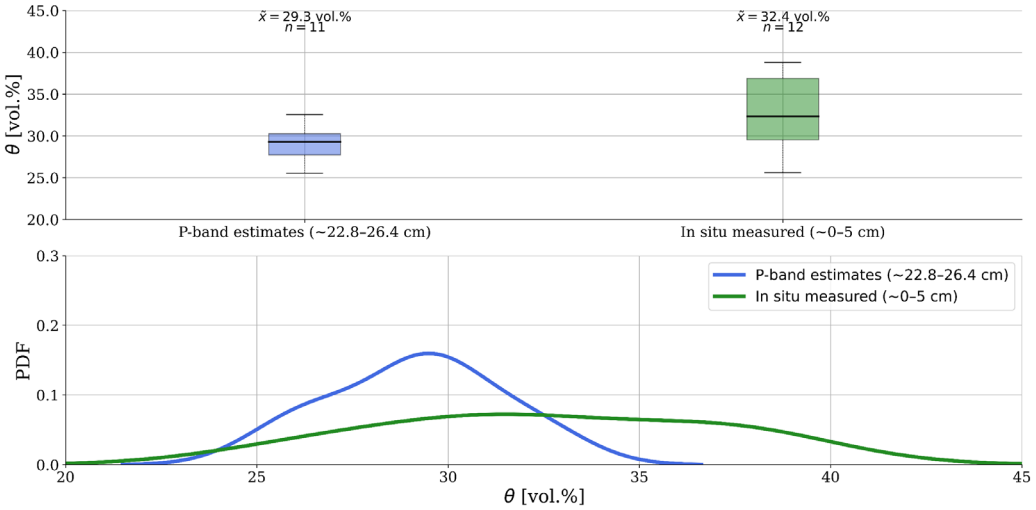

Figure 11. Comparison of retrieved soil moisture values, estimated with the proposed P-band SAR method and converted from permittivity according to the dielectric mixing model from [71], with in situ measured soil moisture values from various networks (cf. Section 2) at the AirMOSS monitoring site Harvard Forest, MA. $\tilde{x}$ represents the respective median value, n is the total amount of values per boxplot.

Hence, with estimated $R^2 = 0.5$ and $RMSE = 4.6$ vol.%, results show that the humid forest site displays a higher correlation and lower error between retrievals and in situ measurements compared to the arid site Walnut Gulch (Figure 10), despite the same discrepancy between measuring depths. In situ measurements are again only available from the soil surface at ~0–5 cm, while retrieval results showed average penetration depths around 24.6 cm, overall varying from 22.8 to 26.4 cm (Figure 9).

Lastly, the comparison of θ values is conducted for MOISST (Figure 12). Only for this site, in situ measurements for comparisons are available from the soil surface (~0–5 cm) and also for greater soil depths at ~5–10 cm and ~10–20 cm. The median values of in situ measured θ are increasing with greater measuring depths, from 16.4 vol.% near the soil surface to 24 vol.% at a soil depth of ~10–20 cm. Concurrently, the in situ value ranges are decreasing with greater soil depths, displaying the smallest deviations in measurements at a depth of ~10–20 cm, varying from 19.3 vol.% to 32.3 vol.%. In comparison, retrieved θ vary between 12.6 vol.% and 47.5 vol.% with a median value of 26.4 vol.%. Conducted statistics show $R^2 = 0.09$ and $RMSE = 13.5$ vol.% for 0–5 cm, $R^2 = 0.13$ and $RMSE = 12$ vol.% for 5–10 cm, and $R^2 = 0.09$ and $RMSE = 12.2$ vol.% for 10–20 cm. Hence, retrieval results correlate slightly worse with in situ measurements from the top-soil at ~0–5 cm compared to other measuring depths, and display the smallest difference in median values of ~2.4 vol.% with in situ measurements at the greatest measuring depth (~10–20 cm). However, estimated θ at MOISST showed a median penetration depth of 25.7 cm, with most values varying from 13.6 to 35 cm for landcover class cultivated crops (Figure 9). Hence, there is still a discrepancy between measuring depths, which explains a remaining difference between in situ (10–20 cm) and SAR-based soil moisture estimates.

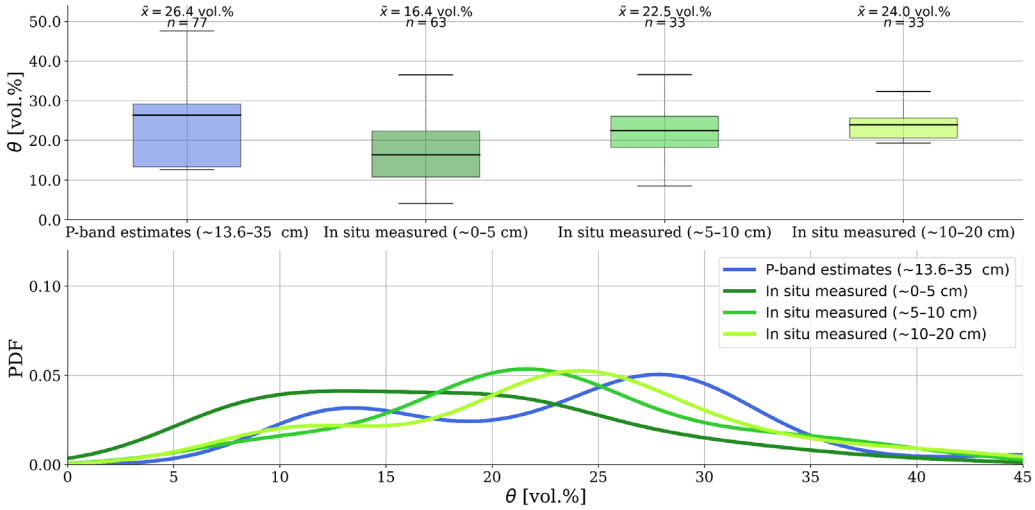

Figure 12. Comparison of retrieved soil moisture values, estimated with the proposed P-band SAR method and converted from permittivity according to the dielectric mixing model from [71], with in situ measured soil moisture values from various networks (cf. Section 2) at the AirMOSS monitoring site MOISST, OK. $\tilde{x}$ represents the respective median value, n is the total amount of values per boxplot.

5. Discussion

In comparison to model- or eigen-based decomposition methods, the hybrid decomposition technique proposed in this study combines both methods and further employs a soil scattering model suitable for P-band. Hence, the proposed P-band SAR moisture estimation method continues the efforts of [24], an iterative approach for soil moisture estimation applied to L-band observations, and of [3], the first hybrid decomposition method applied to P-band SAR data by assuming volume scattering as a cloud of randomly oriented dipoles (cf. Sections 1 and 3.2). Furthermore, the method proposed here is non-iterative with reduced algorithm complexity and, hence, computationally less expensive. It needs no prior assumptions on initial vegetation conditions since it allows the application of a wide range of vegetation cover characteristics in comparison to [3]. Lastly, it is the first of its kind, to the best of our knowledge, for complex soil permittivity estimation from (P-band) SAR data. The well-known problem of decomposition methods to overestimate the volume scattering components (cf. Section 1), e.g., [9,27,33], is solved by excluding any vegetation characterization from further analyses, where scattering intensities become negative (cf. Section 3.2). However, this is only feasible since multiple vegetation characterizations can be considered.

By applying the proposed P-band SAR moisture estimation method to SAR observations at three AirMOSS monitoring sites with varying land cover classes, the scattering contributions of surface, dihedral, or volume mechanisms could be estimated. Results show dominant dihedral scattering over forests at the site Harvard Forest in Massachusetts, and dominant volume scattering over shrub/scrub at the site Walnut Gulch in Arizona as well as over cultivated crops at the site MOISST in Oklahoma. Further, it is interesting to notice that cultivated crops at Walnut Gulch in Arizona show dominant dihedral scattering while cultivated crops at MOISST in Oklahoma display dominant volume scattering (Figure 5). This may be due to the different types and phenological stages of cultivated vegetation. Hence, results in this study suggest dominant dihedral scattering for increasing vegetation volume (height, density) at P-band. These results concur with previous studies. For example, [77] found strong dihedral scattering for P-band measurements across a boreal forest in Canada. They concluded that at P-band the ground and trunks contribute with more relevance to the SAR signal than the branches and leaves, since with "smaller scatterers compared to the wavelength" [77], these layers become more transparent to the incident wave compared to higher frequencies such as L- or C-band. This is supported by findings

of [19] across the AirMOSS monitoring site MOISST, where results also demonstrated that vegetation is more transparent at P-band than at L-band, and that woody vegetation is needed for dihedral scattering to appear in P-band. Similarly, Ref. [78] estimated dominant dihedral scattering contributions due to mainly trunk–ground interactions in P-band SAR signals across eucalyptus species in woodlands on the east coast of Australia. Analogue results at L- or C-band, however, revealed predominant volume scattering from branches and leaves (C-band) or a mix of dihedral and volume scattering, depending on the polarization (L-band). They concluded that with multiple frequencies and polarizations, individual subsets of forest structures could be analyzed [78]. In contrast, findings from [3], which are based on the same AirMOSS dataset employed in this study, showed increasing volume scattering with increasing vegetation. In the case of the monitoring site Harvard Forest, they found mainly volume scattering and less dihedral scattering, contrary to the results presented. One reason may be that the applied method in [3] only considers one type of vegetation (randomly oriented dipoles) across the entire study area, and did not employ any soil scattering model for the determination of the volume intensity component prior to the decomposition of SAR signals. However, the results in this study are supported by the fact that overall lower penetration depths into the soil could be estimated across forests compared to shrub/scrub (Figure 9, Section 4.2.). Over forests, such as at Harvard Forest, P-band microwaves are able to penetrate through vegetation but less into soils, and interact more with trunks. In smaller and less densely vegetated areas such as shrub/scrub at Walnut Gulch, P-band microwaves are able to penetrate deeper into soils but interact more with present branches and leaves due to the absence of trunks (2nd scattering center for dihedral scattering), and thus display a higher volume scattering contribution in contrast to forests. Hence, the characterization of vegetation types within the decomposition method should be carefully addressed. Choosing only one type of representative will likely lead to a biased estimation of volume scattering in P-band SAR signals.

Based on the best fit between simulations and decomposition results, the complex soil permittivity was estimated. Analyses concur with the investigated land cover classes and the climatic circumstances at each monitoring site. Lowest soil permittivity was estimated across shrub/scrub in the hot deserts of Arizona, while the highest permittivity with the smallest deviations in results was determined over forests in Massachusetts, characterized by cold humid continental climates. Accordingly, results at the monitoring site in Oklahoma with a temperate climate displayed soil permittivity in between the former ranges. Lastly, the smallest deviations in results are found in the forest land cover classes, while the largest deviations in results are found for pixels classified as cultivated crops. This fits varying phenological stages of different vegetation types and irrigation situations on agricultural managed lands (Figure 7, Section 4.2).

Converted permittivity to soil moisture was then compared at single locations with in situ measurements. Unfortunately, in situ soil moisture values mainly of the top-soil layer (0–5 cm) are available for comparison, while P-band SAR penetration depth estimates indicate deeper penetration into the soil (mainly around 20–30 cm). Thus, the highest correlation with the lowest deviations was found at Harvard Forest, and the lowest correlations at MOISST, but with slightly increasing correlations for measurements at greater soil depths. Overall, correlations are low and RMSEs are high. The main reason for this is the discrepancy between sensing depths. While in situ soil moisture values are mainly measured near the soil surface at ~0–5 cm, the estimated soil moisture is based on P-band SAR observations, which proved to have penetration depths mainly from 20 cm to 35 cm. Thus, retrievals correlate less with near-surface soil moisture measurements but will more likely correlate with measurements at deeper soil depths, as indicated at MOISST (Figure 12, Section 4.3). At Walnut Gulch, for instance, retrievals are clearly overestimating in situ measurements, showing the highest error (cf. Section 4.3). Several studies revealed increasing soil moisture with greater soil depth until a certain point, e.g., [51,79–81]. For example, [80] showed increasing soil moisture values with increasing soil depth from 5 cm to 30 cm at Kendall, Arizona (Figure 2, Section 2). Further, in hot desert regions such as

Walnut Gulch, the soil surface layer as a land–atmosphere boundary is highly influenced by climate and weather conditions and, hence, the surface tends to dry out faster than the soil layers below [79]. Another source for error is the spatial discrepancy between field measurements and SAR-based observations. While the in situ measurements are point values from single locations (cf. Figure 2, Section 2), the estimated results based on the AirMOSS dataset have a spatial resolution of ~100 m.

Based on the estimated complex soil permittivity, permittivity-based penetration depths were calculated, leading to overall P-band depths from 5 to 35 cm. Highest variations occur in regions, where the land cover is rather heterogeneous or where influences of different phenological stages of the vegetation or irrigation situations lead to varying permittivity estimates. In detail, at the humid forest site the smallest penetration depths at a median value of 24.5 cm with the smallest deviations in results were estimated. Correspondingly, the driest monitoring site shows the greatest variations in penetration depths over cultivated crops, varying mainly from 16.8 to 35 cm around a median value of 27 cm. This is in accordance with previous studies. The authors of [40] showed that P-band can provide soil moisture retrievals for a depth greater than 10 cm when using a frequency lower than 0.5 GHz, while [46] estimated similar P-band penetration depths, varying from 15 to 36 cm, showing significant annual seasonality depending on the soil moisture content.

Lastly, following the assumption of [52], P-band penetration depths between 6.97 and 34.86 cm are realistic (cf. Section 1), which is almost exactly the value range estimated in this study (5 to 35 cm). Hence, depending on soil permittivity and vegetation cover characteristics, P-band is able to penetrate several decimeters into the soil, enabling the estimation of RZSM.

6. Conclusions and Outlook

In this study, a method for complex soil permittivity and permittivity-based penetration depth estimation based on P-band SAR data is proposed and implemented. For that, a hybrid decomposition technique is set up for separating fully polarimetric P-band SAR observations into individual scattering mechanisms (soil, dihedral, volume).

The proposed method extracts the soil scattering component by applying a hybrid (eigen- and model-based) decomposition method and incorporating a soil scattering model suitable for P-band frequency, the multi-layer SPM. To the best of our knowledge, this method is the first of its kind for complex soil permittivity estimation from P-band SAR data. The approach is only limited to fully polarimetric SAR observations as co- and cross-polarized coherency matrix elements are needed within the decomposition. Further, although the proposed approach provides the ability to consider many different types of vegetation structures, the characterization of varying vegetation types within the hybrid decomposition method should be carefully addressed.

Comparisons of retrieved soil moisture with in situ measurements show lower to medium correlations, proving the overall larger penetration of P-band microwaves into soils, since results match less with top-soil layer measurements but more with deeper (~20 cm) measurements. The lack of possibility to analyze retrieval results, presented in this study, with comparable soil moisture measurements, originating at least from similar soil depths, proves the need for measurements at greater soil depths. Overall, P-band penetration depths from 5 to 35 cm were estimated, depending on regional climate and land cover characteristics and heterogeneity.

In summary, the proposed method was further adapted and revised in order to overcome many drawbacks of previous decomposition methods (e.g., overestimation of volume scattering component, consideration of one single vegetation type, missing multi-layer structures for soil scattering at P-band), and to be applicable for complex soil permittivity estimation. Presented decomposition and complex permittivity results agree well with climate and soil conditions at the three different monitoring sites, proving the feasibility of the method. Further, estimated P-band penetration depths are in accordance with previous studies and confirm the overall higher penetration ability of P-band compared to L-band

microwaves. In addition, strong dihedral scattering contributions in the SAR signal at P-band over forests, as shown in Figure 8 (cf. Section 4.2), are encouraging the development of an approach for soil moisture estimation under forests based on the dihedral scattering component instead of the soil scattering component, as proposed by [82].

Finally, since the proposed method only needs fully polarimetric P-band SAR measurements, it can be used to estimate complex soil permittivity and potential P-band penetration depths from space based on the SAR data of the upcoming BIOMASS mission (cf. Section 1) [13].

Author Contributions: Conceptualization, A.F. and T.J.; methodology, A.F. and T.J.; software, A.F.; validation, A.F. and T.J.; formal analysis, A.F. and T.J.; investigation, A.F. and T.J.; resources, A.F., A.T. and H.A.; data curation, A.F., H.A. and P.F.; writing—original draft preparation, A.F.; writing—review and editing, all authors; visualization, A.F.; supervision, T.J.; project administration, A.F., T.J., C.M. and E.F.; funding acquisition, T.J. and C.M. All authors have read and agreed to the published version of the manuscript.

Funding: This research was funded by the German Federal Ministry for Economic Affairs and Energy (BMWi) through the German Aerospace Center within the AssimEO project (50EE1914A).

Data Availability Statement: Not applicable.

Acknowledgments: A.F. and T.J. would like to thank colleagues from the Earth Observation Center at the German Aerospace Center for processing the data on a high-performance computing (HPC) cluster at the Leibniz Supercomputing Center (LRZ) as part of the high-performance data analytics (HPDA) terabyte project.

Conflicts of Interest: The authors declare no conflict of interest.

References

1. GCOS Status of the Global Observing System for Climate, GCOS Report No. 195. 2015. Available online: https://library.wmo.int/index.php?lvl=notice_display&id=18962 (accessed on 16 March 2021).
2. Bojinski, S.; Verstraete, M.; Peterson, T.C.; Richter, C.; Simmons, A.; Zemp, M. The Concept of Essential Climate Variables in Support of Climate Research, Applications, and Policy. *Bull. Am. Meteorol. Soc.* **2014**, *95*, 1431–1443. [CrossRef]
3. Alemohammad, S.H.; Konings, A.G.; Jagdhuber, T.; Moghaddam, M.; Entekhabi, D. Characterization of Vegetation and Soil Scattering Mechanisms across Different Biomes Using P-Band SAR Polarimetry. *Remote Sens. Environ.* **2018**, *209*, 107–117. [CrossRef]
4. Babaeian, E.; Sadeghi, M.; Jones, S.B.; Montzka, C.; Vereecken, H.; Tuller, M. Ground, Proximal, and Satellite Remote Sensing of Soil Moisture. *Rev. Geophys.* **2019**, *57*, 530–616. [CrossRef]
5. Etminan, A.; Tabatabaeenejad, A.; Moghaddam, M. Retrieving Root-Zone Soil Moisture Profile From P-Band Radar via Hybrid Global and Local Optimization. *IEEE Trans. Geosci. Remote Sens.* **2020**, *58*, 5400–5408. [CrossRef]
6. Hoeben, R.; Troch, P.A. Assimilation of Active Microwave Observation Data for Soil Moisture Profile Estimation. *Water Resour. Res.* **2000**, *36*, 2805–2819. [CrossRef]
7. Truong-Loi, M.-L.; Saatchi, S.; Jaruwatanadilok, S. Soil Moisture Estimation Under Tropical Forests Using UHF Radar Polarimetry. *IEEE Trans. Geosci. Remote Sens.* **2015**, *53*, 1718–1727. [CrossRef]
8. Entekhabi, D.; Yueh, S.; De Lannoy, G. *SMAP Handbook*; NASA: Washington, DC, USA, 2014.
9. He, L.; Panciera, R.; Tanase, M.A.; Walker, J.P.; Qin, Q. Soil Moisture Retrieval in Agricultural Fields Using Adaptive Model-Based Polarimetric Decomposition of SAR Data. *IEEE Trans. Geosci. Remote Sens.* **2016**, *54*, 4445–4460. [CrossRef]
10. Kerr, Y.H.; Al-Yaari, A.; Rodriguez-Fernandez, N.; Parrens, M.; Molero, B.; Leroux, D.; Bircher, S.; Mahmoodi, A.; Mialon, A.; Richaume, P.; et al. Overview of SMOS Performance in Terms of Global Soil Moisture Monitoring after Six Years in Operation. *Remote Sens. Environ.* **2016**, *180*, 40–63. [CrossRef]
11. Ulaby, F.T.; Dubois, P.C.; van Zyl, J. Radar Mapping of Surface Soil Moisture. *J. Hydrol.* **1996**, *184*, 57–84. [CrossRef]
12. Wang, H.; Magagi, R.; Goita, K.; Jagdhuber, T.; Hajnsek, I. Evaluation of Simplified Polarimetric Decomposition for Soil Moisture Retrieval over Vegetated Agricultural Fields. *Remote Sens.* **2016**, *8*, 142. [CrossRef]
13. Gelas, C.; Villard, L.; Ferro-Famil, L.; Polidori, L.; Koleck, T.; Daniel, S. Multi-Temporal Speckle Filtering of Polarimetric P-Band SAR Data over Dense Tropical Forests: Study Case in French Guiana for the BIOMASS Mission. *Remote Sens.* **2021**, *13*, 142. [CrossRef]
14. Garrison, J.L.; Shah, R.; Kim, S.; Piepmeier, J.; Vega, M.A.; Spencer, D.A.; Banting, R.; Raymond, J.C.; Nold, B.; Larsen, K.; et al. Analyses Supporting SNoOPI: A P-Band Reflectrometry Demonstration. In Proceedings of the IGARSS 2020—2020 IEEE International Geoscience and Remote Sensing Symposium, Waikoloa, HI, USA, 26 September–2 October 2020; pp. 3349–3352.

15. NASA. 2019. Available online: https://www.nasa.gov/feature/goddard/2019/snoopi-a-flying-ace-for-soil-moisture-and-snow-measurements (accessed on 16 March 2021).
16. Chapin, E.; Chau, A.; Chen, J.; Heavey, B.; Hensley, S.; Lou, Y.; Machuzak, R.; Moghaddam, M. AirMOSS: An Airborne P-Band SAR to Measure Root-Zone Soil Moisture. In Proceedings of the 2012 IEEE Radar Conference, Atlanta, GA, USA, 7–11 May 2012; pp. 693–698.
17. Alberga, V.; Satalino, G.; Staykova, D.K. Comparison of Polarimetric SAR Observables in Terms of Classification Performance. *Int. J. Remote Sens.* **2008**, *29*, 4129–4150. [CrossRef]
18. Yamaguchi, Y.; Yajima, Y.; Yamada, H. A Four-Component Decomposition of POLSAR Images Based on the Coherency Matrix. *IEEE Geosci. Remote Sens. Lett.* **2006**, *3*, 292–296. [CrossRef]
19. Alemohammad, S.H.; Jagdhuber, T.; Moghaddam, M.; Entekhabi, D. Soil and Vegetation Scattering Contributions in L-Band and P-Band Polarimetric SAR Observations. *IEEE Trans. Geosci. Remote Sens.* **2019**, *57*, 8417–8429. [CrossRef]
20. Cloude, S.R. Uniqueness of Target Decomposition Theorems in Radar Polarimetry. In *Direct and Inverse Methods in Radar Polarimetry*; Boerner, W.-M., Brand, H., Cram, L.A., Holm, W.A., Stein, D.E., Wiesbeck, W., Keydel, W., Giuli, D., Gjessing, D.T., Molinet, F.A., Eds.; Springer: Dordrecht, The Netherlands, 1992; pp. 267–296; ISBN 978-94-010-9245-6.
21. Freeman, A.; Durden, S.L. A Three-Component Scattering Model for Polarimetric SAR Data. *IEEE Trans. Geosci. Remote Sens.* **1998**, *36*, 963–973. [CrossRef]
22. van Zyl, J.J.; Arii, M.; Kim, Y. Model-Based Decomposition of Polarimetric SAR Covariance Matrices Constrained for Nonnegative Eigenvalues. *IEEE Trans. Geosci. Remote Sens.* **2011**, *49*, 3452–3459. [CrossRef]
23. Yonezawa, C.; Watanabe, M.; Saito, G. Polarimetric Decomposition Analysis of ALOS PALSAR Observation Data before and after a Landslide Event. *Remote Sens.* **2012**, *4*, 2314–2328. [CrossRef]
24. Jagdhuber, T.; Hajnsek, I.; Papathanassiou, K.P. An Iterative Generalized Hybrid Decomposition for Soil Moisture Retrieval Under Vegetation Cover Using Fully Polarimetric SAR. *IEEE J. Sel. Top. Appl. Earth Obs. Remote Sens.* **2015**, *8*, 3911–3922. [CrossRef]
25. Ballester-Berman, J.D.; Ainsworth, T.L.; Lopez-Sanchez, J.M. On The Physical Quantitative Assessment of Model-Based PolSAR Decompositions. *arXiv* **2020**, arXiv:2001.05872.
26. Chen, S.-W.; Sato, M.; Wang, X.-S.; Xiao, S.-P. *Target Scattering Mechanism in Polarimetric Synthetic Aperture Radar: Interpretation and Application*, 1st ed.; Springer: Singapore, 2018; ISBN 978-981-10-7269-7.
27. Cloude, S. *Polarisation: Applications in Remote Sensing*, 1st ed.; Oxford University Press: Oxford, UK; New York, NY, USA, 2010; ISBN 978-0-19-956973-1.
28. Cloude, S.R.; Pottier, E. A Review of Target Decomposition Theorems in Radar Polarimetry. *IEEE Trans. Geosci. Remote Sens.* **1996**, *34*, 498–518. [CrossRef]
29. Hajnsek, I.; Desnos, Y.-L. *Polarimetric Synthetic Aperture Radar Principles and Application*; Springer: Berlin/Heidelberg, Germany, 2021; ISBN 978-3-030-56504-6.
30. Van Zyl, J.; Kim, Y. *Synthetic Aperture Radar Polarimetry*; JPL Space Science and Technology Series; Wiley: Hoboken, NJ, USA, 2011; ISBN 978-1-118-11607-4.
31. Jagdhuber, T. Soil Parameter Retrieval under Vegetation Cover Using SAR Polarimetry. Ph.D. Thesis, Faculty of Science, University Potsdam, Potsdam, Germany, 2012. Available online: https://publishup.uni-potsdam.de/frontdoor/index/index/docId/5894 (accessed on 18 February 2021).
32. Sato, A.; Yamaguchi, Y.; Singh, G.; Park, S.-E. Four-Component Scattering Power Decomposition With Extended Volume Scattering Model. *IEEE Geosci. Remote Sens. Lett.* **2012**, *9*, 166–170. [CrossRef]
33. van Zyl, J.J.; Kim, Y. Requirements for Model-Based Polarimetric Decompositions. In Proceedings of the 7th European Conference on Synthetic Aperture Radar, Friedrichshafen, Germany, 2–5 June 2008.
34. Kraus, J.D.; Carver, K.R. *Electromagnetics*, 2nd ed.; McGraw-Hill Electrical and Electronic Engineering Series; McGraw-Hill: New York, NY, USA, 1973; ISBN 978-0-07-035396-1.
35. Ulaby, F.T.; Long, D.G. *Microwave Radar and Radiometric Remote Sensing*; The University of Michigan Press: Ann Arbor, MI, USA, 2014; ISBN 978-0-472-11935-6.
36. Bannawat, L.; Boonpoonga, A.; Akkaraekthalin, P. Permittivity Estimation of a Shallow-Layered Medium Using High-Resolution Ground-Penetrating Radar. *Int. J. Remote Sens.* **2020**, *41*, 4626–4643. [CrossRef]
37. Gururaj, P.; Umesh, P.; Shetty, A. Assessment of Surface Soil Moisture from ALOS PALSAR-2 in Small-Scale Maize Fields Using Polarimetric Decomposition Technique. *Acta Geophys.* **2021**, *69*, 579–588. [CrossRef]
38. Shi, H.; Zhao, L.; Yang, J.; Lopez-Sanchez, J.M.; Zhao, J.; Sun, W.; Shi, L.; Li, P. Soil Moisture Retrieval over Agricultural Fields from L-Band Multi-Incidence and Multitemporal PolSAR Observations Using Polarimetric Decomposition Techniques. *Remote Sens. Environ.* **2021**, *261*, 112485. [CrossRef]
39. Chen, R.H.; Tabatabaeenejad, A.; Moghaddam, M. Retrieval of Permafrost Active Layer Properties Using Time-Series P-Band Radar Observations. *IEEE Trans. Geosci. Remote Sens.* **2019**, *57*, 6037–6054. [CrossRef]
40. Shen, X.; Walker, J.P.; Ye, N.; Wu, X.; Boopathi, N.; Yeo, I.-Y.; Zhang, L.; Zhu, L. Soil Moisture Retrieval Depth of P- and L-Band Radiometry: Predictions and Observations. *IEEE Trans. Geosci. Remote Sens.* **2020**, *59*, 6814–6822. [CrossRef]
41. Ulaby, F.T.; Moore, R.K.; Fung, A.K.; Ulaby, F.T. *Microwave Remote Sensing, Active and Passive, Vol. II: Radar Remote Sensing and Surface Scattering and Emission Theory*; ARTECH House: Norwood, MA, USA, 1982; Volume 2, ISBN 978-0-201-10760-9.

42. El Hajj, M.; Baghdadi, N.; Bazzi, H.; Zribi, M. Penetration Analysis of SAR Signals in the C and L Bands for Wheat, Maize, and Grasslands. *Remote Sens.* **2018**, *11*, 31. [CrossRef]
43. Klausing, H.; Holpp, W. *Radar Mit Realer Und Synthetischer Apertur: Konzeption und Realisierung*; Oldenbourg: München, Germany, 2000; ISBN 978-3-486-23475-6.
44. Schaber, G.; McCauley, J.; Breed, C.; Olhoeft, G. Shuttle Imaging Radar: Physical Controls on Signal Penetration and Subsurface Scattenng in the Eastern Sahara. *IEEE Trans. Geosci. Remote Sens.* **1986**, *GE-24*, 603–623. [CrossRef]
45. Wilheit, T.T. Radiative Transfer in a Plane Stratified Dielectric. *IEEE Trans. Geosci. Electron.* **1978**, *16*, 138–143. [CrossRef]
46. Konings, A.G.; Entekhabi, D.; Moghaddam, M.; Saatchi, S.S. The Effect of Variable Soil Moisture Profiles on P-Band Backscatter. *IEEE Trans. Geosci. Remote Sens.* **2014**, *52*, 6315–6325. [CrossRef]
47. Blumberg, D.G.; Freilikher, V.; Lyalko, I.V.; Vulfson, L.D.; Kotlyar, A.L.; Shevchenko, V.N.; Ryabokonenko, A.D. Soil Moisture (Water-Content) Assessment by an Airborne Scatterometer: The Chernobyl disaster area and the Negev Desert. *Remote Sens. Environ.* **2000**, *71*, 309–319. [CrossRef]
48. Zribi, M.; Sahnoun, M.; Baghdadi, N.; Le Toan, T.; Ben Hamida, A. Analysis of the Relationship between Backscattered P-Band Radar Signals and Soil Roughness. *Remote Sens. Environ.* **2016**, *186*, 13–21. [CrossRef]
49. Ochsner, T.E.; Cosh, M.H.; Cuenca, R.H.; Dorigo, W.A.; Draper, C.S.; Hagimoto, Y.; Kerr, Y.H.; Larson, K.M.; Njoku, E.G.; Small, E.E.; et al. State of the Art in Large-Scale Soil Moisture Monitoring. *Soil Sci. Soc. Am. J.* **2013**, *77*, 1888–1919. [CrossRef]
50. Singh, A.; Meena, G.K.; Kumar, S.; Gaurav, K. Analysis of the Effect of Incidence Angle and Moisture Content on the Penetration Depth of L- and S-Band SAR Signals into the Ground Surface. *ISPRS Ann. Photogramm. Remote Sens. Spat. Inf. Sci.* **2018**, *4*, 197–202. [CrossRef]
51. Tabatabaeenejad, A.; Chen, R.H.; Burgin, M.S.; Duan, X.; Cuenca, R.H.; Cosh, M.H.; Scott, R.L.; Moghaddam, M. Assessment and Validation of AirMOSS P-Band Root-Zone Soil Moisture Products. *IEEE Trans. Geosci. Remote Sens.* **2020**, *58*, 6181–6196. [CrossRef]
52. de Lange, R.; Beck, R.; van de Giesen, N.; Friesen, J.; de Wit, A.; Wagner, W. Scatterometer-Derived Soil Moisture Calibrated for Soil Texture With a One-Dimensional Water-Flow Model. *IEEE Trans. Geosci. Remote Sens.* **2008**, *46*, 4041–4049. [CrossRef]
53. Rao, K.S.; Chandra, G.; Narasimha Rao, P.V. Study on Penetration Depth and Its Dependence on Frequency, Soil Moisture, Texture and Temperature in the Context of Microwave Remote Sensing. *J Indian Soc. Remote Sens.* **1988**, *16*, 7–19. [CrossRef]
54. Moghaddam, M.; Tabatabaeenejad, A.; Chen, R.H.; Saatchi, S.; Jaruwatanadilok, S.; Burgin, M.; Duan, X.; Truong-Loi, M.L. *AirMOSS: L2/3 Volumetric Soil Moisture Profiles Derived from Radar, 2012–2015*; ORNL DAAC: Oak Ridge, TN, USA, 2016. [CrossRef]
55. Peel, M.C.; Finlayson, B.L.; McMahon, T.A. Updated World Map of the Köppen-Geiger Climate Classification. *Hydrol. Earth Syst. Sci.* **2007**, *11*, 1633–1644. [CrossRef]
56. Homer, C.; Dewitz, J.; Yang, L.; Jin, S.; Danielson, P.; Xian, G.; Coulston, J.; Herold, N.; Wickham, J.; Megown, K. Completion of the 2011 National Land Cover Database for the Conterminous United States-Representing a Decade of Land Cover Change Information. *Photogramm. Eng. Remote Sens.* **2015**, *81*, 345–354.
57. Pastorello, G.; Trotta, C.; Canfora, E.; Chu, H.; Christianson, D.; Cheah, Y.W.; Poindexter, C.; Chen, J.; Elbashandy, A.; Humphrey, M.; et al. The FLUXNET2015 Dataset and the ONEFlux Processing Pipeline for Eddy Covariance Data. *Sci. Data* **2020**, *7*, 225. [CrossRef]
58. Montzka, C.; Bogena, H.; Zreda, M.; Monerris, A.; Morrison, R.; Muddu, S.; Vereecken, H. Validation of Spaceborne and Modelled Surface Soil Moisture Products with Cosmic-Ray Neutron Probes. *Remote Sens.* **2017**, *9*, 103. [CrossRef]
59. Zreda, M.; Shuttleworth, W.J.; Zeng, X.; Zweck, C.; Desilets, D.; Franz, T.; Rosolem, R. COSMOS: The COsmic-Ray Soil Moisture Observing System. *Hydrol. Earth Syst. Sci.* **2012**, *16*, 4079–4099. [CrossRef]
60. Moghaddam, M.; Silva, A.; Clewley, D.; Akbar, R.; Hussaini, S.A.; Whitcomb, J.; Devarakonda, R.; Shrestha, R.; Cook, R.B.; Prakash, G.; et al. *Soil Moisture Profiles and Temperature Data from SoilSCAPE Sites, USA*; ORNL DAAC: Oak Ridge, TN, USA, 2016. [CrossRef]
61. Bell, J.E.; Palecki, M.A.; Baker, C.B.; Collins, W.G.; Lawrimore, J.H.; Leeper, R.D.; Hall, M.E.; Kochendorfer, J.; Meyers, T.P.; Wilson, T.; et al. U.S. Climate Reference Network Soil Moisture and Temperature Observations. *J. Hydrometeorol.* **2013**, *14*, 977–988. [CrossRef]
62. Larson, K.M.; Small, E.E.; Gutmann, E.D.; Bilich, A.L.; Braun, J.J.; Zavorotny, V.U. Use of GPS Receivers as a Soil Moisture Network for Water Cycle Studies. *Geophys. Res. Lett.* **2008**, *35*, L24405. [CrossRef]
63. Tabatabaeenejad, A.; Moghaddam, M. Bistatic Scattering from Three-Dimensional Layered Rough Surfaces. *IEEE Trans. Geosci. Remote Sens.* **2006**, *44*, 2102–2114. [CrossRef]
64. Tsang, L.; Kong, J.A.; Shin, R.T. *Theory of Microwave Remote Sensing*; Wiley Series in Remote Sensing; Wiley: New York, NY, USA, 1985; ISBN 978-0-471-88860-4.
65. Nicolaides, A. *Pure Mathematics: Complex Numbers*; P.A.S.S: London, UK, 2008; Volume 3, ISBN 978-1-872684-92-5.
66. Rizzoli, P.; Martone, M.; Gonzalez, C.; Wecklich, C.; Borla Tridon, D.; Bräutigam, B.; Bachmann, M.; Schulze, D.; Fritz, T.; Huber, M.; et al. Generation and Performance Assessment of the Global TanDEM-X Digital Elevation Model. *ISPRS J. Photogramm. Remote Sens.* **2017**, *132*, 119–139. [CrossRef]
67. GDAL/OGR contributors GDAL/OGR Geospatial Data Abstraction Software Library. Open Source Geospatial Foundation. 2021. Available online: https://Gdal.Org (accessed on 16 March 2021).

68. QGIS Development Team QGIS Geographic Information System. Open Source Geospatial Foundation Project. 2021. Available online: http://Qgis.Osgeo.Org (accessed on 16 March 2021).
69. Szigarski, C.; Jagdhuber, T.; Baur, M.; Thiel, C.; Parrens, M.; Wigneron, J.-P.; Piles, M.; Entekhabi, D. Analysis of the Radar Vegetation Index and Potential Improvements. *Remote Sens.* **2018**, *10*, 1776. [CrossRef]
70. Kelleners, T.J.; Robinson, D.A.; Shouse, P.J.; Ayars, J.E.; Skaggs, T.H. Frequency Dependence of the Complex Permittivity and Its Impact on Dielectric Sensor Calibration in Soils. *Soil Sci. Soc. Am. J.* **2005**, *69*, 67–76. [CrossRef]
71. Topp, G.C.; Davis, J.L.; Annan, A.P. Electromagnetic Determination of Soil Water Content: Measurements in Coaxial Transmission Lines. *Water Resour. Res.* **1980**, *16*, 574–582. [CrossRef]
72. Dobson, M.; Ulaby, F.; Hallikainen, M.; El-rayes, M. Microwave Dielectric Behavior of Wet Soil-Part II: Dielectric Mixing Models. *IEEE Trans. Geosci. Remote Sens.* **1985**, *GE-23*, 35–46. [CrossRef]
73. Mironov, V.L.; Kosolapova, L.G.; Fomin, S.V. Physically and Mineralogically Based Spectroscopic Dielectric Model for Moist Soils. *IEEE Trans. Geosci. Remote Sens.* **2009**, *47*, 2059–2070. [CrossRef]
74. Park, C.-H.; Behrendt, A.; LeDrew, E.; Wulfmeyer, V. New Approach for Calculating the Effective Dielectric Constant of the Moist Soil for Microwaves. *Remote Sens.* **2017**, *9*, 732. [CrossRef]
75. von Hippel, A.R. *Dielectrics and Waves*; Wiley: New York, NY, USA, 1954.
76. Mironov, V.L.; Dobson, M.C.; Kaupp, V.H.; Komarov, S.A.; Kleshchenko, V.N. Generalized Refractive Mixing Dielectric Model for Moist Soils. In Proceedings of the IEEE International Geoscience and Remote Sensing Symposium, Toronto, ON, Canada, 24–28 June 2002; Volume 6, pp. 3556–3558.
77. Moghaddam, M.; Saatchi, S. Analysis of Scattering Mechanisms in SAR Imagery over Boreal Forest: Results from BOREAS '93. *IEEE Trans. Geosci. Remote Sens.* **1995**, *33*, 1290–1296. [CrossRef]
78. Lucas, R.M.; Moghaddam, M.; Cronin, N. Microwave Scattering from Mixed-Species Forests, Queensland, Australia. *IEEE Trans. Geosci. Remote Sens.* **2004**, *42*, 2142–2159. [CrossRef]
79. Das, N.N.; Mohanty, B.P.; Cosh, M.H.; Jackson, T.J. Modeling and Assimilation of Root Zone Soil Moisture Using Remote Sensing Observations in Walnut Gulch Watershed during SMEX04. *Remote Sens. Environ.* **2008**, *112*, 415–429. [CrossRef]
80. Sivandran, G.; Bras, R.L. Dynamic Root Distributions in Ecohydrological Modeling: A Case Study at Walnut Gulch Experimental Watershed. *Water Resour. Res.* **2013**, *49*, 3292–3305. [CrossRef]
81. Tabatabaeenejad, A.; Burgin, M.; Duan, X.; Moghaddam, M. P-Band Radar Retrieval of Subsurface Soil Moisture Profile as a Second-Order Polynomial: First AirMOSS Results. *IEEE Trans. Geosci. Remote Sens.* **2015**, *53*, 645–658. [CrossRef]
82. Jagdhuber, T. An Approach to Extended Fresnel Scattering for Modeling of Depolarizing Soil-Trunk Double-Bounce Scattering. *Remote Sens.* **2016**, *8*, 818. [CrossRef]

4 Article III

A. Fluhrer, T. Jagdhuber, C. Montzka, M. Schumacher, H. Alemohammad, A. Tabatabaeenejad, H. Kunstmann, and D. Entekhabi, 'Soil Moisture Profile Estimation by Combining P-band SAR Polarimetry with Hydrological and Multi-Layer Scattering Models', in *Elsevier's Remote Sensing of Environment*, Volume 305, 2024, 114067, doi: 10.1016/j.rse.2024.114067.

Remote Sensing of Environment 305 (2024) 114067

Contents lists available at ScienceDirect

Remote Sensing of Environment

journal homepage: www.elsevier.com/locate/rse

Soil moisture profile estimation by combining P-band SAR polarimetry with hydrological and multi-layer scattering models

Anke Fluhrer [a,b,*], Thomas Jagdhuber [a,b], Carsten Montzka [c], Maike Schumacher [d], Hamed Alemohammad [e], Alireza Tabatabaeenejad [f], Harald Kunstmann [b,g], Dara Entekhabi [h]

[a] Microwaves and Radar Institute, German Aerospace Center (DLR), Muenchener Straße 20, 82234 Weßling, Germany
[b] Institute of Geography, University of Augsburg, Alter Postweg 118, 86159 Augsburg, Germany
[c] Institute of Bio- and Geosciences: Agrosphere (IBG-3), Forschungszentrum Juelich, Wilhelm-Johnen-Straße, 52428 Juelich, Germany
[d] Geodesy Group, Department of Planning, Aalborg University, Rendsburggade 14, 9000 Aalborg, Denmark
[e] Center for Geospatial Analytics & Graduate School of Geography, Clark University, Worcester, MA 01610, USA
[f] The Aerospace Corporation, El Segundo, CA 90245, USA
[g] Institute of Meteorology and Climate Research, Karlsruhe Institute of Technology, Kreuzeckbahnstraße 19, 82467 Garmisch-Partenkirchen, Germany
[h] Department of Civil and Environmental Engineering, Massachusetts Institute of Technology (MIT), Cambridge, MA 02139, USA

ARTICLE INFO

Edited by Jing M. Chen

Keywords:
AirMOSS
Hybrid polarimetric decomposition
HYDRUS-1D
Remote sensing

ABSTRACT

An approach for estimating vertically continuous soil moisture profiles under varying vegetation covers by combining remote sensing with soil (hydrological) modeling is proposed. The approach uses decomposed soil scattering components, after the removal of the vegetation scattering components from fully polarimetric P-band SAR observations. By comparing these with hydrological simulations, soil moisture profiles from the soil surface until a soil depth of 30 cm (assumed average P-band penetration depth) are estimated. Here, the hydrological model HYDRUS-1D, as a representative of any soil hydrological model, is employed to simulate an ensemble of realistic soil moisture profiles, which are used for a multi-layer soil scattering model to obtain forward modeled soil scattering components. Compared to the decomposed SAR-based soil scattering components, the most appropriate soil moisture profile from the ensemble is estimated. The approach is able to provide physically (hydraulic) more meaningful soil moisture profile shapes than currently existing profile estimation approaches, like polynomial fitting to few measurements at discrete soil depths. Results are presented across eight *in situ* measuring stations in the U.S. within six test sites of NASA's Airborne Microwave Observatory of Subcanopy and Subsurface (AirMOSS) mission between 2013 and 2015. In-depth analyzes and validations with *in situ* measured soil moisture information demonstrate the feasibility of the proposed approach. Overall, estimated soil moisture profiles at the different sites match the varying local climate, vegetation cover, and soil conditions. Coefficients of determination between estimated and *in situ* measured soil moisture values vary between 0.48 and 0.92, while unbiased errors range from 1.4 vol% to 3.7 vol%, and Fréchet distances (analyzing the similarity of profile shapes) vary between 0.1 and 0.2 [−].

1. Introduction

Although soil moisture as part of the geosphere accounts for only ~0.0089% of the total water on Earth (Dingman, 2015), it significantly contributes to the characterization of the Earth's climate (Bojinski et al., 2014). Soil moisture links exchanges between the land and the atmosphere, and connects the water and carbon cycles through evapotranspiration (Dingman, 2015). In weather forecasting and climate modeling, the soil moisture distribution and variability across the vertical soil column is evident since it has direct impact on land-atmosphere coupling, evapotranspiration as well as heat and water exchanges (Dingman, 2015; Dirmeyer et al., 2016; Feddes et al., 2001). For example, the current state of the soil moisture variability across the vertical soil column, the so-called soil moisture profile, controls how fast

* Corresponding author at: Microwaves and Radar Institute, German Aerospace Center (DLR), Muenchener Straße 20, 82234 Weßling, Germany.
E-mail addresses: Anke.Fluhrer@dlr.de (A. Fluhrer), Thomas.Jagdhuber@dlr.de (T. Jagdhuber), c.montzka@fz-juelich.de (C. Montzka), maikes@plan.aau.dk (M. Schumacher), halemohammad@clarku.edu (H. Alemohammad), alirezat@aero.org (A. Tabatabaeenejad), harald.kunstmann@kit.edu (H. Kunstmann), darae@mit.edu (D. Entekhabi).

https://doi.org/10.1016/j.rse.2024.114067
Received 16 May 2023; Received in revised form 25 January 2024; Accepted 17 February 2024

water can infiltrate and percolate vertically through the soil as well as how quickly a soil dries out (Ford et al., 2014). Hence, it controls, for instance, crop and plant growth, soil erosion, landslides, and forest fires. Up to now, soil moisture and its vertical variability is mainly treated secondarily in climate modeling (Vereecken et al., 2022). However, several studies showed that unrealistic initial assumptions on soil moisture impact the forecast skill of models, stating that remotely sensed soil moisture can have great potential in improving climate modeling by describing the coupled land-atmosphere behavior more realistically (Dirmeyer et al., 2018; Koster et al., 2011). For instance, the second phase of the Global Land-Atmosphere Coupling Experiment (GLACE-2) was intended to investigate how more realistic land surface initializations, notably soil moisture, would improve the forecast skill of climate models. Results showed that in many regions realistic initializations, for example from remotely sensed soil moisture observations, can significantly improve this skill (Koster et al., 2011).

Up to now, remote sensing approaches allow the estimation of soil moistures at the soil surface from L-band measurements (He et al., 2016; Jagdhuber et al., 2015), or at deeper soil depths within the root zone from P-band measurements (Etminan et al., 2020; Fluhrer et al., 2022; Tabatabaeenejad et al., 2015). These approaches represent the behavior of moisture across the soil profile from the soil surface until the sensing depth of the microwave with just one single uniform value. Estimating only single soil moisture values from few radar measurements, however, is prone to errors and often impractical due to the high number of unknowns compared to the available number of measurements (Konings et al., 2014).

Further, the soil moisture variability with depth cannot be estimated from single remote sensing observations despite the fact that the radar backscatter is able to provide information about soil moisture discontinuities. However, knowledge about the soil moisture profile is of utmost importance in climate research and many environmental applications, like land surface, weather and climate monitoring (Walker et al., 2001), or agricultural production and food security (Almendra-Martín et al., 2021).

There already exist different approaches to estimate soil moisture profiles by using land surface modeling or remote sensing data assimilation techniques. The simplest approach to estimate a soil moisture profile is from soil moisture information at discrete soil depths by fitting a polynomial function of certain degree through the few known points. The soil moisture information for that can originate from *in situ* field measurements, L- and P-band remote sensing techniques, or from models. Overall, the polynomial approach is rather imprecise and physically less robust since this mathematical assumption on very few, sometimes just three moisture values, can only represent high level simplifications of the reality, although there are recent attempts to improve the polynomial soil moisture profile estimation, *e.g.*, (Sadeghi et al., 2016). Further, attempts have been made to retrieve RZSM values from prognostics describing the 'average deviations from the equilibrium profile' (Reichle et al., 2017), or by evaluating the degree of association or coupling strength between near surface and *in situ* root zone soil moistures, *e.g.*, (Ford et al., 2014; Short Gianotti et al., 2019). Here, assumptions on theoretical relationships ignore the lack of transferability of soil moisture dynamics across spatio-temporal scales. However, soil moisture in the subsurface responds slower to changes and is less variable compared to near-surface soil moisture (Ford et al., 2014; Short Gianotti et al., 2019). This means, the link between both is highly complex especially after a precipitation event. Another method for soil moisture profiles estimation is the comparison of the observed backscatter from radars with simulated backscatters based on forward models (Konings et al., 2014). However, a radar signal includes all potential scattering mechanisms from soil, vegetation, and the combination of both. Hence, the vegetation volume covering the soil also has to be modeled and considered in backscatter simulations, which requires certain assumptions and adds additional complexity to the modeling. Lastly, several soil moisture approaches have been published based on land data assimilation. For that, spatially or temporally coarse soil moisture *in situ* measurements or satellite-derived soil moisture information are used in a land surface model together with auxiliary information, such as precipitation or soil characteristics. In this way, enhanced model calibration, spatially or temporally upscaled soil moisture information, or RZSM estimates across the vertical soil profile can be achieved (Lei et al., 2020; Liu et al., 2011; Tangdamrongsub et al., 2020). The advantages of the proposed approach compared to assimilation are, for one, that no prior information on soil moisture conditions across the vertical soil profile has to be known, neither from *in situ* measurements, nor satellite-derived. Second, no dense time series of remote sensing observations is required as input, as the comparison of decomposed P-band SAR data and model simulations can be done for every time step individually. However, assimilating temporally coarse remote sensing data, as available from the AirMOSS mission (~4–5 dates per year), is not sufficient enough for valid results. Lastly, the decomposed remote sensing estimate can be compared directly with model simulations without the need for model adaptions.

Besides remote sensing, soil states, like soil moisture, can be modeled with hydrological models based on measured atmospheric (*e.g.* precipitation, solar radiation, wind speed) and soil (*e.g.* temperature, matric potential, conductivity) parameters. In hydrological modeling, one of the general equations for predicting and describing one-dimensional water movement in (partially) saturated or unsaturated soils is the well-known Richards equation (Dingman, 2015), a combination of the mass conservation law (continuity principle) and the Darcy-Buckingham equation (Sadeghi et al., 2016). The Richards equation is a partial differential and highly nonlinear equation due to the dependence of the hydraulic conductivity and the soil water content on the soil matric potential. This means, a closed-form analytical solution of the equation is impossible, except for special cases with many simplifications and certain boundary conditions (Dingman, 2015). However, these can only lead to approximate solutions and are not generally applicable. There exist many hydrological models to numerically solve the Richards equation by either employing "a finite difference, finite volume, or finite element approximation in space" (Farthing and Ogden, 2017), *e.g.*, the Flux-Penn State Integrated Hydrologic Model (Shi et al., 2013), the ParFlow (Ashby and Falgout, 1996), or the RichardsFOAM (Orgogozo et al., 2014).

In this study, a joint approach of remote sensing and soil hydrological modeling is proposed for the estimation of continuous soil moisture profiles. The approach compares decomposed polarimetric P-band SAR estimates with respective simulations from the HYDRUS-1D (soil hydraulic model). The advantage of the proposed approach is, for one, that vegetation scattering contributions to the total SAR signal are removed before the comparison. Second, unlike in standard hydrological modeling, less assumptions on initial conditions are made in order to decrease potential sources for errors within simulations. That way, the proposed approach allows the comparison of actual observed SAR measurements with a set of hydrological simulations in order to estimate the most probable soil moisture profile.

The approach is supposed to lead to physically (hydraulic) more meaningful soil moisture profile shapes than mathematical approximations like polynomial fittings. Further, it provides the advantage of estimating continuous soil moisture profiles under varying vegetation covers (from grassland to forests) and for different climates.

2. Data sources

In this study, the polarimetric P-band SAR dataset from the Airborne Microwave Observatory of Subcanopy and Subsurface (AirMOSS) campaign, compiled between 2012 and 2015 by the National Aeronautics and Space Administration (NASA), is used. During the AirMOSS campaign, fully polarimetric SAR signals at a center frequency of 430 MHz, with a high radiometric calibration accuracy of 0.5 dB, and a noise equivalent of −40 dB were recorded across ten sites in Northern and

Central America. It was the first P-band airborne mission fully dedicated to RZSM estimation. Each monitoring site was revisited at least three times every campaign year and covers an area of ~25 × 100 km at ~90 m spatial resolution (Alemohammad et al., 2018). Detailed information on the campaigns and the instrument can be found in, *e.g.*, (Alemohammad et al., 2018; Chapin et al., 2012).

The proposed approach is validated and analyzed thoroughly with comparison to *in situ* field measurements. The focus in this study is on SAR pixels (where *in situ* data from measuring stations are available) within six AirMOSS sites in the U.S. (Fig. 1). These sites are "Howland Forest" in Maine, "Duke Forest" in North Carolina, "Metolius" in Oregon, "MOISST" in Oklahoma, "Tonzi Ranch" in California, and "Walnut Gulch" in Arizona. Information and locations on the investigated AirMOSS monitoring sites and the *in situ* measuring stations are shown in Fig. 1 and Table 1.

Fig. 1 shows that two sites are located at the east and three sites on the west coast of the U.S., with one site in the center. Hence, the climate regimes vary between cold humid continental climate with warm summers and significant precipitation in all seasons (Dfb), temperate climate with mild, dry, or hot summers (Csa, Csb, Cfa), and arid climate of a desert with warm summers (BSk) (Peel et al., 2007).

The soil textures indicate different types of a loamy soil (Fig. 1), while the landcover classes vary from grasslands, pastures or shrublands of woody savannas (with forest canopy cover between 30 and 60% and forest height exceeding 2 m) to evergreen needleleaf forests (Homer et al., 2015). Further, the amount of available dates for every AirMOSS site, where SAR measurements were recorded, vary between 13 and 22, with three to ten dates per year (in total 143 dates) (Table 1).

For hydrological simulations of soil moisture profiles (see Sec. 3.2.), input parameters from *in situ* measuring stations of the AmeriFlux network (AmeriFlux, 2022) and the US Climate Reference Network (USCRN) (Bell et al., 2013) are used. For the subsequent validation of results, soil moisture measurements at multiple depths from the same *in situ* networks are used (Fig. 1, Table 1). The focus in this study is on presenting and validating the proposed method for estimation of continuous soil moisture profiles from combined P-band polarimetry and soil modeling. Nevertheless, obtained results are additionally compared to two well-known soil moisture products: the European ReAnalysis (ERA5) land product from the European Centre for Medium-Range Weather Forecasts (ECMWF) (Muñoz Sabater, 2019), and the project AirMOSS L4 mission product (Crow et al., 2016). The ERA5-land dataset is a reanalysis product combining available observations with model data based on physics. The core is the Carbon Hydrology-Tiled ECMWF Scheme for Surface Exchanges over Land (CHTESSEL). For the ERA5-land soil moisture, for example, a total of >800 *in situ* sensors from various networks around the globe are used to initialize the model (Muñoz-Sabater et al., 2021). In contrast, the AirMOSS L4 product is based on mathematically integrating (polynomials) the AirMOSS L2/L3 product (Moghaddam et al., 2016), which provides soil moisture estimates at specific depths by using the AirMOSS P-band SAR observations along with several models (vegetation, ground surface scattering, subsurface scattering), with the Penn State Integrated Hydrologic Model (PIHM) and auxiliary information (*e.g.*, land cover classes, soil texture) (Crow et al., 2016). However, no in-depth comparison of the different methods for soil moisture estimation is performed and could be done in a follow-on study, outlining in detail the differences in algorithms, and consequently, results.

3. Methods

In this study, a combined technique of remote sensing and soil hydrological modeling is proposed for estimating continuous soil moisture profiles. As outlined in Fig. 2, the polarimetric soil scattering angle α_s^{SAR} can be determined from radar remote sensing, by decomposing the observed SAR signals into the individual scattering mechanisms (soil, dihedral, and volume) (Fluhrer et al., 2022).

From hydrological modeling, simulated soil moisture profiles θ_{SMPn} from HYDRUS-1D can be used as input to the multi-layer small perturbation method (SPM) (Tabatabaeenejad and Moghaddam, 2006) to forward model the backscatter coefficients from several soil layers, and calculate their polarimetric soil scattering angle $\alpha_s^{Model}n$. In the end, the soil moisture profile is estimated from the best fit between α_s^{SAR} and all $\alpha_s^{Model}n$.

Here, the comparison between decomposed SAR data and forward simulations is performed on the level of the polarimetric soil scattering angle α_s instead of directly comparing the observed and modeled backscatter coefficients. One reason is, that the observed backscatter coefficients contain scattering from all mechanisms (soil, dihedral, volume) and not only soil scattering. Another reason is that from remote sensing fully polarimetric backscatter coefficients are available, while from electromagnetic forward modeling only co-polarized (HH, VV) backscatter coefficients are obtainable. Hence, the use of α_s^{SAR} after the decomposition ensures remotely sensed information from the soil scattering component only but without loss on information since all observed co- and cross-polarized (HH, VV, HV, VH) backscatter coefficients are used within the decomposition.

It is important to emphasize that soil hydrological modeling does not simulate backscatters. A hydrological model (in this study the HYDRUS-1D) is used to compute soil moisture profiles, which in turn are used for backscatter simulations based on an electromagnetic model, in this study the multi-layer SPM.

In the following, both procedures to estimate the respective soil scattering angle α_s and the joint technique will be described in more detail.

3.1. Decomposed polarimetric soil scattering angle from P-band SAR observations

The polarimetric soil scattering angle α_s^{SAR} is estimated by decomposing the observed P-band SAR signal into individual scattering components by applying the hybrid decomposition method from (Fluhrer et al., 2022). This method separates the reflection symmetric, polarimetric coherency matrix $[T]$ from observed SAR signals into the three scattering components (surface $[T_s]$, dihedral $[T_d]$, and volume $[T_v]$):

$$\begin{bmatrix} T_{11} & T_{12} & 0 \\ T_{12}^* & T_{22} & 0 \\ 0 & 0 & T_{33} \end{bmatrix} = [T_s] + [T_d] + [T_v], \tag{1}$$

where T_{12}^* is the complex conjugate (Fluhrer et al., 2022). The volume component is defined by

$$[T_v] = \frac{f_v}{2 + 2A_p^2} \begin{bmatrix} V_{11} & V_{12} & 0 \\ V_{12}^* & V_{22} & 0 \\ 0 & 0 & V_{33} \end{bmatrix}, \tag{2}$$

where f_v is the volume scattering intensity, A_p $[-]$ is the particle anisotropy, and V_{xx} $[-]$ are the parameters to estimate the volume component. The V_{xx} parameters are based on A_p and the width of the orientation angle distribution $\Delta\psi$, describing 'the degree of orientation of the vegetation volume from oriented ($\Delta\psi = 0°$) to random ($\Delta\psi = 90°$)' (Fluhrer et al., 2022). Similar to the study of (Fluhrer et al., 2022), realistic parameter spaces for both variables are used, with $A_p \in [0, 1]$ and $\Delta\psi \in [0°, 90°]$. Further, all $A_p - \Delta\psi$ combinations leading to negative powers are excluded in further analyses. This way, multiple, valid vegetation representatives ensure an improved removal of the vegetation component. Lastly, the eigen-based soil scattering angle α_s^{SAR} can be estimated:

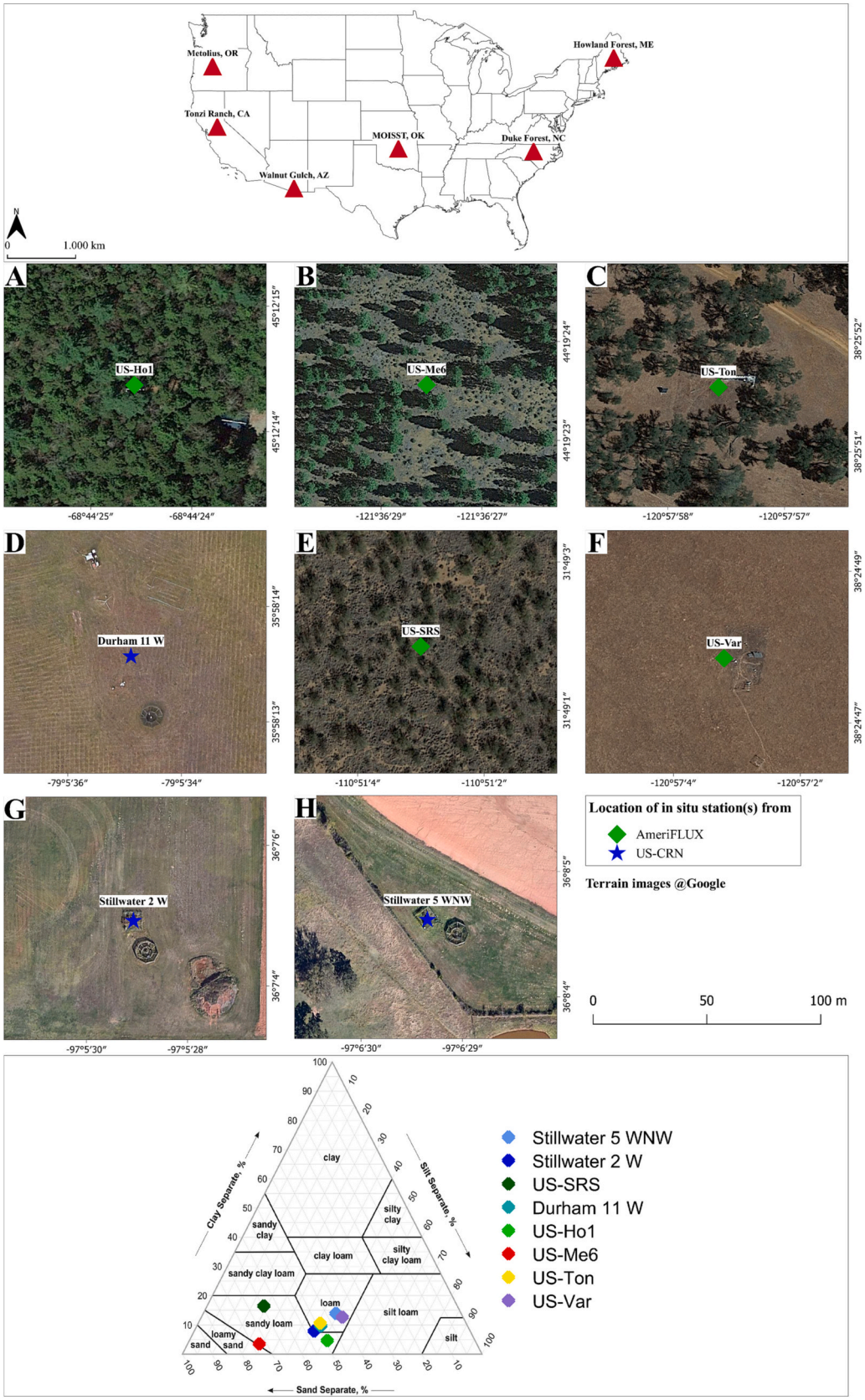

Fig. 1. Overview of employed *in situ* measuring stations at AirMOSS monitoring sites in the U.S.: (A) US-Ho1, Howland Forest, ME. (B) US-Me6 (Metolius Young Pine Burn), Metolius, OR. (C) US-Ton, Tonzi Ranch, *CA*. (D) Durham 11 W, Duke Forest, NC. (E) US-SRS (Santa Rita Savanna), Walnut Gulch, AZ. (F) US-Var (Vaira Ranch Ione), Tonzi Ranch, *CA*. (G) Stillwater 2 W, MOISST, OK. (H) Stillwater 5 WNW, MOISST, OK. Political state boundaries on the top of the U.S. are from (Homeland Infrastructure Foundation-Level Data (HIFLD), 2012). The soil texture triangle at the bottom (modified after (Sandrock and Afshari, 2016)) show indications on soil textures for every station (Table 1).

Table 1
Information on AirMOSS monitoring sites and *in situ* measuring stations.

AirMOSS site	Amount of dates (2013/2014/2015)	climate	*In situ* station	*In situ* network	NLCD Land Cover Class	Soil texture (Fig. 1)
Howland Forest, ME	21 (8/8/5)	Dfb	US-Ho1	AmeriFlux (Hollinger, 2021)	Evergreen Needleleaf Forests	Sandy Loam
Duke Forest, NC	22 (8/10/4)	Cfa	Durham 11 W	US-CRN	Pasture / Hay	Loam
Metolius, OR	21 (5/7/9)	Csb	US-Me6	AmeriFlux (Law, 2021)	Evergreen Needleleaf Forests	Sandy Loam/ Loamy Sand
MOISST, OK	19 (6/9/4)	Cfa	Stillwater 2 W Stillwater 5 WNW	US-CRN	Grassland / Herbaceous	Sandy Loam/ Loam Loam
Tonzi Ranch, CA	13 (3/6/4)	Csa	US-Ton US-Var	AmeriFlux (Ma et al., 2021) AmeriFlux (Ma et al., 2022)	Woody savanna Grassland	Loam
Walnut Gulch, AZ	15 (5/4/6)	BSk	US-SRS	AmeriFlux (Vivoni, 2022)	Woody Savanna / Shrubland	Sandy Loam

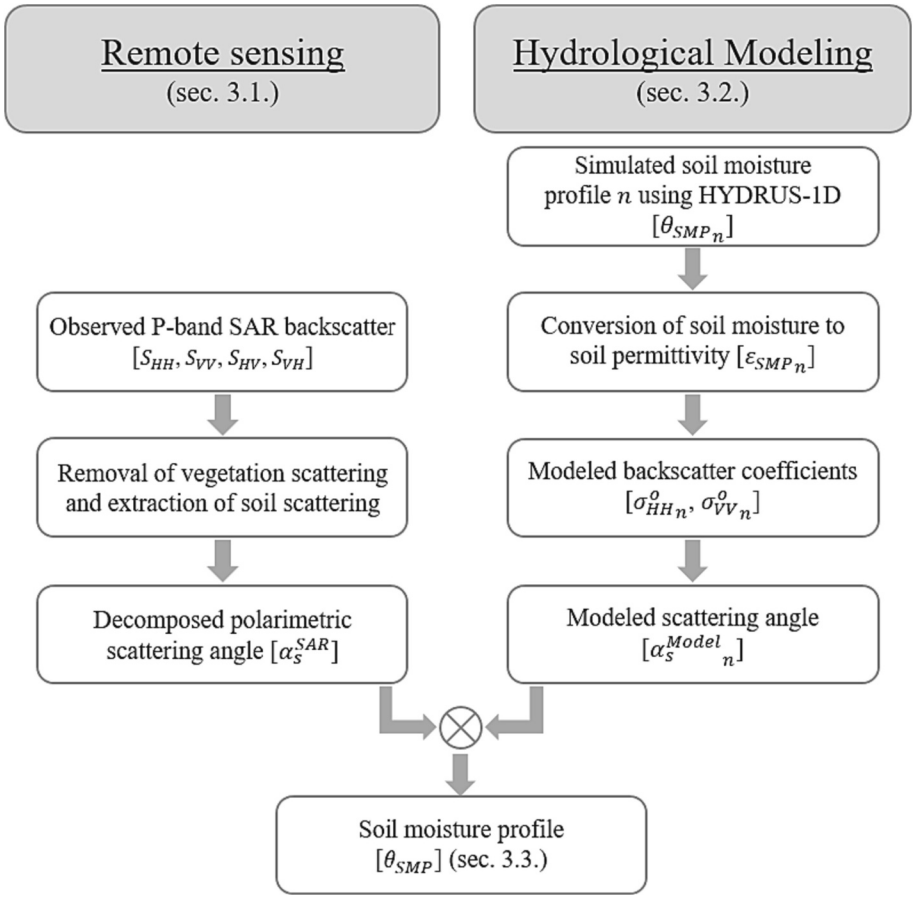

Fig. 2. Flow chart of the proposed joint technique combining remote sensing and soil (hydrological) modeling for estimation of soil moisture profiles.

$$\alpha_s^{SAR} = acos\left(\left(1 + 4^*\left(\frac{T_{12}^* - f_v V_{12}}{T_{11} - T_{22} - f_v V_{11} + f_v V_{22} - \sqrt{RT}}\right)^2\right)^{-\frac{1}{2}}\right), \quad (3)$$

with $RT = \left|T_{11}^2 + \left(T_{22} + f_v V_{11}\right)^2 + 4\left(T_{12} - f_v V_{12}\right)\left(T_{12}^* - f_v V_{12}\right) - 2T_{11}\left(T_{22} + f_v(V_{11} - V_{22})\right) - 2f_v\left(T_{22} + f_v V_{11}\right)V_{22} + f_v^2 V_{22}^2\right|$ (Fluhrer et al., 2022). For more details on the hybrid decomposition and removal of the vegetation component, the reader is referred to (Fluhrer et al., 2022; Jagdhuber et al., 2015).

In summary, for every observed SAR signal, one α_s^{SAR} is estimated from the soil scattering component after removing the dihedral and volume scattering components.

3.2. Modeled soil scattering angle based on coupled HYDRUS-1D and multi-layer SPM simulation

The HYDRUS-1D (Šimůnek et al., 2013) soil hydraulic model is used for simulating one-dimensional water flow with heat and vapor transport in variably saturated, homogeneous soils. The model numerically solves a modified version of the Richards equation by using the linear finite element method (Šimůnek et al., 2013):

$$\frac{\partial\theta}{\partial t} = \frac{\partial}{\partial x}\left[K\left(\frac{\partial h}{\partial x} + cos\alpha\right)\right] - S, \tag{4}$$

where θ is the volumetric water content [L^3/L^3], t is the time [T], x is the spatial coordinate [L], h as the soil matric potential [L], α giving the flow direction (= 0 [°] for vertical flow), S is the sink term [$L^3/L^3/T$] to account for root water uptake, and K is the unsaturated hydraulic conductivity function [L/T]. For simulations, the soil hydraulic properties, the soil water retention, $\theta(h)$, and soil hydraulic conductivity, $K(h)$, functions are given by the Van Genuchten-Mualem analytical model, which uses the statistical pore-size distribution model of (Mualem, 1976):

$$\theta(h) = \begin{cases} \theta_r + \dfrac{\theta_s - \theta_r}{[1 + |\alpha h|^n]^m} & h < 0 \\ \theta_s & h \geq 0 \end{cases}, \tag{5}$$

$$K(h) = K_s S_e^l \left[1 - \left(1 - S_e^{1/m}\right)^m\right]^2, \tag{6}$$

$$S_e = \frac{\theta - \theta_r}{\theta_s - \theta_r}, \tag{7}$$

where θ_r and θ_s are residual and saturated water contents [L^3/L^3], K_s is the saturated hydraulic conductivity [L/T], S_e is the effective saturation [−] given by (7), α is the inverse of the air-entry value (or bubbling pressure) [L^{-1}], n is the pore-size distribution index [−], $m = 1 - 1/n$, and l is the pore-connectivity parameter [−], which is assumed to be equal and set to 0.5 (Mualem, 1976). The Van Genuchten-Mualem parameters for every simulation are calculated in this study based on the pedotransfer function (PTF) of (Tóth et al., 2015) and input parameters from SoilGrids™ at 100 m spatial resolution (Nauman et al., 2017).

Additionally, to account for non-compensated water uptake by plant roots during simulations, the sink term S in (4) is calculated after the root-water uptake model from (Feddes et al., 1978), and the root water uptake stress response function after (Cai et al., 2018).

Within simulations, a non-uniform spatial variation of the potential extraction term is chosen by assuming a linearly decreasing water uptake distribution across the root zone (until assumed root depth) (Šimůnek et al., 2013). The assumed root depth, limiting the zone where root water uptake can occur within the vertical soil profile, was set at the soil depth of −1 m except for landcover class 'forests', where roots were assumed to expand across the entire soil profile. The heat transport parameters, namely the volume fraction of solid phase ($Q_n = 0.6\ [-]$) and organic matter ($Q_o = 0.0001\ [-]$), the longitudinal thermal dispersivity ($\lambda_L = 6\ [cm]$), and the heat capacities of solid phase ($C_n = 1.43327{*}10^{14}$), organic matter ($C_o = 1.8737{*}10^{14}$) and water ($C_w = 3.12035{*}10^{14}$) $[J/m^3/^\circ C]$, are fixed for all HYDRUS-1D simulations (Nakhaei and Šimůnek, 2014; Šimůnek et al., 2013). The parameters in the employed thermal conductivity function after (Chung and Horton, 1987), namely $b_1, b_2,$ and b_3 $[W/m/^\circ C]$, are depending on the respective sand, clay and silt fractions from SoilGrids™ (Nauman et al., 2017) for every SAR pixel.

The required meteorological and atmospheric input parameters at daily time scales, namely precipitation [mm], net solar radiation [MJ/m^2], sunshine hours [h], potential evaporation [mm], air temperature [°C], soil temperatures (for upper & lower boundary of the soil profile) [°C], average humidity [%], and wind speed [km/d], are taken from the *in situ* measuring stations (see Sec. 2.). Here, the number of sunshine hours per day was estimated from the measured incoming shortwave radiation. For that, the sum of hours per day, where the incoming shortwave radiation exceeded 120 $[W/m^2]$ (World Meteorological Organization, 2021) is calculated. The incoming shortwave radiation was taken from *in situ* measurements at every AmeriFlux station. For all other stations, namely Stillwater 2 W, Stillwater 5 WNW, and Durham 11 W (Table 1), the ERA5-land reanalysis product (Muñoz Sabater, 2019) is used.

Overall, the chosen simulation set-up in HYDRUS-1D assumes time-dependent atmospheric boundary conditions with variable runoff (Table 2) at the soil surface, and time-independent atmospheric boundary conditions with free drainage ($\partial h/\partial x = 0$) at the bottom of the profile. For heat transport, the first-type Dirichlet boundary condition at the soil surface (ponded infiltration) with zero gradient (continuous temperature profile) at the bottom was chosen. Further, no hysteresis in soil water retention and hydraulic conductivity is assumed, and initial water flow conditions are specified in terms of the soil matric potential (Šimůnek et al., 2013). For that, the absolute value of the minimum allowed soil matric potential on the soil surface is set to −100,000 [cm] (Cai et al., 2018), and the initial soil matric potential across the soil profile is kept variable (Table 2).

The HYDRUS-1D soil moisture profiles θ_{SMPn}, where n stands for one simulation within the ensemble, are always simulated on daily basis for one entire year with a three-month initialization period, in order to align initial conditions with given weather conditions. Lastly, a total of 101 simulation nodes, which were distributed non-linearly across the soil profile with decreasing density from the soil surface to the lower boundary of the determined soil column, have been defined. The input parameters that were kept flexible within simulations in order to minimize the amount of initial assumptions, and to calculate a variety of potentially occurring soil moisture profiles, are listed in Table 2. This means that for every *in situ* measuring station (Fig. 1, Table 1) and every AirMOSS acquisition year (2013 to 2015) 735 simulations were performed, respectively. All simulated HYDRUS-1D soil moisture profiles θ_{SMPn} are then converted to soil permittivity ε_{SMPn} according to the dielectric mixing model of (Mironov et al., 2009), and used as an ensemble input for backscatter simulations with the multi-layer SPM (Tabatabaeenejad and Moghaddam, 2006) (Fig. 2). Previous studies showed that at P-band, penetration depths between 10 cm to 30 cm soil depth are realistic for the investigated soil conditions in this study (Fluhrer et al., 2022; Konings et al., 2014). Hence, only the simulated soil moisture profile values of individual soil layers from the surface until a soil depth of 30 cm are considered for backscatter simulations in order to align with remotely sensed P-band SAR observations. For an assumed soil depth of 2 m during hydrological simulations, 36 individual soil moisture layers from the corresponding HYDRUS-1D simulation nodes between 0 and 30 cm are considered for backscatter simulations with the multi-layer SPM. For an assumed soil depth of 4 m, 24 individual soil moisture layers are considered (Table 3). This assumption on maximum soil depth of 30 cm for comparison is reasonable although, of course, the penetration depth of P-band SAR signals varies with different soil and vegetation cover conditions (*i.e.*, moisture, texture, density, *etc.*). It can be further improved in the future when sufficient information on penetration depths are available.

The first-order solution of the multi-layer SPM computes backscatter coefficients σ^o_{pp} from multiple subsurface layers by considering "multiple scattering processes between the boundaries" (Tabatabaeenejad and Moghaddam, 2006), suitable for analyzing P-band soil interactions. The required input parameters for modeling $\sigma^o_{pp}n$ and their respective values,

Table 2
Static values of input parameters for HYDRUS-1D soil moisture profile simulations.

HYDRUS-1D input parameter	Static values
Depth of soil profile [m]	2, 4
Maximum allowed soil matrix potential at the soil surface [cm]	0, −1, −5, −10
Initial soil matric potential across the soil profile [cm]	−250, −500, −1000, −2000, −4000, −8000, −16,000
Distribution of the initial soil matric potential across the soil profile [−]	Static, decreasing
Upper boundary condition for water flow [−]	Runoff, zero runoff (water can accumulate at the surface)

Table 3
Required input parameters for the multi-layer SPM to simulate $\sigma^o_{pp}n$, with the applied values in this study.

Parameter	Value
Frequency, f [MHz]	430
Number of layers, N [−]	36 (for soil profile depth of 2 m), 24 (for soil profile depth of 4 m)
Incidence angle in range, ϕ_i, and azimuth, φ_i [°]	ϕ_i from AirMOSS; $\varphi_i = 0$
Scattering angle in range ϕ_s, and azimuth, φ_s [°]	$\phi_s = \phi_i$; $\varphi_s = 180$ (backscattering)
z-coordinates of the respective boundary layers [cm]	Increasing from $\lambda/10$ (6.97) at the soil surface to $\lambda/2$ (34.86) at the profile bottom
Surface roughness parameters of each layer i [cm] (RMS height s, correlation length l)	s_i and l_i are dependent on a roughness indicator derived from TanDEM-X (Table 4)
Autocorrelation function, ACF [−]	Exponential
Permittivity ε_{SMPn} of each layer i [−]	From HYDRUS-1D simulated and converted soil permittivity profiles ε_{SMPn_i}

approximated for the acquisition scenario in this study, are listed in Table 3.

Due to the fact that no roughness information for any soil layers are available for the AirMOSS monitoring sites or *in situ* measuring stations, the DLR TanDEM-X DEM at 90 m resolution (Rizzoli et al., 2017) was used to get first-order roughness indicators for every SAR pixel. For that, the TanDEM-X elevations were converted with the GDAL DEM utility algorithm (GDAL/OGR contributors, 2021) in QGIS© (QGIS Development Team, 2021) to roughness values, giving the degree of irregularity of the surface, and scaled to the employed AirMOSS wavelength at P-band ($\lambda = 69.72$ [cm]) to account for the reduced impact of surface roughness at P-band than at X-band. Thus, depending on the estimated roughness indicator R_{TDX} (Table 4, left column) for every SAR pixel, typical surface roughness parameter sets for each layer i (Table 4, right column) are fixed as input for the multi-layer SPM to account for varying layer roughness (from smooth to rather rough).

The modeled $\sigma^o_{pp}n$ [−], for horizontal and vertical polarization, are then used to calculate for every simulation the model-based $\alpha_s^{Model}n$ after (Cloude, 2010), valid for $0 \leq \alpha_s \leq \frac{\pi}{2}$:

$$\alpha_s^{Model}n = tan^{-1}\left(\frac{\sigma^o_{HH}n - \sigma^o_{VV}n}{\sigma^o_{HH}n + \sigma^o_{VV}n}\right). \quad (8)$$

3.3. Joint technique of remote sensing and hydrological modeling for soil moisture profile estimation

From remote sensing, one α_s^{SAR} value for every resolution cell and recording date can be estimated (see Sec. 3.1.). From soil hydrological modeling, an ensemble of $\alpha_s^{Model}n$ for n simulations can be calculated for every resolution cell and recording date based on varying initial settings (see Sec. 3.2.). In order to determine the most suited soil moisture profile for every resolution cell and recording date, the observed remote sensing information is compared with all hydrological modeling outputs. In detail, the actual observed α_s^{SAR} from measured SAR observations is used to select the most suited soil moisture profile from hydrological modeling. The smallest absolute differences between α_s^{SAR} and all $\alpha_s^{Model}n$ is then used to estimate the final soil moisture profile:

$$\theta_{SMP} = argmin\left(\left|\alpha_s^{SAR} - \alpha_s^{Model}n\right|\right) \quad (9)$$

In Fig. 3A, the ensemble of simulated soil moisture profiles θ_{SMPn}, based on HYDRUS-1D, are displayed at station US-SRS, Walnut Gulch, AZ, on the 12th of July in 2014. It can be seen that the different assumptions on initial model conditions lead to various soil moisture profile shapes. For every simulated soil moisture profile θ_{SMPn}, the procedure described in Sec. 3.2. is applied to obtain the model-based $\alpha_s^{Model}n$. Finally, the best fit between α_s^{SAR} and all $\alpha_s^{Model}n$ is estimated (Fig. 3B). A sensitivity study was conducted to analyze the estimation procedure regarding potential multiple solutions and uncertainties of the best fit. It was found that the method estimates the global minimum (always only one single best fit) with 2nd best and higher best fits deviating at least 1.75% from the best one. In the end, the comparison of the SAR-extracted soil information is indicative for selecting the appropriate soil moisture profile. For one, the estimated θ_{SMP} profile fits best to *in situ* measurements (green stars in Fig. 3B). Second, although the upper soil moisture conditions cannot be confirmed by *in situ* observations, the decrease in soil moisture values between 0 cm and 3.8 cm soil depth match the apparent soil and meteorological conditions, as described in detail in Sec. 4.

Table 4
Surface roughness parameter sets for each layer i (RMS height s, correlation length l; step size equals number of layers) within the multi-layer SPM based on TanDEM-X derived roughness indicators R_{TDX}.

Roughness Indicator From Tandem-X [M]	Input Roughness Parameters [CM]
$R_{TDX} < 5$	$s_i = 0.5 - 0$; $l_i = 30 - 60$
$5 \leq R_{TDX} < 10$	$s_i = 1.5 - 0.75$; $l_i = 25 - 50$
$10 \leq R_{TDX} < 15$	$s_i = 2 - 1$; $l_i = 20 - 40$
$R_{TDX} \geq 15$	$s_i = 3 - 1.5$; $l_i = 15 - 30$

4. Results

In this study, the Pearson's coefficient of determination R^2, the unbiased root mean square error (*ubRMSE*), giving the error between curves without the mean bias (Maity, 2022), and the Fréchet distance F (Fréchet, 1906), representing the curve shape similarity, are employed for statistical analyses. F provides the similarity of curves taking into account not only absolute values but also the ordering of points along the investigated curves (Eiter and Mannila, 1994). Further, since auxiliary products are only available at discrete soil depths (*i.e.* symbols in Fig. 4), a polynomial function of 2nd order is applied to combine these values in order to estimate the approximate profile shapes for comparison. Although it is known that polynomials are physically unrealistic and can only give an approximate of the vertical soil moisture variability (see Sec. 1.), it is used in this study to be able to compare not only results at two to three discrete measuring depths but also across the entire soil column to evaluate the shape of the estimated soil moisture profiles.

In total, three types of typical soil moisture profiles could be observed within all estimated results, depending on prior precipitation events and soil conditions. As shown in Fig. 4A, a typical drying profile with increasing soil moisture at increasing soil depths was estimated when, at the respective station, no precipitation occurred at least seven days prior to the recording date. The soil dries at different rates, according to the soil type and texture, from the soil surface towards deeper soil layers. In contrast, a typical wetting profile could be observed when, at this station, precipitation occurred some days before the recording date (Fig. 4B). The soil moisture profile decreases with increasing soil depth since the water infiltrates from the soil surface downwards to the deeper soil layers. The depth of the inflection point varies depending on the infiltration rate and elapsed time since the rain event. In the presented example, the decrease in soil moisture values at the top (from 0 cm to −4.5 cm) of the soil is rather rapid and the profile below is rather dry at ~18 vol% because of the local conditions around the station US-SRS. At this station in Arizona an (hyper-)arid climate with warm summers led to predominantly shrublands on top of sandy loam soils (62% sand fraction, ~19% silt and clay fractions) (Fig. 1, Sec. 2.). This means, precipitation is less frequent and water can infiltrate rather quickly into the uppermost soil layers. At other stations with different soil and landcover conditions, *e.g.* at the forest station US-Ho1, the decrease in soil moisture values was less rapid and more continuous.

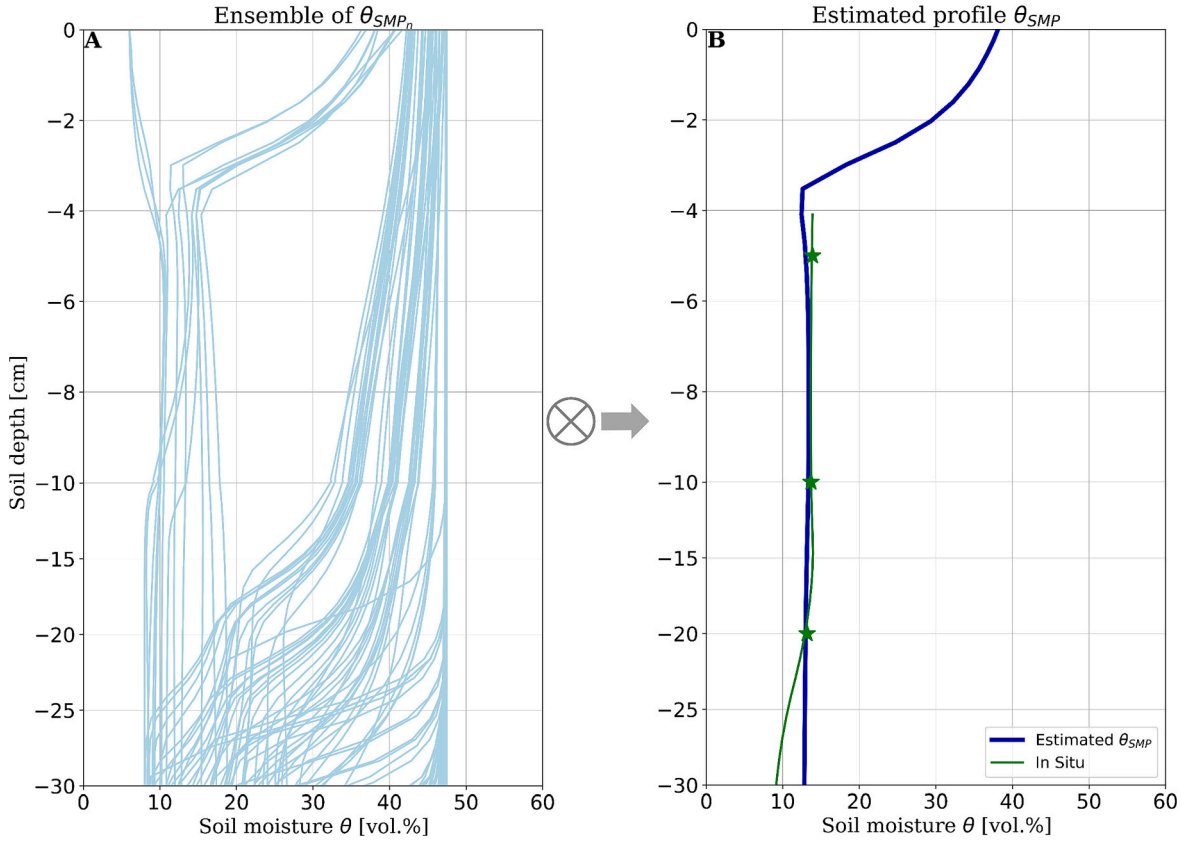

Fig. 3. Visualization of the estimation procedure to determine the best fitting soil moisture profile $\boldsymbol{\theta_{SMP}}$ from all simulated $\boldsymbol{\theta_{SMP_n}}$ by comparing SAR observations with soil modeling. (A) Ensemble of simulated $\boldsymbol{\theta_{SMP_n}}$ from HYDRUS-1D based on varying initial conditions (Table 2, Sec. 3.2.) at station US-SRS, Walnut Gulch, AZ, on the 12th of July 2014. (B) Estimated soil moisture profile $\boldsymbol{\theta_{SMP}}$ at station US-SRS, Walnut Gulch, AZ, on the 12th of July 2014, in comparison to *in situ* observations from the same day.

Lastly, saturated profiles at higher moisture values with almost no variation across the vertical soil column were estimated after heavy precipitation events prior to the recording date (Fig. 4C). Unfortunately, no soil moisture comparison data could be found for soil depths between 0 to −5 cm to confirm the upper conditions. However, it can be seen that all three estimated profiles from the proposed method (SAR with hydrological modeling) fit best to the *in situ* measurements with overall highest correlation coefficients, lowest *ubRMSE* and smallest Fréchet distances, hence, highest similarity not only in absolute values but also in profile shape along the vertical soil column (Table 5, upper rows). Further, statistics are overall better between estimated profiles and *in situ* measurements compared to statistics between *in situ* measurements and auxiliary products (ERA5-land, AirMOSS L4) (Table 5, lower rows). While significantly high $R^2 \geq 0.93$ are found between estimated soil moisture profiles and *in situ* measured profiles, overall lower $R^2 \leq 0.64$ are found between *in situ* measurements and auxiliary products. Correspondingly, overall higher *ubRMSE* and *F* are found, except for the wetting profile at station US-SRS (Fig. 4b), where the same *ubRMSE* of 1 vol% for all comparisons and slightly better *F* between *in situ* measurements and the AirMOSS L4 product are found (Table 5).

In this study, soil moisture profiles are only shown from the soil surface until a depth of 30 cm, since this part of the simulated soil moisture profiles are used for comparison with P-band SAR observations (see Sec. 3.2.). In the following, soil moisture profiles are presented first for all measuring stations (see Sec. 4.1.), and then detailed analyzes are performed at two selected stations (see Sec. 4.2.).

4.1. Soil moisture profile results for all measuring stations

In Figs. 5 and 6, estimated soil moisture values between 0 cm to −30 cm soil depth for all available AirMOSS dates are compared with corresponding auxiliary profiles. Here, individual plots of kernel density estimates show the conditional distribution of values with indications on the density of values (the darker the color, the higher the amount of values) and the fitted linear regression (solid line). First, the measuring stations with landcover types forest (Fig. 5, 1st and 2nd row), woody savanna (Fig. 5, 3rd row) or shrublands (Fig. 5, 4th row) are displayed (Fig. 1, Sec. 2.). Noticeable is the overestimation of soil moisture values from all three auxiliary products at the two forest stations, with more significant overestimation at the more homogeneously vegetated station, US-Ho1, covered by dense forests (Fig. 5, 1st row). At the less densely vegetated forest station, US-Me6 (Fig. 1, Sec. 2.), estimated soil moisture values range between 10 vol% and 38 vol%, while *in situ* measurements only indicate values between 2 vol% and 22 vol%. Here, the rather dry *in situ* measured values (highest density at 6.9 vol%) are overestimated with the proposed approach, similar to the ERA5-land product. In contrast, good agreement between estimated values and the AirMOSS L4 product can be observed, with highest density of values around the 1:1 line (Fig. 5, 2nd row). Further, at the woody savanna station, US-Ton, the highest density of values is located close to the 1:1 line, with a slight overestimation of rather dry *in situ* measurements and ERA5-land values. Noticeable at this station are the two additional, very dominant accumulations of values.

One at low estimated soil moisture values around 18 vol% and high *in situ* measurements around 37 vol%. And one around the 1:1 line between 35 vol% and 40 vol%. This means, correlations between estimated and *in situ* measured soil moisture values increase, when *in situ* measured values increase, but with some exceptions, where higher field measurements are in turn underestimated with the proposed approach (Fig. 5, 3rd row). Unfortunately, no AirMOSS L4 soil moisture profiles

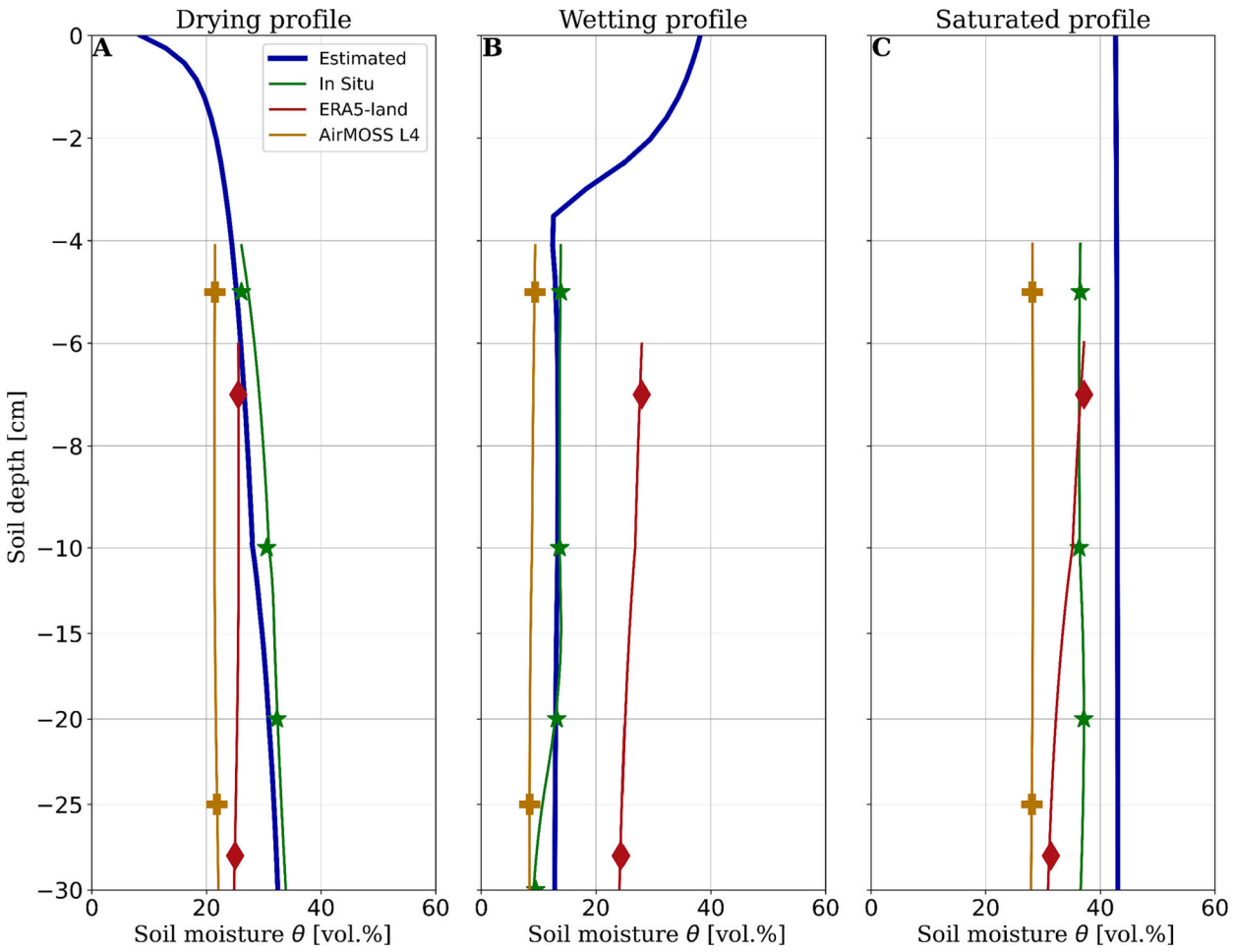

Fig. 4. Typical profile shapes of estimated soil moisture profiles based on the proposed approach in comparison with auxiliary soil moistures products of the same day. (A) Drying profile on the 21st of October 2014 at station Stillwater 2 W, MOISST, OK (no precipitation). (B) Wetting profile on the 12th of July 2014 at station US-SRS, Walnut Gulch, AZ (51.6 mm of precipitation in the week before the recording date). (C) Saturated profile on the 17th of June 2013 at station Stillwater 5 WNW, MOISST, OK (in total 57.6 mm of precipitation two days before the recording date). The y-axis is stretched between 0 cm and − 10 cm to emphasize the most dynamic part of the soil moisture profile.

Table 5
Statistical measures between estimated (upper rows) or *in situ* measured (lower rows) soil moisture profiles and auxiliary profiles displayed in Fig. 4.

Statistical measure	Drying profile			Wetting profile			Saturated profile		
	Estimated *vs.*			**Estimated *vs.***			**Estimated *vs.***		
	In Situ	**ERA5**	**AirMOSS L4**	***In Situ***	**ERA5**	**AirMOSS L4**	***In Situ***	**ERA5**	**AirMOSS L4**
R^2 [−]	0.95	0.71	0.61	0.93	0.64	0.57	0.95	0.58	0.22
ubRMSE [vol%]	0.3	1.2	1.6	1	1.1	2.1	0.3	2	0.1
F [−]	0.02	0.08	0.1	0.08	0.1	0.09	0.07	0.1	0.2
	In situ vs.			***In situ vs.***			***In situ vs.***		
	ERA5		**AirMOSS L4**	**ERA5**		**AirMOSS L4**	**ERA5**		**AirMOSS L4**
R^2 [−]	0.61		0.45	0.59		0.37	0.64		0.13
ubRMSE [vol%]	2		2	1		1	2		0
F [−]	0.09		0.12	0.15		0.05	0.06		0.09

are available at this station and two others (Fig. 6). Lastly, at the desert station US-SRS in Arizona, similar patterns as describe before can be seen. While estimated soil moisture values range between 10 vol% and 45 vol%, *in situ* measurements range between 10 vol% and 20 vol%. Again, the estimated values overestimate the rather dry *in situ* measurements (highest density at 8.8 vol%), similar as to the AirMOSS L4 product, which, at this station, shows the smallest value range of all (between 8.4 vol% to 17.3 vol%). Only the ERA5-land product achieves similar value ranges compared to the estimated values, with the highest density of values deviating approximately 6 vol% from the perfect fit (1:1 line) (Fig. 5, 4th row).

When analyzing all results at the pasture station Durham 11 W (Fig. 6, 3rd row), most estimated and *in situ* measured soil moisture values are close to the 1:1 line, with a tendency to an overestimation of

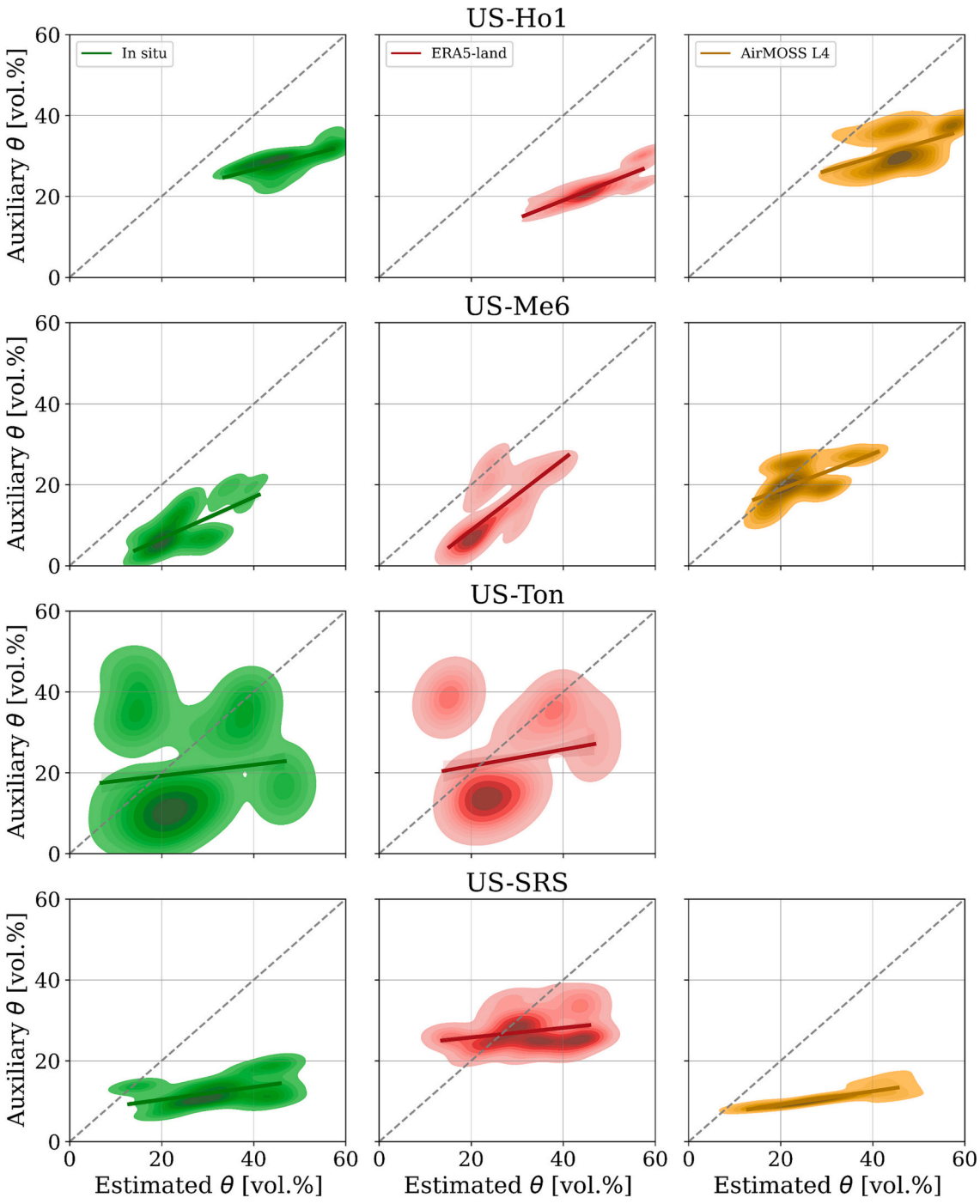

Fig. 5. Comparison of estimated soil moisture values for all layers from soil depths between 0 cm to −30 cm, with auxiliary soil moisture products of the corresponding same recording day (including all AirMOSS overflight dates between 2013 and 2015). 1st row: US-Ho1, Howland Forest, ME. 2nd row: US-Me6, Metolius, OR. 3rd row: US-Ton, Tonzi Ranch, *CA*. 4th row: US-SRS, Walnut Gulch, AZ.

estimated moisture values for decreasing *in situ* measurements. In contrast, the comparison between estimated values and the ERA5-land product shows a slight underestimation, as most ERA5-land soil moisture values are in the range of 38 vol% to 42 vol%, whereas most estimated values range between 22 vol% and 40 vol% (Fig. 6, 3rd row). Lastly, analyzing the results at the two grassland and one shrubland station (Fig. 6, 1st, 2nd and 4th row) similar results as those for the previously described stations can be seen, except for the station Stillwater 2 W in Oklahoma (Fig. 6, 2nd row). Here, estimated and *in situ* measured soil moisture values are closest to the 1:1 line with lowest deviations, confirmed by the overall highest correlation of all stations with a R^2 of 0.92 (Table 6). Similar to the first station at the AirMOSS site Tonzi Ranch, US-Ton (Fig. 5, 3rd row), the second shrubland station US-Var also shows a large variety in soil moisture values with several accumulation spots (Fig. 6, 4th row). The highest density of estimated and *in situ* measured values, however, are located at the 1:1 line, which explain the clearly higher R^2 of 0.81 compared to the R^2 of just 0.59 at US-Ton.

Further, compared to all other stations, these two stations in California show the overall highest *ubRMSE* of 2.9 vol% and 3.7 vol%, respectively (Table 6). In Table 6, the statistical measures between estimated soil moisture profiles and the corresponding auxiliary products (upper rows) as well as between *in situ* measurements and ERA5-

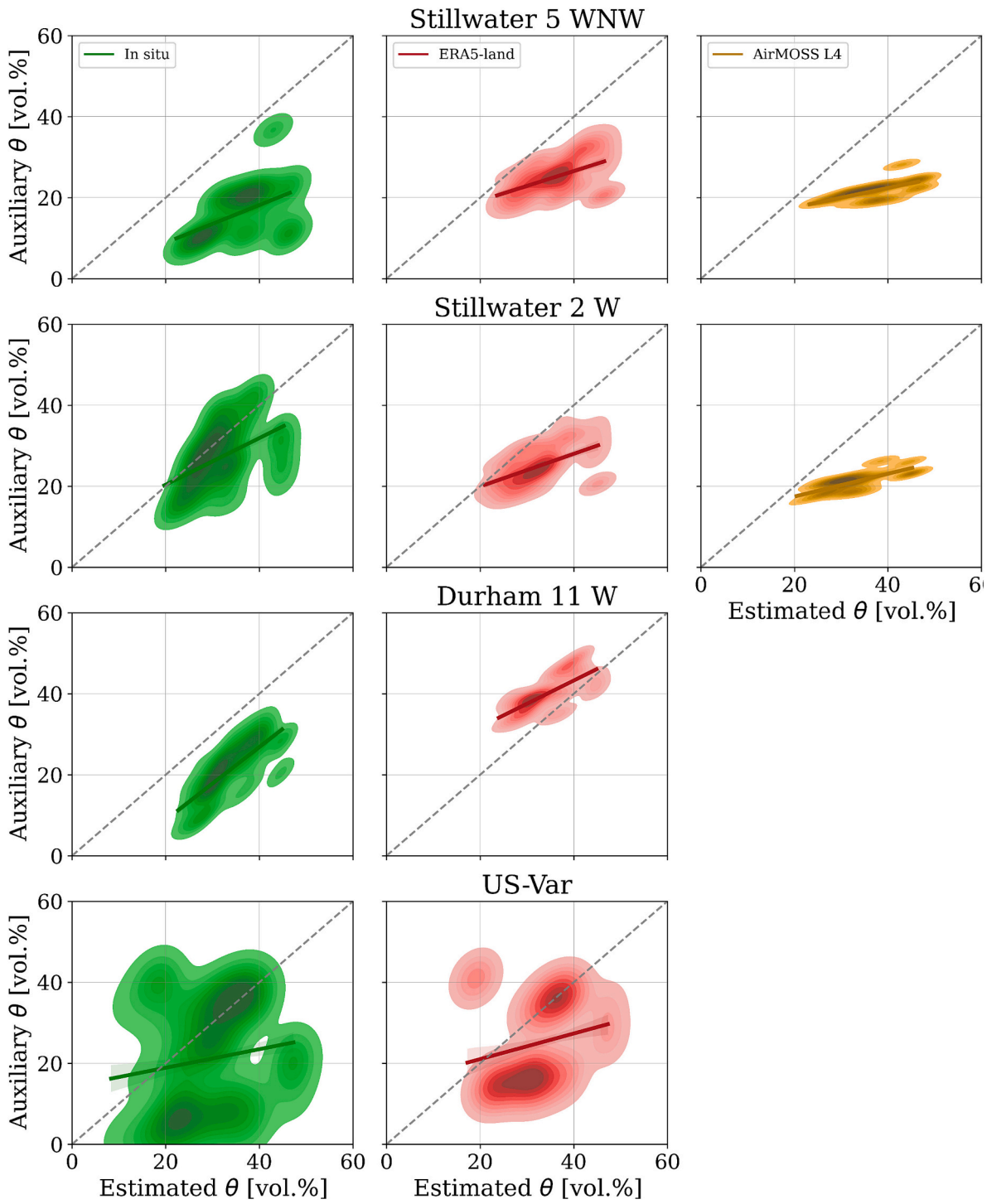

Fig. 6. Comparison of estimated soil moisture values for all layers from soil depths between 0 cm to −30 cm, with auxiliary soil moisture products of the corresponding same recording day (including all AirMOSS overflight dates between 2013 and 2015). 1st row: Stillwater 5 WNW, MOISST, OK. 2nd row: Stillwater 2 W, MOISST, OK. 3rd row: Durham 11 W, Duke Forest, NC. 4th row: US-Var, Tonzi Ranch, *CA*.

land or AirMOSS L4 products (lower rows) are displayed. In general, when comparing the estimated soil moisture profiles with all auxiliary products, the R^2 varies between 0.32 and 0.94, the *ubRMSE* ranges from 0.7 vol% to 3.7 vol%, and the *F* varies between 0.07 and 0.26 [−]. In detail, the overall highest R^2, lowest *ubRMSE* and smallest *F* are found between estimated soil moisture profiles and the ERA5-land product. This simply means, that the proposed method and the reanalysis method for soil moisture estimation agree well for soil depths between −7 cm and − 30 cm (ERA5-land values are available for −7 cm and − 28 cm), where changes in the soil moisture profile are less prominent (see Sec. 1).

With focus on the *in situ* observations, R^2 between 0.48 and 0.92 are reached in comparison with the estimated soil moisture profiles. Further, *F* varies between 0.1 and 0.23 [−], overall confirming the high similarity in profile shapes along the vertical soil column, since *F* varies in total between 0 (identical lines) and 0.4 (no similarity between lines) in this study. In absolute values (*ubRMSE* varying between 1.4 vol% and 3.7 vol%) the estimated results deviate from the *in situ* measured soil

Table 6
Statistical measures between estimated (upper rows) or *in situ* measured (lower rows) soil moisture profiles from 0 cm to −30 cm soil depth and auxiliary products at all measuring stations and all available AirMOSS dates. R^2 gives Pearson's coefficient of determination, *ubRMSE* the unbiased error, and *F* the Fréchet distance.

Statistical measure	Estimated results *vs.*	Station							
		US-Ho1	US-Me6	US-Ton	US-SRS	Durham 11 W	Stillwater 5 WNW	Stillwater 2 W	US-Var
R^2 [−]	*In situ*	0.52	0.71	0.59	0.49	0.48	0.59	0.92	0.81
	ERA5-land	0.78	0.87	0.79	0.9	0.76	0.89	0.94	0.88
	AirMOSS L4	0.32	0.49		0.81		0.76	0.86	
ubRMSE [vol%]	*In situ*	1.84	1.38	3.69	2.47	1.86	1.61	2.89	2.92
	ERA5-land	1.05	0.95	0.77	1.47	1.41	1.05	1.32	1.46
	AirMOSS L4	1.67	1.65		1.88		0.71	1.29	
F [−]	*In situ*	0.22	0.17	0.19	0.23	0.13	0.22	0.1	0.19
	ERA5-land	0.26	0.13	0.12	0.1	0.09	0.13	0.1	0.13
	AirMOSS L4	0.17	0.07		0.21		0.17	0.14	
	In situ results vs.								
R^2 [−]	ERA5-land	0.53	0.69	0.89	0.43	0.53	0.66	0.9	0.56
	AirMOSS L4	0.62	0.41		0.52		0.54	0.79	
ubRMSE [vol%]	ERA5-land	1.32	1.48	0.77	1.4	2.45	1.06	3.37	1.38
	AirMOSS L4	1.2	1.9		1.13		1.5	3.88	
F [−]	ERA5-land	0.08	0.06	0.05	0.17	0.21	0.11	0.1	0.07
	AirMOSS L4	0.07	0.16		0.02		0.08	0.13	

moisture profiles. However, the overall profile shapes are very well captured with this approach. The reasons why the *in situ* measurements fit a bit less to the estimated profile results (compared to the ERA5-land results) are, on the one hand, because they are constantly really low. For example, at the forest station US-Me6 in Oregon no *in situ* measured soil moisture value exceeds 24 vol%, and in average a soil moisture value of just 9.5 vol% was observed. On the other hand, because they vary quite much along the profile, indicating a high change in soil moistures within only a few cm of soil depth. Here, the highest change within *in situ* measured soil moisture values are observed at the forest station US-Me6 with a change of 13.2 vol% between −10 cm (7.1 vol%) and − 30 cm (20.3 vol%) soil depth. Further, in average soil moisture differences of 6.3 vol% within just 20 cm soil depth (between −10 cm and − 30 cm) are measured at this station across all dates.

Lastly, comparing estimated soil moisture profiles with the AirMOSS L4 product, the lowest R^2 of all stations and products can be found at the forest station US-Ho1. Here, the AirMOSS L4 product almost always significantly underestimates the estimated profiles. This is exacerbated by the fact, that the AirMOSS L4 products almost always leads to more or less uniform soil moisture profiles, showing no changes is soil moisture values across the vertical soil column, as displayed in the three examples of Fig. 4.

For comparison, additional statistics between *in situ* measurements and the two auxiliary soil moisture products are conducted. At some stations, the statistics between *in situ* measurements and the ERA5-land or AirMOSS L4 product are better (*i.e.*, US-Ho1), but at others not (*i.e.*, Stillwater 2 W). The slightly better performance of the two auxiliary products at the homogeneous forest station US-Ho1, with higher R^2 and lower *ubRMSE* and *F*, is the consequence of the already described overestimation of estimated values compared to the *in situ* measurements (Fig. 5, 1st row). Overall however, no clear pattern can be found when comparing the performance of statistics at all stations, dates and depths.

4.2. Detailed analyses at the two measuring stations US-Ho1 and Stillwater 2 W

In this section, results for estimated soil moisture profiles are

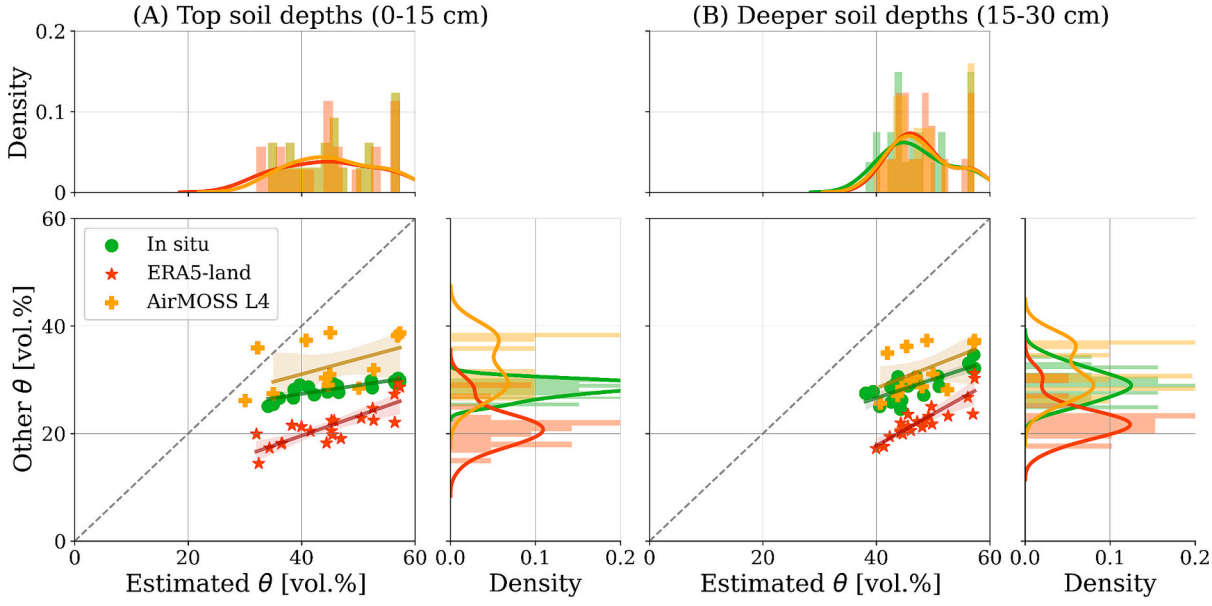

Fig. 7. Comparison of estimated soil moisture values between 2013 and 2015 at specific depths with auxiliary soil moistures products at monitoring stations US-Ho1, Howland Forest, ME. (A) Top soil depths (0–15 cm). (B) Deeper soil depths (15–30 cm).

analyzed in more detail at two selected stations, the most homogeneous forest station US-Ho1, and the grassland station Stillwater 2 W (Fig. 1 & Table 1, Sec. 2.).

In Figs. 7 and 8, auxiliary soil moisture values at actual measuring depths are compared to the respective estimated soil moisture values. The measuring depths are hereby divided into two groups, top soil and deeper soil depths. This way, different layers of the soil moisture profiles can be analyzed in addition. *In situ* measurements at station US-Ho1 are available from the AmeriFLX network at −10 cm and − 20 cm, and at station Stillwater 2 W from the US-CRN network at −5 cm, −10 cm, and − 20 cm soil depth (see Sec. 2.). ERA5-land soil moisture values are available for soil depths at −7 cm and − 28 cm, while the AirMOSS L4 product provides values for the integrals between 0 and 10 cm and 10–40 cm. For the latter, the average depths at −5 cm and − 25 cm were considered for comparison. This simplification does not affect the analyzes since the AirMOSS L4 product, as shown before, almost always results in more or less uniform soil moisture profiles (Fig. 4).

At the forest station, US-Ho1, estimated soil moisture values at deeper soil depths (Fig. 7B) overestimate auxiliary soil moisture products considerably more than estimated values at top soil depths (Fig. 7A). Here, results are almost always beyond 40 vol%, while auxiliary values mostly range between 20 vol% to 40 vol%. This is also supported by statistical measures since the R^2 between estimates and *in situ* measurements decreases from 0.68 for top soil depths to 0.61 for deeper soil depths. In contrast, the R^2 between estimates and ERA5-land or AirMOSS L4 values increases from 0.67 to 0.77 or 0.2 to 0.26 from top soil to deeper soil depths due to less variations within results. This is confirmed by the improved *ubRMSE* from 5.5 vol% to 2.7 vol% for ERA5-land, and from 6.5 vol% to 4.6 vol% for AirMOSS L4. Moreover, the probability density plots (PDFs) next to the scatterplots show that at this station the auxiliary products are not overlapping and deviate from another. The value ranges of the ERA5-land and AirMOSS L4 products hardly overlap with the *in situ* measured values at top soil depths (Fig. 7A). Only at deeper soil depths, the value ranges of the AirMOSS L4 product and the *in situ* measured ones converge (Fig. 7B).

In contrast, at measuring station Stillwater 2 W in Oklahoma, estimated values are overall closer to auxiliary values with always higher correlations for top soil values (Fig. 8). Here, the R^2 between estimates and *in situ* measurements decreases from 0.41 for top soil depths to 0.08 for deeper soil depths. Similar, the R^2 decreases from 0.43 for top soil depths to 0.15 for deeper soil depths between estimates and ERA5-land values, as well as from 0.58 for top soil depths to 0.55 for deeper soil depths between estimates and AirMOSS L4 values. Further, auxiliary products at this station are more overlapping since the value ranges clearly overlap with another as shown in the PDFs of Fig. 8. Only for deeper soil depths, the *in situ* measurements reach considerably higher values compared to the ERA5-land and AirMOSS L4 product (Fig. 8B).

5. Discussion

In this study, soil moisture profile shapes for drying, wetting and saturated soil conditions are estimated (Fig. 4, Sec. 4.). In order to obtain continuous soil moisture profiles, the decomposed SAR remote sensing scattering component of the soil is compared to soil hydrological simulations with HYDRUS-1D, converted to a soil scattering component by the multi-layer SPM scattering model. The comparison of the soil components is performed on the level of the polarimetric soil scattering angle α_s (see Sec. 3.). In previous studies, soil moisture retrieval approaches are mainly conducted on the level of backscattering, *e.g.* (Huang et al., 2021; Kim and Liao, 2021; Konings et al., 2014). This way, remotely sensed backscatter coefficient can be used without the preceding application of a decomposition technique. However, since SAR backscatter coefficients contain scattering mechanisms of all targets within the SAR footprint (soil, vegetation, and the combination of both), this circumstance in turn complicates the modeling of backscattering. In order to compare SAR backscatter coefficients with modeled backscatters, the combined soil and vegetation scattering has to be modeled first. Fortunately, in this study, only soil scattering has to be modeled since the decomposed soil scattering component of the total SAR signal is used for comparison. Certainly, the application of a decomposition method to extract the soil scattering from the SAR signal is not that simple and requires certain preconditions, like fully polarimetric SAR observations. However, as emphasized in Sec. 3., the comparison on the level of α_s instead of backscatters has several advantages (*e.g.*, no modeling of complex vegetation). Nevertheless, one of the main restrictions of this approach, for sure, is the correct removal of the vegetation component from the SAR signal. As outlined in many previous studies, *e.g.* (He et al., 2016; Jagdhuber, 2012; Sato et al., 2012; van Zyl et al., 2011), decomposition techniques tend to overestimate the vegetation scattering component, which leads to (physically impossible) negative

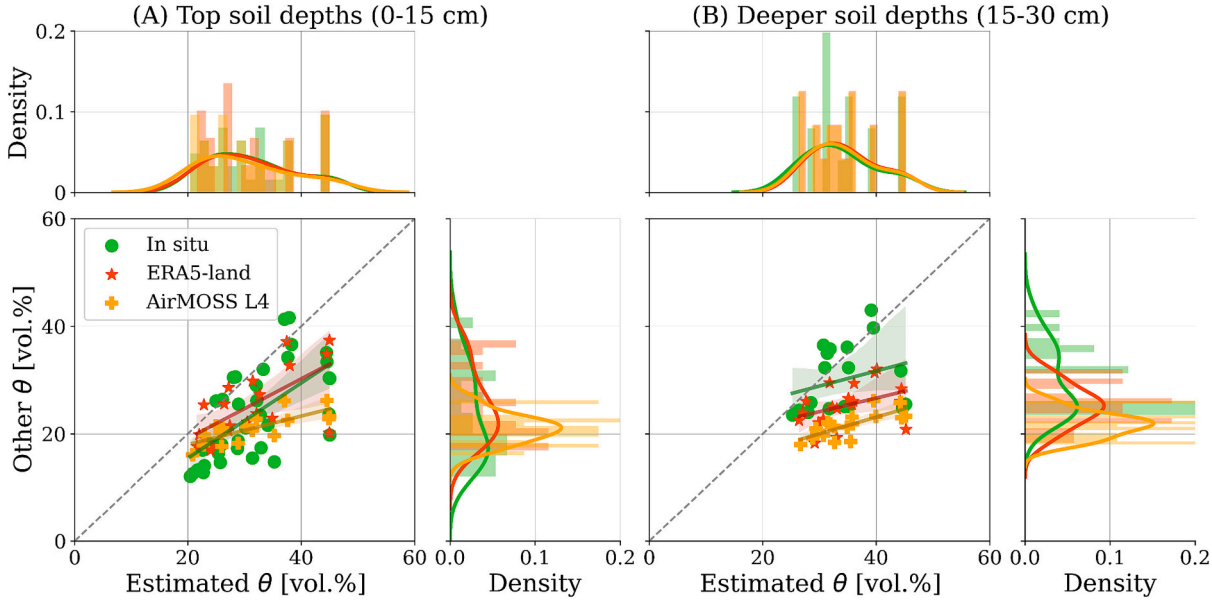

Fig. 8. Comparison of estimated soil moisture values between 2013 and 2015 at specific depths with auxiliary soil moistures products at monitoring station Stillwater 2 W, MOISST, OK. (A) Top soil depths (0–15 cm). (B) Deeper soil depths (15–30 cm).

decomposed powers (Fluhrer et al., 2022). Similar to the study of (Fluhrer et al., 2022), this problem is solved here by allowing multiple vegetation representations (see Sec. 3.1.), instead of fixing them to, for instance, 'a cloud of randomly oriented dipoles' (Alemohammad et al., 2018). This potential overestimation of vegetation during the decomposition is considered as one of the reasons why at the dense forest station US-Ho1 an overestimation of *in situ* measurements occurs (Fig. 5, Sec. 4.1.). Here, an improved removal of the vegetation scattering component by, for instance, including machine learning, may even decrease the overestimation of soil moisture profile estimates as indicated by (Fluhrer et al., 2022). Another reason could be that, as shown from (Fluhrer et al., 2022), in strongly vertically oriented vegetated areas, like the boreal forest at US-Ho1, the dihedral scattering mechanism is dominant in the total SAR signal. However, in this study the soil scattering mechanism is considered within the retrieval, which hence, may not be representative enough under dense and strongly oriented forests. This explanation is strengthend by the fact that at the other, less vegetated stations overall higher correlations with less pronounced overestimation are determined. Further, the highest correlation between estimates, based on this approach, and *in situ* measurements are found at the grassland station Stillwater 2 W (Sec. 4.). Also other studies, *e.g.* (Lucas et al., 2004; Moghaddam and Saatchi, 1995), outlined 'that at P-band the ground and trunks contribute with more relevance to the SAR signal than the branches and leaves'(Fluhrer et al., 2022), leading to dominant dihedral scattering components. However, using the dihedral scattering components instead of the soil scattering component is not an option for the proposed method. The main reason is that the estimation of soil moisture profiles with depth requires SAR observations from a comparable integral of the soil surface until the main scattering center within the soil. Here, the actual sensitivity depth of the soil part within the dihedral scattering component has to be further analyzed beforehand.

One of the advantages of the proposed approach is that profiles can be estimated more continuously along their vertical gradient and without the assumptions of empirical mathematical functions (*i.e.* polynomials of certain degree), *e.g.* (Etminan et al., 2020; Sadeghi et al., 2016; Tabatabaeenejad et al., 2015). As shown in the results section, no auxiliary soil moisture values could be found for continuous validation with soil depth since *in situ* measurements are done once between 0 and 5 cm soil depth or lower. However, this circumstance in turn emphasizes the need for the proposed approach (or similar ones), since it is able to provide continuous soil moisture profiles also for near-surface soil depths, and hence, capture this most variable uppermost part of soil moisture profiles more closely and reliable. This is of utmost importance since, as outlined in section one, near-surface soil moisture responds faster to environmenal changes because of, *e.g.*, precipitation or evaporation, and is more variable compared to subsurface soil moisture. Further, the approach provides the advantage that simulations are not restricted to a single model set-up. Admittingly, the simulation of an ensemble of soil moisture profiles for varying model set-ups and potentially for different locations is computationally expensive. However, the practicality of the proposed approach benefits from the circumstance, that the computationally highly expensive hydrological model simulations can be done independently from processing of the remote sensing observations, *e.g.*, on HPC (high performance computing) clusters. Further, the model simulations only need to be done once for the desired time series and can then be endlessly analyzed for different remote sensing observations (in case the model set-up fits the remote sensing set-up). Hence, the final comparison of hydrological model outputs and remote sensing observations for soil moisture profile estimation is less computationally expensive and can further be done for every SAR observation date separately, enabling, *e.g.*, parallel processing. This allows soil moisture profile simulations to be less prone to errors since variable assumptions on critical input parameters, such as the initial pressure head or the upper soil condition, reduce the potential for erroneous model runs. Here, the decomposed SAR observations, after the removal of the vegetation and double-bounce scattering components, is employed to provide the most realistic simulation compared to actual observations and hence, the most suited initial model set-up. In a follow-on study, this approach could be even used to analyze and improve initial model conditions and their susceptibility to errors. Additionally, since remote sensing is able to provide areal observations, simulations could be improved even in regions, where less or no *in situ* point measurements for initializing the model are available, similar as outlined from (Ottlé et al., 1989). For instance, results indicate a potential need for improving the estimation of the soil hydraulic input parameters during model simulations, since the model was not able to capture dry soil conditions (*i.e.* below 8 vol%), *e.g.* at station US-SRS in Arizona, or overestimated soil moisture values at the dense forest station US-Ho1 in Maine (Fig. 5, Sec. 4.1.). At the dry station US-SRS, the highest deviations between estimated soil moisture profiles and *in situ* measurements are found during extended dry downs with no precipitation event, where the *in situ* measured soil moistures are most variable. Here, high changes in *in situ* measured soil moisture could be found within only a few centimeters of soil (see Sec. 4.1.). This raises the question of how reliable *in situ* soil moisture measurements are, when only few measurements at specific dates are picked out (instead of looking at continuous time series). Further, results at the woody savanna station, US-Ton, showed that static initial model parameters, such as the soil texture, are a strong assumption, which can lead to opposing soil moisture profiles (Fig. 5, 3rd row, Sec. 4.1.). Here, static soil conditions prevent that changes in soil hydraulic properties, due to precipitation or root water uptake, can be captured correctly in HYDRUS-1D model simulations. Not only depend the soil hydraulic properties on soil texture, but several studies showed that soil texture mediates the soil moisture dynamics to some degree (Case and Staver, 2018), and affect the soil moisture retention (Bouma and Bryla, 2000; Sperry and Hacke, 2002). Soil texture composition and its spatio-temporal variability determines how soils response to precipitation events due to its effect on water infiltration and surface runoff. For one, soils with low water permeability (*e.g.* clay soils) are more susceptible to high rates of water runoff, which decreases the available moisture in the soil (Case and Staver, 2018). Second, the study of Sperry and Hacke showed that rather loamy soils can have lower soil water potentials, and hence, lower soil moisture (Dingman, 2015), during summers than rather sandy soils, despite the higher precipitation over the loam site (Sperry and Hacke, 2002). Although, soil types are not that different at employed measuring stations (Fig. 1, Sec. 2.), this finding can be confirmed to some extent at the two in detail investigated stations, US-Ho1 and Stillwater 2 W (see Sec. 4.2.). While at the grassland station Stillwater 2 W the overall precipitation sum during the summer months (1164.9 mm) and the clay percentage (11%) is higher compared to at the forest station US-Ho1 (sum of 1092.8 mm, and 7% of clay), Stillwater 2 W shows overall lower soil moisture profile values (Figs. 5 & 6, Sec. 4.1., Figs. 7 & 8, Sec. 4.2.). In average, during the summer months at Stillwater 2 W, soil moisture profile values of 33.3 vol% are estimated compared to that at US-Ho1 of 46.6 vol%. These results also confirm the influence of vegetation cover on soil moisture profile results, since the influence of soil textures is potentially higher in non-vegetated areas (Gómez-Plaza et al., 2001). Further, studies proved that changes in soil textures over time due to plant and root growth influences how water flows in soils (Fatichi et al., 2020), and hence, affect the soil moisture profiles. In order to improve the performance of the proposed approach, or soil hydraulic models in general, variable soil texture or structure information over time during model simulations should be considered, but can not be realized in common models until now. Additional analyses between *in situ* measurements and the two auxiliary soil moisture products showed that sometimes, the auxiliary products outperform the proposed approach with better statistics. This is true, for example, for the dense forest station US-Ho1 due to the overestimation of retrieved soil moisture values (Fig. 5, Table 6). In the end however, all products showed reasonable results, but the proposed method has the advantage of

continuous determination of soil moisture information with depth without the assumption of non-physical polynomials and is able to provide soil moisture information at depths, where other *in situ* or remote sensing products cannot provide any continuous information with depth (mainly 0–5 cm).

In this study, estimated soil moisture profiles match the local climate and soil conditions. On the one hand, lower soil moisture values are estimated at drier measuring stations, like US-SRS or US-Var, and higher soil moisture values are found at wetter measuring stations, like US-Ho1 (Figs. 5 & 6, Sec. 4.1.). Further, the steepest profile shapes with rather quick changes in soil moisture values across the profile could be found at the driest station, US-SRS in Arizona, as shown in Fig. 4 (see Sec. 4.1.). By contrast, the most uniform profile shapes with less variabilities in soil moisture values across the vertical profile were estimated at the wet and most dense forest station US-Ho1 in Maine. Hence, the statement from (Wu et al., 2002) 'that soil wetness influences how quickly soil wetting/drying moves through the soil column' (Ford et al., 2014) can be confirmed here. On the other hand, analyses regarding average soil moisture profiles for respective dry and wet seasons of the three years (not shown) confirm that during the wet seasons soil moisture is more independent of the soil depth as variabilities across the vertical soil column average out, as demonstrated in (Konings et al., 2014). Further, deeper soil depths have an overall higher persistence of soil moisture than near the surface, as described by (Georgakakos and Bae, 1994), since the highest variabilities are always found in the uppermost part of the soil moisture profiles due to land-atmosphere interactions and feedback. Further, several studies have shown that near-surface and root zone soil moisture are correlated (Ford et al., 2014; Short Gianotti et al., 2019; Akbar et al., 2018). Hence, combining L-band and P-band microwave observations may even advance soil moisture profile approaches and help to analyze the complex link between near-surface and subsurface soil moisture in the future.

6. Conclusions

An approach for estimating continuous soil moisture profiles by combining remotely sensed SAR observations and soil hydraulic model simulations is proposed in this study. The advantages of this approach are, for one, the usage of soil scattering information from remotely sensed SAR observations after the removal of vegetation scattering from the total signal by a polarimetric decomposition. Hence, solely the soil component without influences of the vegetation are employed and no vegetation scattering effects have to be simulated. Second, regarding the soil hydraulic model, a variable set-up of initial assumptions is less prone to model errors. Instead of using just one model realization, as done in standard climate modeling, with potentially false initial assumptions, an ensemble of (realistic) simulations with varying initial assumptions is created, and then compared to actual SAR observations in order to receive the most realistic model set-up and soil moisture profile simulation.

The estimated soil moisture profiles are analyzed in the context of varying climatic and soil conditions as well as validated against several auxiliary soil moisture products (*in situ* measurements, the ERA5-land reanalysis, and the AirMOSS L4). Overall, estimated results agree with satisfying accuracy to *in situ* measurements and other auxiliary products (ERA5-land reanalysis and AirMOSS L4 mission products). The coefficients of determination between estimates and *in situ* values vary between 0.48 and 0.92. The lowest correlations could be found at rather dry desert stations since the employed soil hydraulic model almost always overestimates values. Here, higher correlations might be achieved by improving model initialization parameters, like the soil hydraulic properties, or using non-static soil property information over time. However, the achieved low Fréchet distances, varying between 0.1 and 0.23, showed, that the shape of estimated soil moisture profiles overall fit well to *in situ* measured profiles, what is needed in climate modeling (see Sec. 1.).

In summary, the proposed approach enables the possibility to estimate continuous soil moisture profiles with reasonable shape and accuracy based on remotely sensed observations and hydrological simulations. However, because of the coarse temporal resolution of the AirMOSS SAR observations (recorded from an airplane), no continuous time series analyzes for soil moisture estimations could be performed. Although, theoretically, estimations of timely-dense soil moisture profiles are feasible with this approach, since model simulations can be performed at any temporal scale. Changes in long-term soil moisture profile estimations are important as indicators, *e.g.*, for emerging droughts, with direct impact on agricultural productivity and food security (Almendra-Martín et al., 2021). Further, temporally continuous SAR observations would provide the opportunity to evaluate the performance of the HYDRUS-1D and its ability to capture temporal variations in soil moisture.

The first P-band SAR observations from space will be available from ESA's BIOMASS mission from 2024 onwards with a three-daily repeat pass configuration and 50 m to 200 m resolution (Gelas et al., 2021). As our approach makes use of SAR signals in combination with hydrological simulations, this opens the potential for the assimilation of BIOMASS mission data into hydrological models, using the multilayer SPM as observation operator for comparison with P-band SAR scattering angle observations, to finally update the upper soil states in the prediction step.

Lastly, the proposed approach can be easily used for estimating soil moisture profiles in space. In this study, estimations and analyses are conducted at selected *in situ* measuring stations only since all required input parameters are available from detailed field measurements at high quality, and in order to evaluate the overall performance of the proposed method. However, since remote sensing observations are available over larger areas, only the hydrological model would have to be initialized and driven with the required input parameters in space at comparable spatial resolution. Hence, with this approach the generation of soil moisture profile maps for providing soil moisture information in the horizontal, vertical, and z-direction are possible and will be analyzed in an add-on study.

CRediT authorship contribution statement

Anke Fluhrer: Conceptualization, Data curation, Formal analysis, Investigation, Methodology, Software, Validation, Visualization, Writing – original draft, Writing – review & editing. **Thomas Jagdhuber:** Conceptualization, Funding acquisition, Investigation, Methodology, Project administration, Supervision, Writing – review & editing. **Carsten Montzka:** Funding acquisition, Investigation, Project administration, Supervision, Writing – review & editing. **Maike Schumacher:** Supervision, Writing – review & editing. **Hamed Alemohammad:** Data curation, Resources, Writing – review & editing. **Alireza Tabatabaeenejad:** Software, Writing – review & editing. **Harald Kunstmann:** Investigation, Methodology, Supervision, Writing – review & editing. **Dara Entekhabi:** Methodology, Supervision, Writing – review & editing.

Declaration of competing interest

The authors declare that they have no known competing financial interests or personal relationships that could have appeared to influence the work reported in this paper.

Data availability

The authors do not have permission to share data.

Acknowledgements

This research was funded by the German Federal Ministry for

Economic Affairs and Energy (BMWi) through the German Aerospace Center within the AssimEO project (50EE1914A).

References

Akbar, R., Gianotti, D.S., McColl, K.A., Haghighi, E., Salvucci, G.D., Entekhabi, D., 2018. Hydrological storage length scales represented by remote sensing estimates of soil moisture and precipitation. Water Resour. Res. 54, 1476–1492. https://doi.org/10.1002/2017WR021508.

Alemohammad, S.H., Konings, A.G., Jagdhuber, T., Moghaddam, M., Entekhabi, D., 2018. Characterization of vegetation and soil scattering mechanisms across different biomes using P-band SAR polarimetry. Remote Sens. Environ. 209, 107–117. https://doi.org/10.1016/j.rse.2018.02.032.

Almendra-Martín, L., Martínez-Fernández, J., González-Zamora, Á., Benito-Verdugo, P., Herrero-Jiménez, C.M., 2021. Agricultural drought trends on the Iberian Peninsula: an analysis using modeled and reanalysis soil moisture products. Atmosphere 12, 236. https://doi.org/10.3390/atmos12020236.

AmeriFlux, 2022. https://ameriflux.lbl.gov (accessed on 15 March 2022).

Ashby, S.F., Falgout, R.D., 1996. A parallel multigrid preconditioned conjugate gradient algorithm for groundwater flow simulations. Nucl. Sci. Eng. 124, 145–159. https://doi.org/10.13182/NSE96-A24230.

Bell, J.E., Palecki, M.A., Baker, C.B., Collins, W.G., Lawrimore, J.H., Leeper, R.D., Hall, M.E., Kochendorfer, J., Meyers, T.P., Wilson, T., Diamond, H.J., 2013. U.S. climate reference network soil moisture and temperature observations. J. Hydrometeorol. 14, 977–988. https://doi.org/10.1175/JHM-D-12-0146.1.

Bojinski, S., Verstraete, M., Peterson, T.C., Richter, C., Simmons, A., Zemp, M., 2014. The concept of essential climate variables in support of climate research, applications, and policy. Bull. Am. Meteorol. Soc. 95, 1431–1443. https://doi.org/10.1175/BAMS-D-13-00047.1.

Bouma, T.J., Bryla, D.R., 2000. On the assessment of root and soil respiration for soils of different textures: interactions with soil moisture contents and soil CO2 concentrations. Plant Soil 227, 215–221. https://doi.org/10.1023/A:1026502414977.

Cai, G., Vanderborght, J., Couvreur, V., Mboh, C.M., Vereecken, H., 2018. Parameterization of root water uptake models considering dynamic root distributions and water uptake compensation. Vadose Zone J. 17, 160125 https://doi.org/10.2136/vzj2016.12.0125.

Case, M.F., Staver, A.C., 2018. Soil texture mediates tree responses to rainfall intensity in African savannas. New Phytol. 219, 1363–1372. https://doi.org/10.1111/nph.15254.

Chapin, E., Chau, A., Chen, J., Heavey, B., Hensley, S., Lou, Y., Machuzak, R., Moghaddam, M., 2012. AirMOSS: An airborne P-band SAR to measure root-zone soil moisture. In: 2012 IEEE Radar Conference. Presented at the 2012 IEEE Radar Conference (RadarCon). IEEE, Atlanta, GA, pp. 0693–0698. https://doi.org/10.1109/RADAR.2012.6212227.

Chung, S.-O., Horton, R., 1987. Soil heat and water flow with a partial surface mulch. Water Resour. Res. 23, 2175–2186. https://doi.org/10.1029/WR023i012p02175.

Cloude, S., 2010. Polarisation: Applications in Remote Sensing, 1st ed. Oxford University Press, Oxford, New York.

Crow, W.T., Milak, S., Reichle, R.H., 2016. AirMOSS: L4 Modeled Volumetric Root Zone Soil Moisture, 2012-2015 739558.31901 MB. https://doi.org/10.3334/ORNLDAAC/1421.

Dingman, S.L., 2015. Physical Hydrology, 3. ed. Waveland Press, Long Grove, Ill.

Dirmeyer, P.A., Wu, J., Norton, H.E., Dorigo, W.A., Quiring, S.M., Ford, T.W., Santanello, J.A., Bosilovich, M.G., Ek, M.B., Koster, R.D., Balsamo, G., Lawrence, D. M., 2016. Confronting weather and climate models with observational data from soil moisture networks over the United States. J. Hydrometeorol. 17, 1049–1067. https://doi.org/10.1175/JHM-D-15-0196.1.

Dirmeyer, P.A., Halder, S., Bombardi, R., 2018. On the harvest of predictability from land states in a global forecast model. J. Geophys. Res. Atmos. 123 https://doi.org/10.1029/2018JD029103.

Eiter, T., Mannila, H., 1994. Computing Discrete Fréchet Distance. Technical report CD-TR 94/64. Technical University Vienna.

Etminan, A., Tabatabaeenejad, A., Moghaddam, M., 2020. Retrieving root-zone soil moisture profile from P-band radar via hybrid global and local optimization. IEEE Trans. Geosci. Remote Sensing 58, 5400–5408. https://doi.org/10.1109/TGRS.2020.2965569.

Farthing, M.W., Ogden, F.L., 2017. Numerical solution of Richards' equation: a review of advances and challenges. Soil Sci. Soc. Am. J. 81, 1257–1269. https://doi.org/10.2136/sssaj2017.02.0058.

Fatichi, S., Or, D., Walko, R., Vereecken, H., Young, M.H., Ghezzehei, T.A., Hengl, T., Kollet, S., Agam, N., Avissar, R., 2020. Soil structure is an important omission in earth system models. Nat. Commun. 11, 522. https://doi.org/10.1038/s41467-020-14411-z.

Feddes, Reinder A., Kowalik, Piotr J., Zaradny, Henryk, Feddes, R.A., Kowalik, P.J., Zaradny, H., 1978. Simulation of Field Water Use and Crop Yield, Simulation Monographs. Centre for Agricultural Publishing and Documentation, Wageningen.

Feddes, R.A., Hoff, H., Bruen, M., Dawson, T., de Rosnay, P., Dirmeyer, P., Jackson, R.B., Kabat, P., Kleidon, A., Lilly, A., Pitman, A.J., 2001. Modeling root water uptake in hydrological and climate models. Bull. Amer. Meteor. Soc. 82, 2797–2809. https://doi.org/10.1175/1520-0477(2001)082<2797:MRWUIH>2.3.CO;2.

Fluhrer, A., Jagdhuber, T., Tabatabaeenejad, A., Alemohammad, H., Montzka, C., Friedl, P., Forootan, E., Kunstmann, H., 2022. Remote sensing of complex permittivity and penetration depth of soils using P-band SAR polarimetry. Remote Sens. 14, 2755. https://doi.org/10.3390/rs14122755.

Ford, T.W., Harris, E., Quiring, S.M., 2014. Estimating root zone soil moisture using near-surface observations from SMOS. Hydrol. Earth Syst. Sci. 18, 139–154. https://doi.org/10.5194/hess-18-139-2014.

Fréchet, M., 1906. Sur quelques points du calcul fonctionnel. Rendiconti del Circolo Matematico di Palermo (1884–1940) 22 (1), 1–72.

GDAL/OGR contributors, 2021. GDAL/OGR Geospatial Data Abstraction software Library. Open Source Geospatial Foundation. https://gdal.org.

Gelas, C., Villard, L., Ferro-Famil, L., Polidori, L., Koleck, T., Daniel, S., 2021. Multi-temporal speckle filtering of polarimetric P-band SAR data over dense tropical forests: study case in French Guiana for the BIOMASS Mission. Remote Sens. 13, 142. https://doi.org/10.3390/rs13010142.

Georgakakos, K.P., Bae, D.-H., 1994. Climatic variability of soil water in the American Midwest: Part 2. Spatio-temporal analysis. J. Hydrol. 162, 379–390. https://doi.org/10.1016/0022-1694(94)90237-2.

Gómez-Plaza, A., Martínez-Mena, M., Albaladejo, J., Castillo, V.M., 2001. Factors regulating spatial distribution of soil water content in small semiarid catchments. J. Hydrol. 253, 211–226. https://doi.org/10.1016/S0022-1694(01)00483-8.

He, L., Panciera, R., Tanase, M.A., Walker, J.P., Qin, Q., 2016. Soil moisture retrieval in agricultural fields using adaptive model-based polarimetric decomposition of SAR data. IEEE Trans. Geosci. Remote Sensing 54, 4445–4460. https://doi.org/10.1109/TGRS.2016.2542214.

Hollinger, D., 2021. AmeriFlux US-Ho1 Howland Forest (main tower), Ver. 7-5, AmeriFlux AMP, (dataset). https://doi.org/10.17190/AMF/1246061.

Homeland Infrastructure Foundation-Level Data (HIFLD), 2012. Political Boundaries. https://hifld-geoplatform.opendata.arcgis.com/ [Accessed 06/24/2019].

Homer, C., Dewitz, J., Yang, L., Jin, S., Danielson, P., Xian, G., Coulston, J., Herold, N., Wickham, J., Megown, K., 2015. Completion of the 2011 National Land Cover Database for the conterminous United States-representing a decade of land cover change information. Photogramm. Eng. Remote. Sens. 81, 345–354.

Huang, H., Liao, T.-H., Kim, S.B., Xu, X., Tsang, L., Jackson, T.J., Yueh, S., 2021. L-band radar scattering and soil moisture retrieval of wheat, canola and pasture fields for smap active algorithm. PIER 170, 129–152. https://doi.org/10.2528/PIER21020702.

Jagdhuber, T., 2012. Soil parameter retrieval under vegetation cover using SAR polarimetry. Ph.D. dissertation, Faculty of Science, Univ. Potsdam, Potsdam, Germany, 2012 [Online]. Available: http://opus.kobv.de/ubp/volltexte/2012/6051/.

Jagdhuber, T., Hajnsek, I., Papathanassiou, K.P., 2015. An iterative generalized hybrid decomposition for soil moisture retrieval under vegetation cover using fully polarimetric SAR. IEEE J. Sel. Top. Appl. Earth Observ. Remote Sensing 8, 3911–3922. https://doi.org/10.1109/JSTARS.2014.2371468.

Kim, S.-B., Liao, T.-H., 2021. Robust retrieval of soil moisture at field scale across wide-ranging SAR incidence angles for soybean, wheat, forage, oat and grass. Remote Sens. Environ. 266, 112712 https://doi.org/10.1016/j.rse.2021.112712.

Konings, A.G., Entekhabi, D., Moghaddam, M., Saatchi, S.S., 2014. The effect of variable soil moisture profiles on P-band backscatter. IEEE Trans. Geosci. Remote Sensing 52, 6315–6325. https://doi.org/10.1109/TGRS.2013.2296035.

Koster, R.D., Mahanama, S.P.P., Yamada, T.J., Balsamo, G., Berg, A.A., Boisserie, M., Dirmeyer, P.A., Doblas-Reyes, F.J., Drewitt, G., Gordon, C.T., Guo, Z., Jeong, J.-H., Lee, W.-S., Li, Z., Luo, L., Malyshev, S., Merryfield, W.J., Seneviratne, S.I., Stanelle, T., van den Hurk, B.J.J.M., Vitart, F., Wood, E.F., 2011. The second phase of the global land–atmosphere coupling experiment: soil moisture contributions to subseasonal forecast skill. J. Hydrometeorol. 12, 805–822. https://doi.org/10.1175/2011JHM1365.1.

Law, B., 2021. AmeriFlux US-Me6 Metolius Young Pine Burn, Ver. 15-5, AmeriFlux AMP, (Dataset). https://doi.org/10.17190/AMF/1246128.

Lei, F., Crow, W.T., Kustas, W.P., Dong, J., Yang, Y., Knipper, K.R., Anderson, M.C., Gao, F., Notarnicola, C., Greifeneder, F., McKee, L.M., Alfieri, J.G., Hain, C., Dokoozlian, N., 2020. Data assimilation of high-resolution thermal and radar remote sensing retrievals for soil moisture monitoring in a drip-irrigated vineyard. Remote Sens. Environ. 239, 111622 https://doi.org/10.1016/j.rse.2019.111622.

Liu, Q., Reichle, R.H., Bindlish, R., Cosh, M.H., Crow, W.T., de Jeu, R., De Lannoy, G.J. M., Huffman, G.J., Jackson, T.J., 2011. The contributions of precipitation and soil moisture observations to the skill of soil moisture estimates in a land data assimilation system. J. Hydrometeorol. 12, 750–765. https://doi.org/10.1175/JHM-D-10-05000.1.

Lucas, R.M., Moghaddam, M., Cronin, N., 2004. Microwave scattering from mixed-species forests, Queensland, Australia. IEEE Trans. Geosci. Remote Sensing 42, 2142–2159. https://doi.org/10.1109/TGRS.2004.834633.

Ma, S., Xu, L., Verfaillie, J., Baldocchi, D., 2021. AmeriFlux US-Ton Tonzi Ranch, Ver. 13-5, AmeriFlux AMP, (Dataset). https://doi.org/10.17190/AMF/1245971.

Ma, S., Xu, L., Verfaillie, J., Baldocchi, D., 2022. AmeriFlux US-Var Vaira ranch- Ione, Ver. 15-5, AmeriFlux AMP, (Dataset). https://doi.org/10.17190/AMF/1245984.

Maity, R., 2022. Statistical Methods in Hydrology and Hydroclimatology, Second, edition. ed. Springer transactions in civil and environmental engineering, Springer, Singapore.

Mironov, V.L., Kosolapova, L.G., Fomin, S.V., 2009. Physically and mineralogically based spectroscopic dielectric model for moist soils. IEEE Trans. Geosci. Remote Sensing 47, 2059–2070. https://doi.org/10.1109/TGRS.2008.2011631.

Moghaddam, M., Saatchi, S., 1995. Analysis of scattering mechanisms in SAR imagery over boreal forest: results from BOREAS '93. IEEE Trans. Geosci. Remote Sensing 33, 1290–1296. https://doi.org/10.1109/36.469495.

Moghaddam, M., Tabatabaeenejad, A., Chen, R.H., Saatchi, S., Jaruwatanadilok, S., Burgin, M., Duan, X., Truong-Loi, M.L., 2016. AirMOSS: L2/3 Volumetric Soil Moisture Profiles Derived From Radar, 2012-2015 2551.326499 MB. https://doi.org/10.3334/ORNLDAAC/1418.

Mualem, Y., 1976. A new model for predicting the hydraulic conductivity of unsaturated porous media. Water Resour. Res. 12, 513–522. https://doi.org/10.1029/WR012i003p00513.

Muñoz Sabater, J., 2019. ERA5-Land hourly data from 1981 to present. Copernicus Climate Change Service (C3S) Climate Data Store (CDS) (Accessed on 10-08-2022). https://doi.org/10.24381/CDS.E2161BAC.

Muñoz-Sabater, J., Dutra, E., Agustí-Panareda, A., Albergel, C., Arduini, G., Balsamo, G., Boussetta, S., Choulga, M., Harrigan, S., Hersbach, H., Martens, B., Miralles, D.G., Piles, M., Rodríguez-Fernández, N.J., Zsoter, E., Buontempo, C., Thépaut, J.-N., 2021. ERA5-Land: a state-of-the-art global reanalysis dataset for land applications. Earth Syst. Sci. Data 13, 4349–4383. https://doi.org/10.5194/essd-13-4349-2021.

Nakhaei, M., Šimůnek, J., 2014. Parameter estimation of soil hydraulic and thermal property functions for unsaturated porous media using the HYDRUS-2D code. J. Hydrol. Hydromech. 62, 7–15. https://doi.org/10.2478/johh-2014-0008.

Nauman, T., Ramcharan, A., Brungard, C., Thompson, J., Wills, S., Waltman, S., Hengl, T., 2017. Soil Properties and Class 100m Grids United States. https://doi.org/10.18113/S1KW2H.

Orgogozo, L., Renon, N., Soulaine, C., Hénon, F., Tomer, S.K., Labat, D., Pokrovsky, O.S., Sekhar, M., Ababou, R., Quintard, M., 2014. An open source massively parallel solver for Richards equation: mechanistic modelling of water fluxes at the watershed scale. Comput. Phys. Commun. 185, 3358–3371. https://doi.org/10.1016/j.cpc.2014.08.004.

Ottlé, C., Vidal-Madjar, D., Girard, G., 1989. Remote sensing applications to hydrological modeling. J. Hydrol. 105, 369–384. https://doi.org/10.1016/0022-1694(89)90114-5.

Peel, M.C., Finlayson, B.L., McMahon, T.A., 2007. Updated world map of the Köppen-Geiger climate classification. Hydrol. Earth Syst. Sci. 11, 1633–1644. https://doi.org/10.5194/hess-11-1633-2007.

QGIS Development Team, 2021. QGIS Geographic Information System. Open Source Geospatial Foundation Project. http://qgis.osgeo.org.

Reichle, R.H., De Lannoy, G.J.M., Liu, Q., Ardizzone, J.V., Colliander, A., Conaty, A., Crow, W., Jackson, T.J., Jones, L.A., Kimball, J.S., Koster, R.D., Mahanama, S.P., Smith, E.B., Berg, A., Bircher, S., Bosch, D., Caldwell, T.G., Cosh, M., González-Zamora, Á., Holifield Collins, C.D., Jensen, K.H., Livingston, S., Lopez-Baeza, E., Martínez-Fernández, J., McNairn, H., Moghaddam, M., Pacheco, A., Pellarin, T., Prueger, J., Rowlandson, T., Seyfried, M., Starks, P., Su, Z., Thibeault, M., van der Velde, R., Walker, J., Wu, X., Zeng, Y., 2017. Assessment of the SMAP Level-4 surface and root-zone soil moisture product using in situ measurements. J. Hydrometeorol. 18, 2621–2645. https://doi.org/10.1175/JHM-D-17-0063.1.

Rizzoli, P., Martone, M., Gonzalez, C., Wecklich, C., Borla Tridon, D., Bräutigam, B., Bachmann, M., Schulze, D., Fritz, T., Huber, M., Wessel, B., Krieger, G., Zink, M., Moreira, A., 2017. Generation and performance assessment of the global TanDEM-X digital elevation model. ISPRS J. Photogramm. Remote Sens. 132, 119–139. https://doi.org/10.1016/j.isprsjprs.2017.08.008.

Sadeghi, M., Tabatabaeenejad, A., Tuller, M., Moghaddam, M., Jones, S., 2016. Advancing NASA's AirMOSS P-band radar root zone soil moisture retrieval algorithm via incorporation of Richards' equation. Remote Sens. 9, 17. https://doi.org/10.3390/rs9010017.

Sandrock, C., Afshari, S., 2016. alchemyst/ternplot: DOI version (v1.1.0). Zenodo [Accessed 05/15/2020]. Zenodo. https://doi.org/10.5281/ZENODO.166760.

Sato, A., Yamaguchi, Y., Singh, G., Park, Sang-Eun, 2012. Four-component scattering power decomposition with extended volume scattering model. IEEE Geosci. Remote Sensing Lett. 9, 166–170. https://doi.org/10.1109/LGRS.2011.2162935.

Shi, Y., Davis, K.J., Duffy, C.J., Yu, X., 2013. Development of a coupled land surface hydrologic model and evaluation at a critical zone observatory. J. Hydrometeorol. 14, 1401–1420. https://doi.org/10.1175/JHM-D-12-0145.1.

Short Gianotti, D.J., Salvucci, G.D., Akbar, R., McColl, K.A., Cuenca, R., Entekhabi, D., 2019. Landscape water storage and subsurface correlation from satellite surface soil moisture and precipitation observations. Water Resour. Res. 55, 9111–9132. https://doi.org/10.1029/2019WR025332.

Šimůnek, J., Šejna, M., Saito, H., Sakai, M., Van Genuchten, M.Th., 2013. The HYDRUS-1D software package for simulating the one-dimensional movement of water, heat, and multiple solutes in variably-saturated media (Manual Version 4.17). Riverside, California.

Sperry, J.S., Hacke, U.G., 2002. Desert shrub water relations with respect to soil characteristics and plant functional type: *desert shrub water relations*. Funct. Ecol. 16, 367–378. https://doi.org/10.1046/j.1365-2435.2002.00628.x.

Tabatabaeenejad, A., Moghaddam, M., 2006. Bistatic scattering from three-dimensional layered rough surfaces. IEEE Trans. Geosci. Remote Sensing 44, 2102–2114. https://doi.org/10.1109/TGRS.2006.872140.

Tabatabaeenejad, A., Burgin, M., Duan, Xueyang, Moghaddam, M., 2015. P-band radar retrieval of subsurface soil moisture profile as a second-order polynomial: first AirMOSS results. IEEE Trans. Geosci. Remote Sensing 53, 645–658. https://doi.org/10.1109/TGRS.2014.2326839.

Tangdamrongsub, N., Han, S.-C., Yeo, I.-Y., Dong, J., Steele-Dunne, S.C., Willgoose, G., Walker, J.P., 2020. Multivariate data assimilation of GRACE, SMOS, SMAP measurements for improved regional soil moisture and groundwater storage estimates. Adv. Water Resour. 135, 103477 https://doi.org/10.1016/j.advwatres.2019.103477.

Tóth, B., Weynants, M., Nemes, A., Makó, A., Bilas, G., Tóth, G., 2015. New generation of hydraulic pedotransfer functions for Europe: new hydraulic pedotransfer functions for Europe. Eur. J. Soil Sci. 66, 226–238. https://doi.org/10.1111/ejss.12192.

van Zyl, J.J., Arii, M., Kim, Y., 2011. Model-based decomposition of polarimetric SAR covariance matrices constrained for nonnegative eigenvalues. IEEE Trans. Geosci. Remote Sensing 49, 3452–3459. https://doi.org/10.1109/TGRS.2011.2128325.

Vereecken, H., Amelung, W., Bauke, S.L., Bogena, H., Brüggemann, N., Montzka, C., Vanderborght, J., Bechtold, M., Blöschl, G., Carminati, A., Javaux, M., Konings, A.G., Kusche, J., Neuweiler, I., Or, D., Steele-Dunne, S., Verhoef, A., Young, M., Zhang, Y., 2022. Soil hydrology in the Earth system. Nat Rev Earth Environ 3, 573–587. https://doi.org/10.1038/s43017-022-00324-6.

Vivoni, E., 2022. AmeriFlux US-SRS Santa Rita Experimental Range Mesquite Savanna, Ver. 3-5, AmeriFlux AMP, (Dataset). https://doi.org/10.17190/AMF/1660351.

Walker, J.P., Willgoose, G.R., Kalma, J.D., 2001. One-dimensional soil moisture profile retrieval by assimilation of near-surface observations: a comparison of retrieval algorithms. Adv. Water Resour. 24, 631–650. https://doi.org/10.1016/S0309-1708(00)00043-9.

World Meteorological Organization, 2021. Comission for Observation, Infrastructure And Information Systems, Abridged Final Report of the First Session, WMO-No. 1251.

Wu, W., Geller, M.A., Dickinson, R.E., 2002. The response of soil moisture to long-term variability of precipitation. J. Hydrometeorol. 3, 604–613.

5 Synthesis

In this chapter, answers to the previously posed overarching research questions (see chapter 1.3) are given. In addition, the synthesis of the three presented research articles is discussed.

5.1 Answers to Research Questions

In chapter 1.3, three overarching research questions guiding the presented study were posed for analyzing remotely sensed microwave observations regarding geophysical soil parameter estimation. Based on the presented research articles, the following answers and conclusions can be given:

1. How can the combination of active and passive microwave remote sensing data be used to determine soil roughness parameters, and what are the advantages and disadvantages?

Microwave observations from radar and radiometer sensors can be combined through a quasi-linear relationship between the active backscatter and passive emissivity based on their covariation (Eqs. (8) & (9), chapter 1.2). This covariation-based approach provides the advantage of simultaneous estimation of both soil surface roughness parameters, the vertical RMS height s and the horizontal correlation length l. By combining active radar and passive radiometer measurements, the potential parameter search space for possible solutions is reduced, as shown in Figure 1 of article I (Fluhrer et al., 2020). Hence, the space for potential retrieval errors is reduced. Further, individual strengths are amplified while certain limitations are mitigated. For example, radar observations are sensitive to soil moisture and achieve a high spatial resolution (in terms of meters). In contrast, radiometer measurements are more sensitive to soil surface roughness and yield rather coarse spatial resolutions (in terms of kilometers). Thus, by combining both, the susceptibility of radar sensors to soil moisture and the susceptibility of radiometer sensors to surface roughness is reduced, and the better spatial resolution of radar sensors enhances resulting roughness maps in comparison to, for instance, radiometer-only approaches. Drawback of the covariation-based approach is the assumption of a linear relationship between active radar and passive radiometer measurements. As outlined by the study of (Zeng et al., 2022), this assumption generally holds but can significantly be affected by environmental factors, such as the amount of vegetation cover and particularly small or large dynamics in soil moisture conditions. In this study, this assumption is acceptable since only bare or low vegetated areas in dry (semi) deserts are analyzed. Therefore, article I provides the basis for simultaneous soil surface roughness

parameter estimation. However, continuing research on the covariation-based approach regarding vegetation covers and its variation is necessary. Another future research question would be to what degree the linear relationship holds true in order to fully explore the combination of active and passive microwave observations.

2. How do longwave (P-band) microwaves behave in interactions with different soil types and vegetation covers in terms of scattering mechanisms, soil moisture, and penetration depth?

Analyses showed that P-band microwaves at low frequencies (~430 MHz) can penetrate up to 5 cm to 35 cm through vegetation and into the soil, depending on the vegetation cover and soil characteristics (i.e., density, moisture, texture) that were investigated in this study. It was shown that at the dense forest campaign site in Harvard Forest, Massachusetts, on the more humid east coast of the U.S., soil permittivity (moisture) is higher, and hence, penetration depths are lower compared to other, less dense vegetated sites, such as the grassland site in Oklahoma. The lowest soil moisture and hence, highest penetration depths were found at the dry and sandy desert site in Arizona on the southern west coast of the U.S. (Fluhrer et al., 2022). In addition, after the separation of the total P-band SAR signal into individual scattering mechanisms by applying a hybrid decomposition technique, it was found that across the agricultural site in Oklahoma and the shrubland site in Arizona the volume scattering mechanism is dominant, compared to the soil- or dihedral-only scattering mechanisms. In contrast, over the dense forest site Harvard Forest, MA, the dihedral scattering mechanism is dominant. The strongly oriented vertical trunks of the trees and the overall higher penetration ability of P-band microwaves into the soil lead to this dominant dihedral scattering mechanism. Hence, it was found that at P-band, only SAR pixels with dominant soil scattering should be used for soil moisture retrievals. In contrast, in case of dominant dihedral scattering, an adapted approach is more suited for strongly vertical oriented forest types and designed to estimate soil and vegetation moisture. However, analyses also showed, that the removal of the vegetation component from the total SAR signal can only be an approximation and never be exact, leading to remaining artifacts of volume scattering in the extracted soil scattering component. Here, on-going research and the incorporation of, for example, machine learning can improve the extraction of relevant scattering components for moisture retrievals.

3. How can polarimetric active microwave remote sensing and soil hydrological modeling be combined for the estimation of vertically continuous soil moisture profiles?

The standard way to combine active microwave remote sensing with soil hydrological modeling is the comparison of radar backscatter observations and simulations, e.g., (Konings et al., 2014). On the one hand, polarimetric SAR systems record the backscatter coefficients of the land surface at co- (HH, VV) and cross- (HV, VH) polarizations. On the other hand, an ensemble of simulated soil moisture information from hydrological modeling based on varying input parameters can be used in an electromagnetic scattering model to compute representative backscatter coefficients at co-polarizations. Hence, by comparing the co-polarized SAR observations with the co-polarized simulations, soil moisture can be estimated. In this study, however, the comparison of remote sensing and hydrological modeling (including a soil scattering model) is done on the level of the polarimetric soil scattering angle α_s. This provides a more sophisticated and improved retrieval of soil moisture information, because soil moisture is estimated based on the soil scattering mechanism directly (after the removal of the vegetation scattering component) instead of using the total SAR signal, which contains all types of scattering. Second, no information is lost in the comparison with model simulations, since all co- and cross-polarized backscatter coefficients are used in the decomposition of the total SAR signal into individual scattering mechanisms (fully polarimetric approach). When using only co-polarized backscatters observations, important information gets lost since cross-polarized backscatters are particularly sensitive to vegetation structures and underlying soil characteristics (Jagdhuber 2012).

5.2 Discussion

The main drawbacks of remote sensing from space are the limitation of microwave sensors to narrow frequency bands within the electromagnetic spectrum and their rather coarse spatial resolution (predominantly passive remote sensing) (see chapter 1.2). Further, with regard to data availability, many frequencies are occupied by various applications, such as communications and navigation (Federal Communications Commission, 2022), and hence, not available for research sensors. Luckily, microwave sensors can be installed on any platform and thus, be used at field scale on a tower, e.g. (O'Neill et al., 2006), on UAVs, e.g., (Luo et al., 2019) and from airplanes, e.g., (Chapin et al., 2012), at sometimes lower temporal (ability to fly depends on weather and costs) but therefore significantly higher spatial resolution (in the order of tens of meters). The advantages and drawbacks of airborne and space-

borne remote sensing are shown and investigated in detail in this study. For one, due to the lack of operating P-band satellites in orbit, airborne SAR observations from NASA's AirMOSS mission are employed to provide basic as well as advanced knowledge on the scattering and penetration behavior of P-band microwaves across various landcover and soil types. In turn, the drawback of airborne acquisitions is, that only a small number of recording dates are available for every year, which is not sufficient enough for continuous time series evaluations and assessments of time-dynamic processes. Further, analyses showed that the varying incidence angles (20° to 60°) as a result of the airborne acquisition geometry has significant impact on the retrieval results (Fluhrer et al., 2022). This problem is obsolete in satellite remote sensing because of the static recording from one orbit at almost constant incidence angles across the swath, e.g., (Entekhabi et al., 2014). In return, satellite remote sensing faces some other difficulties, such as the much coarse spatial resolution or the challenge of ionospheric distortions at L- and P-band for the different polarization records due to atmospheric heterogeneities (Grima et al., 2015). The spatial resolution of the employed L-band active and passive microwave data from NASA's SMAP mission (Entekhabi et al., 2014) at ~36 km limits the feasible applications, and analyses can only provide large-scale roughness patterns as indication on land surface heterogeneity.

Regardless of whether airborne or space-borne observations are analyzed, a very well-known problem in the field of polarimetry and decomposition techniques is the overestimation of the vegetation scattering component (Cloude, 2010; He et al., 2016; van Zyl and Kim, 2008), which needs to be subtracted before soil moisture retrievals. This is solved in this study by including a large variety of vegetation characteristics during the modeling part, and by performing a pre-selection of realistic vegetation scattering components (excluding negative decomposed powers, using the radar vegetation index (RVI) to filter for outliers). However, this approach can be extended by assuming not only three scattering mechanisms (soil, vegetation, and double-bounce from combination of soil and vegetation) in the total SAR signal, but include a forth component to account, for instance, for pixel heterogeneity due to man-made objects and structures like (obliquely) oriented urban buildings, as done by (Yajima et al., 2008; Yamaguchi et al., 2011).

The presented research study deals with active and passive microwave remote sensing observations of different spatial and temporal resolutions. It is always necessary to carefully review which type of remote sensing data is needed for a specific research study. For example, remote sensing applications for weather monitoring and forecasting need a high temporal resolution because changes in weather can appear within just a few hours. Hence, sensors onboard of geostationary satellites are

required, as, for example, the Meteosat third generation (MTG) program from the European Organization for the Exploitation of Meteorological Satellites (EUMETSAT), which is significantly advancing Europeans geostationary meteorological satellite fleet (Holmlund et al., 2021), and the Geosynchronous Interferometric Infrared Sounder (GIIRS) onboard of a weather satellite (Ma et al., 2021). In contrast, when analyzing seasonal changes in soils and vegetation covers over an entire growing period, high temporal resolution can be traded for a high spatial resolution. This means, sensors onboard of polar sun-synchronous satellites are more useful with revisit times of two (e.g., Entekhabi et al., 2014) to 16 (e.g., Ihlen and Zanter, 2019) days but potentially high (in the order of meters) spatial resolution to be able to distinguish between different fields or even species and habitats. In this study, on the one hand, radar and radiometer observations from the SMAP mission are used with moderate temporal resolution (2-3 days) and rather coarse spatial resolution (36 km) in order to investigate the potential of the proposed active-passive microwave retrieval approach for simultaneous soil surface roughness estimation (Fluhrer et al., 2020). Since surface roughness changes mainly occur after precipitation, through wind effects or agricultural practices (Marzahn et al., 2012; Marzahn and Ludwig, 2009), the chosen dataset fits the research design and enables the investigation of large-scale land surface heterogeneity. In this study, the focus was more driven by the fact that the proposed approach needs active and passive microwave measurements with comparable acquisition geometry, spatio-temporal resolution and recording time, which cannot be found that easily among operating microwave remote sensing sensors. On the other hand, airborne SAR data at good spatial resolution (~ 90 m) but coarse temporal resolution (4 to 5 dates per year) are employed for soil moisture retrieval analyses (Fluhrer et al., 2024, 2022). Since soil moisture changes may occur within just a few meters, a high (in the order of centimeters to meters) spatial resolution is required. However, due to the airborne acquisition and lack of currently existing P-band satellites in orbit, the coarse temporal resolution of the employed AirMOSS dataset prohibits any time series analyses, although *in situ* measurements and soil hydrological modeling outputs are available at high temporal resolution. Here, a comparable high temporal resolution of the P-band SAR microwave data would significantly enhance the presented research but is unfortunately not obtainable at the time of finalizing the research study.

Up to now, studies for estimating soil moisture profiles from the land surface up to the upper root zone generally include polynomial fitting (e.g., (Sadeghi et al., 2016)), regression (e.g., (Jackson et al., 1987; Zotova and Geller, 1985)), knowledge-based approaches with a priori information (e.g., (Mkrtchjan et al., 1988; Ragab, 1995)), inversion (e.g., (Entekhabi et al., 1994)), combinations of remote sensing data with soil

water balance or hydrological models (e.g., (Bernard et al., 1986; Konings et al., 2014; Ragab, 1995)), and assimilation (e.g., (Crosson et al., 2002; Tobin et al., 2020)). All of these techniques have their individual strengths and limitations. The drawbacks are model-specific and include a high-degree of simplification of reality (e.g., polynomial fitting, regression), a lack of transferability from one study area to another (e.g., regression), a high demand for a priori knowledge on the hydrological state of the investigated soil (e.g., knowledge-based approach), as well as a demand for multiple remote sensing datasets (e.g., inversion). In this study, remote sensing data with soil models (hydraulics and electromagnetics) are combined. This way, the knowledge gained from remote sensing is merged with model simulations based on physical, hydrological laws (i.e., Richards equation) in order to extend the retrieval of lateral soil moisture (as can be done from remote sensing alone) to vertically continuous profiles (not possible with single-pass space-borne remote sensing). Hence, the proposed approach is able to provide soil moisture information continuously with depth from remote sensing combined with modeling. Conducted sensitivity analyses showed that soil moisture profile simulations based on the hydrological model can vary significantly depending on pre-defined model constraints, such as initial assumptions on certain input parameters, like the initial pressure head and the upper boundary condition for water flow. By using an ensemble-based set-up of hydrological model simulations in combination with observed information from remote sensing, vertically continuous and physically realistic soil moisture profiles with reasonable accuracy in absolute values as well as in profile shapes can be estimated. At some stations (dense forest and dry semi-desert), an overestimation of *in situ* measurements lead to a decrease in correlations. Despite this decrease in correlations, it was found that the shape of the estimated soil moisture profiles fit quite well to *in situ* measurements and low Fréchet distances, which represent the shape similarity. This similarity in shape is an important outcome that is necessary, for instance, in weather forecasting and climate modeling (Dirmeyer et al., 2016; Koster et al., 2010).

For the comparison of electromagnetic model simulations and remote sensing observations, knowledge on the scattering and penetration behavior of the microwaves is required. It was found that for increasing vegetation volume (forests), the dihedral scattering mechanism becomes the dominant mechanism at P-band wavelengths, which is in line with previous studies, e.g., (Lucas et al., 2004; Moghaddam and Saatchi, 1995). This fact influences the soil moisture retrieval performance and hence, estimation of penetration capabilities, since the extracted soil scattering component (used for the soil moisture retrieval) may be too weak to retrieve reliable soil moisture information across strongly stem-dominated (vertically oriented) forests.

6 Conclusions

In this research study, microwave remote sensing observations of low frequencies (430 MHz to 1.4 GHz) are analyzed regarding their scattering behavior, their interaction with soil and/or vegetation, and their applicability for retrieval of important soil parameters. The presented results confirmed the feasibility of the proposed methods and showed them to be consistent with either atmospheric conditions, soil characteristics or *in situ* field measurements.

The proposed L-band active/passive microwave retrieval approach highlighted the benefits of combining radar and radiometer observations for a joint estimation of geophysical parameters. It could be demonstrated that with this approach realistic soil surface roughness patterns across bare and low vegetated areas can be estimated. The approach can even be extended for vegetated soils in an add-on study and hence, provide global, time- variable surface roughness maps of horizontal (l) and vertical soil roughness (s). These are needed, for instance, in electromagnetic, weather and climate, runoff as well as soil erosion models. The main drawback of this approach is the coarse spatial resolution of the radiometer data. Here, latest research seeks to improve the spatial resolution of passive microwave remote sensing, e.g., (Sugihara El Maghraby et al., 2018; Luetzner et al., 2022), which in turn would improve the soil roughness retrieval approach and its possible applications.

Thorough P-band SAR data analyses also confirmed the great potential of low frequency radar data for soil moisture estimation and emphasize the demand for temporally and spatially high-resolution P-band observations at global scale. Detailed analyses regarding the scattering behavior of the P-band SAR signal across various types of landscapes showed that over dense forests the decomposed dihedral scattering mechanism is dominant in the total SAR signal compared to soil- or vegetation-only scattering. This finding originates from the strong vertical structure of tree trunks and showed to concur with previous studies. Hence, based on the presented study and results, on-going research regarding soil and vegetation moisture estimation from P-band dihedral scattering components is recommended. At the time of writing, only soil moisture can be estimated from the extracted soil scattering components of the total SAR signal. However, by analyzing the dihedral scattering component of the P-band SAR signal, soil and vegetation moisture can be estimated simultaneously, enabling global vegetation moisture maps in volumetric units from active remote sensing observations (not available from polarimetric SAR at the time of this writing).

Overall, knowledge about the penetration depth of microwaves is of enormous importance with regard to the determination of geophysical quantities as well as the assessment of sensing volumes and actual sensitivity of remote sensing. Through the combination of microwave remote sensing and soil hydrological modeling, and the subsequent derived soil moisture profiles, which indicate the variation in soil moisture between the land surface to the upper root zone, it is confirmed that soil moisture can be highly variable with depth, depending on soil type and atmospheric conditions. And since the propagation behavior of an electromagnetic wave is highly dependent on moisture, the wave penetration ability plays an important role in soil moisture estimation. Based on the estimated complex soil permittivity from P-band SAR signals it is shown that soil penetration depths of P-band microwaves are 5 cm to 35 cm for given soil conditions. However, the calculation of the penetration depth is limited on the sensor frequency and the complex soil permittivity, although it is known that the penetration capability of microwaves depends on many more factors, such as sensor characteristics (e.g., incidence angle, transmitted energy, band width) and soil characteristics (e.g., texture, bulk density, microstructure) (see chapter 1.2). Hence, more sophisticated equations for defining the penetration depth may improve microwave remote sensing estimates.

In addition, estimated soil moisture variation with soil depth depends on the soil hydrological modeling with HYDRUS-1D, which can always only approximate the reality. Here, research regarding the initial hydraulic soil conditions (i.e., Van Genuchten parameters) or employed sub-models (i.e., the root water uptake model) could improve hydrological model simulations and currently insufficient model performances across very dry desert regions (see chapter 4). In addition, a combination of L- and P-band remote sensing information can enhance the estimation of soil moisture profiles, especially near the soil surface (first 5 cm in depth) where *in situ* measurements are insufficiently available. Further, the removal of the volume scattering component during the hybrid decomposition technique is identified as an option for enhancing soil moisture (profile) estimation from fully polarimetric SAR data. Here, machine learning can be implemented to improve the modeling of the volume scattering prior to the extraction of the soil scattering component from the total SAR signal. Overall, all on-going research regarding P-band SAR scattering decomposition and moisture estimation is relevant in the context of the upcoming BIOMASS mission from ESA and the future SNOOPI mission from NASA (see chapter 1.2). Although, BIOMASS will not be allowed to record microwave data at P-band over North America and Central Europe, especially interesting regions, like the tropical rain forest, can be analyzed and investigated with this mission.

7 Outlook

In this PhD study, remote sensing observations from always one sensor system together with suitable models are used for geophysical parameter estimation. In the last years, machine learning has shown to be able to exceed the limits of possibilities not only in satellite remote sensing. With data fusion techniques and artificial intelligence approaches significant advances in science are feasible. The possibilities in this direction seem endless and are developing rapidly. For example, by combining observations from multiple sensors (e.g., radar, radiometer, optical, hyperspectral, infrared) and by employing machine learning (e.g., support vector machines, ensemble algorithms) or artificial neural networks, more advanced estimation of important parameters, like soil moisture (Ben Abbes and Jarray, 2023; Singh and Gaurav, 2023; Yuan et al., 2019), or improved downscaling of spatially coarse resoluted satellite data (Zhao et al., 2018) are possible. Hence, it will be interesting, e.g., to combine high resolution P-band satellite observation of the BIOMASS mission with already available higher frequency (L- to C-band) satellite (i.e., Sentinel-1, ALOS PALSAR, SMAP) and optical (i.e., Landsat, MODIS) data through data fusion techniques, and analyze the different compartments of the tropical and temperate rainforests, which are known for the different vegetation and moisture levels from forest floor and understory to the top of the canopy. Here, remote sensing sensors with varying microwave frequencies record different layers due to their specific penetration capabilities. Moreover, all the planned future satellite missions, like BIOMASS, NASA-ISRO SAR (NISAR) (Rosen and Kumar, 2021), Radar Observing System for Europe at L-band (ROSE-L) (Davidson and Furnell, 2021), ESA's Sentinel-1 next generation (NG) (Torres et al., 2023), and many other, promise constantly growing availability of spatially and temporally high resolution remote sensing data, which can only advance Earth system research.

Last but not least, not only data fusion of different remote sensing systems can facilitate advanced Earth system and climate change research, but also assimilation of remote sensing parameters in hydrological modeling. Varying assimilation techniques of remotely sensed soil parameters, such as soil moisture, in hydrological models already improve model performances (Montzka et al., 2013). Here, research regarding the assimilation of, for instance, high resolution soil moisture patterns from remote sensing in hydrological models, such as the mesoscale hydrological model (mHm) (Samaniego et al., 2010) and Weather Research and Forecasting model (WRF-Hydro) (Fersch et al., 2020), may facilitate the prediction accuracy of models, and improve our understanding of essential hydrological and environmental processes within ecosystem.

List of Symbols

α	Attenuation factor, [-]
α_{P-PP}	Intercept of linear regression for given polarization P, [-]
α_s	Soil scattering angle, [°]
β_{P-PP}	Slope of linear regression for given polarization P, called covariation parameter, [-]
β_{P-PP}^{Data}	Data-based covariation parameter, [-]
β_{P-PP}^{Model}	Model-based covariation parameter, [-]
δ_P	Penetration depth, [cm]
e	Euler's number, mathematical constant ~2.71828, [-]
ε	Actual permittivity of a dielectric, $[F/m]$
ε_0	Permittivity of vacuum, $[F/m]$; $\varepsilon_0 = 8.85 * 10^{-12}$ $[F/m]$
E_P	Emissivity for given polarization P, [-]
ε_r	Relative permittivity, [-]
ε_s	Soil permittivity, [-]
$\varepsilon_s{}'$	Real part of the soil permittivity, [-]
$\varepsilon_s{}''$	Imaginary part of the soil permittivity, [-]
F	Fréchet distance, [-]
H_R	Passive roughness parameter, [-]
j	Imaginary unit to describe a complex number, [-]
k	Wave number, [cm^{-1}]
ks	Wave number scaled vertical RMS height s, [-]
kl	Wave number scaled horizontal correlation length l, [-]
l	Horizontal correlation length, [cm]
λ	Wavelength, [cm]

μ_r	Relative magnetic permeability, [-]
ω	Effective vegetation scattering albedo, [-]
ω_f	Angular frequency, [rad/s]
π	Mathematical constant, the ratio of a circle's circumference to its diameter, [-]
R	Pearson's correlation coefficient [-]
R^2	Pearson's coefficient of determination, [-]
s	Vertical root mean square height, [cm]
S	Siemens, unit of electric conductance, susceptance, and admittance, [$kg^{-1} \cdot m^{-2} \cdot s^3 \cdot A^2$]
$\lvert S_{PP} \rvert^2$	Backscattering coefficient for given polarization P, [dB]
σ	Soil conductivity, [S/m]
τ	Vegetation optical depth, [Np]
θ_s	Soil moisture, [-] or [vol.%]

List of Abbreviations

AirMOSS	Airborne Microwave Observatory of Subcanopy and Subsurface
ALOS	Advanced Land Observing Satellite
CONUS	Continental United States
DEM	Digital Elevation Model
ESA	European Space Agency
EUMETSAT	European Organization for the Exploitation of Meteorological Satellites
I^2EM	improved Integral Equation Model
IEEE	Institute of Electrical and Electronics Engineer
IPCC	Intergovernmental Panel on Climate Change
ISRO	Indian Space Research Organization
GEO	Geostationary
GHz	Gigahertz
GIIRS	Geosynchronous Interferometric Infrared Sounder
mHm	mesoscale hydrological model
MHz	Megahertz
MODIS	Moderate-resolution Imaging Spectroradiometer
MTG	Meteosat Third Generation
NASA	National Aeronautics and Space Administration
NG	Next Generation
NISAR	NASA-ISRO SAR
NMM3D	Numerical Maxwell Model in 3D
P	Polarization
PALSAR	Phased Array type L-band Synthetic Aperture Radar

RMS	Root Mean Square
$RMSE$	Root Mean Square Error
ROSE-L	Radar Observing System for Europe in L-band
RVI	Radar Vegetation Index
SAR	Synthetic Aperture Radar
SMAP	Soil Moisture Active Passive
SMOS	Soil Moisture Ocean Salinity
SNOOPI	SigNals Of Opportunity P-band Investigation
SPM	Small Perturbation Method
UAV	Unmanned Aerial Vehicles
$ubRMSE$	unbiased Root Mean Square Error
U.S.	United States
WRF	Weather Research and Forecasting

Bibliography

Alemohammad, S.H., Konings, A.G., Jagdhuber, T., Moghaddam, M., Entekhabi, D., 2018. Characterization of vegetation and soil scattering mechanisms across different biomes using P-band SAR polarimetry. Remote Sensing of Environment 209, 107–117. https://doi.org/10.1016/j.rse.2018.02.032

Almendra-Martín, L., Martínez-Fernández, J., González-Zamora, Á., Benito-Verdugo, P., Herrero-Jiménez, C.M., 2021. Agricultural Drought Trends on the Iberian Peninsula: An Analysis Using Modeled and Reanalysis Soil Moisture Products. Atmosphere 12, 236. https://doi.org/10.3390/atmos12020236

Álvarez-Mozos, J., Verhoest, N., Larrañaga, A., Casalí, J., González-Audícana, M., 2009. Influence of Surface Roughness Spatial Variability and Temporal Dynamics on the Retrieval of Soil Moisture from SAR Observations. Sensors 9, 463–489. https://doi.org/10.3390/s90100463

Babaeian, E., Sadeghi, M., Jones, S.B., Montzka, C., Vereecken, H., Tuller, M., 2019. Ground, Proximal, and Satellite Remote Sensing of Soil Moisture. Rev. Geophys. 57, 530–616. https://doi.org/10.1029/2018RG000618

Bakker, M., Nieber, J.L., 2004. Analytic Element Modeling of Cylindrical Drains and Cylindrical Inhomogeneities in Steady Two-Dimensional Unsaturated Flow. Vadose Zone Journal 3, 1038–1049. https://doi.org/10.2136/vzj2004.1038

Bannawat, L., Boonpoonga, A., Akkaraekthalin, P., 2020. Permittivity estimation of a shallow-layered medium using high-resolution ground-penetrating radar. International Journal of Remote Sensing 41, 4626–4643. https://doi.org/10.1080/01431161.2020.1723177

Ben Abbes, A., Jarray, N., 2023. Unsupervised self-training method based on deep learning for soil moisture estimation using synergy of sentinel-1 and sentinel-2 images. International Journal of Image and Data Fusion 14, 1–14. https://doi.org/10.1080/19479832.2022.2106317

Bernard, R., Soares, J.V., Vidal-Madjar, D., 1986. Differential Bare Field Drainage Properties From Airborne Microwave Observations. Water Resour. Res. 22, 869–875. https://doi.org/10.1029/WR022i006p00869

Bojinski, S., Verstraete, M., Peterson, T.C., Richter, C., Simmons, A., Zemp, M., 2014. The Concept of Essential Climate Variables in Support of Climate Research, Applications, and Policy. Bulletin of the American Meteorological Society 95, 1431–1443. https://doi.org/10.1175/BAMS-D-13-00047.1

Chapin, E., Chau, A., Chen, J., Heavey, B., Hensley, S., Lou, Y., Machuzak, R., Moghaddam, M., 2012. AirMOSS: An Airborne P-band SAR to measure root-zone soil moisture, in: 2012 IEEE Radar Conference. Presented at the 2012 IEEE Radar Conference (RadarCon), IEEE, Atlanta, GA, pp. 0693–0698. https://doi.org/10.1109/RADAR.2012.6212227

Choudhury, B.J., Schmugge, T.J., Chang, A., Newton, R.W., 1979. Effect of surface roughness on the microwave emission from soils. J. Geophys. Res. 84, 5699. https://doi.org/10.1029/JC084iC09p05699

Cloude, S., 2010. Polarisation: applications in remote sensing, 1st ed. ed. Oxford University Press, Oxford ; New York.

Crosson, W.L., Laymon, C.A., Inguva, R., Schamschula, M.P., 2002. Assimilating remote sensing data in a surface flux-soil moisture model. Hydrol. Process. 16, 1645–1662. https://doi.org/10.1002/hyp.1051

Davidson, M.W.J., Furnell, R., 2021. ROSE-L: Copernicus L-Band Sar Mission, in: 2021 IEEE International Geoscience and Remote Sensing Symposium IGARSS. Presented at the IGARSS 2021 - 2021 IEEE International Geoscience and Remote Sensing Symposium, IEEE, Brussels, Belgium, pp. 872–873. https://doi.org/10.1109/IGARSS47720.2021.9554018

Dingman, S.L., 2015. Physical hydrology, 3. ed. ed. Waveland Press, Long Grove, Ill.

Dirmeyer, P.A., Halder, S., Bombardi, R., 2018. On the Harvest of Predictability From Land States in a Global Forecast Model. J. Geophys. Res. Atmos. 123. https://doi.org/10.1029/2018JD029103

Dirmeyer, P.A., Wu, J., Norton, H.E., Dorigo, W.A., Quiring, S.M., Ford, T.W., Santanello, J.A., Bosilovich, M.G., Ek, M.B., Koster, R.D., Balsamo, G., Lawrence, D.M., 2016. Confronting Weather and Climate Models with Observational Data from Soil Moisture Networks over the United States. Journal of Hydrometeorology 17, 1049–1067. https://doi.org/10.1175/JHM-D-15-0196.1

Dobson, M., Ulaby, F., Hallikainen, M., El-rayes, M., 1985. Microwave Dielectric Behavior of Wet Soil-Part II: Dielectric Mixing Models. IEEE Trans. Geosci. Remote Sensing GE-23, 35–46. https://doi.org/10.1109/TGRS.1985.289498

Engelhardt, W. von, Zimmermann, J., 1988. Theory of earth science. Cambridge University Press, Cambridge [England] ; New York.

Entekhabi, D. et al., 2014. SMAP handbook.

Entekhabi, D., Nakamura, H., Njoku, E.G., 1994. Solving the inverse problem for soil moisture and temperature profiles by sequential assimilation of multifrequency remotely sensed observations. IEEE Trans. Geosci. Remote Sensing 32, 438–448. https://doi.org/10.1109/36.295058

Etminan, A., Tabatabaeenejad, A., Moghaddam, M., 2020. Retrieving Root-Zone Soil Moisture Profile From P-Band Radar via Hybrid Global and Local Optimization. IEEE Trans. Geosci. Remote Sensing 58, 5400–5408. https://doi.org/10.1109/TGRS.2020.2965569

Federal Communications Commission, 2022. Radio Spectrum Allocation. Accessible at https://www.fcc.gov/engineering-technology/policy-and-rules-division/general/radio-spectrum-allocation [last accessed on May, 8th, 2023].

Fersch, B., Senatore, A., Adler, B., Arnault, J., Mauder, M., Schneider, K., Völksch, I., Kunstmann, H., 2020. High-resolution fully coupled atmospheric–hydrological modeling: a cross-compartment regional water and energy cycle evaluation. Hydrol. Earth Syst. Sci. 24, 2457–2481. https://doi.org/10.5194/hess-24-2457-2020

Fluhrer, A., Jagdhuber, T., Akbar, R., O'Neill, P.E., Entekhabi, D., 2020. Simultaneous Retrieval of Surface Roughness Parameters for Bare Soils From Combined Active-Passive Microwave SMAP Observations. IEEE Trans. Geosci. Remote Sensing 1–13. https://doi.org/10.1109/TGRS.2020.3035204

Fluhrer, A., Jagdhuber, T., Montzka, C., Schumacher, M., Alemohammad, H., Tabatabaeenejad, A., Kunstmann, H., Entekhabi, D., 2024. Soil moisture profile estimation by combining P-band SAR polarimetry with hydrological and multi-layer scattering models. Elsevier Remote Sensing of Environment 305. https://doi.org/10.1016/j.rse.2024.114067

Fluhrer, A., Jagdhuber, T., Tabatabaeenejad, A., Alemohammad, H., Montzka, C., Friedl, P., Forootan, E., Kunstmann, H., 2022. Remote Sensing of Complex Permittivity and Penetration Depth of Soils Using P-Band SAR Polarimetry. Remote Sensing 14, 2755. https://doi.org/10.3390/rs14122755

Fung, A.K., Liu, W.Y., Chen, K.S., Tsay, M.K., 2002. An Improved Iem Model for Bistatic Scattering From Rough Surfaces. Journal of Electromagnetic Waves and Applications 16, 689–702. https://doi.org/10.1163/156939302X01119

Garrison, J.L., Vega, M.A., Shah, R., Mansell, J.R., Nold, B., Raymond, J., Banting, R., Bindlish, R., Larsen, K., Kim, S., Li, W., Kurum, M., Piepmeier, J., Khalifi, H., Tanner, F.A., Horgan, K., Kielbasa, C.E., Babu, S.R., 2024. SNOOPI: Demonstrating Earth remote sensing using P-band signals of opportunity (SoOp) on a CubeSat. Advances in Space Research 73, 2855–2879. https://doi.org/10.1016/j.asr.2023.10.050

GCOS, 2015. Status of the Global Observing System for Climate, GCOS Report No. 195, https://library.wmo.int/index.php?lvl=notice_display&id=18962.

Gelas, C., Villard, L., Ferro-Famil, L., Polidori, L., Koleck, T., Daniel, S., 2021. Multi-Temporal Speckle Filtering of Polarimetric P-Band SAR Data over Dense Tropical Forests: Study Case in French Guiana for the BIOMASS Mission. Remote Sensing 13, 142. https://doi.org/10.3390/rs13010142

Gómez, C., White, J.C., Wulder, M.A., 2016. Optical remotely sensed time series data for land cover classification: A review. ISPRS Journal of Photogrammetry and Remote Sensing 116, 55–72. https://doi.org/10.1016/j.isprsjprs.2016.03.008

Grima, C., Blankenship, D.D., Schroeder, D.M., 2015. Radar signal propagation through the ionosphere of Europa. Planetary and Space Science 117, 421–428. https://doi.org/10.1016/j.pss.2015.08.017

Gururaj, P., Umesh, P., Shetty, A., 2021. Assessment of surface soil moisture from ALOS PALSAR-2 in small-scale maize fields using polarimetric decomposition technique. Acta Geophys. 69, 579–588. https://doi.org/10.1007/s11600-021-00557-x

He, L., Panciera, R., Tanase, M.A., Walker, J.P., Qin, Q., 2016. Soil Moisture Retrieval in Agricultural Fields Using Adaptive Model-Based Polarimetric Decomposition of SAR Data. IEEE Trans. Geosci. Remote Sensing 54, 4445–4460. https://doi.org/10.1109/TGRS.2016.2542214

Hoeben, R., Troch, P.A., 2000. Assimilation of active microwave observation data for soil moisture profile estimation. Water Resour. Res. 36, 2805–2819. https://doi.org/10.1029/2000WR900100

Holmlund, K., Grandell, J., Schmetz, J., Stuhlmann, R., Bojkov, B., Munro, R., Lekouara, M., Coppens, D., Viticchie, B., August, T., Theodore, B., Watts, P., Dobber, M., Fowler, G., Bojinski, S., Schmid, A., Salonen, K., Tjemkes, S., Aminou, D., Blythe, P., 2021. Meteosat Third Generation (MTG): Continuation and Innovation of Observations from Geostationary Orbit. Bulletin of the American Meteorological Society 102, E990–E1015. https://doi.org/10.1175/BAMS-D-19-0304.1

Ihlen, V., Zanter, K., 2019. Landsat 8 (L8) Data Users Handbook, version 5.0, available at https://www.usgs.gov/media/files/landsat-8-data-users-handbook. Department of the Interior U.S. Geological Survey (USGS).

IPCC, 2021. Summary for Policymakers. In: Climate Change 2021: The Physical Science Basis. Contribution of Working Group I to the Sixth Assessment Report of the Intergovernmental Panel on Climate Change [Masson-Delmotte, V., P. Zhai, A. Pirani, S.L. Connors, C. Péan, S. Berger, N. Caud, Y. Chen, L. Goldfarb, M.I. Gomis, M. Huang, K. Leitzell, E. Lonnoy, J.B.R. Matthews, T.K. Maycock, T. Waterfield, O. Yelekçi, R. Yu, and B. Zhou (eds.)]. . Cambridge University Press, Cambridge, United Kingdom and New York, NY, USA 3–32. https://doi.org/10.1017/9781009157896.001

Jackson, T.J., Hawley, M.E., O'Neill, P.E., 1987. PREPLANTING SOIL MOISTURE USING PASSIVE MICROWAVE SENSORS. J Am Water Resources Assoc 23, 11–19. https://doi.org/10.1111/j.1752-1688.1987.tb00779.x

Jagdhuber, T., 2012. "Soil parameter retrieval under vegetation cover using SAR polarimetry," Ph.D. dissertation, Faculty of Science, Univ. Potsdam, Potsdam, Germany, 2012 [Online]. Available: http://opus.kobv.de/ubp/volltexte/2012/6051/.

Jagdhuber, T., Hajnsek, I., Papathanassiou, K.P., 2015. An Iterative Generalized Hybrid Decomposition for Soil Moisture Retrieval Under Vegetation Cover Using Fully Polarimetric SAR. IEEE J. Sel. Top. Appl. Earth Observations Remote Sensing 8, 3911–3922. https://doi.org/10.1109/JSTARS.2014.2371468

Kamutzki, F., Schneider, S., Barowski, J., Gurlo, A., Hanaor, D.A.H., 2021. Silicate dielectric ceramics for millimetre wave applications. Journal of the European Ceramic Society 41, 3879–3894. https://doi.org/10.1016/j.jeurceramsoc.2021.02.048

Kelleners, T.J., Robinson, D.A., Shouse, P.J., Ayars, J.E., Skaggs, T.H., 2005. Frequency Dependence of the Complex Permittivity and Its Impact on Dielectric Sensor Calibration in Soils. Soil Sci. Soc. Am. J. 69, 67–76. https://doi.org/10.2136/sssaj2005.0067a

Kerr, Y.H., Al-Yaari, A., Rodriguez-Fernandez, N., Parrens, M., Molero, B., Leroux, D., Bircher, S., Mahmoodi, A., Mialon, A., Richaume, P., Delwart, S., Al Bitar, A., Pellarin, T., Bindlish, R., Jackson, T.J., Rüdiger, C., Waldteufel, P., Mecklenburg, S., Wigneron, J.-P., 2016. Overview of SMOS performance in terms of global soil moisture monitoring after six years in operation. Remote Sensing of Environment 180, 40–63. https://doi.org/10.1016/j.rse.2016.02.042

Kim, S., Garrison, J.L., Kurum, M., 2023. Retrieval of Subsurface Soil Moisture and Vegetation Water Content from Multi-frequency SoOp-Reflectometry: Sensitivity Analysis. IEEE Trans. Geosci. Remote Sensing 1–1. https://doi.org/10.1109/TGRS.2023.3284800

Klausing, H., Holpp, W., 2000. Radar mit realer und synthetischer Apertur: Konzeption und Realisierung. Oldenbourg, München.

Klenk, P., Schmidt, K., Kraus, T., Bachmann, M., Schwerdt, M., 2022. TerraSAR-X / TanDEM-X Mission and Calibration Status. EUSAR 2022; 14th European Conference on Synthetic Aperture Radar, Leipzig, Germany; 1–5.

Konings, A.G., Entekhabi, D., Moghaddam, M., Saatchi, S.S., 2014. The Effect of Variable Soil Moisture Profiles on P-Band Backscatter. IEEE Trans. Geosci. Remote Sensing 52, 6315–6325. https://doi.org/10.1109/TGRS.2013.2296035

Koster, R.D., Mahanama, S.P.P., Yamada, T.J., Balsamo, G., Berg, A.A., Boisserie, M., Dirmeyer, P.A., Doblas-Reyes, F.J., Drewitt, G., Gordon, C.T., Guo, Z., Jeong, J.-H., Lawrence, D.M., Lee, W.-S., Li, Z., Luo, L., Malyshev, S., Merryfield, W.J., Seneviratne, S.I., Stanelle, T., van den Hurk, B.J.J.M., Vitart, F., Wood, E.F., 2010. Contribution of land surface initialization to subseasonal forecast skill: First results from a multi-model experiment: GLACE-2-SOIL MOISTURE AND FORECASTING. Geophys. Res. Lett. 37, n/a-n/a. https://doi.org/10.1029/2009GL041677

Koster, R.D., Mahanama, S.P.P., Yamada, T.J., Balsamo, G., Berg, A.A., Boisserie, M., Dirmeyer, P.A., Doblas-Reyes, F.J., Drewitt, G., Gordon, C.T., Guo, Z., Jeong, J.-

H., Lee, W.-S., Li, Z., Luo, L., Malyshev, S., Merryfield, W.J., Seneviratne, S.I., Stanelle, T., van den Hurk, B.J.J.M., Vitart, F., Wood, E.F., 2011. The Second Phase of the Global Land–Atmosphere Coupling Experiment: Soil Moisture Contributions to Subseasonal Forecast Skill. Journal of Hydrometeorology 12, 805–822. https://doi.org/10.1175/2011JHM1365.1

Kraus, J.D., Carver, K.R., 1973. Electromagnetics, 2d ed. ed, McGraw-Hill electrical and electronic engineering series. McGraw-Hill, New York.

Lansbury Hall, N., Crosby, L., 2022. Climate Change Impacts on Health in Remote Indigenous Communities in Australia. International Journal of Environmental Health Research 32, 487–502. https://doi.org/10.1080/09603123.2020.1777948

Lee, J.-S., Pottier, E., 2009. Polarimetric radar imaging: from basics to applications, Optical science and engineering. CRC Press, Boca Raton.

Lillesand, T.M., Kiefer, R.W., Chipman, J.W., 2013. Remote sensing and image interpretation, 6. ed., student ed. ed. Wiley, New Delhi.

Lucas, R.M., Moghaddam, M., Cronin, N., 2004. Microwave scattering from mixed-species forests, Queensland, Australia. IEEE Trans. Geosci. Remote Sensing 42, 2142–2159. https://doi.org/10.1109/TGRS.2004.834633

Luetzner, M., Jagdhuber, T., Camps, A., Park, H., Peichl, M., Forstner, R., Jirousek, M., 2022. Orbit Design for a Satellite Swarm-Based Motion Induced Synthetic Aperture Radiometer (MISAR) in Low-Earth Orbit for Earth Observation Applications. IEEE Trans. Geosci. Remote Sensing 60, 1–16. https://doi.org/10.1109/TGRS.2022.3152898

Luo, W., Xu, X., Liu, W., Liu, M., Li, Z., Peng, T., Xu, C., Zhang, Y., Zhang, R., 2019. UAV based soil moisture remote sensing in a karst mountainous catchment. CATENA 174, 478–489. https://doi.org/10.1016/j.catena.2018.11.017

Ma, Z., Li, J., Han, W., Li, Z., Zeng, Q., Menzel, W.P., Schmit, T.J., Di, D., Liu, C., 2021. Four-Dimensional Wind Fields From Geostationary Hyperspectral Infrared Sounder Radiance Measurements With High Temporal Resolution. Geophysical Research Letters 48. https://doi.org/10.1029/2021GL093794

Marzahn, P., Ludwig, R., 2009. On the derivation of soil surface roughness from multi parametric PolSAR data and its potential for hydrological modeling. Hydrol. Earth Syst. Sci. 13, 381–394. https://doi.org/10.5194/hess-13-381-2009

Marzahn, P., Rieke-Zapp, D., Ludwig, R., 2012. Assessment of soil surface roughness statistics for microwave remote sensing applications using a simple photogrammetric acquisition system. ISPRS Journal of Photogrammetry and Remote Sensing 72, 80–89. https://doi.org/10.1016/j.isprsjprs.2012.06.005

McColl, K.A., Alemohammad, S.H., Akbar, R., Konings, A.G., Yueh, S., Entekhabi, D., 2017. The global distribution and dynamics of surface soil moisture. Nature Geosci 10, 100–104. https://doi.org/10.1038/ngeo2868

Mengen, D., Jagdhuber, T., Balenzano, A., Mattia, F., Vereecken, H., Montzka, C., 2023. High Spatial and Temporal Soil Moisture Retrieval in Agricultural Areas Using Multi-Orbit and Vegetation Adapted Sentinel-1 SAR Time Series. Remote Sensing 15, 2282. https://doi.org/10.3390/rs15092282

Mironov, V.L., Dobson, M.C., Kaupp, V.H., Komarov, S.A., Kleshchenko, V.N., 2002. Generalized refractive mixing dielectric model for moist soils, in: IEEE International Geoscience and Remote Sensing Symposium. Presented at the IEEE International Geoscience and Remote Sensing Symposium. IGARSS 2002, IEEE, Toronto, Ont., Canada, pp. 3556–3558. https://doi.org/10.1109/IGARSS.2002.1027247

Mironov, V.L., Kosolapova, L.G., Fomin, S.V., 2009. Physically and Mineralogically Based Spectroscopic Dielectric Model for Moist Soils. IEEE Trans. Geosci. Remote Sensing 47, 2059–2070. https://doi.org/10.1109/TGRS.2008.2011631

Mkrtchjan, F.A., Reutov, E.A., Shutko, A.M., Kostov, K.G., Michalev, M.A., Nedeltchev, N.M., 1988. Microcomputer-based Radiometer Data Acquisition And Processing System For Large-area Mapping Of Soil Moisture Content In The Top One Meter Layer, in: International Geoscience and Remote Sensing Symposium, "Remote Sensing: Moving Toward the 21st Century". Presented at the International Geoscience and Remote Sensing Symposium, "Remote Sensing: Moving Toward the 21st Century"., IEEE, Edinburgh, UK, pp. 1563–1564. https://doi.org/10.1109/IGARSS.1988.569523

Mo, T., Choudhury, B.J., Schmugge, T.J., Wang, J.R., Jackson, T.J., 1982. A model for microwave emission from vegetation-covered fields. J. Geophys. Res. 87, 11229. https://doi.org/10.1029/JC087iC13p11229

Moghaddam, M., Saatchi, S., 1995. Analysis of scattering mechanisms in SAR imagery over boreal forest: results from BOREAS '93. IEEE Trans. Geosci. Remote Sensing 33, 1290–1296. https://doi.org/10.1109/36.469495

Montzka, C., Grant, J.P., Moradkhani, H., Franssen, H.-J.H., Weihermüller, L., Drusch, M., Vereecken, H., 2013. Estimation of Radiative Transfer Parameters from L-Band Passive Microwave Brightness Temperatures Using Advanced Data Assimilation. Vadose Zone Journal 12, vzj2012.0040. https://doi.org/10.2136/vzj2012.0040

Narvekar, P.S., Entekhabi, D., Kim, S.-B., Njoku, E.G., 2015. Soil Moisture Retrieval Using L-Band Radar Observations. IEEE Trans. Geosci. Remote Sensing 53, 3492–3506. https://doi.org/10.1109/TGRS.2014.2377714

Njagi, D.M., Routh, J., Odhiambo, M., Luo, C., Basapuram, L.G., Olago, D., Klump, V., Stager, C., 2022. A century of human-induced environmental changes and the combined roles of nutrients and land use in Lake Victoria catchment on eutrophication. Science of The Total Environment 835, 155425. https://doi.org/10.1016/j.scitotenv.2022.155425

Njoku, E.G., Wilson, W.J., Yueh, S.H., Dinardo, S.J., Li, F.K., Jackson, T.J., Lakshmi, V., Bolten, J., 2002. Observations of soil moisture using a passive and active low-frequency microwave airborne sensor during SGP99. IEEE Trans. Geosci. Remote Sensing 40, 2659–2673. https://doi.org/10.1109/TGRS.2002.807008

O'Neill, P.E., Lang, R.H., Kurum, M., Utku, C., Carver, K.R., 2006. Multi-Sensor Microwave Soil Moisture Remote Sensing: NASAų Combined Radar/Radiometer (ComRAD) System, in: 2006 IEEE MicroRad. Presented at the 2006 IEEE MicroRad, IEEE, San Juan, Puerto Rico, pp. 50–54. https://doi.org/10.1109/MICRAD.2006.1677061

Pablos, M., González-Zamora, Á., Sánchez, N., Martínez-Fernández, J., 2018. Assessment of Root Zone Soil Moisture Estimations from SMAP, SMOS and MODIS Observations. Remote Sensing 10, 981. https://doi.org/10.3390/rs10070981

Pan, R., Martinez, A., Brito, T., Seidel, E., 2018. Processes of Soil Infiltration and Water Retention and Strategies to Increase Their Capacity. JEAI 20, 1–14. https://doi.org/10.9734/JEAI/2018/39132

Park, C.-H., Behrendt, A., LeDrew, E., Wulfmeyer, V., 2017. New Approach for Calculating the Effective Dielectric Constant of the Moist Soil for Microwaves. Remote Sensing 9, 732. https://doi.org/10.3390/rs9070732

Peterson, A.M., Helgason, W.D., Ireson, A.M., 2016. Estimating field-scale root zone soil moisture using the cosmic-ray neutron probe. Hydrol. Earth Syst. Sci. 20, 1373–1385. https://doi.org/10.5194/hess-20-1373-2016

Ragab, R., 1995. Towards a continuous operational system to estimate the root-zone soil moisture from intermittent remotely sensed surface moisture. Journal of Hydrology 173, 1–25. https://doi.org/10.1016/0022-1694(95)02749-F

Reed, K.A., Wehner, M.F., Zarzycki, C.M., 2022. Attribution of 2020 hurricane season extreme rainfall to human-induced climate change. Nat Commun 13, 1905. https://doi.org/10.1038/s41467-022-29379-1

Reichardt, K., Timm, L.C., 2020. Soil, Plant and Atmosphere: Concepts, Processes and Applications. Springer International Publishing, Cham. https://doi.org/10.1007/978-3-030-19322-5

Rosen, P.A., Kumar, R., 2021. NASA-ISRO SAR (NISAR) Mission Status, in: 2021 IEEE Radar Conference (RadarConf21). Presented at the 2021 IEEE Radar Conference (RadarConf21), IEEE, Atlanta, GA, USA, pp. 1–6. https://doi.org/10.1109/RadarConf2147009.2021.9455211

Sadeghi, M., Tabatabaeenejad, A., Tuller, M., Moghaddam, M., Jones, S., 2016. Advancing NASA's AirMOSS P-Band Radar Root Zone Soil Moisture Retrieval Algorithm via Incorporation of Richards' Equation. Remote Sensing 9, 17. https://doi.org/10.3390/rs9010017

Samaniego, L., Kumar, R., Attinger, S., 2010. Multiscale parameter regionalization of a grid-based hydrologic model at the mesoscale. Water Resources Research 46, 2008WR007327. https://doi.org/10.1029/2008WR007327

Schaber, G., McCauley, J., Breed, C., Olhoeft, G., 1986. Shuttle Imaging Radar: Physical Controls on Signal Penetration and Subsurface Scattenng in the Eastern Sahara. IEEE Trans. Geosci. Remote Sensing GE-24, 603–623. https://doi.org/10.1109/TGRS.1986.289677

Schowengerdt, R.A., 2007. Remote sensing: models and methods for image processing, 3rd ed. ed. Academic Press, Burlington, MA.

Sentinel-1 Team (ESA), 2013. Sentinel-1 User Handbook. Availbable at https://sentinel.esa.int/, accessed on 14th of April 2023.

Shi, H., Zhao, L., Yang, J., Lopez-Sanchez, J.M., Zhao, J., Sun, W., Shi, L., Li, P., 2021. Soil moisture retrieval over agricultural fields from L-band multi-incidence and multitemporal PolSAR observations using polarimetric decomposition techniques. Remote Sensing of Environment 261, 112485. https://doi.org/10.1016/j.rse.2021.112485

Shukla, M., 2014. Soil physics: an introduction. CRC Press, Boca Raton.

Šimůnek, J., Šejna, M., Saito, H., Sakai, M., Van Genuchten, M.Th., 2013. The HYDRUS-1D software package for simulating the one-dimensional movement of water, heat, and multiple solutes in variably-saturated media (Manual Version 4.17). Riverside, California.

Singh, A., Gaurav, K., 2023. Deep learning and data fusion to estimate surface soil moisture from multi-sensor satellite images. Sci Rep 13, 2251. https://doi.org/10.1038/s41598-023-28939-9

Srivastava, P.K., O'Neill, P., Cosh, M., Kurum, M., Lang, R., Joseph, A., 2015. Evaluation of Dielectric Mixing Models for Passive Microwave Soil Moisture Retrieval Using Data From ComRAD Ground-Based SMAP Simulator. IEEE J. Sel. Top. Appl. Earth Observations Remote Sensing 8, 4345–4354. https://doi.org/10.1109/JSTARS.2014.2372031

Sugihara El Maghraby, A.K., Grubisic, A., Colombo, C., Tatnall, A., 2018. A Novel Interferometric Microwave Radiometer Concept Using Satellite Formation Flight for Geostationary Atmospheric Sounding. IEEE Trans. Geosci. Remote Sensing 56, 3487–3498. https://doi.org/10.1109/TGRS.2018.2800534

Thirel, G., Andréassian, V., Perrin, C., 2015. On the need to test hydrological models under changing conditions. Hydrological Sciences Journal 60, 1165–1173. https://doi.org/10.1080/02626667.2015.1050027

Tobin, K.J., Torres, R., Bennett, M.E., Dong, J., Crow, W.T., 2020. Long-Term Trends in Root-Zone Soil Moisture across CONUS Connected to ENSO. Remote Sensing 12, 2037. https://doi.org/10.3390/rs12122037

Topp, G.C., Davis, J.L., Annan, A.P., 1980. Electromagnetic determination of soil water content: Measurements in coaxial transmission lines. Water Resour. Res. 16, 574–582. https://doi.org/10.1029/WR016i003p00574

Torres, R., Geudtner, D., Davidson, M., 2023. Copernicus Sentinel-1 Next Generation Mission: Enhanced C-Band Data Continuity and Novel Imaging Capabilities, in: IGARSS 2023 - 2023 IEEE International Geoscience and Remote Sensing Symposium. Presented at the IGARSS 2023 - 2023 IEEE International Geoscience and Remote Sensing Symposium, IEEE, Pasadena, CA, USA, pp. 4564–4567. https://doi.org/10.1109/IGARSS52108.2023.10281871

Truong-Loi, M.-L., Saatchi, S., Jaruwatanadilok, S., 2015. Soil Moisture Estimation Under Tropical Forests Using UHF Radar Polarimetry. IEEE Trans. Geosci. Remote Sensing 53, 1718–1727. https://doi.org/10.1109/TGRS.2014.2346656

Tsang, L., Koh, I.-S., Liao, T.-H., Huang, S., Xu, X., Njoku, E.G., Kerr, Y.H., 2013. Active and Passive Vegetated Surface Models With Rough Surface Boundary Conditions From NMM3D. IEEE J. Sel. Top. Appl. Earth Observations Remote Sensing 6, 1698–1709. https://doi.org/10.1109/JSTARS.2013.2257694

Ulaby, F.T., Long, D.G., 2014. Microwave radar and radiometric remote sensing. The University of Michigan Press, Ann Arbor.

Ulaby, F.T., Moore, R.K., Fung, A.K., Ulaby, F.T., 1982. Microwave remote sensing, Active and Passive, Vol. II: Radar remote sensing and surface scattering and emission theory. ARTECH House, MA, USA.

Upadhyay, V., Kumar, A., 2018. Hyperspectral Remote Sensing of Forests: Technological advancements, Opportunities and Challenges. Earth Sci Inform 11, 487–524. https://doi.org/10.1007/s12145-018-0345-7

van Zyl, J.J., Kim, Y., 2008. Requirements for Model-Based Polarimetric Decompositions. 7th European Conference on Synthetic Aperture Radar.

Vereecken, H., Amelung, W., Bauke, S.L., Bogena, H., Brüggemann, N., Montzka, C., Vanderborght, J., Bechtold, M., Blöschl, G., Carminati, A., Javaux, M., Konings, A.G., Kusche, J., Neuweiler, I., Or, D., Steele-Dunne, S., Verhoef, A., Young, M., Zhang, Y., 2022. Soil hydrology in the Earth system. Nat Rev Earth Environ 3, 573–587. https://doi.org/10.1038/s43017-022-00324-6

von Hippel, A.R., 1954. Dielectrics and Waves. Wiley, New York.

Wagner, A., Fersch, B., Yuan, P., Rummler, T., Kunstmann, H., 2022. Assimilation of GNSS and Synoptic Data in a Convection Permitting Limited Area Model: Improvement of Simulated Tropospheric Water Vapor Content. Front. Earth Sci. 10, 869504. https://doi.org/10.3389/feart.2022.869504

Wagner, W., Lemoine, G., Rott, H., 1999. A Method for Estimating Soil Moisture from ERS Scatterometer and Soil Data. Remote Sensing of Environment 70, 191–207. https://doi.org/10.1016/S0034-4257(99)00036-X

Ward, R.C., Robinson, M., 1990. Principles of hydrology, 3rd ed. ed. McGraw-Hill, London ; New York.

Wigneron, J.-P., Jackson, T.J., O'Neill, P., De Lannoy, G., de Rosnay, P., Walker, J.P., Ferrazzoli, P., Mironov, V., Bircher, S., Grant, J.P., Kurum, M., Schwank, M., Munoz-Sabater, J., Das, N., Royer, A., Al-Yaari, A., Al Bitar, A., Fernandez-Moran, R., Lawrence, H., Mialon, A., Parrens, M., Richaume, P., Delwart, S., Kerr, Y., 2017. Modelling the passive microwave signature from land surfaces: A review of recent results and application to the L-band SMOS & SMAP soil moisture retrieval algorithms. Remote Sensing of Environment 192, 238–262. https://doi.org/10.1016/j.rse.2017.01.024

Wilheit, T.T., 1978. Radiative Transfer in a Plane Stratified Dielectric. IEEE Trans. Geosci. Electron. 16, 138–143. https://doi.org/10.1109/TGE.1978.294577

Yajima, Y., Yamaguchi, Y., Sato, R., Yamada, H., Boerner, W.-M., 2008. POLSAR Image Analysis of Wetlands Using a Modified Four-Component Scattering Power Decomposition. IEEE Trans. Geosci. Remote Sensing 46, 1667–1673. https://doi.org/10.1109/TGRS.2008.916326

Yamaguchi, Y., Sato, A., Boerner, W.-M., Sato, R., Yamada, H., 2011. Four-Component Scattering Power Decomposition With Rotation of Coherency Matrix. IEEE Trans. Geosci. Remote Sensing 49, 2251–2258. https://doi.org/10.1109/TGRS.2010.2099124

Yuan, Q., Li, S., Yue, L., Li, T., Shen, H., Zhang, L., 2019. Monitoring the Variation of Vegetation Water Content with Machine Learning Methods: Point–Surface Fusion of MODIS Products and GNSS-IR Observations. Remote Sensing 11, 1440. https://doi.org/10.3390/rs11121440

Zeng, J., Shi, P., Chen, K.-S., Ma, H., Bi, H., Cui, C., 2022. On the Relationship Between Radar Backscatter and Radiometer Brightness Temperature From SMAP. IEEE Trans. Geosci. Remote Sensing 60, 1–16. https://doi.org/10.1109/TGRS.2021.3115140

Zhang, Jiang, Zhao, Chai, Li, Pan, 2019. Development of a Parameterized Model to Estimate Microwave Radiation Response Depth of Frozen Soil. Remote Sensing 11, 2028. https://doi.org/10.3390/rs11172028

Zhao, W., Sánchez, N., Lu, H., Li, A., 2018. A spatial downscaling approach for the SMAP passive surface soil moisture product using random forest regression. Journal of Hydrology 563, 1009–1024. https://doi.org/10.1016/j.jhydrol.2018.06.081

Zotova, E.N., Geller, A.G., 1985. Soil moisture content estimation by radar survey data during the sowing campaign. International Journal of Remote Sensing 6, 353–364. https://doi.org/10.1080/01431168508948449